

MODELING AND APPLICATION OF ARTIFICIAL MUSCLE ACTUATORS

A THESIS SUBMITTED TO  
THE GRADUATE SCHOOL OF NATURAL AND APPLIED SCIENCES  
OF  
MIDDLE EAST TECHNICAL UNIVERSITY

BY

FAHRI BUĞRA ÇAMLICA

IN PARTIAL FULFILLMENT OF THE REQUIREMENTS  
FOR  
THE DEGREE OF DOCTOR OF PHILOSOPHY  
IN  
MECHANICAL ENGINEERING

APRIL 2019



Approval of the thesis:

**MODELING AND APPLICATION OF ARTIFICIAL MUSCLE  
ACTUATORS**

submitted by **FAHRI BUĞRA ÇAMLICA** in partial fulfillment of the requirements  
for the degree of **Doctor of Philosophy in Mechanical Engineering Department,  
Middle East Technical University** by,

Prof. Dr. Halil Kalıpçılar  
Dean, Graduate School of **Natural and Applied Sciences**

\_\_\_\_\_

Prof. Dr. M. A. Sahir Arıkan  
Head of Department, **Mechanical Engineering**

\_\_\_\_\_

Prof. Dr. Y. Samim Ünlüsoy  
Supervisor, **Mechanical Engineering, METU**

\_\_\_\_\_

**Examining Committee Members:**

Prof. Dr. R. Tuna Balkan  
Mechanical Engineering Department, METU

\_\_\_\_\_

Prof. Dr. Y. Samim Ünlüsoy  
Mechanical Engineering, METU

\_\_\_\_\_

Prof. Dr. Yavuz Yaman  
Aerospace Engineering Department, METU

\_\_\_\_\_

Assist. Prof. Dr. Kutluk Bilge Arıkan  
Mechanical Engineering Department, TED University

\_\_\_\_\_

Assist. Prof. Dr. Emir Kutluay  
Mechanical Engineering Department, Hacettepe University

\_\_\_\_\_

Date: 10.04.2019

**I hereby declare that all information in this document has been obtained and presented in accordance with academic rules and ethical conduct. I also declare that, as required by these rules and conduct, I have fully cited and referenced all material and results that are not original to this work.**

Name, Surname: Fahri Buğra Çamlıca

Signature:

## ABSTRACT

### MODELING AND APPLICATION OF ARTIFICIAL MUSCLE ACTUATORS

Çamlıca, Fahri Buğra  
Doctor of Philosophy, Mechanical Engineering  
Supervisor: Prof. Dr. Y. Samim Ünlüsoy

April 2019, 284 pages

*Electro Active Polymers (EAPs)* are the group of polymeric materials which are also known as the *Artificial Muscles* that are already available commercially or can be manufactured in laboratory conditions. Artificial muscle actuators are considered as alternatives to conventional electric/pneumatic/hydraulic devices in certain applications which require lightweight actuators. Artificial muscle actuators are not yet capable of completing heavy duty missions, however these flexible actuators do not require additional mechanisms for actuation and their high efficiency outputs make them a strong alternative to conventional systems in future applications.

This study is motivated by the potential of the materials known as artificial muscles in replacing the conventional actuators, particularly in aero structures where the weight and cost advantages are strongly emphasized. An exhaustive experimental study of the properties of a suitable representative material is carried out and the mathematical characterization of the material is performed. A model as a typical example of an aero structure in the form of a wing trailing edge is used to establish the capabilities and to ascertain the possibility of application in aero structures.

Keywords: Dielectric Elastomer, Material Characterization, Electromechanical Characterization, Smart Material, Soft Actuator

## ÖZ

### YAPAY KAS EYLEYİCİLERİN MODELLENMESİ VE UYGULAMASI

Çamlıca, Fahri Buğra  
Doktora, Makina Mühendisliği  
Tez Danışmanı: Prof. Dr. Y. Samim Ünlüsoy

Nisan 2019, 284 sayfa

Polimer malzeme grubu içinde yer alan *Elektro Aktif Polimerler (EAP)* aynı zamanda *Yapay Kaslar* olarak da bilinmektedirler. Bu malzemeler ticari olarak bulunabildiği gibi laboratuvar koşullarında da üretilebilirler. Yapay kas eyleyiciler, hafifliğin gerektiği özel uygulamalarda konvansiyonel elektrik/pnömatik/hidrolik cihazlara alternatif olarak düşünülebilirler. Yapay kas eyleyiciler günümüz koşullarında ağır yük işlerini tamamlayabilecek kapasitede olmamakla birlikte, bu esnek eyleyiciler çalışmak için de ek mekanizmalara ihtiyaç duymamaktadırlar. Yüksek verimle çalışmaları gelecekte onları konvansiyonel sistemlere göre güçlü bir alternatif haline getirmektedir.

Bu çalışmanın motivasyonu yapay kas olarak bilinen malzemelerin özellikle ağırlık ve maliyet unsurlarının önem kazandığı havacılık yapılarında mevcut konvansiyonel eyleyicilerin yerine kullanılacak alternatifler oluşturabilmeleridir. Bu çalışmada örnek bir malzeme seçilerek, tüm özellikleri bütünleşik bir deneysel sistem ile belirlenmiş ve matematiksel modellemesi yapılmıştır. Tipik bir uçak kanadının fırrar kenarının modelini temsil eden bir düzenek kullanılarak, yapay kas malzemenin hava yapılarındaki kabiliyeti ve uygulanabilirliği incelenmiştir.

Anahtar Kelimeler: Dielektrik Elastomer, Malzeme Karakterizasyonu, Elektromekanik Karakterizasyon, Akıllı Malzemeler, Yumuşak Eyleyiciler



To My Sons..

## ACKNOWLEDGMENTS

This project is supported and funded by Turkish Aerospace according to the SAYP protocol signed between Presidency of Defense Industries (SSB), Turkish Aerospace and Middle East Technical University (METU).

This study involved many drawbacks including uncertainties, planning, engineering issues and collaborations with many parties. Prof. Dr. Y. Samim Ünlüsoy is the most critical advisor who guided me to solve all of these engineering and inter-relational conflicts with all his expertise. His incontrovertible support to this new era of research will be mentioned among the ones who will study to similar projects in the future. I am very grateful for his calm and focus oriented guidance. His approach to problem solving will be the greatest earning for the rest of my life. I am very proud to be one of his students.

Next, I would like to thank to Prof. Dr. R. Tuna Balkan and Prof. Dr. Yavuz Yaman who were my thesis committee members for their valuable feedbacks and supports.

Then, I am also grateful to Sinan Özgün Demir, Dr. Gökhan Özgen and Dr. Ulaş Yaman who helped and supported me during my journey.

Finally, I would like to thank to my wife Özge for her endless support. While I was studying for days and nights, she believed in me and took care of our family.

## TABLE OF CONTENTS

ABSTRACT .....	v
ÖZ .....	vii
ACKNOWLEDGMENTS .....	x
TABLE OF CONTENTS .....	xi
LIST OF TABLES .....	xv
LIST OF FIGURES .....	xvi
LIST OF ABBREVIATIONS .....	xxiv
CHAPTERS	
1. INTRODUCTION .....	1
1.1. Motivation and Contribution .....	3
1.2. Thesis Overview .....	4
2. LITERATURE REVIEW .....	7
2.1. Introduction .....	7
2.2. Background of EAPs .....	9
2.2.1. Ionic Polymers .....	13
2.2.2. Electronic Polymers .....	16
2.2.3. Smart Like Materials .....	19
2.3. In Depth Review of Dielectric Elastomers .....	20
2.3.1. Materials .....	22
2.3.2. Electrodes .....	25
2.3.3. Design and Manufacturing Performance Parameters .....	28
2.3.4. Pre-straining .....	31

2.3.5. Actuator Configurations .....	32
2.3.6. Dielectric Constant .....	34
2.3.7. Failure Types .....	34
2.4. Conclusion .....	36
3. MODELING OF ELASTOMERIC MATERIALS .....	37
3.1. Introduction .....	37
3.2. Kinematics of Deformation .....	38
3.2.1. Uniaxial Tension Deformation State .....	41
3.2.2. Simple Shear Deformation State .....	43
3.2.3. Volumetric Compression Deformation State .....	44
3.3. Mechanics of Hyperelastic Materials .....	47
3.4. Strain Energy Representation .....	58
3.4.1. Mooney–Rivlin Strain Energy Function .....	59
3.4.2. Ogden Strain Energy Function .....	64
3.4.3. Yeoh Strain Energy Function .....	68
3.5. Viscoelastic Materials .....	73
3.5.1. Elastomer Design .....	75
3.5.2. Linear Viscoelasticity .....	75
3.5.3. Linear Viscoelastic Models .....	79
3.5.4. Modeling Linear Relaxation Behavior .....	81
3.5.5. Modeling Linear Creep Behavior .....	84
3.5.6. Nonlinear Viscoelasticity .....	86
3.6. Force Balance .....	88
4. MATERIAL CHARACTERIZATION TESTS .....	91

4.1. Introduction .....	91
4.2. Material Characterization Tests.....	91
4.2.1. Uniaxial Tensile Tests .....	92
4.2.2. Volumetric Compression Tests.....	97
4.2.3. Quad Lap Shear Tests .....	103
4.2.4. Creep and Relaxation Tests .....	110
5. ELECTROMECHANICAL TESTS.....	117
5.1. Introduction .....	117
5.2. DEA Manufacturing .....	117
5.3. Hardware and Software Design.....	129
5.4. Software Design .....	134
5.5. Effect of Pre-stretching on Design .....	140
5.6. DEA Relaxation Tests .....	141
5.7. DEA Blocking Force Tests.....	147
5.8. DEA Creep Tests.....	150
5.9. DEA Voltage Induced Creep Tests .....	152
5.10. Observed Failure Modes .....	156
6. MATHEMATICAL MODELING OF MATERIAL AND DEA.....	159
6.1. Introduction .....	159
6.2. Assumptions .....	159
6.3. Adjusting Raw Test Data .....	160
6.4. Curve Fitting Procedure .....	164
6.5. Material Modeling .....	165
6.5.1. Uniaxial Tension Modeling .....	166

6.5.2. Quad Lap Shear Modeling .....	171
6.5.3. Volumetric Compression Modeling .....	174
6.5.4. Relaxation and Creep Modeling .....	178
6.6. DEA Creep Response Modeling .....	193
6.7. DEA Voltage Induced Creep Response Modeling .....	205
7. APPLICATION TO 3D MODEL TRAILING EDGE.....	219
7.1. Introduction.....	219
7.2. Trailing Edge Design .....	219
7.3. Draft Model for Actuation .....	224
7.4. 3D Printing and Installation .....	226
7.5. Installation of DEA to 3D Model Wing.....	232
7.6. Mathematical Modeling of DEA and Trailing Edge.....	234
7.7. Simulation and Control .....	240
8. CONCLUSION .....	257
8.1. Concluding Remarks.....	257
8.2. Future Research Concerns .....	259
REFERENCES .....	263
APPENDICES	
A. WIRING DIAGRAM.....	273
B. GALIL CODE.....	274
CURRICULUM VITAE.....	283

## LIST OF TABLES

### TABLES

Table 2-1 Main and sub class-based comparison chart.....	11
Table 2-2 Main, sub and sub II class-based comparison chart .....	12
Table 2-3 VHB acrylic foam tape series technical specifications.....	24
Table 2-4 Comparison of most widely used DE materials .....	25
Table 2-5 Comparison of most widely used DEA configurations .....	33
Table 4-1 Uniaxial tension test matrix .....	92
Table 5-1 Prestretching frame dimensions.....	121
Table 6-1 Optimized hyperelastic material model parameters at %100 and %1300 strain levels for uniaxial test .....	170
Table 6-2 Optimized hyperelastic material model parameters using Quad-Lap shear test .....	174
Table 6-3 Estimated shear modulus of VHB 4910 material .....	174
Table 6-4 Optimized hyperelastic material model parameters for compression test .....	177
Table 6-5 Estimated bulk modulus of VHB 4910 material .....	177
Table 6-6 Estimated Poisson ratio.....	178
Table 6-7 Optimized parameter sets from material relaxation tests .....	179
Table 6-8 Optimized parameters of Prony series fit function .....	182
Table 6-9 Hyperelastic material properties obtained from relaxation test.....	185
Table 6-10 Optimized parameter sets from material creep tests.....	186
Table 6-11 Optimized parameters of Prony series fit function .....	188
Table 6-12 Hyperelastic material properties obtained from creep test .....	193
Table 7-1 Dimension parameters of the trailing edge connection .....	237
Table 7-2 Angular displacement and applied voltage relationship.....	251

## LIST OF FIGURES

### FIGURES

Figure 2-1 Structural categorization of polymers [2], [3].....	8
Figure 2-2 Working principle of DEAs .....	21
Figure 3-1 Deformation of a body from initial state to its current State .....	38
Figure 3-2 Elongation in principle direction .....	39
Figure 3-3 Elastomeric material subjected to uniaxial deformation.....	41
Figure 3-4 Physical interpretation of simple shear deformation .....	43
Figure 3-5 Physical interpretation of pure volumetric compression .....	45
Figure 3-6 Physical interpretation of quasi-volumetric compression test .....	46
Figure 3-7 Response of elastomer w.r.t. constant uniaxial loading [90, p. 1] .....	73
Figure 3-8 (a) Applied constant uniaxial load from $t_0$ to $t_1$ (b) Deformation response of material.....	74
Figure 3-9 Creep rupture envelope and expected material life [90] .....	75
Figure 3-10 Viscoelastic creep response (a) Applied constant stress, $\sigma_i$ (b) Observed strain, $\epsilon_i$ .....	76
Figure 3-11 Applied constant loading, $\sigma_i$ versus the strain deformation, $\epsilon_i$ .....	76
Figure 3-12 Linear-nonlinear transition of stress strain relationship with respect to different time levels [90] .....	78
Figure 3-13 Constitutive elements to model viscoelasticity .....	79
Figure 3-14 Bergström-Boyce Rheological Model [87].....	87
Figure 3-15 Schematic of the actuation response of dielectric elastomers.....	88
Figure 3-16 Change of Maxwell stress w.r.t. applied voltage and initial thickness ..	89
Figure 4-1 Specimen preparation for uniaxial tensile test (a) Punch machine (b) VHB 4905 and VHB 4910 specimens (c) Dog bone shaped and red liner removed specimen .....	93

Figure 4-2 Uniaxial tensile testing (a) Mounting the specimen (b) Zwick testing machine (c) Elongation of material during testing.....	94
Figure 4-3 Uniaxial tension test results (a) %20 Strain level (b) %50 Strain level ...	95
Figure 4-4 Uniaxial tension test results (a) %100 Strain level (b) %100 Strain level with cyclic loading .....	96
Figure 4-5 Uniaxial tension test results (a) Direct rapture (b) Rapture after cyclic loading.....	96
Figure 4-6 Volumetric compression test specimen preparation (a) Cutting punch (b) Cutting laminated tape with special knife (c) The circular shaped specimens .....	98
Figure 4-7 Volumetric compression test specimen stacking (a) Cut samples are stacked in the hole of fixture (b) Multiple samples are used to form the required thickness (c) Total number of samples stacked in fixture.....	98
Figure 4-8 Volumetric compression test specimen fixtures (a) Test fixture (b) One cylindrical specimen (c) Fixture mounted on test machine .....	99
Figure 4-9 The Samples are removed from test fixture and then measured .....	100
Figure 4-10 Volumetric compression test result of VHB 4910 specimen bundles (all trials) .....	101
Figure 4-11 Volumetric compression test result of VHB 4905 specimen bundles (all trials) .....	101
Figure 4-12 Volumetric compression test result of VHB 4905 specimen bundles..	102
Figure 4-13 Volumetric compression test result of VHB 4910 specimen bundles..	102
Figure 4-14 Volumetric compression test result of VHB 4905 & VHB 4910 specimen bundles - third trials .....	103
Figure 4-15 Text fixture preparation for quad lap shear test (a) Metal blocks (b) Test configuration .....	104
Figure 4-16 Bonding for quad lap shear test (a) Bonding step (b) Completed test apparatus .....	105
Figure 4-17 Heat chamber used to speed up bonding process .....	105
Figure 4-18 Bonded quad lap shear test fixtures (a) Bonded fixtures (b) Closer look to bond area .....	106

Figure 4-19 Quad lap shear test (a) Test fixtures are mounted on the testing machine (b) Peel off starts (c) Complete rapture .....	107
Figure 4-20 Quad lap shear test results of VHB 4905 at breakdown .....	108
Figure 4-21 Quad lap shear test results of VHB 4910 at breakdown .....	108
Figure 4-22 Quad lap shear test results (a) VHB 4905 sample 1 (b) VHB 4910 sample 1 (c) VHB 4905 sample 2 (d) VHB 4910 sample 2 (e) VHB 4905 sample 3 (f) VHB 4910 sample 3 .....	109
Figure 4-23 Creep and relaxation testing (a) Test environment (b) Pyris diamond dynamic mechanical analyzer .....	110
Figure 4-24 Creep and relaxation test samples .....	111
Figure 4-25 Creep and relaxation test sample mounting (a) Each sample was fixed on DMA (b) Metal covers were screwed and rest of the sample was not used. ....	112
Figure 4-26 Creep test results (a) VHB 4905 at 0.05 N step input (b) VHB 4910 at 0.10 N step input (c) VHB 4905 at 0.10 N step input (d) VHB 4910 at 0.20 N step input (e) VHB 4905 at 0.15 N step input (f) VHB 4910 at 0.30 N step input .....	113
Figure 4-27 Creep test results (a) Overall results for VHB 4905 material (b) Overall results for VHB 4910 material .....	114
Figure 4-28 Relaxation test results (a) VHB 4905 at 1250 $\mu$ Strain step input (b) VHB 4910 at 1250 $\mu$ Strain step input (c) VHB 4905 at 2500 $\mu$ Strain step input (d) VHB 4910 at 2500 $\mu$ Strain step input (e) VHB 4905 at 5000 $\mu$ Strain step input (f) VHB 4910 at 5000 $\mu$ Strain step input .....	115
Figure 5-1 Prestretching scissor mechanism .....	119
Figure 5-2 (a) 3M's VHB tapes raw roll form (b) Cut of VHB tapes for actuator manufacturing .....	120
Figure 5-3 100 x 200 mm kestamid stretching frame and VHB band strip .....	122
Figure 5-4 Stretched VHB tape on scissor mechanism .....	122
Figure 5-5 (a) 100 x 100 mm VHB Band stretched on scissor stretching mechanism (b) 400 x 400 mm Kestamid stretching frame and stretched VHB band on it using scissor mechanism .....	123

Figure 5-6 Ketjenblack aggregated dust particles .....	124
Figure 5-7 Nyogel 756P carbon grease application .....	125
Figure 5-8 Oily paper masking stencil .....	126
Figure 5-9 Applied carbon black on stretched VHB tape .....	127
Figure 5-10 Final DEA .....	128
Figure 5-11 Linear translation stage from H2W .....	130
Figure 5-12 ESP4 – 100 N (10 kg) load cell is mounted on Linear Stage.....	130
Figure 5-13 Linear translation stage and its controller unit .....	130
Figure 5-14 Linear stage fixture and actuator holder design .....	131
Figure 5-15 Linear stage fixture and actuator holder manufacturing and installation .....	132
Figure 5-16 Linear stage fixture design detail view.....	132
Figure 5-17 Schematic definition of structural electromechanical test components	133
Figure 5-18 Installation direction definitions of DEA .....	134
Figure 5-19 Schematic definition of logic of generated Galil control codes .....	136
Figure 5-20 Schematic definition of logic of electromechanical test components ..	136
Figure 5-21 Matlab GUI opening screen to connect Galil controller .....	137
Figure 5-22 Matlab GUI relaxation test module .....	138
Figure 5-23 Matlab GUI creep test module .....	138
Figure 5-24 Matlab GUI voltage application test module .....	139
Figure 5-25 DEA manufacturing and activation chart.....	141
Figure 5-26 A Sample of a manufactured DEA.....	142
Figure 5-27 DEA installed to test bench .....	143
Figure 5-28 DEA shape in relaxation test .....	143
Figure 5-29 Single layer DEA relaxation test results for short run .....	144
Figure 5-30 Single layer DEA relaxation test results for long run .....	145
Figure 5-31 Mullins effect observed on relaxation test results for single layer DEA .....	146
Figure 5-32 Mullins effect encountered in DEA relaxation tests - detailed .....	146
Figure 5-33 Double layer DEA relaxation test results for short run .....	147

Figure 5-34 Blocking force test .....	149
Figure 5-35 Single layered DEAs blocking force results .....	149
Figure 5-36 Single layered DEAs creep test results for short run .....	150
Figure 5-37 Single layered DEA creep test results for long run.....	151
Figure 5-38 Mullins effect observed on creep test results for single layer DEA ....	151
Figure 5-39 Double layer DEA creep test results for short run.....	152
Figure 5-40 Single layer DEA voltage induced creep test results .....	153
Figure 5-41 Single layer DEA applied voltage levels .....	154
Figure 5-42 Single layer DEA 2kV applied voltage results at various creep loads	154
Figure 5-43 Double layer DEA voltage induced creep test results .....	155
Figure 5-44 Double layer DEA 2 kV applied voltage results at various creep loads .....	155
Figure 5-45 Edge arcing failure mode .....	157
Figure 5-46 Edge waviness at DEA supports .....	158
Figure 5-47 Face crimping failure mode .....	158
Figure 6-1 Shifting the measured strain value to origin .....	161
Figure 6-2 Shifting measured stress value to origin .....	162
Figure 6-3 Curve fitting procedure .....	164
Figure 6-4 Mooney-Rivlin model fit w.r.t. three uniaxial test at %100 strain .....	168
Figure 6-5 Yeoh model fit w.r.t. three uniaxial test at %100 strain .....	169
Figure 6-6 Ogden model fit w.r.t. three uniaxial test at %100 strain .....	169
Figure 6-7 Curve fitting results of hyperelastic material models to %1300 strain ..	170
Figure 6-8 Curve fitting of Yeoh model to k=1 mm shear deformation .....	172
Figure 6-9 Curve fitting of Ogden model to k=1 mm shear deformation .....	172
Figure 6-10 Curve fitting of Mooney-Rivlin model to k=1 mm shear deformation	173
Figure 6-11 Curve fitting of Yeoh model compression deformation .....	175
Figure 6-12 Curve fitting of Ogden model compression deformation .....	176
Figure 6-13 Curve fitting of Mooney-Rivlin model compression deformation .....	176
Figure 6-14 Material relaxation results with applied curve fitting .....	180
Figure 6-15 Material relaxation functions, $S_{\infty}(t)$ .....	180

Figure 6-16 Prony series fit to mean relaxation function, $S_{\infty}(t)$ .....	181
Figure 6-17 Prony series fit function for material relaxation test .....	182
Figure 6-18 Yeoh strain energy function fit to material relaxation test.....	184
Figure 6-19 Ogden strain energy function fit to material relaxation test.....	185
Figure 6-20 Material creep curve fitting results.....	187
Figure 6-21 Material creep compliance functions $S_{\infty}, c(t)$ .....	188
Figure 6-22 Normalized creep compliance functions $S_{\infty}, c(t)$ .....	189
Figure 6-23 Prony series fit function used in creep analysis .....	189
Figure 6-24 Yeoh strain energy function fit to material creep test .....	191
Figure 6-25 Ogden strain energy function fit to material creep test .....	192
Figure 6-26 Mooney-Rivlin strain energy function fit to material creep test .....	192
Figure 6-27 Matlab GUI for DEA analysis.....	194
Figure 6-28 Extraction raw creep DEA test data for DEA analysis .....	195
Figure 6-29 Linearity check of DEA .....	197
Figure 6-30 Creep test strain outputs of DEA and its estimated values.....	198
Figure 6-31 Normalized test creep, means and predicted compliances .....	199
Figure 6-32 Variation of creep compliance end point vs applied force values.....	200
Figure 6-33 Actual test strain results and their predicted strain results .....	200
Figure 6-34 Normalized test creep compliances of all test (first run) and predictions .....	201
Figure 6-35 Test creep compliances' final values (first run) and applied loads .....	202
Figure 6-36 Normalized creep compliances of all tests (second run) and predictions .....	202
Figure 6-37 Test creep compliances' final values (first run) and applied loads .....	203
Figure 6-38 DEA creep simulation .....	204
Figure 6-39 DEA creep simulation for long run .....	205
Figure 6-40 Material analyzer run for voltage induced creep test .....	206
Figure 6-41 Detemination of data split point for DEA response .....	208
Figure 6-42 Splitted DEA response .....	208
Figure 6-43 Predicted DEA hyperelastic response .....	209

Figure 6-44 DEA creep response due to applied voltage input .....	210
Figure 6-45 DEA normalized creep compliance due to applied voltage input.....	211
Figure 6-46 DEA normalized creep compliance fit to Prony series .....	212
Figure 6-47 DEA voltage induced strain prediction.....	212
Figure 6-48 DEA voltage induced overall strain prediction.....	213
Figure 6-49 DEA voltage induced and creep loaded strain results .....	214
Figure 6-50 DEA applied voltage and observed maximum strain results .....	215
Figure 6-51 DEA voltage induced and creep loaded normalized strain results .....	216
Figure 6-52 DEA applied voltage and residual force relation .....	217
Figure 7-1 Cross section view of NACA 6520 profile .....	220
Figure 7-2 3D Model cross section view of NACA 6520 profile including trailing edge location .....	221
Figure 7-3 3D Model of the wing structure .....	222
Figure 7-4 3D Model trailing edge installation .....	223
Figure 7-5 3D Model trailing edge connection.....	223
Figure 7-6 Prototype wooden functional model .....	224
Figure 7-7 DEAs for prototype model.....	225
Figure 7-8 Installation of DEAs to prototype model .....	226
Figure 7-9 3D printing machine .....	227
Figure 7-10 Installed 3D manufactured items .....	228
Figure 7-11 Installation details .....	229
Figure 7-12 Installation details – sensor mounting.....	230
Figure 7-13 DEA actuator .....	232
Figure 7-14 DEA installed trailing edge configuration .....	233
Figure 7-15 DEA installation.....	233
Figure 7-16 Kinematic illustration of trailing edge .....	235
Figure 7-17 Kinematic illustration of trailing edge on Matlab.....	237
Figure 7-18 Moments generated due to trailing edge rotation .....	238
Figure 7-19 Required DEA force according to trailing edge angle, $\theta$ .....	239
Figure 7-20 Required DEA Stretch Ratio according to Angle, $\theta$ .....	240

Figure 7-21 Sensor positioning and fin attachment .....	242
Figure 7-22 Sketch of sensor and fin position .....	242
Figure 7-23 Sensor measurement vs angle deviation.....	244
Figure 7-24 Matlab GUI for real time simulation.....	245
Figure 7-25 Structure of voltage application module .....	245
Figure 7-26 Control block diagram.....	246
Figure 7-27 Main execution tasks of the GUI voltage module .....	247
Figure 7-28 The response of DEA to 1 kV applied step voltage .....	249
Figure 7-29 The response of DEA to 2 kV applied step voltage .....	249
Figure 7-30 The angular response of TE to applied step voltages.....	250
Figure 7-31 The angular reduction of TE with applied step voltage inputs.....	252
Figure 7-32 Target applied 25-degree camber position .....	254
Figure 7-33 Target applied 16-degree camber position .....	254
Figure 7-34 Target applied 2-degree camber position .....	255
Figure 7-35 Applied voltage levels for target 2 degree camber position.....	256

## LIST OF ABBREVIATIONS

### ABBREVIATIONS

AC	Alternative Current
ACN	Acrylonitrile
ASTM	American Society for Testing and Materials
BR	Butadiene Rubber
CAD	Computer Aided Design
CFRP	Carbon Fiber Reinforced Plastic
CNT	Carbon Nano Tubes
CP	Conjugated Polymers
DC	Direct Current
DE	Dielectric Elastomer
DEA	Dielectric Elastomer Actuator
DEHP	Di-(-2-ethyl hexyl) phthalate
DIN	Deutsches Institut für Normung
DMA	Dynamic Mechanical Analysis
EAC	Electro Active Ceramic
EAP	Electro Active Polymer
EGE	Electrostrictive Graft Elastomer
ERF	Electro Rheological Fluids
FP	Ferroelectric Polymers

GUI	Graphical User Interface
IEP	Ionic Electro Active Polymers
IPG	Ionic Polymer Gels
IPMC	Ion Polymer Metallic Composites
ISO	International Organization for Standardization
LCE	Liquid Crystal Elastomer
LCR	Inductance,L, Capacitance,C, Resistance, R
MSA	Magneto Strictive Alloy
NACA	National Advisory Committee for Aeronautics
NBR	Nitrile Butadien Rubber
PANI	Polyaniline
PDMS	Poly Dimethylsiloxane
PLA	Poly Lactic Acid
PPy	Polypyrrole
PVA	Poly Vinyl Alcohol
PZT	Piezoelectric Ceramics
PVDF	Polyvinylidene Difluoride
PU	Polyester Urethane
QLV	Quasi Linear Viscoelasticity
SMA	Shape Memory Alloy
VHB	Very High Bond



## CHAPTER 1

### INTRODUCTION

Many electric/pneumatic/hydraulic actuators are available in various sizes and specifications. The design and operating characteristics of these conventional devices are well understood. They are capable of performing heavy duties and commercially available at affordable prices. They are not necessarily direct driven and thus may require additional components like belts or gears to satisfy the requirements of the specific application. They are heavy, rigid and their costs are high. The geometric space allocation requirements of them force to enlarge system dimensions for proper operating conditions. The structural integrity of the appliance (small or large) is highly affected due to cost considerations.

Actuators that can be used instead of conventional devices described above have been the focus of researchers for a long time. In particular, actuators that are miniaturized and capable of sustaining small and/or large loads applicable to various applications are a popular concern. Actuators that can drive the mechanisms without needing additional components and capable to perform on land, underwater or aerial missions require new technologies to study on.

One of the alternatives as new era actuators is the *Artificial Muscles*. They are a group of polymeric materials which are also known as the *Electro Active Polymers (EAPs)*. They are already available commercially or can be manufactured in laboratory conditions. These actuators are made of soft and formable materials. Different types of these materials have been developed, studied, and published in the literature recently. These materials do not need additional mechanisms to actuate. They can be tailored for specific needs. These materials are candidates for use in new concepts of

actuators to replace conventional devices as they possess suitable characteristics with respect to light weight, low cost, low design space requirements among others.

Biological muscles are an evolutionary optimized motion generator of species. They are driven by chemical mechanisms resulting in toughness, reliability, compliance, and capability of operation with large strains. Muscle cells are cylindrically shaped with very thin diameters and bundled together capable of generating large forces with short response times. Muscles produce linear forces by the use of actin and myosin interaction. Artificial muscles are similar to biological muscles in terms of direction of motion capability, large straining, and compliance. Artificial muscles, on the other hand, generate force by activation of a magnetic field. Thin layers of artificial muscles can be grouped and ordered to generate high forces. The toughness, reliability, and the order of lifting capability of artificial muscles are not yet sufficient for heavy applications, however they are capable of emulating the behavior of natural muscles in the near future to develop biologically inspired mechanisms.

As an example to visualize the motion concept can be a mimetic motion of a human face. There are 43 different muscles that control all our emotions [1]. Muscles are biological actuators that are stimulated by instant nerve reactions. However, no conventional group of motors are capable to simulate these 43 different muscles simultaneously with the desired actuation speed and magnitude. Additionally, daily life electric motors will need gear systems, enough space to properly locate and have to operate in various environmental conditions while on a human face. It is apparent that a more convenient actuation mechanism is required for efficient design of an artificial face. At this point, it will be proper to introduce artificial muscles for actuation concept. These artificial muscle materials can be programmed to actuate in different directions with varying speeds and amplitudes without need of a weight, space allocation and rigidity constraint.

## 1.1. Motivation and Contribution

This study is motivated by the potential of the materials known as artificial muscles in replacing the conventional actuators for use in a wide range of applications, particularly in aero structures where the weight and cost advantages are strongly emphasized.

In the thesis study, an exhaustive experimental study of the properties of a suitable representative material is carried out and the identification of the material is made in all aspects related to the application as an actuator which is called *Dielectric Elastomer Actuator (DEA)* in full detail. Mathematical characterization of the material using the test results is obtained. The capabilities and the potential use of the selected material to ascertain the possibility of application in aero structures is established.

Following the selection of a suitable artificial muscle material, a set of experiments are performed to analyze the material characterization which will be used in manufacturing of an artificial muscle actuator. The manufacturing process of artificial muscle actuator is detailed and the possible manufacturing defects are outlined. The capabilities of artificial muscle actuator are also analyzed with a bunch of static and electro activated test systems.

Modeling of such materials are generally defined using strain energy functions. Most of the time, these functions are empirically obtained based on partial use of full material models or statistical approaches. In literature, the use of strain energy functions are limited to static models like modeling uniaxial tension or combined tests which well suit most of the time. Meanwhile, the strain energy function models are capable to capture relaxation behavior of the material. On the other hand, the use of these strain energy models in creep response is not available in literature due that the mathematical interpretations are cumbersome. In this study, the use of these models in creep response modeling is introduced with a unique technique beside static and relaxation behavior models. It is also shown that the hyperelastic strain energy

function coefficients can be identified using the relaxation and creep experiments results.

The use of strain energy functions is not suitable for real time applications due to high computational effort. Direct approaches, such as using the voltage as the input and the stretch ratio of the material as the output from such models are possible. On the other hand, the reversal of the input and output variables is not handy either in case of quadratic nature of the models. It is shown in this study that, there are simpler mathematical models that are capable to fit the material in action during real time voltage applications. The use of these models are real time capable, experiment friendly and able to predict material behavior correctly.

Meanwhile, regardless of the applied creeping load, the effect of high voltage is isolated from the DEA response and a novel approach is proposed to estimate the DEA actuation strain using the voltage strain effect.

In literature, different set of experiments were performed in material and DEA actuator level. In this study, a complete way forward to characterize such a soft material into an actuating mechanism is fully outlined and a representative application is demonstrated using a typical aerial wing structure's trailing edge and the camber potential of the artificial muscle actuator is investigated.

## **1.2. Thesis Overview**

This thesis describes the way of application of dielectric elastomer actuator on a demonstrative trailing edge in the following chapters:

**Chapter 2 – Literature Review** presents the current state of the art on electroactive polymers, their classification and dielectric elastomer design prospects.

**Chapter 3 – Modeling of Elastomeric Materials** provides a brief summary on how to model hyperelastic and viscoelastic response of elastomer materials.

**Chapter 4 – Material Characterization Tests** outlines the simple material tests performed to analyze material properties as obtained from manufacturer.

**Chapter 5 – Electromechanical Tests** give information on production of a dielectric elastomer actuator and provide information on the tools and processes that are required. The tests to detail exhaustively material behavior from a simple material level perspective up to tailored actuator configuration is outlined.

**Chapter 6 – Mathematical Modeling of Material and DEA** presents the interactions between mathematical models and performed tests for both material and produced DEA levels.

**Chapter 7 – Application to 3D Model Trailing Edge** summarizes the steps to build a demonstrative aircraft wing like trailing edge model, installation of the soft actuator, test system, actuating the DEA and its angular position capability results.

**Chapter 8 – Conclusion** restates the objective of the thesis and discusses the results of this study. A concise summary is presented and recommendations for further study are discussed.



## CHAPTER 2

### LITERATURE REVIEW

#### 2.1. Introduction

Rubber, also named as elastomer, is a kind of polymer which is built up by long chain molecules. Polymers or the elastomers are the base of artificial muscle structures which are so called *Electro Active Polymers (EAPs)*. The basic motivation of research in polymers has initially been the simulation of the behavior and performance of actual mammalian muscles. These polymers have functional similarities to biological muscles including resilience, damage tolerance and large actuation strain. Efforts have been focused on materials that are able to change their volume or shape as a consequence of an external excitation.

The actuators manufactured from these smart materials do not need traditional components like gears, belts and bearings, which present high costs, weights and possible sources of failures. As long as these materials lead to new alternative actuator designs, they are also classified as the future sensing and energy harvesting devices. Before getting into the comparison of polymeric materials with biological muscles, a general categorization of polymers is presented in Figure 2-1.

*Biological muscles* are the real actuators of human and animal movements. They are chemically activated biological elastic mechanisms and are capable of lifting large loads at short (millisecond) response times. They produce linear forces and able to operate for billions of cycles over a period of hundred years or more. They are energy efficient, have a high contraction ratio, compliant and their stiffness can be varied smoothly and dynamically. They can also act as sensory mechanisms. Mechanical properties of natural muscles are widely studied in [4]–[8]. EAP materials are classified as rubber and used to emulate the movement of actual muscles. The

properties of rubber should be well outlined to understand the actuation mechanism of EAPs.

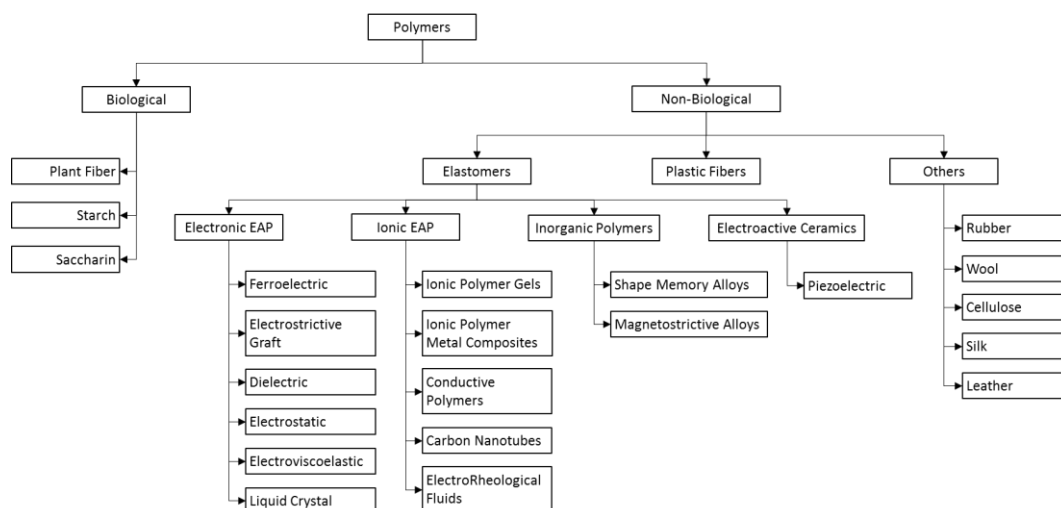


Figure 2-1 Structural categorization of polymers [2], [3]

Rubber is a hyperelastic material that can be strained up to 500-800% in any direction. The mechanical behavior of rubber is not always linear and has a time dependent response in nature. It is usually described by a S-shaped stress- stretch curve. The bulk modulus of rubber is usually 1000-2000 times higher than its shear modulus which makes it nearly incompressible. Thus, in many design cases, the approximation of incompressibility is quite appropriate and a well-known assumption [9]. When rubber is subjected to cyclic loading, viscoelasticity is observed leading to a phenomenon so called *hysteresis*. Hysteresis is defined as the dependence of the state of a material on its history which effects its stiffness. The reasons of hysteresis but not limited to are the internal friction, strain induced crystallization, stress softening, structural breakdown and domain deformation [10].

Mechanical properties of rubber are controlled by the amount carbon black mixed in the material. A higher amount of carbon black leads to a phenomenon called *Mullins*

*Effect.* Mullins effect is the response of filled rubbers in which the stress-strain curve depends on the maximum loading previous encountered. That means, the first time a material is stretched to a certain level, the stress will be higher than the next time the material is stretched to the same level. The reason is the breakdown of cross-links between the molecular chains. It is worth noting that it is necessary to subject the material to more than one loading–unloading cycle, as the stretch-induced softening occurs mainly between the first and second cycle [11], [12].

Compared to the mammalian muscle, EAP technology still does not offer all the features of a human muscle. So far, one of the most obvious difference between humans or animals and today's robots is the missing capability of robots to combine perception and actuation. In natural muscles, proprioception means the feedback from neurons located in natural muscles, which make it possible to execute complex and sensitive movements. To simulate it in robotics, the use of EAP is a promising possibility to combine sensing and actuation in one device, which is then easy to call self-sensing actuator [13].

## **2.2. Background of EAPs**

Generally, all EAP materials can generate force and strain with considerably high response speed, lower density, light weight, pliability and improving resilience. On the other hand, these developed forces and reliability are not capable to complete heavy-duty missions. The efficiency of these materials is considered to be high but limited publication is available for the common standardization [12]. However, the reason of the motivation of the research community on these materials is the increasing need for miniature, low mass, less power consuming, flexible, direct drive and inexpensive actuators. EAPs ability to generate large displacements will be the future of the mechanisms.

EAPs are active materials mainly categorized into two major groups based on their actuation mechanism. Materials which are driven by the mobility or the diffusion of

ions – known as *Ionic (Wet) EAPs* and materials which are driven by electric fields or Maxwell forces known as *Electronic (Dry) EAPs*.

In comparison with active materials, several “smart materials” have been proposed as artificial muscles including *Electro Active Ceramics (EACs)*, *Shape memory Alloys (SMAs)*, *Magneto Strictive Alloys (MSAs)* and *Piezoelectric Ceramics (PZTs)*. However, while EAPs can undergo large strains, perform short response time and their densities are lower, these smart like materials cannot hold all these properties at the same time.

PVA gels, Nafion and flemion, Copoly (Aam/bdMG) gels and electrochromic polymers (ProDOT-(CH<sub>3</sub>)) and liquid crystal elastomers are the future EAP materials that have been studied in literature recently [3]. On the other hand, studies on these materials have not been published widely. Materials like molecular actuators and carbon nanotubes are called high-tech materials and are still need a strong development.

A property comparison and classification of artificial muscle class materials are provided in Table 2-1. A detailed comparison of Electronic and Ionic Electroactive polymers is provided in Table 2-2. Detailed information about materials will be given in preceding chapters.

Table 2-1 Main and sub class-based comparison chart

Main Class	Sub Class	Advantages	Disadvantages
Electro Active Polymers (EAPs)	Ionic Electroactive Polymers (Wet EAP)	<ol style="list-style-type: none"> <li>1. Natural bi-directional actuation that depends on the voltage polarity [14]</li> <li>2. Some Ionic EAP like CPs have a unique capability of bi-stability [14]</li> <li>3. Low voltage requirement [14]</li> </ol>	<ol style="list-style-type: none"> <li>1. Requires electrolyte medium for proper actuation[14]–[16]</li> <li>2. Electrolysis occurs in aqueous systems at &gt;1.23 V [14]</li> <li>3. Require encapsulation or protective layer in order to operate in open air conditions [14]</li> <li>4. Low electromechanical coupling efficiency [14]</li> <li>5. Except for CPs and NTs, Ionic EAPs do not hold strain under DC voltage [14]</li> <li>6. Slow response time [14]</li> <li>7. Bending EAP’s induce a relatively low actuation force [14]</li> <li>8. High currents require electrodes such as gold or platinum [14]</li> <li>9. Except for CPs, it is difficult to produce a consistent material (particularly IPMC) [14]</li> <li>10. To keep the actuator in a defined position, energy shall be sustained throughout the process [14]–[16]</li> <li>11. Bandwidth is typically in the upper range of tens of Hertz due to ionic motion [14]–[16]</li> </ol>
	Electronic Polymers (Dry EAP)	<ol style="list-style-type: none"> <li>1. High mechanical energy density [14]</li> <li>2. Large actuation forces [14]</li> <li>3. Can operate for a long time in room conditions [14]</li> <li>4. Fast response time [14]</li> <li>5. Can hold strain/displacement under DC voltage activation [14]</li> <li>6. Can be operated in air with no major constraints [14]</li> </ol>	<ol style="list-style-type: none"> <li>1. Independent of the voltage polarity, it produces mostly mono polar actuation due to associated electrostriction effect [14]</li> <li>2. High voltage requirement (~100 MV/m) [14]</li> <li>3. High activation field close to breakdown level required [14]</li> </ol>
Inorganic Polymers	Shape Memory Alloy (SMA)	<ol style="list-style-type: none"> <li>1. Large displacements [5]</li> <li>2. Actuates quickly using resistive heating [5]</li> <li>3. Large force generation [8], [17]</li> <li>4. High energy density [17]</li> <li>5. High material strength [17]</li> <li>6. High elasticity [17]</li> </ol>	<ol style="list-style-type: none"> <li>1. Low bandwidth [17]</li> <li>2. Low frequency [17]</li> <li>3. High hysteresis [17]</li> <li>4. Limited operating temperature range [17]</li> <li>5. Long time required to cool down and return to rest position [5], [8]</li> <li>6. Fatigue problem [8]</li> <li>7. Large energy requirement [8]</li> </ol>
	Magneto Strictive Alloy (MSA)	<ol style="list-style-type: none"> <li>1. High stiffness [5]</li> <li>2. High frequency [17]</li> <li>3. Wide operating temperature range [17]</li> <li>4. Controllable via magnetic field [17]</li> </ol>	<ol style="list-style-type: none"> <li>1. Small strain [5]</li> <li>2. Low tensile strength [17]</li> <li>3. Brittle [17]</li> </ol>
Electroactive Ceramics	Piezoelectric (PZT)	<ol style="list-style-type: none"> <li>1. Fast reaction time [8], [17], [18]</li> <li>2. High force potential [18]</li> <li>3. Precise and high electromechanical responses [8]</li> <li>4. Easily formed [8]</li> <li>5. High bandwidth [17]</li> <li>6. Low actuation power [17]</li> <li>7. Wide operating temperature range [17]</li> <li>8. Electromechanical coupling is linear</li> </ol>	<ol style="list-style-type: none"> <li>1. Auxiliary equipment required [17]</li> <li>2. Low tensile strength [17]</li> <li>3. Brittle [4], [14], [17]</li> <li>4. Striction-limited [4], [14]</li> <li>5. Stiff/rigid [4], [5], [14]</li> <li>6. Limited displacement levels [17], [19]</li> </ol>

Table 2-2 Main, sub and sub II class-based comparison chart

Main Class	Sub Class	Sub II Class	Advantages	Disadvantages	
Electro Active Polymers (EAPs)	Ionic Electroactive Polymers (Wet EAP)	Ionic Polymer Metallic Composites (IPMCs)	<ol style="list-style-type: none"> <li>1. Large bending capabilities [15]</li> <li>2. Difficult to sustain DC driven displacements [15]</li> <li>3. Wide operating temperature range also capable of actuation below 0 degree [15]</li> </ol>	<ol style="list-style-type: none"> <li>1. Must be improved to increase the maximum stress output [15]</li> <li>2. Small displacement and force outputs [15]</li> <li>3. Even with special construction techniques, 2 Volts of energy can generate %50 strain with a net blocked force of approximately 1.16 kPa [15]</li> </ol>	
		Ionic Polymer Gels (IPGs)	<ol style="list-style-type: none"> <li>1. Responds to electric fields [5]</li> </ol>	<ol style="list-style-type: none"> <li>1. Still in the exploratory stages [5]</li> </ol>	
		Conjugated (Conducted) Polymers (CDs)	<ol style="list-style-type: none"> <li>1. Light and biocompatible [15]</li> </ol>	<ol style="list-style-type: none"> <li>1. Must be encapsulated [5]</li> </ol>	
		Carbon Nanotubes (CNS)	<ol style="list-style-type: none"> <li>1. Lifetime and actuation rate is higher than for most ionic EAPs [5]</li> <li>2. Recently super elastic CNT aerogel muscles are reported [5]</li> </ol>	<ol style="list-style-type: none"> <li>1. They are stiff, strain amplifiers to be required [5]</li> <li>2. High creep rate [5]</li> <li>3. Cost, health and safety concerns [2]</li> </ol>	
	Electronic Polymers (Dry EAP)	Dielectric Elastomers (DEs)	<ol style="list-style-type: none"> <li>1. The bandwidth and force outputs of DEs are generally exceed ionic EAPs [15], [20]</li> <li>2. Softness, cost effectiveness, manufacturability, low weight, inexpensive, mechanically robust, flexible, silent, reliable, simple and scalable [2], [15], [20]–[23]</li> <li>3. Most feasible materials for actuation [15]</li> <li>4. Efficient at low velocities [24]</li> <li>5. High strain rates [2], [8], [21], [23], [25]–[27]</li> <li>6. High energy densities [2], [20], [23]</li> <li>7. High electro-mechanical coupling efficiencies [2], [26]</li> <li>8. Low cycling hysteresis [2]</li> <li>9. Fast response times [20], [22], [25]–[27]</li> <li>10. Excellent conversion time [25]</li> <li>11. High specific energy [20], [25], [27]</li> <li>12. Negligible viscoelastic behavior [22]</li> <li>13. Low Power Consumption [20]</li> </ol>	<ol style="list-style-type: none"> <li>1. Stress relaxation and creep are an issue [15]</li> <li>2. Typical operating voltages range from 500 V to 10 kV [5], [28]</li> <li>3. Require large electric fields [2]</li> </ol>	
			ElectroStrictive Polymers	<ol style="list-style-type: none"> <li>1. Spontaneous electric polarization [5]</li> <li>2. Fast response speeds for electrically activated ones [5]</li> <li>3. The required electric fields are lower than for most other field activated EAP technologies [5]</li> </ol>	<ol style="list-style-type: none"> <li>1. Response speed is limited due to the requirement for heat diffusion. [5]</li> <li>2. The use of stiffer polymers yields small strains and a work densities [5]</li> <li>3. The actuation strains are small. [2], [5]</li> <li>4. Slow response times for thermally activated ones [5]</li> </ol>
			Ferroelectric	<ol style="list-style-type: none"> <li>1. Lightweight, flexible, easily formed, and are not brittle [5]</li> </ol>	

### 2.2.1. Ionic Polymers

*Ionic Electroactive Polymers (IEPs)* can be activated by ion displacement. Diffusion or mobility of ions results in shape deformation of material. Few volts are needed for actuation but higher electrical power is needed with respect to Electronic Polymers. To keep the actuator in a defined position, energy shall be sustained throughout the process. Their bandwidths are typically in the upper range of tens of Hertz due to ionic motion. These polymer groups require electrolyte (wet environment) for proper actuation mechanism, which is a property to be preferred in underwater applications compared to Electronic Polymers [14]–[16]. The use of IEPs are not within the scope of this study but a brief summary information on the types of IEPs are provided below.

*Ionic Polymer Metallic Composites (IPMCs)* are ion-exchange polymer membrane films coated with thin flexible metallic or carbon electrode plates on its surfaces. When an electric field or magnetic field is applied, the mobile cations available in the membrane are driven through stationary anion groups. This causes, in turn, one side of the membrane to swell whereas the other side experiences contraction, thus resulting in large bending displacements under low input voltages [2], [5], [15].

Nafion and Flemion are the most important and widely used base materials. Nafion has thermal and chemical stability and good mechanical properties. Flemion is selected when higher bending capabilities are required [15], [29], [30].

IPMCs can easily be processed and miniaturized for many applications. They can work in within a wide temperature range also capable to actuate below 0 °C. They require low driving voltage typically on the order of a few volts or less (nearly equal to 1-5V) and actuation strains and stresses of >3 % and 30 MPa have been reported. Due to the generated low strains and the environmental condition of actuation their applications as artificial muscles are limited. Even with special construction techniques, with 2 V and 3 V applied voltages, a maximum of 2.94 mm and 3.78 mm tip displacement that exert 1.4g and 1.7g forces were reported in literature [2], [5], [15], [20].

Electrodes that cover the base IEPs strongly influence the mechanical and thermal behavior of the actuator system. Precious electrode materials, Gold (Au) and Platinum (Pt) nanoparticles are widely used [15].

IPMCs are constructed as linear, stacked and parallel linear actuators to generate large actuation forces. They can be used as actuators in micro pumps, mechanical grippers, metering valves, as artificial muscles in robotic applications and energy harvester for battery chargers and as sensors in accelerometers, force, pressure, displacement and velocity measurement [5], [15].

*Ionic Polymer Gels (IPGs)* are polyacrylic gel acid in an electrolyte solution and responds to electric fields. These materials are a class of hydrogels that swell in water. A hydrogel placed into an aqueous solution can change in shape and volume by a change in the polymer-liquid interaction and hence the degree of swelling. Because of the diffusion of ions through the multilayered gel, the actuation of these materials is slow [2], [5], [31].

One of the most promising study is to combine ionic gels with McKibben artificial muscles. The intension is to replace conventional pneumatic system with a chemical actuation mode to improve the response speed and reducing system complexity [5].

*Conjugated (Conducted) Polymers (CPs)* work based on mass transport induced by ion movement during reduction-oxidation phase. It is considered to be the primary mechanism responsible for volume change and the reason of actuation. PPy and PANI are the base materials used for actuator design. Several different electrolytes can be used according to system requirements, due that most CP actuators must be encapsulated [5], [15].

Actuation behavior of CP actuators is strongly dependent on the fabrication process and the operating environment. CPs require low actuation voltage (1-5 V or lower) and generate considerable achievable stress up to 100 MPa which is larger than mammalian skeletal muscle. Large strain output that range from 1 to  $\approx 40\%$  can be achieved. They are light weight and biocompatible, simple mechanisms can be

constructed, they consume small electrical power, easily shaped and can operate silently [5], [15], [31]. On the other hand, CPs suffer from a very low operating efficiency of  $\approx 1\%$  and electromechanical coupling under 1%.

These advantages make them attractive for a wide range of applications like robotics, biomedical devices, biomimetic systems, bio manipulation blood vessel reconnection, displays devices (i.e. dynamic Braille, haptic, electrochromic), valves, power suits, artificial limbs, toys and gadgets, control devices and catheters, sensor applications, printed circuit boards, various semi-conductor devices [3], [5], [15], [31]–[35].

*Carbon Nano Tubes (CNTs)* are allotropes of carbon with a cylindrical nanostructure. The application of a bias on single-walled carbon nanotubes suspended in an electrolyte suspension causes the electrolyte ions to migrate to the surface of the CNTs. This surface charge accumulation is compensated by a rearrangement in the electric charge within the tube. These effects together with the Coulombic forces produce the CNT actuation [2].

Beside conventional CNT actuators, super elastic CNT aerogel muscles are introduced in literature that requires no electrolyte medium and the actuation results from applying a positive voltage with respect to a counter electrode. The CNT actuators have gas-like density and highly anisotropic mechanical properties, with Poisson's ratios reaching to 15 [5].

CNTs present several positive characteristics for their use as EAP, such as low actuation voltages ( $\approx 1$  V), high operating stress (26 MPa), high effective power to mass ratios (270 W/kg) and millisecond level response time. Individual CNTs output a high tensile modulus (640 GPa) and high tensile strengths (20-40 GPa), which are an order of magnitude larger than any other continuous fiber. Lifetime and actuation rates are higher than for most ionic EAPs [2], [5].

However, the cost of CNTs are very high, their applicability is limited because their actuation strains are typically below 2% and they require strain amplifiers to be used

as artificial muscles. Also, manufacturing an EAP from CNTs is difficult due to health and safety concerns [2], [5].

*Electro Rheological Fluids (ERFs)* can rapidly solidify and increase their viscosity dramatically, in response to an applied electric field. These materials are made by suspending particles in a liquid whose dielectric constant or conductivity is mismatched in order to create dipolar particle interactions in the presence of an AC or a DC electric field. Potential applications of ERFs include shock absorbers, engine mounts and acoustic dampers [16], [31].

### **2.2.2. Electronic Polymers**

Electronic Polymers are materials that can sustain the induced displacement with an applied DC voltage. This property makes them suitable for most of the robotic applications. They have high mechanical energy density and can be operated in air with no major constraints. They can generate relatively large actuation forces and exhibits fast responses. On the other hand, they require high electric field to activate which is close to its breakdown strength level.

Electronic EAPs work based on electrostriction and exerts Maxwell stress effect actuation mechanisms. Therefore, the electro-mechanical response of a given polymer can be explained by either one of them or by a mixture of both. The typical materials of these actuation mechanisms are PVDF or liquid crystal elastomers for electrostriction and silicones or acrylics for Maxwell stress [2].

Dielectric Elastomer Actuators (DEAs) are basically soft and flexible compliant capacitors. They are composed of a thin elastomeric membrane sandwiched between two compliant electrodes that are able to convert electrical energy into mechanical energy, as actuators, and vice versa as sensors. The dielectric medium consists of incompressible and highly deformable elastomeric materials. When all the dipoles in a material align in this way to an applied electric field, the material is known as a

dielectric [28]. The electrodes are designed to be able to comply with the deformations of the elastomer. As for any capacitor, when an electric field is applied to the electrodes, positive charges appear on one electrode, and negative charges on the other. This gives rise to Coulomb forces between opposite charges, generating a pressure, known as the Maxwell stress. The Maxwell stress forces the electrodes to move closer, thereby squeezing the elastomer. As the elastomer is thinned, it elongates in the directions perpendicular to the applied force. Exploiting this simple principle, materials can be designed and processed, as well as the design of actuator geometries [2], [5], [24], [28], [36]. Deformation characteristics and response time of DEA place them between PZTs and shape memory alloys [27].

DEAs have a lot of advantages such as high energy efficiency, unrivaled power-to-weight ratio and soft structure. Furthermore, they are capable of sensing its deformation and status without additional sensing devices [13]. The bandwidth and force outputs of DEAs generally exceed ionic EAPs [15].

High voltage requirements ( $> 1$  kV) can be a concern, especially in biomedical and toy applications. Generally, there is a need to convert line or battery voltages up to kilovolt potentials, which adds cost and consumes volume. Relatively small DC-DC converters are available for moderate to low power applications [37] but the cost and size at present are prohibitive for application in small portable devices.

Dielectric breakdown can limit actuator yield strength limit especially when imperfections exist within films. The materials can actuate at high stresses (up to 7.7 MPa in acrylic and 3.2 MPa in silicone base materials). However, in practical devices the maximum stress is typically lower due to the reduced electric field required to avoid breakdown and to imperfect mechanical coupling with the load.

DEA applications can be grouped as Braille displays, life-like robots, tunable lens, power generators, lightweight artificial muscles for robots, diaphragm actuators for pumps, speakers and flow control devices such as dimples or vibrating surfaces for aerodynamic applications, heating valves, tissue engineering, surgical tools, wind

turbine flaps, toys, rotary motors, grippers for material handling [8], [20], [25], [26], [36], [38].

Maximum linear strains of up to 380% were demonstrated but there is a tradeoff between strain and life cycles when loaded. For applications that require high lifetimes, the actuator must be designed to operate at strain levels below 15%. The strain is also dependent on the actuation frequency. As the frequency is increased, the strain decreases.

*Liquid Crystal Elastomers (LCEs)* combine the orientational ordering properties of liquid crystals with the elastic properties of elastomer networks. It was observed that the reorientation of mesogens in liquid crystals during a phase transition could result in bulk stresses and strains [5].

LCEs can be divided into two categories namely the nematic and smectic. The actuation mechanism for these two systems is different. The change in orientation can be affected via thermal and electrical stimuli. Thermally activated LCEs (including optical, electrical, and direct magnetism) can extend up to 400% strains but their response speed is limited due to the requirement for heat diffusion. On the other hand, thermal relaxation is still an issue for LCEs.

Electrically activated LCEs have polarized mesogens that can realign in the presence of an electric field. These have much faster response speeds (10 ms) than the thermally activated ones and require fewer electric fields according to most other EAP technologies. However, the actuation strains are relatively small (<10%) [2], [5].

Additional improvements in strain and work density will be required to use LCEs as an artificial muscle. These are possibly a good actuator candidate if there is no need for large actuation strains and the properties of liquid crystals, like their known electro-optic or electro-chromic capabilities, are desired. An iris like LCE is developed recently as a demonstrative application [2].

*Electrostrictive Graft Elastomers (EGEs)* consist of a flexible non-crystallizable macromolecule chain with a grafted polar polymer that is able to crystallize. The application of an external electric field induces the reorientation of the polar crystallites, which results in deformation. This field-induced deformation is maintained until the electric field is removed. This type of materials offers very low strain values (around 4%) but relatively high energy densities [2], [5]. Unimorph and bimorph bending actuators made of EGEs were demonstrated in literature [5].

### **2.2.3. Smart Like Materials**

*Piezoelectric Ceramics (PZTs)* have been used as sensor and active force generator for a long time. They present numerous advantages, such as precise and high electromechanical responses, elevated response speeds and being easily formed. On the other hand, PZTs can generate only 0.2% of strain at maximum. Single crystal PZTs can generate slightly more strain levels around 1.7%. PZT are capable to work with low energy densities [5], [8], [18].

*The Shape Memory Alloys (SMAs)* are famous for being a large-displacement sensor/actuator material. They can produce considerable amount of linear displacements and generate large forces. Their maximum strain is limited to around 8% and gets lower when the material is subjected to cyclic loading. On the other hand, low fatigue life, temperature control problems, small response speeds and large energy requirements are still serious concerns [8].

The use of SMAs as artificial muscle is not practical due to the time required to cool the alloy and return to the initial position. In order to obtain good operating frequencies, the SMA must be actively cooled which increase the bulkiness, complexity and cost of the system [5]. SMAs and PZTs both suffer from small strains and high stiffness. Thus, these materials are not particularly suited to artificial muscle applications.

*Ferroelectric Polymers (FPs)* have a non-centro-symmetric structure that exhibits permanent electric polarization. These materials possess dipoles that can be aligned in an electric field and maintain their polarization. The induced polarization can be removed by applying a reverse electric field or by heating above the material's Curie temperature. The polymers exhibiting these properties are limited mainly to PVDF and some PDVF copolymers such as Nylon 7, Nylon 11 and their odd numbered combinations [2], [5].

These materials may act piezoelectric responses after appropriate poling. Their piezoelectric actuation properties are typically worse than ceramic piezoelectric crystals. However, they have the advantages of being lightweight, flexible, easily formed, and are not brittle. Additionally, while ceramics are limited to strains on the order of 0.2%, ferroelectric polymers are capable of strains of 10% and very high electromechanical coupling efficiencies [5].

### **2.3. In Depth Review of Dielectric Elastomers**

DEAs work mainly by the effect of electrostatic attraction between compliant conductive layers applied on the two surfaces of elastomeric films. When voltage is exerted, the conductive layers induce compressive forces and the film counteracts in perpendicular directions. The film shrinks in thickness and expands in area accordingly. The actuation mechanism of *Dielectric Elastomers (DEs)* is as illustrated in Figure 2-2. Elastomers are sufficiently compliant that large strains are induced and there is efficient coupling between the electrical energy input called the Maxwell Stress and mechanical energy output. Typically, the spacing between conductive layers is less than 0.1 mm. Although the output planar strains are large, the displacement in thickness direction is small. Since elastomers maintain constant volume, contraction in one direction leads to expansion in the other two directions. Most mechanisms make use of the expansion perpendicular to the direction of the applied electric field due to large displacements. By pre-straining one of the two axes

most of the expansion is directed perpendicular to the pre-strain. The pre-straining can also result in higher breakdown strengths [15].

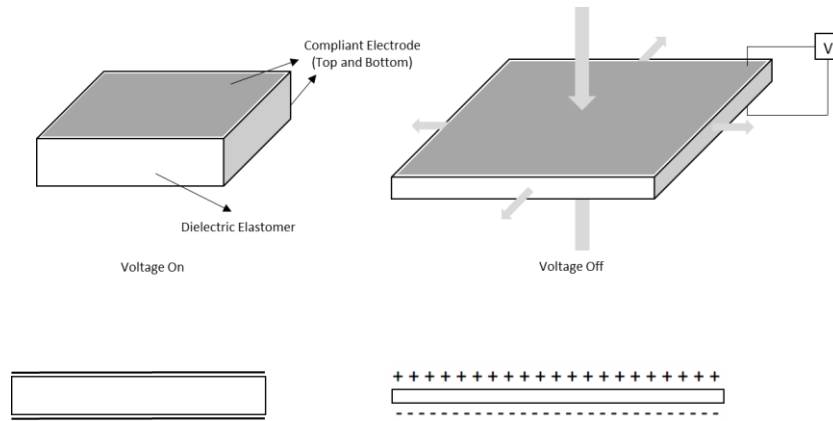


Figure 2-2 Working principle of DEAs

DEA produce linear motion while electric motors generate rotary motion [28]. They have fast response time [20], [22], [25]–[27], excellent conversion time [25], high specific energy value [20], [25], [27], exhibits large actuation strains which are typically in the range of % 10 to % 100 but can reach up more than % 380 [2], [8], [21], [23], [25]–[27]. They are light weight [2], [15], [21], [23], structurally flexible [21], high electromechanical efficiency i.e. >% 90 [2], simple to construct [23] and reach up to high electric fields (usually around 100 V/  $\mu\text{m}$ ) [2]. They have high energy density (>8 MJ/m<sup>3</sup>) [2], [20], [23]. They are silent [20], [23], reliable [22] and power consumption is low [20]. They can work in large bandwidths especially in silicone (1400 Hz) and moderate bandwidths are possible in 3M's acrylic VHB tapes (10 Hz typical) but small displacements can be achieved at tens of kilohertz in both silicone and acrylic materials [20]. They can operate over relatively high temperature ranges, silicone in particular can operate over a temperature range of -100 to +250 °C. Both can also act as generators and sensors. They are cost effective [15] and show low cycling hysteresis [2].

On the other hand, high driving voltages which are typically lie in the range of 1 to 10 kV [28] is a major concern. The range of applied maximum voltage depends on the polymer breakdown field and the thickness of the polymer film. However, switch-mode amplifiers (very small sizes, 2.5 mm x 2.5 mm x 2.5 mm) able of convert 10 V to 1000 V are under development, allowing the possibility of incorporating low to high voltage conversion [28].

DEs can be tailored to make rotary motors which is feasible and possibly even advantageous, to replace traditional electromagnetic motors with dielectric elastomer motors in conventional robots [39].

### **2.3.1. Materials**

Dielectric materials are capable to polarize when exposed to electric field. In theory, any elastomer or soft thermoplastic may act as a dielectric layer. These materials are composed of small dipoles. These dipoles are aligned accordingly to the applied electric field and a certain time is required to complete response. This time is known as the relaxation time and governs the dynamic response of the dielectric material.

Widely used dielectric materials are silicone, polyurethane and acrylic elastomers. Indeed, a large number of elastomer materials have been tested for DE devices, including PU, isoprene or natural rubber [40], acrylic rubbers, silicone elastomers [41], fluoro elastomers and even thermoplastic copolymers [2]. Besides, PDMS [40], PVDF [28] and Elastosil 625 [28] are the future promising dielectric materials that are currently under investigation. However, literature community is focused on acrylic and silicone elastomers where these materials are the most promising and commercially available ones.

Vulcanization is a process that generates cross linkages between the polymer chains of the rubber molecules [15]. Dielectric elastomers can be chemically formulated and

fabricated with conventional polymer processing techniques such as spin coating and casting in laboratory conditions.

Among all, acrylic elastomers are a kind of Polyacrylate [22], [25], [41] which are commercially available as brand names VHB F4969PC [23], VHB 4910 and VHB 4905 from 3M company.

VHB 4905 and VHB 4910 are acrylic foam elastomers available in the form of a membrane. These materials are made from the mixture of aliphatic acrylate, which are based on the structure of a vinyl group and a carboxylic acid terminus. VHB is in the form of tape material and can exert very large strains. They show a dissipative behavior, incompressible and viscoelastic in nature. These tapes have excellent durability and excellent solvent and moisture resistance [28], [38], [42]. However, these materials suffer from important viscoelastic effects, which result in long-term relaxations and slow response times [2]. They are very sensitive to humidity and temperature with an optimum operation temperature at around 20 °C for un-modified acrylates [2]. The handling of these products is quite difficult because of their sticky nature. The manufacturer declared and research community extracted specifications of VHB tapes are tabulated in Table 2-3. According to the material specifications sheet [43], young's modulus of VHB tapes is defined three times more than its shear modulus.

On the other hand, there are other materials recently defined as a good alternative material for actuation purposes [15], [41]. Nitrile Butadien Rubber (NBR) is a synthetic elastomer which is manufactured by combining the copolymerized Acrylonitrile (ACN) and Butadiene Rubber (BR). This material performs better mechanicals properties with respect to silicone and acrylic elastomers. PDMS, commonly known as silicone, is a mixed inorganic–organic polymer based on silicon and oxygen backbone (Si–O), which provides low elastic modulus and high mechanical dissipation factors [2]. Silicones possess relatively low dielectric constant and energy density ( $\epsilon' = 2.5\text{--}3.0$  at 1 kHz, and  $e = 0.75 \text{ MJ/m}^3$ , respectively) and

modest electro-mechanical actuation strain (about 120% of linear strain [2], about %30 actuation strain [25]) when compared with acrylic elastomers [2]. Nevertheless, they have the advantage of a lower viscoelasticity, resulting in a faster response time and low viscoelastic losses, good resilience and low electric leakage [2]. Moreover, they also exhibit the advantage of a wide temperature range (from  $-100$  to  $260$  °C) and have low rates of moisture absorption, which have resulted in their use in most commercial products [2]. To use as an actuator, silicone elastomers require compliant electrodes [25]. However, silicones are available as viscous liquids that can be polymerized after casting to form membranes of any desired thickness [22].

Table 2-3 VHB acrylic foam tape series technical specifications

Property	VHB 4905	VHB 4910
Thickness [mm]	0.5	1.0
Width (used) [mm]	1180	1140
Thickness tolerance	$\pm 15\%$	$\pm 10\%$
Adhesive type	General Purpose	General Purpose
Density [ $\text{kg}/\text{m}^3$ ]	960	960
90° peel adhesion [ $\text{N}/\text{cm}$ ]	21	26
Normal tensile [kPa]	690	690
Dynamic overlap shear [kPa]	480	480
Static shear weight in grams at (22 °C)	1000	1000
Dielectric breakdown strength [ $\text{V}/\mu\text{m}^{-1}$ ]	31 [44]	
Dielectric constant	4.5 at 1/8 Hz [44]	3.21 at 1kHz 2.68 at 1 MHz
Poisson's ratio	0.49	0.49
Volume resistivity [ohm-cm]	$3.1 \cdot 10^{15}$	$3.1 \cdot 10^{15}$
Shear modulus at 25°C, 1 Hz [Pa]	$6 \cdot 10^5$	$6 \cdot 10^5$
Young's modulus [MPa]	-	1-2 [44]
Young's modulus at 50% [MPa]	0.04 [44]	
Elongation [%]	>600 [44]	>600 [44]
Strain at break [%]	879 [44]	879 [44]
Long term use temperature [°C]	93 [44]	93 [44]
Energy density [ $\text{MJ}/\text{m}^3$ ]	3.4 [2]	3.4 [2]
Creep [%]	70 [44]	70 [44]
Thermal conductivity (W/mK)	0.16	0.16
Thermal coefficient of expansion ( $\text{m}/\text{m}/^\circ\text{C}$ )	$180 \cdot 10^{-6}$	$180 \cdot 10^{-6}$

\*: All other material values are from [43] otherwise referenced.

Examples to silicone elastomers are CF19-KE441 [15], Sylgard 186 [22] from Dow Corning, CF18-2186 [22] and CF19-2186 from Nusil [15] where CF18 exhibits higher elongation at break point and is 3.5 times softer than Dow Corning’s Sylgard 186 [22].

Danfoss PolyPower material [20], [21], [27] is a DE material that is fabricated using a silicone elastomer in conjunction with compliant metal electrode technology. PolyPower actuator is produced in thin sheets of 40  $\mu\text{m}$  thickness and the reported dielectric field strength is 40  $\text{V}/\mu\text{m}$  and dielectric constant is around 3.1 [20]. High performance DE materials, including P(VDF-TrFE-CTFE) polymer doped with DEHP plasticizer are currently being investigated for their reasonably low stiffness ( $\sim 35\text{MPa}$ ) and high dielectric constant ( $>50$ ) [23]. A simple comparison of most widely used materials are provided in Table 2-4.

Table 2-4 Comparison of most widely used DE materials

Property vs Material	VHB 4905/4910	KE441	NBR
Dielectric Constant	4.7	2.8	14
Elastic Modulus	0.25 MPa	0.24 MPa	3 MPa
Stress Relaxation	high	small	very small
Time Response	good	bad	close to good

\* Measured according to a sample test configuration 50 [L] x 15 [W] mm x [0.5, 0.15, 0.2] [T] mm where T stands for VHB 4905, KE441 and NBR [15].

### 2.3.2. Electrodes

To use DEs as an actuator, sensor or a generator, electrodes play a key role in DEA fabrication. They are required to generate electric fields. The elastomer material is squeezed between the electrodes to generate motion. Dielectric material is coated on both sides with compliant electrodes. The electrodes must adhere to the elastomer membrane and be compliant to elastomer deformation without constraining it either mechanically or electrically, that is, they should be able to sustain large deformations without losing conductivity [44]. Practically, it means that compliant electrode

material should deform while the dielectric material is changing its shape during actuation without losing their conductivity and without generating opposing stress.

In theory, compliant electrodes should be conductive, sustain large deformations, adhere well to membrane, softer than the elastomer, easily patterned, not to alter the membrane properties, have low mechanical and electrical losses, be self-clearing and sustain millions of cycles without loss of performance [44]. The properties of different types of electrode materials are summarized below.

*Gold Electrodes* are available in thin layers of 250 nm of beaten gold. They have the advantage that so-called ‘self-healing’ effect. It means that at the position of the electrode where an electrical breakdown occurs, the thin gold layer evaporates and the actuator does not fail. On the other hand, the gold electrodes constrain the elongation of the actuator mechanically and cost ineffective [45].

*Silicone/Graphite Electrodes* are a mixture of 11 g graphite powder (TIMREX SP30 or Superior Graphite, ABG1005, 20g) and 10 ml silicone oil (DC 200/100 cs or 45 g Dow Corning, DC 200/50 cs). This graphite electrodes are used in many applications [45]–[52]. As an assumption, the Silicone/Graphite electrodes do not constrain the elongation of the actuator mechanically. The electrode thickness is approximately 20–40  $\mu\text{m}$  [45], [48]–[50]. Note that the thinnest electrode applied is measured to be approximately 5  $\mu\text{m}$  [46].

*Carbon Conductive Grease Electrodes* are assumed to be another compliant electrode type. The carbon conductive grease is smeared on the elastomer material. Carbon grease electrodes are the most commonly used solution as they provide good conductivity even at very high strains [7], [47], [53]–[55]. They are cheap and easy to apply, and they provide good adhesion to most DE materials while having minimal impacts on actuation performances. They result in slippage between adjacent layers in multilayer actuator applications [5]. Among the commercially available compliant conductive grease electrodes Chemtronics conductive grease CW7100 and CW7200

[15], [21], [52] and Tecnolube Nyogel 755G [56] are considered as reliable compliant electrodes.

Carbon-based electrodes (usually based on carbon black and graphite) are the most widely used ones, mainly because of their low cost, low impact on stiffness and ease of fabrication. They are generally used as loose particles (carbon powder), dispersed into a viscous media (carbon grease), or dispersed into an elastomer (conductive rubber) [44].

In contrast to greases, conductive powder electrodes do not use any binder to enhance the stability of the electrode. Conductive powders are commonly carbon-based materials, which are usually sprayed onto the surface of the dielectric. Graphite and carbon black electrodes have similar properties. Recently, transparent electrodes have been shown by using carbon nanotubes [21]. Ketjenblack EC-300J [57] and Ketjenblack EC-600JD [58] are nano powder electrode materials that are widely used as compliant electrodes [23]. On the other hand, a mixture of carbon black particles and silicone oil ELBESIL B50 serves also as a compliant electrode with sheet resistances in the range of 10-60 k $\Omega$  [38].

*Metal Electrodes* are not compliant. They are generally made of brass. They do not change their shape while the elastomer material is being squeezed. While these electrodes provide good electrical conductivity, they limit the strain of %~1 [5], [21], [35], [59], [60].

*Mixture Electrodes* are composed of two materials. Carbon Powder and Ethyl Alcohol are mixed to produce the electrode. Alcohol evaporates before actuation and a thin layer of carbon dust remains on the elastomer [61]. The graphite powder electrodes are tested in some of applications [47], [61]. Meanwhile, the mixture of silicone elastomer and carbon black are also tested [55], [62], [63]. The use of Ketjenblack and silicone glue mixture is also another application of mixture electrode. The mixture is viscous enough to spray on the elastomer for stable DEA application [28]. Beside all, graphite powder and silicone rubber compounds are also tested [28]. Other mixtures

like silicone matrix which is solved in trichloroethylene is combined with carbon black powder are currently under investigation [63]. Membrane is coated with a mixture of graphite powder (TIMREX SP30, 11 g) and silicone oil (DC 200/100 cs, 10 ml) for the electrodes [64].

*Silver Grease Electrodes* [47], [55] and *Conductive Polymer Electrodes* [53] are used rarely in applications.

### **2.3.3. Design and Manufacturing Performance Parameters**

DEA performance is highly affected and typically measured by a number of basic parameters. These parameters are summarized below.

*Strain* as the deformation response of a DEA depends on the loading configuration [25], typical DEAs provide strains greater than 100% in actuation [38], it was also demonstrated in literature that, controlling the electric charge instead of voltage during actuation may also induce additional strains [25]. Linking multiple actuators in series results in greater deformation, whereas multiple actuators in parallel results in larger force output [23], high voltage-triggered linear deformations up to 360% strain with clamped boundary conditions, 488% area strain with membrane under dead loads and 1692% area strain on membranes mounted on an air chamber have been reported using polyacrylate VHB films from 3M [22], capable of sustaining very high stretches [28].

*Energy Density* is defined as the mechanical output energy per stroke per unit volume or mass of material. Output stress varies quadratically with electric field. However, due to the compliance of the materials, the force that can be coupled to a load will decrease with increasing strain for a particular electric field. Maximum force is available at zero strain and at maximum strain the elastomer will not generate any output forces. For a given strain, the output force and DE stiffness can be tuned by varying the applied field. This is an important feature for artificial muscle applications as it allows the DEAs to heal themselves as natural muscles due to maintain stability

or prevent damage [5] and high energy density [22]. Precise measurement of DE film thickness is important parameter that needs to be determined to accurately estimate the applied electric field. When measuring film thickness, contact method is not recommended. Instead, using optical methods, capacitive methods to measure dielectric constant are preferred [12].

*Response Time* is the reaction speed of the DEA to an applied input. The input may be due to applied electric field or strain. Silicone elastomers are demonstrated to be faster (as low as a few ms) than acrylic elastomers in actuation response [8], [22].

*Theoretical Efficiency* is defined as the efficiency obtained with ideal electronics. Viscoelastic effects play a key role in reducing efficiency [5], elastomers have very little mechanical loss [28], humidity, temperature and strain rate effects the actuator performance [65]. The endurance limit or generated force are highly effected by the efficiency of the DEA [8]. Stress relaxation is not desirable for an actuator, it needs to be maintained as small as possible [15].

*Dielectric Constant* is proportional with the induced stress. As this value gets higher, the larger mechanical pressure and energy density can be obtained for the same driving voltage which means larger actuation forces [15]. The elastic modulus needs to be small to enhance the strain but the deliverable output force decreases with smaller modulus [15].

*Power Consumption* needs to be small. The driving currents are very low and the device is electrostatic in nature, so it will theoretically only consume power during an active area expansion (thickness reduction) and no power will be consumed to maintain the DE at a stable actuated state. Furthermore, some of the energy can be recovered after the actuation cycle is complete. In practice, however, there will be some leakage current through the dielectric, the amount will depend on the material and its thickness, and thus the DE will consume a small amount of power when maintained in a stable actuation state [5].

*Driving Voltage* is an important fact and needs to be kept minimum using thin dielectric layers [21], a low voltage driven DEA was developed using piezoelectric transformers [20]. Typical driving voltages for dielectric elastomer actuators lie in the range between 1 to 10 kV, depending on the polymer breakdown field and thickness of the polymer film [20]. Voltage requirement highly affected by the breakdown field and film thickness [28]. On the other hand, electric field is required to generate the high forces [20].

*Shear Modulus* is an important mechanical parameter. Elastomers become flexible as the shear modulus decreases [66], materials that have low shear modulus are preferred in flexible mechanism designs.

Some of the DE materials are commercially available but these materials perform limited actuation capability. On the other hand, fabrication of dielectric materials is another common option. The fabrication process may vary according to design requirements. Spin coating is a common manufacturing technique [21]. In spin coating, two components of uncured PDMS are mixed and applied onto the disk of a spin coater. The rotational speed defines the resulting thickness of the dielectric. After completing the first step, a heating process is applied to cross-link the elastomer which accelerates the curing process. Finally, graphite powder may be sprayed onto the PDMS surface if needed in defined master geometry.

Many studies are performed in literature to study the response of DEA under constant load with or without electrical activation. Different actuation concepts are studied with DEAs. Significant amount of force generation (around 400 gr) is observed with different pre-stretch values at applied around 5 kV [12], [56], [59], [62], [67]. The displacement characteristics studied for DEA [68] where voltage is sinusoidally varied from 0 to 2.7 kV at a quasi-static frequency. Pulse width modulated response characteristics are also studied [41].

Various voltage input signals are applied like ramp (as low as possible), step-wise, sinusoidal, triangular and saw-tooth wave voltage to investigate electrical failure limits [12], [69]. The breakdown shall be observed in three minutes [12]. Also, free stroke vs frequency studies are performed. Blocking force tests are performed for dynamic behavior characterization.

#### **2.3.4. Pre-straining**

Pre-straining is a common method used in manufacturing of DEAs. As long as, pre-strain a DE has several negative effects on actuation performance, there are mechanical differences between pre-strained and non-pre-strained configurations.

Pre-straining is not a pre-request but provides higher actuator performances. It influences the mechanical and electrical properties [15]. When an elastomer is pre-strained, DE film thickness and driving voltage is reduced [21]. Pre-straining results in suppression or elimination of electromechanical instability, leading to large actuation strains [25]. In literature, both pre-straining and pre-stretching nomenclatures are commonly used to depict the same state. Uniaxial pre-stretching a DEA is an effective technique to obtain large deformation results compared to biaxial pre-stretching [22]. Pre-stretching helps to increase the actuation force and reduces the displacement decrease during actuation [41]. DEs are pre-stretched, typically up to five times their in-plane dimensions, in order to improve their performance due to reduced thickness [7], [45], [46], [56], [70].

The performance of a DEA is time-dependent and degrades after several cycles of actuation due to the continuous reduction of the pre-strain with time. When the pre-strain reduces, the actuation force and displacement decrease [15], [41].

Development of actuators without pre-strain is very important in robotic applications due to eliminate the negative effect of pre-straining [15]. On the other hand, pre-

straining of a DE is very cumbersome. Pre-straining jigs are commonly used in manufacturing of DEAs [26].

It is shown in literature that the electrical breakdown strength increases more than ten times by equi-biaxial pre-stretching of the DE film where the so-called pull-in failures are avoided. Meanwhile, it keeps the DEA in tension in all times which prevents buckling [7], [45], [60], [70].

Usually, the electrode material is sprayed onto the insulating elastomer film while it is strained at least about 75% [62]. Higher pre-stretch ratios result in high electrode effectivities.

### **2.3.5. Actuator Configurations**

Different types of DEAs are manufactured in literature for various purposes. The most common actuator types are sketched in Table 2-5. Among them, circular, single or multiple layered planar, stacked, rolled, tubular, and diaphragm designed actuators are widely preferred. The selected design of actuator serves for specific application needs. A rolled or a tubular actuator design generates large deformations and high force values but needs extremely large pre-strains to amplify strain and force [41]. Note that, different actuator designs need different manufacturing techniques.

On the other hand, the working principle of these DEA designs differ. Actuation mechanics of these DEA based on similar extension modules. Some of these use the uniaxial extension capabilities of DE while other use equi-biaxial, shear deformation capabilities.

Table 2-5 Comparison of most widely used DEA configurations

#	DEA Design Type	DEA Schematic View	Reference
1	Circular Actuators	<p>The diagram shows three circular cross-sections. The first, labeled (a), is divided into Region A (outer) and Region B (inner) with radii <math>R_A</math> and <math>R_B</math>. The second, labeled (b) Voltage Off, shows a smaller inner circle with radii <math>A\lambda_{off}</math> and <math>B\lambda_{off}</math>. The third, labeled (c) Voltage On, shows a larger inner circle with radii <math>A\lambda_{on}</math> and <math>B\lambda_{on}</math> and an outer radius <math>r</math>.</p>	[25]
2	Membrane, Single or Multi-Layer Planar Actuators	<p>The diagram shows a cross-section of a planar actuator. On the left, it is at rest with a voltage source connected to compliant electrodes (top and bottom) sandwiching an elastomer. On the right, it is shown under voltage, with arrows indicating 'Electrostatic Force' and 'Displacement'.</p>	[26]
3	Stacked Actuators	<p>The diagram shows two cylindrical stacks of alternating red and blue layers. The right stack is connected to a voltage source <math>V</math>.</p>	[21]
4	Rolled Actuators	<p>The diagram shows a schematic (a) of a rolled actuator with width <math>w_0</math> and thickness <math>t_0</math>, and a photograph (b) of the physical device.</p>	[27]
5	Tubular Actuators	<p>The diagram shows a vertical tube on a base, connected to a voltage source <math>V</math>. A double-headed arrow indicates vertical displacement.</p>	[71]
6	Diaphragm Actuators	<p>The diagram shows a diaphragm actuator with a central vertical rod and a 'Polymer film' at the bottom. Arrows indicate upward and downward displacement.</p>	[71]

### **2.3.6. Dielectric Constant**

Dielectric constant or the dielectric permittivity is defined as the ability of a material to store electrical energy in an electric field which characterizes the degree of electric polarization a material experiences under the influence of an external electric field. It is demonstrated that its value decreases by increasing pre-strain [45] and different excitation frequencies [49], [72]. The dielectric constant of VHB material is about 3.2 in pre-strained configuration and not equal to theoretical value of 4.7 and used by many researchers [45].

Actually, dielectric permittivity,  $\epsilon_r$  has real and imaginary parts [12]. Real part directly governs the amount of electrical energy available for conversion into mechanical energy. It also determines the actual effective Maxwell stress. The imaginary part accounts for the amount of electrical energy lost as electrical dissipation in the elastomer. The permittivity of a material is measured with broadband dielectric analyzers, LCR bridges, potentiostats/galvanostats and vector network analyzers by applying sinusoidal input. Real and imaginary parts can be obtained by circuit analysis.

It has been shown in literature that the dielectric constant of elastomeric films is frequency dependent. As the frequency of excitation increases the dielectric constant gets lower than theoretical values. Meanwhile, the strain response of the film is affected by the sinusoidal input.

### **2.3.7. Failure Types**

There are various failure types that need to be considered when designing and manufacturing DEAs. It is reported that over-stretching leads to material rupture [25]. On the other hand, tearing, cracking, sparking and strain hardening are observed common DEA failures [28]. Molecular weight breakdown as a results of a slipping of

chains and surmounting of intermolecular forces [66] and aggregation which is a material problem appears as the volume percentage filler particles is raised [8], [9].

Also, electrical breakdown is commonly observed actuator failure which is observed in case of high voltage application [25]. In many cases, voltage-induced deformation is limited by electrical breakdown [73]. Electric breakdown is observed when a defect region occurs due to voltage application on the DEA, where sparks can jump from one electrode to the other which means death to an actuator [28]. Dielectric breakdown in silicone actuators seems confined to defects but acrylic actuators breakdown due to the applied electric field reaching defined maximum value [28]. Loss of tension in the axial direction always precedes electromechanical instability [74].

*Electromechanical Instability* which is also known as pull-in instability is observed due to a positive feedback between an increasing electric field and a thinning DE, which may lead to electrical breakdown. This instability may be suppressed or eliminated by pre-stretch or by designing an elastomer with “short” polymer chains that restricts the limiting elastic strain to a sufficiently small value. The suppression or elimination of electromechanical instability leads to a significant enhancement in the actuation strain [25]. For a compliant dielectric such as an elastomer, the voltage-induced deformation is often limited by electromechanical instability [73].

A DEA may respond in failure to voltage in two ways: One is the electromechanical instability, characterized by a peak in the voltage-stretch response and the other one is a monotonic voltage-stretch response. When electromechanical instability is suppressed or eliminated, large actuation strains exceeding 100% may be attained. Electromechanical instability may be suppressed or eliminated by pre-stretching and/or selecting/designing another elastomer with a smaller limiting stretch [25].

*Stress softening* is observed under repeated application of loads, stress softening of elastomers occurs due to breakage of chains and weak bonds. This reduction in stress is also known as Mullins effect [66].

## **2.4. Conclusion**

When the literature is reviewed it is seen that the ionic EAPs require aqueous environment to actuate which is not a scope of this study. Among electronic EAPs, it is easy to select the acrylic dielectric elastomer material to study on based on several factors including commercial availability, ease of processability, well suit to intended application needs and behavioral similarity to the muscles of animals which show great application potentials in the field of small biomimetic robots. There is a high risk of dealing with the viscous nature of the acrylic material but the alternative silicone material is not available commercially and needs to be manufactured in laboratory conditions which is not a task for mechanical engineering discipline.

Throughout this study, Akzo Nobel's Ketjenblack EC-600JD is used as the electrode material for DEA applications. The compliant nature of the carbon particles combined with the sticky nature of the acrylic elastomer shall be a good combination to work. On the other hand, alternative Nyogel 755G is also tested as an electrode material and compared with respect to carbon dust.

As experienced from literature, pre-straining is a must and shall be applied in planer directions to increase the effectiveness of the manufactured DEA.

## CHAPTER 3

### MODELING OF ELASTOMERIC MATERIALS

#### 3.1. Introduction

In Chapter 2, the properties of dielectric materials are summarized in detail. The design and manufacturing prospects are outlined. The dielectric materials used in this thesis are 3M's VHB 4905 and VHB 4910 series acrylic tapes which are hyperelastic and viscoelastic in nature. In this Chapter, the mathematical modeling of such elastomeric material will be detailed.

Electroactive polymers are mathematically modeled based on phenomenological network models. Elastic behavior is identified based on energy function models. The viscoelastic behavior of these material is modeled by using Prony series. Prony series are generalized Maxwell models which are a part of micromechanical network model [26], [75]. According to the quasi-linear viscoelasticity (QLV) assumption, the relaxation and so the creep behavior of a material is independent of the imposed deformation which might not hold true for all materials [75].

The most widely used strain energy functions to simulate hyperelastic behavior of a elastomeric material are Hooke's, Neo-Hookean, Mooney-Rivlin, Ogden, Yeoh, Arruda and Boyce, Gent and Eight Chain models. All of these models fit to hyperelastic material test data in a certain amount of level. In this study Ogden, Yeoh and Mooney-Rivlin strain energy functions are selected for modeling purposes based on literature which will be described briefly in the next pages.

The fundamentals of Continuum Mechanics used in modeling are adopted from [76]–[79] unless otherwise specified. Reader should refer to related references for detailed proofs and concepts.

### 3.2. Kinematics of Deformation

Deformation of a body can be represented by its initial and current states as illustrated in Figure 3-1.

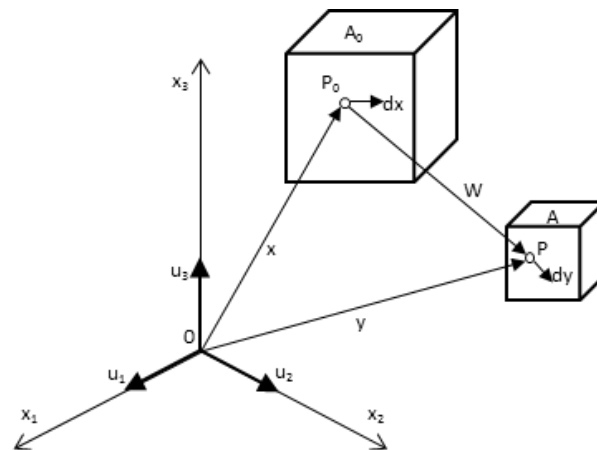


Figure 3-1 Deformation of a body from initial state to its current State

Let  $x$  and  $y$  denote the initial and the current states of a point,  $P$  on a deforming body. The current position of the point,  $y = y(x, t)$  is a function of its initial position and time. The transformation between initial,  $P_0$  and current,  $P$  points can be described with linear mapping as given in eqn. (3.2-1),

$$dy = Fdx \tag{3.2-1}$$

Where,  $F$  is the *deformation gradient tensor* and defined in eqn. (3.2-2) in its explicit form. It is possible to calculate any deformation of a body when deformation gradient is known.

$$F_{ij} = \frac{\partial y_i}{\partial x_j} = \begin{bmatrix} \frac{\partial y_1}{\partial x_1} & \frac{\partial y_2}{\partial x_1} & \frac{\partial y_3}{\partial x_1} \\ \frac{\partial y_1}{\partial x_2} & \frac{\partial y_2}{\partial x_2} & \frac{\partial y_3}{\partial x_2} \\ \frac{\partial y_1}{\partial x_3} & \frac{\partial y_2}{\partial x_3} & \frac{\partial y_3}{\partial x_3} \end{bmatrix} \quad (3.2-2)$$

Deformation of a body will result in volume change and this transformation can be expressed as given in eqn. (3.2-3), where,  $V_0$  indicates the *initial volume* and  $J$  is defined as the *incompressibility constraint* or the *volume ratio*.

$$dV = JdV_0 \quad (3.2-3)$$

*Stretch ratio*,  $\lambda$  is defined as the current length divided by the original length of the material. The eigenvalues of the deformation gradient tensor,  $F$  are defined as the *principal stretch ratios*,  $\lambda_i$ . The corresponding eigenvectors are called *principal direction of stretch*, and define an orthonormal basis along which the principal stretches are measured. Denoting  $l_{0,i}$  and  $l_i$  are the initial and the actual lengths in  $i^{\text{th}}$  principal direction, the stretch ratio,  $\lambda_i$  can be expressed as given in eqn. (3.2-4) and illustrated in Figure 3-2.

$$\lambda_i = \frac{l_i}{l_{0,i}} \quad (3.2-4)$$

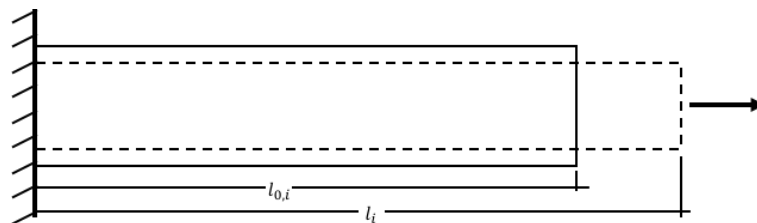


Figure 3-2 Elongation in principle direction

The derivative solutions of stretch ratios,  $\lambda_i$  are as given in eqn. (3.2-5).

$$\begin{aligned} l_i &= l_{0,i}\lambda_i \rightarrow \lambda_i = \frac{l_i}{l_{0,i}} \\ \dot{l}_i &= l_{0,i}\dot{\lambda}_i \rightarrow \dot{\lambda}_i = \frac{\dot{l}_i}{l_{0,i}} \\ \ddot{l}_i &= l_{0,i}\ddot{\lambda}_i \rightarrow \ddot{\lambda}_i = \frac{\ddot{l}_i}{l_{0,i}} \end{aligned} \quad (3.2-5)$$

The symmetric and positive definite *right Cauchy-Green tensor*,  $C$  also referred as the *Green deformation tensor* is defined in terms of deformation gradient tensor,  $F$  and given in eqn. (3.2-6).

$$C = F^T F \quad (3.2-6)$$

The *engineering strain*,  $\varepsilon_{e,i}$  is defined as the change in length divided by the original length and can be calculated in terms of stretch ratio as presented in eqn. (3.2-7).

$$\varepsilon_{e,i} = \frac{\Delta l}{l} = \frac{l_i - l_{0,i}}{l_{0,i}} = \frac{l_i}{l_{0,i}} - 1 = \lambda_i - 1 \quad (3.2-7)$$

*Left Cauchy-Green tensor*,  $B$  given in eqn. (3.2-8) is also named as *Finger deformation tensor* and is used to describe the local area change of the material. It is an important strain measure in terms of spatial coordinates. It is symmetric and positive definite. It can be defined based on the deformation gradient tensor,  $F$  and its eigenvalues are the principle stretches,  $\lambda_i$ .

$$B = FF^T \quad (3.2-8)$$

When there is no deformation, Finger tensor,  $B$  is equal to identity matrix,  $I$ . The *engineering strain tensor*,  $\varepsilon_{eng}$  can be written based on Finger tensor,  $B$  as given in

eqn. (3.2-9). Note that all elements of the engineering strain tensor,  $\varepsilon_{eng}$  is equal to zero when there is no deformation.

$$\varepsilon_{eng} = B - I \quad (3.2-9)$$

The *strain invariants*,  $I_i$  of the left Cauchy-Green tensor,  $B$  and right Cauchy-Green tensor,  $C$  are same and shares the same eigenvalues, which are the squares of the principal stretches,  $\lambda_i^2$ . The strain invariants,  $I_i$  can be calculated as given in eqn. (3.2-10).

$$\begin{aligned} I_1 &= C_{ii} = B_{ii} = \lambda_1^2 + \lambda_2^2 + \lambda_3^2 \\ I_2 &= \frac{1}{2} [(B_{ii})^2 - (B^2)_{ii}] = \frac{1}{2} [(C_{ii})^2 - (C^2)_{ii}] \\ I_2 &= \lambda_1^2 \lambda_2^2 + \lambda_2^2 \lambda_3^2 + \lambda_1^2 \lambda_3^2 = \frac{1}{\lambda_1^2} + \frac{1}{\lambda_2^2} + \frac{1}{\lambda_3^2} \\ I_3 &= \det B_{ii} = \det C_{ii} = \lambda_1^2 \lambda_2^2 \lambda_3^2 \end{aligned} \quad (3.2-10)$$

### 3.2.1. Uniaxial Tension Deformation State

Assume an elastomeric strip is extending uniaxially as illustrated in Figure 3-3. The material is only stretched in tension direction and the rest of two dimensions are free to deform.

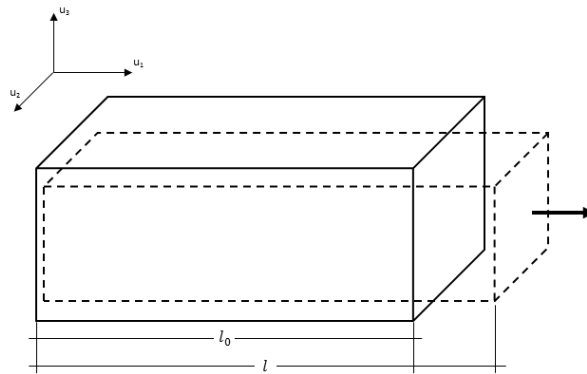


Figure 3-3 Elastomeric material subjected to uniaxial deformation

The stretch ratio,  $\lambda$  in tension direction,  $u_1$  can be defined as  $\lambda_1 = l/l_0$  where  $l_0$  and  $l$  are the material initial and deformed lengths. The stretch ratios of the free directions can be calculated as  $\lambda_2 = \lambda_3 = 1/\sqrt{\lambda_1}$  using the constant volume assumption. This results in stress free deformations as the material is free to deform in  $u_2$  and  $u_3$  directions. Then the strain invariants,  $I_1$  and  $I_2$  can be calculated as given in eqn. (3.2-10).

$$\begin{aligned}
 I_1 &= \lambda_1^2 + \left(\frac{1}{\sqrt{\lambda_1}}\right)^2 + \left(\frac{1}{\sqrt{\lambda_1}}\right)^2 = \lambda_1^2 + \frac{2}{\lambda_1} \\
 I_2 &= \frac{1}{\lambda_1^2} + \frac{1}{\left(\frac{1}{\sqrt{\lambda_1}}\right)^2} + \frac{1}{\left(\frac{1}{\sqrt{\lambda_1}}\right)^2} = \frac{1}{\lambda_1^2} + 2\lambda_1 \\
 I_3 &= 1
 \end{aligned} \tag{3.2-11}$$

Using the state definition, the deformation gradient,  $F$  can be expressed as given in eqn. (3.2-12).

$$F = \begin{bmatrix} \lambda_1 & 0 & 0 \\ 0 & \lambda_2 & 0 \\ 0 & 0 & \lambda_3 \end{bmatrix} = \begin{bmatrix} \lambda_1 & 0 & 0 \\ 0 & 1/\sqrt{\lambda_1} & 0 \\ 0 & 0 & 1/\sqrt{\lambda_1} \end{bmatrix} \tag{3.2-12}$$

The right Cauchy Green deformation tensor,  $B$  and  $BB$  matrix (which will be needed in next Chapters) can also be calculated as given in eqn. (3.2-13),

$$B = FF^T = \begin{bmatrix} \lambda_1^2 & 0 & 0 \\ 0 & \frac{1}{\lambda_1} & 0 \\ 0 & 0 & \frac{1}{\lambda_1} \end{bmatrix}, \quad BB = B^2 = \begin{bmatrix} \lambda_1^4 & 0 & 0 \\ 0 & \frac{1}{\lambda_1^2} & 0 \\ 0 & 0 & \frac{1}{\lambda_1^2} \end{bmatrix} \tag{3.2-13}$$

### 3.2.2. Simple Shear Deformation State

Assume an elastomeric strip is subjected to simple shear deformation as illustrated in Figure 3-4. The material is only stretched in one plane with a tilt motion keeping one dimension free and the other one constant.

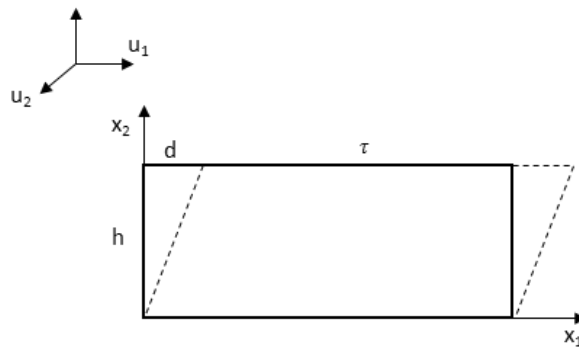


Figure 3-4 Physical interpretation of simple shear deformation

The amount of shear deformation is defined as  $k = d/h$  where  $d$  is the relative displacement of the upper and lower planes and  $h$  is the thickness of the material. The deformed configuration,  $x_i$  and undeformed configuration,  $X_i$  of the material and the related deformation tensor,  $F$  are given in eqns. (3.2-14) and (3.2-15) respectively.

$$\begin{aligned}x_1 &= X_1 + kX_2 \\x_2 &= X_2 \\x_3 &= X_3\end{aligned}\tag{3.2-14}$$

$$F = \begin{bmatrix} 1 & k & 0 \\ 0 & 1 & 0 \\ 0 & 0 & 1 \end{bmatrix}\tag{3.2-15}$$

The right Cauchy Green deformation tensor,  $C$  and left Cauchy Green deformation tensor,  $B$  can be calculated using the deformation gradient tensor,  $F$  defined in eqn. (3.2-15).

$$C = F^T F = \begin{bmatrix} 1 & k & 0 \\ k & 1 + k^2 & 0 \\ 0 & 0 & 1 \end{bmatrix} \quad (3.2-16)$$

$$B = F F^T = \begin{bmatrix} 1 + k^2 & k & 0 \\ k & 1 & 0 \\ 0 & 0 & 1 \end{bmatrix}$$

For simple shear case, the strain invariants can be constructed substituting the right Cauchy Green deformation tensor,  $C$  given in eqn. (3.2-16) into eqn. (3.2-10), which is presented in eqn. (3.2-17),

$$I_1 = B_{ii} = 1 + 1 + k^2 + 1 = 3 + k^2$$

$$I_2 = \frac{1}{2} [(B_{ii})^2 - (B^2)_{ii}] = 3 + k^2 \quad (3.2-17)$$

$$I_3 = 1$$

### 3.2.3. Volumetric Compression Deformation State

In a true/pure volumetric compression test, the applied hydrostatic pressure is equal on each outer plane of the material as sketched in Figure 3-5. The best way to perform a pure volumetric compression test is to use an aquarius environment that can easily exert the applied pressure on all surfaces. In a pure volumetric compression test, the stretch ratios,  $\lambda_i = \lambda_v$  observed in all principal directions are assumed to be equal. Therefore, the deviatoric strain invariants are equal,  $\bar{I}_1 = \bar{I}_2 = 3$  and the corresponding volume ratio will be,  $J = \lambda_v^3 = V_0/V$  where  $V_0$  is the initial volume and  $V$  is the actual volume of the material.

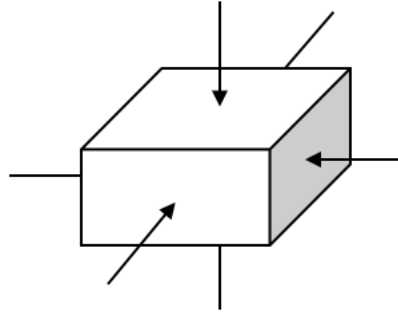


Figure 3-5 Physical interpretation of pure volumetric compression

Using the polynomial form of the strain energy potential, the total pressure,  $P$  on the material can be calculated assuming that the infinitesimal work of strain will be due to exerted pressure where,  $P_v = -\partial U/\partial J$  [80] as given in eqn. (3.2-18) which can be used to determine the  $D_i$  values (will be defined in strain energy functions) from volumetric test data. Note that  $\lambda_v^3 = J$  in compression case.

$$P_v = -\left(\frac{\sigma_1 + \sigma_2 + \sigma_3}{3}\right) = -\sum_{i=1}^N 2i \frac{1}{D_i} (\lambda_v^3 - 1)^{2i-1} \quad (3.2-18)$$

The strain energy functions which will be detailed in the next sections involve two parts. One is the deviatoric part, which describes the response of material to hyperelastic excitation and the other one is the volumetric part. Although both volumetric and deviatoric deformations are present, the deviatoric stresses are several orders of magnitude smaller than the hydrostatic stresses (because the bulk modulus is much higher than the shear modulus) and can be neglected for volume conservative material models [81]. Generally, the elastomeric materials have a Poisson's ratio approaching to 0.5 which indicates to an assumption that the material is volume conservative and the  $D_i$  values are assumed to be zero. That case is considered as incompressibility and infinite bulk modulus,  $K$  [80], [82].

Performing a pure volumetric compression is not simple and applicable for all times. Quasi-volumetric compression test is an alternative to pure volumetric compression test and can be used to determine the volumetric properties of a material instead [10, p. 43], [66, p. 45], [80], [81]. The quasi-volumetric compression test is performed by restricting the material in two principal directions and compressing through the free direction as sketched in Figure 3-6.

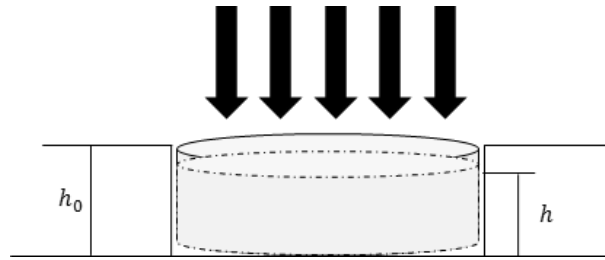


Figure 3-6 Physical interpretation of quasi-volumetric compression test

In a quasi-volumetric compression test, the *volumetric strain*,  $\varepsilon_v$  can be calculated as given in eqn. (3.2-19) using test parameters where,  $h_0$  is the initial and  $h$  is the actual material heights during test.

$$\varepsilon_v = \frac{V_0 - V}{V_0} = \frac{h_0 - h}{h_0} \quad (3.2-19)$$

In a pure volumetric compression test, the first and second deviatoric strain invariants are defined as given in eqn. (3.2-20) [80].

$$\begin{aligned} \bar{I}_1 &= \bar{\lambda}_1^2 + \bar{\lambda}_2^2 + \bar{\lambda}_3^2 \\ \bar{I}_2 &= \bar{\lambda}_1^{-2} + \bar{\lambda}_2^{-2} + \bar{\lambda}_3^{-2} \end{aligned} \quad (3.2-20)$$

Deviatoric stretches can be expressed as  $\bar{\lambda}_i = J^{-1/3} \lambda_i$  where  $\lambda_i$  are the principle stretches. When quasi-volumetric compression is considered, the corresponding principle stretches of the material will be as given in eqn. (3.2-21).

$$\lambda_1 = 1, \quad \lambda_2 = 1, \quad \lambda_3 = \frac{h}{h_0} \quad (3.2-21)$$

The volume ratio,  $J$  in volumetric compression test, can be calculated as given in eqn. (3.2-22) where,  $e_{pd}$  is the plunger displacement and  $r$  is the plunger radius.

$$J = \frac{\Delta V}{V_0} = \frac{\pi r^2 \Delta h}{\pi r^2 h_0} = \frac{h_0 - e_{pd}}{h_0} \quad (3.2-22)$$

For the calculation of  $D_i$  coefficients, the applied pressure,  $P_v$  and the corresponding volume ratio,  $J$ , throughout the quasi-volumetric compression test are required to be measured. The compressive stress imposed by the plunger is effectively the applied pressure,  $P_v$ .

### 3.3. Mechanics of Hyperelastic Materials

A material is called *Cauchy-elastic* or *Elastic* if the stress field at time,  $t$  depends only on the state of deformation and boundary condition including temperature at that time,  $t$  and not on the deformation or temperature history.

According to the theories of Continuum Mechanics, hyperelasticity is defined as a kind of constitutive modeling for ideally elastic materials that exhibit large strains. Let a stress,  $t = t(\varepsilon)$  is defined as a function of strain,  $\varepsilon$  where the work,  $W$  of stress on strain can be defined as given in eqn. (3.3-1).

$$W = \int t(\varepsilon) d\varepsilon \quad (3.3-1)$$

For an infinitesimal body, the incremental work of the external forces is equal to the incremental work of internal forces and can be determined as given in eqn. (3.3-2),

$$dW = P:dF \quad (3.3-2)$$

where,  $P$  is defined as the 1<sup>st</sup> Piola-Kirchhoff stress tensor,  $F$  is the deformation gradient tensor and  $W$  is the scalar form of Helmholtz free-energy function so called the *strain energy function*. The value of the strain energy function increases with the induced deformation.

The Helmholtz free energy function,  $W$  definition also contains the thermal energy and mechanical strain energy. On the other hand, in most discussions, the thermal energy part is usually neglected and mechanical part,  $W$  is considered including the *medium density*,  $\rho_o$ . The materials that satisfy eqn. (3.3-2) are so called *Hyperelastic*. The hyperelastic response of any material is obtained when the internal force equilibrium of mass, linear and angular momentum balance is achieved. This condition is satisfied either material is at rest or in equilibrium with respect to external force excitation. The balance equation of 1<sup>st</sup> Piola-Kirchhoff stress,  $P$  is given in terms of deformation gradient,  $F$  tensor and given in eqn. (3.3-3). It is the force measured per unit surface area defined in the reference configuration so called the *engineering stress*.

$$P(F, t) = Jt(F, t)F^{-T} \quad (3.3-3)$$

Where,  $t$  is defined as the ‘true’ *Cauchy stress*. The constitutive equation of an isothermal elastic body relates the Cauchy stress tensor,  $t = t(F, t)$  at each place with the deformation gradient tensor,  $F$ . Cauchy assumption is defined as the Newton’s law of action and counteraction and the appearance of stress tensor which is in equilibrium in the body. It is the force measured per unit surface area defined in the current configuration. Cauchy stress,  $t$  and 1<sup>st</sup> Piola-Kirchhoff stress,  $P$  point in the same

direction. Using eqn. (3.3-2), 1<sup>st</sup> Piola-Kirchhoff stress,  $P$  can also be written in terms of right Cauchy-Green deformation tensor,  $C$  as given in eqn. (3.3-4) to use where appropriate.

$$P = \frac{\partial W(F)}{\partial F} = 2F \frac{\partial W(C)}{\partial C} \quad (3.3-4)$$

The 1<sup>st</sup> Piola-Kirchhoff stress tensor,  $P$  is not a symmetric tensor so it is convenient to introduce 2<sup>nd</sup> Piola-Kirchhoff stress tensor,  $S$  which is symmetric and can be expressed in terms of deformation gradient tensor,  $F$  and right Cauchy-Green deformation tensor,  $C$  as presented in eqn. (3.3-5).

$$S = F^{-1}P = F^{-1} \frac{\partial W(F)}{\partial F} = 2 \frac{\partial W(C)}{\partial C} \quad (3.3-5)$$

The Cauchy stress,  $t$  definition is used to model hyperelastic material behavior and the balance equation given in eqn. (3.3-3) can be re-ordered to express Cauchy stress,  $t$  in terms of the 1<sup>st</sup> Piola-Kirchhoff stress,  $P$  as given in eqn. (3.3-6).

$$t = J^{-1}PF^T \quad (3.3-6)$$

Using the transformations provided in eqn. (3.3-4), the Cauchy stress,  $t$  can be re-written in reduced forms as given in eqn. (3.3-7).

$$t = J^{-1} \left( \frac{\partial W(F)}{\partial F} \right) F^T = 2J^{-1} \left( F \frac{\partial W(C)}{\partial C} \right) F^T \quad (3.3-7)$$

In hyperelasticity, the use of strain measure that are insensitive to rigid body motion are preferable. Right Cauchy-Green deformation tensor,  $C$  is insensitive to rigid body

motion so it is appropriate to introduce in equations. The Cauchy stress,  $t$  can also be written in terms of 2<sup>nd</sup> Piola-Kirchhoff stress,  $S$  as given in eqn. (3.3-8) using the equalities defined in eqn. (3.3-5).

$$\begin{aligned} t &= J^{-1}(FS)F^T = J^{-1}\left(F\left(2\frac{\partial W(C)}{\partial C}\right)\right)F^T \\ &= 2J^{-1}\left(F\frac{\partial W(C)}{\partial C}\right)F^T \end{aligned} \quad (3.3-8)$$

In order to determine constitutive equations for isotropic hyperelastic materials in terms of strain invariants,  $I_i$  differentiation of  $W(C) = W(I_1, I_2, I_3)$  with respect to right Cauchy-Green deformation tensor,  $C$  is considered using the chain rule as presented in eqn. (3.3-9).

$$\frac{\partial W(C)}{\partial C} = \frac{\partial W}{\partial I_1} \frac{\partial I_1}{\partial C} + \frac{\partial W}{\partial I_2} \frac{\partial I_2}{\partial C} + \frac{\partial W}{\partial I_3} \frac{\partial I_3}{\partial C} \quad (3.3-9)$$

Where,

$$\frac{\partial I_1}{\partial C} = I, \quad \frac{\partial I_2}{\partial C} = I_1 1 - C, \quad \frac{\partial I_3}{\partial C} = I_3 C^{-1} \quad (3.3-10)$$

Substituting eqn. (3.3-10) into eqn. (3.3-9) will result in eqn. (3.3-11) as follows,

$$\frac{\partial W(C)}{\partial C} = \frac{\partial W}{\partial I_1} 1 + \frac{\partial W}{\partial I_2} (I_1 1 - C) + \frac{\partial W}{\partial I_3} (I_3 C^{-1}) \quad (3.3-11)$$

Then, one can write the 2<sup>nd</sup> Kirchhoff stress,  $S$  as given eqn. (3.3-12),

$$S = 2 \frac{\partial W(C)}{\partial C} = 2 \left[ \left( \frac{\partial W}{\partial I_1} + I_1 \frac{\partial W}{\partial I_2} \right) I - \frac{\partial W}{\partial I_2} C + I_3 \frac{\partial W}{\partial I_3} C^{-1} \right] \quad (3.3-12)$$

For isotropic materials, assuming that the Cauchy stress,  $t$  depends on the left Cauchy Green deformation tensor,  $B$  and substituting eqn. (3.3-11) into eqn. (3.3-8), the Cauchy stress,  $t$  definition can be obtained as defined in eqn. (3.3-13).

$$t = 2J^{-1} \left\{ \frac{\partial W}{\partial I_1} FF^T + \frac{\partial W}{\partial I_2} (I_1 FF^T - CFF^T) + I_3 \frac{\partial W}{\partial I_3} C^{-1} FF^T \right\} \quad (3.3-13)$$

The most general Cauchy stress,  $t$  definition presented in eqn. (3.3-14) in terms of stress invariants is obtained by substituting right Cauchy Green tensor,  $C$  given in eqn. (3.2-6) and Left Cauchy-Green tensor,  $B$  given in eqn. (3.2-8).

$$t = 2J^{-1} \left[ \left( \frac{\partial W}{\partial I_1} + I_1 \frac{\partial W}{\partial I_2} \right) B - \frac{\partial W}{\partial I_2} B^2 + I_3 \frac{\partial W}{\partial I_3} I \right] \quad (3.3-14)$$

The resulting Cauchy stress,  $t$  given in eqn. (3.3-8) can be redefined in terms of principal stretches,  $\lambda_i$  representation.

$$dW(C) = dW(\lambda_1, \lambda_2, \lambda_3) = \frac{\partial W}{\partial \lambda_1} d\lambda_1 + \frac{\partial W}{\partial \lambda_2} d\lambda_2 + \frac{\partial W}{\partial \lambda_3} d\lambda_3 \quad (3.3-15)$$

Using eqn. (3.3-15), 2<sup>nd</sup> Piola-Kirchhoff stress tensor,  $S$  and principal direction based,  $S_i$  shall be introduced as given in eqn. (3.3-16) where  $u_i$  is the direction vector.

$$S = 2 \frac{\partial W}{\partial C} = \sum_{i=1}^3 \frac{1}{\lambda_i} \frac{\partial W}{\partial \lambda_i} u_i \times u_i \quad (3.3-16)$$

$$S_i = \frac{1}{\lambda_i} \frac{\partial W}{\partial \lambda_i}$$

Then the Cauchy stress tensor,  $t$  equation will result as given in eqn. (3.3-17).

$$t = J^{-1}(FS)F^T = \frac{1}{\lambda_1 \lambda_2 \lambda_3} \sum_{i=1}^3 \lambda_i \frac{\partial W}{\partial \lambda_i} u_i \times u_i \quad (3.3-17)$$

$$t_i = \frac{\lambda_i}{\lambda_1 \lambda_2 \lambda_3} \frac{\partial W}{\partial \lambda_i}$$

Many soft materials resist volume changes much stronger than shape changes. In case of incompressible material assumption which can be considered as a restriction for volume deformation, the volume ratio,  $J$  can be introduced as defined in eqn. (3.3-18). For an incompressible material, the volume ratio,  $J$  is equal to unity.

$$J = \frac{dV}{dV_0} = \lambda_1 \lambda_2 \lambda_3 = \det F = 1 \quad (3.3-18)$$

Strain energy function,  $W$  can be regarded as a function of the principal stretches,  $\lambda_i$ . It can be represented in the form,  $W(C) = W(\lambda_1, \lambda_2, \lambda_3)$ . It can be redefined introducing the incompressibility constraint which can be rearranged as  $J - 1 = 0$  as given in eqn. (3.3-19),

$$W = W(F) - p(J - 1) \quad (3.3-19)$$

Where,  $p$  is defined as the *hydrostatic pressure* or *Lagrangean multiplier* to enforce incompressibility constraint,  $J$  which is called the workless stress component and can

only be determined from equilibrium equations and the boundary conditions. Using the equality introduced in eqn. (3.3-19), the 1<sup>st</sup> Piola Kirchhoff stress,  $P$  can be differentiated with respect to deformation gradient,  $F$  as given in eq. (3.3-20) using the property  $\frac{\partial J}{\partial F} = JF^{-T}$ .

$$P = \frac{\partial W(F)}{\partial F} = -pF^{-T} + \frac{\partial W(F)}{\partial F} \quad (3.3-20)$$

Multiplying eqn. (3.3-20) by  $F^{-1}$  from left hand side, the resulting 2<sup>nd</sup> Piola Kirchhoff stress tensor,  $S$  can be re-stated as,

$$S = -pF^{-1}F^{-T} + F^{-1} \frac{\partial W(F)}{\partial F} = -pC^{-1} + \frac{\partial W(C)}{\partial C} \quad (3.3-21)$$

Multiplying eqn. (3.3-20) by  $F^T$  from right hand side, the resulting Cauchy stress,  $t$  can be re-written as,

$$t = -pI + \frac{\partial W(F)}{\partial F} F^T = -pI + F \left( \frac{\partial W(F)}{\partial F} \right)^T \quad (3.3-22)$$

The equations given in (3.3-20), (3.3-21) and (3.3-22) are the most general forms used to define incompressible hyperelastic materials at finite strains. In case of incompressible isotropic hyperelasticity, strain energy function,  $W$  may be expressed in terms of strain invariants,  $I_i$ . Noting that  $\det B = \det C = I_3 = 1$ , only  $I_1$  and  $I_2$  will be the independent deformation variables.

$$W = W[I_1(C), I_2(C), I_3(C)] = W[I_1(B), I_2(B), I_3(B)] \quad (3.3-23)$$

$$W = W[I_1(C), I_2(C)] - \frac{1}{2}p(I_3 - 1) \quad (3.3-24)$$

Where,  $\frac{p}{2}$  serves for Lagrange multiplier. Deriving eqn. (3.3-24) with respect to right Cauchy Green deformation tensor,  $C$  and substituting the chain rule elements given in eqn. (3.3-10), the same equation with eqn. (3.3-12) where  $I_3 \frac{\partial W}{\partial I_3}$  is replaced by  $-p/2$  is obtained.

$$\begin{aligned} S &= 2 \frac{\partial W[I_1, I_2]}{\partial C} - \frac{\partial W[p(I_3 - 1)]}{\partial C} \\ S &= -pC^{-1} + 2 \left( \frac{\partial W}{\partial I_1} + I_1 \frac{\partial W}{\partial I_2} \right) I - 2 \frac{\partial W}{\partial I_2} C \end{aligned} \quad (3.3-25)$$

Where, Cauchy stress,  $t$  is as given in eqn. (3.3-26).

$$t = J^{-1}(P)F^T = 2 \left[ \left( \frac{\partial W}{\partial I_1} + I_1 \frac{\partial W}{\partial I_2} \right) B - \frac{\partial W}{\partial I_2} B^2 \right] - pI \quad (3.3-26)$$

Using the property,  $B^2 = I_1 B - I_2 I + I_3 B^{-1}$  and eliminating  $B^2$  in favor of  $B^{-1}$ , one can rewrite eqn. (3.3-26) as,

$$t = J^{-1}(P)F^T = 2 \left[ \frac{\partial W}{\partial I_1} B - \frac{\partial W}{\partial I_2} B^{-1} \right] - pI \quad (3.3-27)$$

In terms of principal stretches,  $\lambda_i$  and principal component basis, the governing Cauchy stress,  $t$  equation can be written as given below using the hydrostatic pressure constraint,  $p$ .

$$W = W(\lambda_1, \lambda_2, \lambda_3) - p(J - 1) \quad (3.3-28)$$

Where,  $\frac{\partial J}{\partial \lambda_i} = J\lambda_i^{-1}$ , so analogously.

$$t_i = \lambda_i \frac{\partial W}{\partial \lambda_i} - p \quad (3.3-29)$$

$$P_i = \frac{\partial W}{\partial \lambda_i} - \frac{1}{\lambda_i} p \quad (3.3-30)$$

$$S_i = \frac{1}{\lambda_i} \frac{\partial W}{\partial \lambda_i} - \frac{1}{\lambda_i^2} p \quad (3.3-31)$$

The *engineering stress*,  $\sigma_i$  (force per unit area of the undeformed configuration) is calculated as for a totally incompressible material as given in eqn. (3.3-32),

$$\sigma_i = P_i = \frac{t_i}{\lambda_i} \quad (3.3-32)$$

The Cauchy stress,  $t$  can be evaluated to model all deformation states. But, in case of simple shear deformation a special and practical approach is available. The definition of simple shear deformation state was previously introduced at Section 3.2.2. Using the eqns. (3.2-16) and (3.2-17) which are calculated based on shear deformation,  $k$ , Cauchy stress,  $t$  given in eqn. (3.3-26) can be evaluated as,

$$t = 2 \left[ \left( \frac{\partial W}{\partial I_1} + (3 + k^2) \frac{\partial W}{\partial I_2} \right) \begin{bmatrix} 1 + k^2 & k & 0 \\ k & 1 & 0 \\ 0 & 0 & 1 \end{bmatrix} - \frac{\partial W}{\partial I_2} \begin{bmatrix} (1 + k^2)^2 + k^2 & 2k + k^3 & 0 \\ 2k + k^3 & 1 + k^2 & 0 \\ 0 & 0 & 1 \end{bmatrix} \right] - p \mathbf{1} \quad (3.3-33)$$

The shear stress component,  $t_{12}$  of stress tensor,  $t$  can be given as presented in eqn. (3.3-34).

$$t_{12} = 2 \left[ \left( \frac{\partial W}{\partial I_1} + (3 + k^2) \frac{\partial W}{\partial I_2} \right) k - \frac{\partial W}{\partial I_2} (2k + k^3) \right] \quad (3.3-34)$$

$$t_{12} = 2k \left( \frac{\partial W}{\partial I_1} + \frac{\partial W}{\partial I_2} \right)$$

The strain energy function,  $W$  in general defined in terms of strain invariants as  $W(I_1, I_2, I_3)$ . This equation will lead to  $W(I_1, I_2)$  in case of incompressibility is valid. Substituting the strain invariants  $I_1$  and  $I_2$  which can be written in terms of shear deformation  $k$  as calculated in eq. (3.2-17), it is possible to rewrite the strain energy function in terms of shear deformation as given in eqn. (3.3-35).

$$W(I_1, I_2, I_3) = W(I_1, I_2) = W((3 + k^2), (3 + k^2)) = W(k) \quad (3.3-35)$$

To evaluate the shear stress equation, one needs to find the derivatives of strain energy function,  $\partial W / \partial I_i$ . This expression can be remodified in terms of shear strain by taking the derivative using chain rule given in eqn. (3.3-36).

$$\begin{aligned}
W'(k) &= \frac{\partial W}{\partial k} = \frac{\partial W}{\partial I_1} \frac{\partial I_1}{\partial k} + \frac{\partial W}{\partial I_2} \frac{\partial I_2}{\partial k} \\
W'(k) &= \frac{\partial W}{\partial I_1} (2k) + \frac{\partial W}{\partial I_2} (2k) = 2k \left( \frac{\partial W}{\partial I_1} + \frac{\partial W}{\partial I_2} \right)
\end{aligned} \tag{3.3-36}$$

Where,  $W'(k) = t_{12}$  which is a special case solution for simple shear deformation mode. In shear case, the principal directions  $u_1, u_2, u_3$  are translated and rotated thus principle stretches,  $\lambda_i$  shall be recalculated. Note that the modified principal stretches,  $\lambda_i$  are the square roots of the eigenvalues of  $C$ . Then, the eigenvalue problem can be defined as given in eqn. (3.3-37),

$$(C - \lambda_i^2 I) = 0 \tag{3.3-37}$$

Principle stretches,  $\lambda_i$  can be evaluated based on shear deformation,  $k$  by solving the eqn. (3.3-37) [83] assuming that  $\lambda_3 = 1$ , as given in eqn. (3.3-38),

$$\begin{aligned}
\lambda_1 &= \sqrt{1 + \frac{k^2}{2} + \frac{k\sqrt{k^2 + 4}}{2}} = \frac{k}{2} + \sqrt{\frac{k^2}{4} + 1} \\
\lambda_2 &= \sqrt{1 + \frac{k^2}{2} - \frac{k\sqrt{k^2 + 4}}{2}} = -\frac{k}{2} + \sqrt{\frac{k^2}{4} + 1}
\end{aligned} \tag{3.3-38}$$

If one can substitute the equations given in eqn. (3.3-38) to strain energy function then the corresponding  $W(k)$  can be calculated and taking the derivate will result in final shear stress component.

### 3.4. Strain Energy Representation

Elastomers that are used as DEA material exhibit rubbery behavior. For isotropic materials, Ronald Rivlin found the base representation for the strain energy,

$$W(C) = W(I_1, I_2, I_3) \quad (3.4-1)$$

Hyperelastic materials can be defined through various strain energy density potentials,  $W$  which are a scalar valued function and  $I_i$  are the first, second and third strain invariants of the left Cauchy-Green deformation tensor,  $C$  respectively. The third invariant  $I_3$  is assumed to be equal to unity in case of material incompressibility.

A large number of constitutive equations represented by various forms of strain energy functions have been proposed for rubbery materials. Mechanical and electrical properties of unfilled and carbon-black filled rubber products are affected from the percentage of carbon-black. These materials are modeled with different constitutive equations such as Hooke's, Neo-Hookean, Rivlin, Mooney-Rivlin, Polynomial, Reduced Polynomial, Yeoh, Ogden, Arruda and Boyce, Van Der Waals Models and so on. Each of these models either use statistical approach, the strain invariant approach or principal stretch-based approaches.

Regardless of which strain energy function is used, the number of deformation states of a material is infinite. To understand the deformation mechanism, ease of modeling and application to parameter estimation, some basic deformation modes are preferred to study.

For all the deformation states described below,  $u_i$  will denote the principal deformation direction. All derivations are performed using the constant volume assumption where  $I_3 = \lambda_1 \lambda_2 \lambda_3 = 1$ . Strain energy function,  $W(I_1, I_2)$  and the strain invariants are calculated according to the equations given in eq. (3.2-10). Stretch ratio,  $\lambda_i$  definition is used instead of strain.

### 3.4.1. Mooney–Rivlin Strain Energy Function

Generalized Rivlin strain energy function which is also called the polynomial hyperelastic model is the most commonly used model in analysis of unfilled rubber vulcanizate rubber like materials and given in eqn. (3.4-2).

$$W = \sum_{i,j=0}^N C_{ij} (\bar{I}_1 - 3)^i (\bar{I}_2 - 3)^j + \sum_{i=1}^N \frac{1}{D_i} (J_{el} - 1)^{2i} \quad (3.4-2)$$

Where,  $W$  is the strain energy density function,  $C_{ij}$  are material parameters that describes the shear behavior,  $\bar{I}_i$ 's are the measure of distortion in the material namely the first and second invariants of the deviatoric strain,  $D_i$ 's are the material incompressibility parameters and  $J_{el}$  is the elastic volume ratio. The order parameter,  $N$  can be selected up to six however values of  $N$  greater than 2 are rarely used [84].  $C_{00}$  is the first term of this power series and set equal to 0 to reflect zero strain energy when the material is unstretched [85].

Mooney-Rivlin model is an expanded version of Neo-Hookean Model. Neo-Hookean strain energy function model is given in eqn. (3.4-3) and obtained from generalized Rivlin model by taking the first term  $C_{00} = 0$  and second index  $j = 0$  ( $C_{01}$  is also set to zero) [28], [78], [85].

$$W = C_{10} (\bar{I}_1 - 3) \quad (3.4-3)$$

Neo-Hookean model gives a good experimental fit up to %40 strain in uniaxial tension and up to %90 strains in simple shear where,  $C_1 = \frac{\mu}{2}$  is the material constant and  $\mu$  is defined as the shear modulus [66]. Mooney-Rivlin model is a phenomenological model and involves some basic assumptions. When the experimental data is fit to mathematical model, it is required to truncate the additional terms. If order is set to

unity, then 2 term Mooney-Rivlin strain energy function is obtained where it is given in eqn. (3.4-4).

$$W = C_{10}(\bar{I}_1 - 3) + C_{01}(\bar{I}_2 - 3) + \frac{1}{D_1}(J_{el} - 1)^2 \quad (3.4-4)$$

The most commonly used model assuming the volumetric part as  $J = 1$  [78], [86] is given in eqn. (3.4-5).

$$W = C_{10}(I_1 - 3) + C_{01}(I_2 - 3) \quad (3.4-5)$$

The second and third order Mooney-Rivlin strain energy functions are given in eqns. (3.4-6) and (3.4-7).

$$W = C_{10}(I_1 - 3) + C_{01}(I_2 - 3) + C_{11}(I_1 - 3)(I_2 - 3) + C_{20}(I_1 - 3)^2 \quad (3.4-6)$$

$$W = C_{10}(I_1 - 3) + C_{01}(I_2 - 3) + C_{11}(I_1 - 3)(I_2 - 3) + C_{20}(I_1 - 3)^2 + C_{30}(I_1 - 3)^3 \quad (3.4-7)$$

Regardless of the value of the order, the initial shear modulus,  $\mu_0$  and the bulk modulus,  $K_0$  of the material extracted from Mooney-Rivlin model depend only on the polynomial coefficient  $N = 1$  and are given in eqns. (3.4-8) and (3.4-9).

$$\mu_0 = 2(C_{01} + C_{10}) \quad (3.4-8)$$

$$K_0 = \frac{2}{D_i} \quad (3.4-9)$$

### Uniaxial deformation equations

The Cauchy stress,  $t$  is calculated based on the stretch ratios observed in principle directions using the eqn. (3.3-29). The term,  $\lambda_i \frac{\partial W}{\partial \lambda_i}$  is determined using the eqn. (3.4-5) where  $I_1$  and  $I_2$  are defined in eqn. (3.2-10),

$$\begin{aligned}\lambda_1 \frac{\partial W}{\partial \lambda_1} &= \lambda_1 (2C_{10}\lambda_1 + 2C_{01}(\lambda_1\lambda_2^2 + \lambda_1\lambda_3^2)) \\ \lambda_1 \frac{\partial W}{\partial \lambda_1} &= 2C_{10}\lambda_1^2 + 2C_{01}\lambda_1^2(\lambda_2^2 + \lambda_3^2)\end{aligned}\tag{3.4-10}$$

Analogously, similar derivative equation can be obtained for

$$\lambda_3 \frac{\partial W}{\partial \lambda_3} = 2C_{10}\lambda_3^2 + 2C_{01}\lambda_3^2(\lambda_1^2 + \lambda_2^2)\tag{3.4-11}$$

Cauchy stress,  $t_1$  can be evaluated using the boundary conditions  $t_2 = t_3 = 0$  where the material is free to deform in  $u_2$  and  $u_3$  directions. Where, hydrostatic pressure,  $p$  can be evaluated from eqn. (3.4-12).

$$t_3 = \lambda_3 \frac{\partial W}{\partial \lambda_3} - p = 0 \xrightarrow{\text{yields}} p = \lambda_3 \frac{\partial W}{\partial \lambda_3}\tag{3.4-12}$$

The resulting Cauchy stress,  $t_1$  is given in eqn. (3.4-13).

$$\begin{aligned}t_1 &= \lambda_1 \frac{\partial W}{\partial \lambda_1} - p = \lambda_1 \frac{\partial W}{\partial \lambda_1} - \lambda_3 \frac{\partial W}{\partial \lambda_3} \\ t_1 &= 2\lambda_1^2(C_{10} + C_{01}(\lambda_2^2 + \lambda_3^2)) - 2\lambda_3^2(C_{10} + C_{01}(\lambda_1^2 + \lambda_2^2))\end{aligned}\tag{3.4-13}$$

Substituting  $\lambda_1 = \lambda_1$  and  $\lambda_2 = \lambda_3 = \frac{1}{\sqrt{\lambda_1}}$  using the incompressibility  $I_3 = \lambda_1\lambda_2\lambda_3 = 1$  property, final Cauchy stress equation,  $t_1$  can be stated as given in eqn. (3.4-14).

$$t_1 = 2C_{10}\left(\lambda_1^2 - \frac{1}{\lambda_1}\right) + 2C_{01}\left(\lambda_1 - \frac{1}{\lambda_1^2}\right)\tag{3.4-14}$$

The equation given in (3.4-14) can also be evaluated using the equation given in (3.3-26). Using the eqn. (3.4-5), the derivative of strain energy function,  $W$  with respect to stress invariants  $I_1$  and  $I_2$  are calculated in eqn. (3.4-15).

$$\frac{\partial W}{\partial I_1} = C_{10} \quad , \quad \frac{\partial W}{\partial I_2} = C_{01} \quad (3.4-15)$$

Substituting eqns. (3.2-11), (3.2-13) and (3.4-15) in eqn. (3.3-26) results in multidimensional Cauchy stress tensor,  $t$  as given in eqn. (3.4-16).

$$t = 2 \left[ \left( C_{10} + \left( \lambda_1^2 + \frac{2}{\lambda_1} \right) C_{01} \right) \begin{bmatrix} \lambda_1^2 & 0 & 0 \\ 0 & \frac{1}{\lambda_1} & 0 \\ 0 & 0 & \frac{1}{\lambda_1} \end{bmatrix} - (C_{01}) \begin{bmatrix} \lambda_1^4 & 0 & 0 \\ 0 & \frac{1}{\lambda_1^2} & 0 \\ 0 & 0 & \frac{1}{\lambda_1^2} \end{bmatrix} \right] - p \begin{bmatrix} 1 & 0 & 0 \\ 0 & 1 & 0 \\ 0 & 0 & 1 \end{bmatrix} \quad (3.4-16)$$

Evaluating eqn. (3.4-16), the Cauchy stress component,  $t_{11} = t_1$  is calculated as given in eqn. (3.4-17).

$$t_1 = 2\lambda_1^2 C_{10} + 4\lambda_1 C_{01} - p \quad (3.4-17)$$

Where, the boundary conditions to calculate the hydrostatic pressure,  $p$  can be computed as given in eqn. (3.4-18).

$$t_3 = \frac{2}{\lambda_1} C_{10} + 2\lambda_1 C_{01} + \frac{2}{\lambda_1^2} C_{01} - p = 0 \quad (3.4-18)$$

$$p = \frac{2}{\lambda_1} C_{10} + 2\lambda_1 C_{01} + \frac{2}{\lambda_1^2} C_{01}$$

Substituting eqn. (3.4-18) into eqn. (3.4-17) will result in same stress value which is provided in eqn. (3.4-14). The engineering stress equation is also given in eqn. (3.4-19).

$$\sigma_1 = \frac{t_1}{\lambda_1} = 2C_{10} \left( \lambda_1 - \frac{1}{\lambda_1^2} \right) + 2C_{01} \left( 1 - \frac{1}{\lambda_1^3} \right) \quad (3.4-19)$$

### Simple shear deformation equations

Using the strain energy function given in eqns. (3.4-5) and (3.4-15), the eqn. (3.3-34) can be evaluated as given in eqn. (3.4-20).

$$\begin{aligned} \sigma_{12} &= 2k \left( \frac{\partial W}{\partial I_1} + \frac{\partial W}{\partial I_2} \right) \\ \sigma_{12} &= 2k(C_{10} + C_{01}) \end{aligned} \quad (3.4-20)$$

The hyperelastic material coefficients  $C_{10} > 1$  and  $C_{01} > 1$ . The infinitesimal shear modulus is calculated as given in eqn. (3.4-21).

$$\mu = 2(C_{10} + C_{01}) \quad (3.4-21)$$

### Volumetric Compression Equations

The quasi-volumetric compression test may be performed instead of pure volumetric compression test. The volumetric part of the strain energy function is obtained from eqn. (3.4-2) and used as described in Section 3.2.3. The  $N$  is equal to unity as the parameter variable is  $i = 1$ . In Mooney-Rivlin strain energy function the resultant volumetric compression equation is given in eqn. (3.4-22).

$$P_v = - \sum_{i=1}^N 2i \frac{1}{D_i} (J - 1)^{2i-1} = - \frac{2}{D_1} (J - 1) \quad (3.4-22)$$

### 3.4.2. Ogden Strain Energy Function

Mooney-Rivlin polynomial and Ogden models theoretically provide the similar results. However, there is a difference between the methods in terms of their formula. Mooney-Rivlin model present the strain energy density based on the principal strain invariants, whereas, Ogden model offers the strain energy density based on three principal stretches. As the principal stretches are directly measurable, it is advantageous to use model [66], [84], [87]. The general form of Ogden strain energy potential is given in eqn. (3.4-23).

$$W = \sum_{i=1}^N \frac{2\mu_i}{\alpha_i^2} (\bar{\lambda}_1^{\alpha_i} + \bar{\lambda}_2^{\alpha_i} + \bar{\lambda}_3^{\alpha_i} - 3) + \sum_{i=1}^N \frac{1}{D_i} (J_{el} - 1)^{2i} \quad (3.4-23)$$

Where,  $\bar{\lambda}_i = J^{-1/3} \lambda_i$ ,  $\lambda_i$  is a principal stretch ratio,  $N$  is the model order,  $\mu_i$ ,  $\alpha_i$  and  $D_i$  are material parameters which may be functions of temperature.  $J_{el}$ ,  $J$  and  $D_i$  have the same definitions as in the polynomial form. Simple hyperelastic models, which are not successful at high strain levels, are preferred at low strain levels. Therefore, Ogden model is more suitable for the cases where the material undergoes large strains. Additionally, it is more convenient to use the Ogden model, where compressibility should also be taken into account, i.e. where the material is slightly compressible [66]. By setting  $N = 0$ ,  $\alpha_i = 0$  and  $\alpha_2 = -2$  in the Ogden model, the Mooney-Rivlin model can be constructed [84].

Mooney-Rivlin model may capture the stress-strain response up to a strain of approximately 300% while the Ogden model typically captures the stress-strain response up to 700% [88]. The shear modulus obtained in Ogden model is given in eqn. (3.4-24).

$$\begin{aligned} \mu_i \alpha_i &> 0 \quad i = 1, \dots, N \\ \sum_{i=1}^N \mu_i \alpha_i &= 2\mu \end{aligned} \quad (3.4-24)$$

Where  $\mu$  is the shear modulus of the material in its reference configuration and the condition given in eqn. (3.4-24) is not necessary for every  $i$  if  $N \geq 3$  [78].

### Uniaxial Deformation equations

The Cauchy stress,  $t$  can be calculated using stretch ratio in principle directions as the equation given in eqn. (3.3-29). To calculate the Cauchy stress equation,  $\lambda_i \frac{\partial W}{\partial \lambda_i}$  shall be determined as given in eqn. (3.4-25).

$$\begin{aligned} \lambda_1 \frac{\partial W}{\partial \lambda_1} &= \lambda_1 \left( \frac{\mu_1}{\alpha_1} \alpha_1 \lambda_1^{\alpha_1-1} + \frac{\mu_2}{\alpha_2} \alpha_2 \lambda_1^{\alpha_2-1} \right) \\ \lambda_1 \frac{\partial W}{\partial \lambda_1} &= \mu_1 \lambda_1^{\alpha_1} + \mu_2 \lambda_1^{\alpha_2} \end{aligned} \quad (3.4-25)$$

Analogously, similar derivative equation can be obtained for

$$\lambda_3 \frac{\partial W}{\partial \lambda_3} = \mu_1 \lambda_3^{\alpha_1} + \mu_2 \lambda_3^{\alpha_2} \quad (3.4-26)$$

Cauchy stress equation for uniaxial stretch can be evaluated for  $t_1$ , using the boundary conditions  $t_2 = t_3 = 0$  where the material is free to move in  $u_2$  and  $u_3$  directions.

$$t_3 = \lambda_3 \frac{\partial W}{\partial \lambda_3} - p = 0 \xrightarrow{\text{yields}} p = \lambda_3 \frac{\partial W}{\partial \lambda_3} \quad (3.4-27)$$

Thus, hydrostatic pressure,  $p$  given in eqn. (3.4-27) can be evaluated from boundary conditions and can be used in eqn. (3.3-29) to evaluate Cauchy stress,  $t_1$ . The final equation is given in eqn. ).

$$\begin{aligned} t_1 &= \lambda_1 \frac{\partial W}{\partial \lambda_1} - p = \lambda_1 \frac{\partial W}{\partial \lambda_1} - \lambda_3 \frac{\partial W}{\partial \lambda_3} \\ t_1 &= \mu_1 \lambda_1^{\alpha_1} + \mu_2 \lambda_1^{\alpha_2} - \mu_1 \lambda_3^{\alpha_1} - \mu_2 \lambda_3^{\alpha_2} \\ t_1 &= \mu_1 (\lambda_1^{\alpha_1} - \lambda_3^{\alpha_1}) + \mu_2 (\lambda_1^{\alpha_2} - \lambda_3^{\alpha_2}) \end{aligned} \quad (3.4-28)$$

Substituting  $\lambda_1 = \lambda_1$  and  $\lambda_2 = \lambda_3 = \frac{1}{\sqrt{\lambda_1}}$  due to deformation mechanism in eqn. ), final Cauchy stress expression in stretch direction can be obtained as given in eqn. (3.4-29),

$$\begin{aligned} t_1 &= \mu_1 \left( \lambda_1^{\alpha_1} - \left( \frac{1}{\sqrt{\lambda_1}} \right)^{\alpha_1} \right) + \mu_2 \left( \lambda_1^{\alpha_2} - \left( \frac{1}{\sqrt{\lambda_1}} \right)^{\alpha_2} \right) \\ t_1 &= \mu_1 \left( \lambda_1^{\alpha_1} - \lambda_1^{(-\alpha_1/2)} \right) + \mu_2 \left( \lambda_1^{\alpha_2} - \lambda_1^{(-\alpha_2/2)} \right) \end{aligned} \quad (3.4-29)$$

The equation given in (3.4-29) can not be written using the equation given in (3.3-26) due that Ogden model uses principal stretches instead of strain invariants. Engineering stress definition can be given as provided in eqn. (3.4-30).

$$\sigma_1 = \frac{t_1}{\lambda_1} = \mu_1 \left( \lambda_1^{\alpha_1-1} - \lambda_1^{(-\alpha_1/2-1)} \right) + \mu_2 \left( \lambda_1^{\alpha_2-1} - \lambda_1^{(-\alpha_2/2-1)} \right) \quad (3.4-30)$$

#### Simple shear deformation equations

Substituting the derivations provided in eqn. (3.3-38) to a two term Ogden model strain energy function given in eqn. (3.4-23), the  $W(k)$  strain energy function can be calculated as given in eqn. (3.4-31).

$$\begin{aligned} W(k) &= \frac{2\mu_1}{\alpha_1^2} \left( \left( \frac{k}{2} + \sqrt{\frac{k^2}{4} + 1} \right)^{\alpha_1} + \left( -\frac{k}{2} + \sqrt{\frac{k^2}{4} + 1} \right)^{\alpha_1} - 2 \right) \\ &\quad + \frac{2\mu_2}{\alpha_2^2} \left( \left( \frac{k}{2} + \sqrt{\frac{k^2}{4} + 1} \right)^{\alpha_2} + \left( -\frac{k}{2} + \sqrt{\frac{k^2}{4} + 1} \right)^{\alpha_2} \right. \\ &\quad \left. - 2 \right) \end{aligned} \quad (3.4-31)$$

According to the equation given in (3.3-36), to calculate the shear stress component of Ogden model, the derivative of eqn. (3.4-31) shall be taken with respect to  $k$ . The resulting shear stress equation is provided in eqn. (3.4-32).

$$\begin{aligned}
t_{12} = W'(k) = & \frac{\mu_1}{\alpha_1} \frac{1}{\sqrt{\frac{k^2}{4} + 1}} \left[ \left( \frac{k}{2} + \sqrt{\frac{k^2}{4} + 1} \right)^{\alpha_1} \right. \\
& \left. - \left( -\frac{k}{2} + \sqrt{\frac{k^2}{4} + 1} \right)^{\alpha_1} \right] \\
& + \frac{\mu_2}{\alpha_2} \frac{1}{\sqrt{\frac{k^2}{4} + 1}} \left[ \left( \frac{k}{2} + \sqrt{\frac{k^2}{4} + 1} \right)^{\alpha_2} \right. \\
& \left. - \left( -\frac{k}{2} + \sqrt{\frac{k^2}{4} + 1} \right)^{\alpha_2} \right]
\end{aligned} \tag{3.4-32}$$

Where,  $\mu_i > 0$  is the infinitesimal shear modulus and  $\alpha_i$  are a stiffening parameters. By setting,  $N = 0$ ,  $\alpha_1 = 0$  and  $\alpha_2 = -2$  in the Ogden model, Mooney-Rivlin model is obtained where  $C_{10} = \frac{\mu_1}{2}$  and  $C_{01} = -\frac{\mu_2}{2}$  [84].

#### Volumetric compression deformation equations

The quasi-volumetric compression test may be performed instead of pure volumetric compression test. The volumetric part of the strain energy function is obtained from eqn. (3.4-2) and used as described in Section 3.2.3. The  $N$  is equal to 2 as the parameter variable is  $i = 2$ . In Ogden strain energy function the resultant volumetric compression equation is given in eqn. ).

$$P_v = - \sum_{i=1}^N 2i \frac{1}{D_i} (J - 1)^{2i-1} = -\frac{2}{D_1} (J - 1) - \frac{4}{D_2} (J - 1)^3 \tag{3.4-33}$$

### 3.4.3. Yeoh Strain Energy Function

The Yeoh strain energy function is a reduced polynomial model with  $N = 3$  and generated from Rivlin model [45], [84], [85]. Yeoh studied the effect of the second order invariance on the general polynomial series expansion, and stated that the sensitivity of the strain energy function to changes in the second invariant is generally much smaller than the sensitivity to the changes in the first invariant. In addition, the  $\bar{I}_2$  dependence was difficult to measure and hence it was preferable to neglect it completely instead of using erroneous values. This model is an output of a sensitivity analysis of Rivlin model which is performed following Tschogel model results. The model provides more accurate results for unfilled rubber vulcanizates. As the elastomer materials are made of carbon free acrylic and silicone, Yeoh model in theory provides the best for them. It is applicable for a much wider range of deformations. It is demonstrated that the Yeoh form based on left Cauchy-Green deformation tensor shows excellent agreement with the response of experimental actuators [26]. The general form of Yeoh strain energy function given in eqn. (3.4-34) which is a function of strain invariant,  $I_1$  only.

$$W(I_1) = \sum_{i=1}^3 C_{i0} (\bar{I}_1 - 3)^i + \sum_{i=1}^3 \frac{1}{D_i} (J_{el} - 1)^{2i} \quad (3.4-34)$$

Also, in eqn. (3.4-35), the reduced form of the equation considering incompressibility assumption,  $J_{el} = 1$ , [86] is presented.

$$W(I_1) = C_{10}(I_1 - 3) + C_{20}(I_1 - 3)^2 + C_{30}(I_1 - 3)^3 \quad (3.4-35)$$

Where,  $\mu_0 = 2C_{10}$  is the initial shear modulus and  $K_0 = \frac{2}{D_1}$  is the initial bulk modulus [45], [84]. The material constants,  $C_i$  given in eqn. (3.4-35) can also be approximated from the initial shear modulus as given in eqn.(3.4-36) [9].

$$\begin{aligned}
C_{10} &= \frac{\mu_0}{2} \\
C_{20} &= -\frac{\mu_0}{20} \\
C_{30} &= \frac{\mu_0}{200}
\end{aligned}
\tag{3.4-36}$$

Yeoh model is applicable for a much wider range of deformation and it is able to predict the stress-strain behaviour in different deformation modes from data gained in one simple deformation mode like uniaxial tension [10], [84].

#### Uniaxial deformation equations

For  $n^{\text{th}}$  order Yeoh model [89], the tension / compression equation can also be expressed as given in eqn. (3.4-37).

$$\sigma(\lambda) = \sum_{i=1}^n 2C_i i (\lambda - \lambda^{-2}) (\lambda^2 + 2\lambda^{-1} - 3)^{i-1}
\tag{3.4-37}$$

For a hyperelastic material, Cauchy stress,  $t$  can be calculated using stretch ratios,  $\lambda_i$  in principle directions according to eqn. (3.3-29). To calculate the Cauchy stress equation,  $\lambda_1 \frac{\partial W}{\partial \lambda_1}$  term shall be determined as given in eqn. (3.4-38),

$$\begin{aligned}
\lambda_1 \frac{\partial W}{\partial \lambda_1} &= \lambda_1 (2\lambda_1 C_{10} + 4\lambda_1 (\lambda_1^2 + \lambda_2^2 + \lambda_3^2 - 3) C_{20} \\
&\quad + 6\lambda_1 (\lambda_1^2 + \lambda_2^2 + \lambda_3^2 - 3)^2 C_{30}) \\
\lambda_1 \frac{\partial W}{\partial \lambda_1} &= 2\lambda_1^2 C_{10} + 4\lambda_1^2 (\lambda_1^2 + \lambda_2^2 + \lambda_3^2 - 3) C_{20} \\
&\quad + 6\lambda_1^2 (\lambda_1^2 + \lambda_2^2 + \lambda_3^2 - 3)^2 C_{30}
\end{aligned}
\tag{3.4-38}$$

Analogously, similar derivative equation can be written for  $\lambda_3 \frac{\partial W}{\partial \lambda_3}$  term as given in eqn. (3.4-39).

$$\lambda_3 \frac{\partial W}{\partial \lambda_3} = 2\lambda_3^2 C_{10} + 4\lambda_3^2 (\lambda_1^2 + \lambda_2^2 + \lambda_3^2 - 3) C_{20} + 6\lambda_3^2 (\lambda_1^2 + \lambda_2^2 + \lambda_3^2 - 3)^2 C_{30} \quad (3.4-39)$$

Using the boundary conditions  $t_2 = t_3 = 0$  where the material is free to deform in  $u_2$  and  $u_3$  directions, hydrostatic pressure,  $p$  can be obtained through eqn. (3.4-40).

$$t_3 = \lambda_3 \frac{\partial W}{\partial \lambda_3} - p = 0 \xrightarrow{\text{yields}} p = \lambda_3 \frac{\partial W}{\partial \lambda_3} \quad (3.4-40)$$

The eqn. (3.4-40) can be substituted in eqn. (3.3-29) to evaluate Cauchy stress,  $t_1$ . The resulting equation is given in eqn. (3.4-41).

$$\begin{aligned} t_1 &= \lambda_1 \frac{\partial W}{\partial \lambda_1} - p = \lambda_1 \frac{\partial W}{\partial \lambda_1} - \lambda_3 \frac{\partial W}{\partial \lambda_3} \\ t_1 &= 2\lambda_1^2 C_{10} + 4\lambda_1^2 (\lambda_1^2 + \lambda_2^2 + \lambda_3^2 - 3) C_{20} \\ &\quad + 6\lambda_1^2 (\lambda_1^2 + \lambda_2^2 + \lambda_3^2 - 3)^2 C_{30} \\ &\quad - (2\lambda_3^2 C_{10} + 4\lambda_3^2 (\lambda_1^2 + \lambda_2^2 + \lambda_3^2 - 3) C_{20} \\ &\quad + 6\lambda_3^2 (\lambda_1^2 + \lambda_2^2 + \lambda_3^2 - 3)^2 C_{30}) \\ t_1 &= 2(\lambda_1^2 - \lambda_3^2) (C_{10} + 2C_{20} (\lambda_1^2 + \lambda_2^2 + \lambda_3^2 - 3) \\ &\quad + 3C_{30} (\lambda_1^2 + \lambda_2^2 + \lambda_3^2 - 3)^2) \end{aligned} \quad (3.4-41)$$

For uniaxial tension case,  $\lambda_1 = \lambda_1$  and  $\lambda_2 = \lambda_3 = \frac{1}{\sqrt{\lambda_1}}$  using incompressibility assumption. Substituting the stretch transformations into eqn. (3.4-41), final Cauchy stress in stretch direction,  $u_1$  can be obtained as given in eqn. (3.4-42).

$$\begin{aligned} t_1 &= 2C_{10} \left( \lambda_1^2 - \frac{1}{\lambda_1} \right) + 4C_{20} \left( \lambda_1^2 - \frac{1}{\lambda_1} \right) \left( \lambda_1^2 + \frac{2}{\lambda_1} - 3 \right) \\ &\quad + 6C_{30} \left( \lambda_1^2 - \frac{1}{\lambda_1} \right) \left( \lambda_1^2 + \frac{2}{\lambda_1} - 3 \right)^2 \\ t_1 &= 2 \left( \lambda_1^2 - \frac{1}{\lambda_1} \right) \left( C_{10} + 2C_{20} \left( \lambda_1^2 + \frac{2}{\lambda_1} - 3 \right) \right. \\ &\quad \left. + 3C_{30} \left( \lambda_1^2 + \frac{2}{\lambda_1} - 3 \right)^2 \right) \end{aligned} \quad (3.4-42)$$

The eqn. (3.4-42) can also be written using the equation given in (3.3-26). Using the eqn. (3.4-35), the derivative of strain energy function,  $W$  with respect to stress invariants  $I_1$  and  $I_2$  are calculated in eqn. (3.4-43).

$$\begin{aligned} \frac{\partial W}{\partial I_1} &= C_{10} + 2C_{20}(I_1 - 3) + 3C_{30}(I_1 - 3)^2 \\ \frac{\partial W}{\partial I_2} &= 0 \end{aligned} \quad (3.4-43)$$

Substitute eqns. (3.2-11), (3.2-13) and (3.4-43) in eqn. (3.3-26) results in multidimensional Cauchy tensor notation,  $T$  given in eqn. (3.4-44). Note that  $\frac{\partial W}{\partial I_2} = 0$ .

$$T = 2 \begin{bmatrix} (C_{10} + 2C_{20}(I_1 - 3) + 3C_{30}(I_1 - 3)^2) \begin{bmatrix} \lambda_1^2 & 0 & 0 \\ 0 & \frac{1}{\lambda_1} & 0 \\ 0 & 0 & \frac{1}{\lambda_1} \end{bmatrix} \\ -p \begin{bmatrix} 1 & 0 & 0 \\ 0 & 1 & 0 \\ 0 & 0 & 1 \end{bmatrix} \end{bmatrix} \quad (3.4-44)$$

Evaluating the eqn. (3.4-44) and using the eqn. (3.2-11), the Cauchy stress component,  $T_{11} = t_1$  can be calculated as given in eqn. (3.4-45).

$$t_1 = 2\lambda_1^2 \left( C_{10} + 2C_{10} \left( \lambda_1^2 + \frac{2}{\lambda_1} - 3 \right) + 3C_{10} \left( \lambda_1^2 + \frac{2}{\lambda_1} - 3 \right)^2 \right) - p \quad (3.4-45)$$

Where,

$$\begin{aligned} t_3 &= 2\frac{1}{\lambda_1} \left( C_{10} + 2C_{10} \left( \lambda_1^2 + \frac{2}{\lambda_1} - 3 \right) + 3C_{10} \left( \lambda_1^2 + \frac{2}{\lambda_1} - 3 \right)^2 \right) \\ &\quad - p = 0 \\ p &= \frac{2}{\lambda_1} \left( C_{10} + 2C_{10} \left( \lambda_1^2 + \frac{2}{\lambda_1} - 3 \right) + 3C_{10} \left( \lambda_1^2 + \frac{2}{\lambda_1} - 3 \right)^2 \right) \end{aligned} \quad (3.4-46)$$

Substitute eqn. (3.4-46) into eqn. (3.4-45) will result in same stress expression given in eqn. (3.4-42). Finally, the engineering stress equation will be as defined in eqn. (3.4-47).

$$\sigma_1 = \frac{t_1}{\lambda_1} = 2 \left( \lambda_1 - \frac{1}{\lambda_1^2} \right) \left( C_{10} + 2C_{20} \left( \lambda_1^2 + \frac{2}{\lambda_1} - 3 \right) + 3C_{30} \left( \lambda_1^2 + \frac{2}{\lambda_1} - 3 \right)^2 \right) \quad (3.4-47)$$

### Simple shear deformation Equations

$N^{\text{th}}$  order Yeoh simple shear deformation mode [89] can also be written as given in eqn. (3.4-48).

$$\tau(\gamma) = \sum_{i=1}^n 2\gamma C_i i \gamma^{2(i-1)} \quad (3.4-48)$$

Using the strain energy function,  $W$  given in eqn. (3.4-35) and the derivations provided in eqn. (3.4-43), the eqn. (3.3-34) can be rewritten as given, and the initial shear modulus of Yeoh model can be approximated according to eqn. (3.4-36).

$$\begin{aligned} \sigma_{12} &= 2k \left( \frac{\partial W}{\partial I_1} + \frac{\partial W}{\partial I_2} \right) \\ \sigma_{12} &= 2k(C_{10} + 2C_{20}(I_1 - 3) + 3C_{30}(I_1 - 3)^2) \\ \sigma_{12} &= 2k \left( C_{10} + 2C_{20}((3 + k^2) - 3) + 3C_{30}((3 + k^2) - 3)^2 \right) \\ \sigma_{12} &= 2k(C_{10} + 2C_{20}k^2 + 3C_{30}k^4) \\ \sigma_{12} &= 2kC_{10} + 4k^3C_{20} + 6k^5C_{30} \end{aligned} \quad (3.4-49)$$

### Volumetric compression equations

The quasi-volumetric compression test may be performed instead of pure volumetric compression test. The volumetric part of the strain energy function is obtained from eqn. (3.4-2) and used as described in Section 3.2.3. The  $N$  is equal to 3 as the parameter

variable is  $i = 3$ . In Yeoh Energy function the resultant volumetric compression equation is given in eqn. (3.4-50).

$$P_v = - \sum_{i=1}^N 2i \frac{1}{D_i} (J - 1)^{2i-1} \quad (3.4-50)$$

$$P_v = - \frac{2}{D_1} (J - 1) - \frac{4}{D_2} (J - 1)^3 - \frac{6}{D_3} (J - 1)^5$$

### 3.5. Viscoelastic Materials

The time dependent material behavior is often referred to as *viscoelasticity*. When an elastomer material is subjected to a constant load, it deforms continuously. It continues to deform slowly with time indefinitely or until rupture or yielding caused failure. An example to a life span of an idealized elastomer material is given in Figure 3-7. The primary region is the early stage of loading, then it reaches a steady state which is called the creep stage (secondary region) followed by a rapid increase (tertiary stage) and finally rupture. This phenomenon of deformation under load with time is called *Creep*. All elastomeric materials creep to a certain level, some may not show a secondary region and tertiary creep only occurs at high stresses. The degree of creep depends on several factors, such as type of material, magnitude of load, temperature and time [90, p. 1].

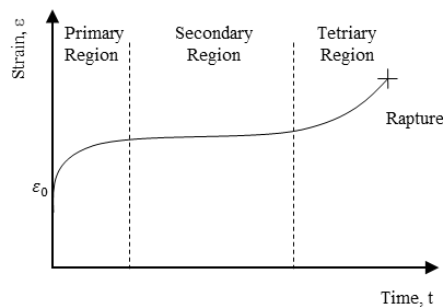


Figure 3-7 Response of elastomer w.r.t. constant uniaxial loading [90, p. 1]

If the applied load is released before the creep rupture occurs, an immediate elastic recovery equal to the elastic deformation, followed by a period of slow recovery is observed as shown in Figure 3-8. The material in most cases does not recover to the original shape and a permanent deformation remains. The magnitude of the permanent deformation depends on length of time, amount of stress applied and temperature [90].

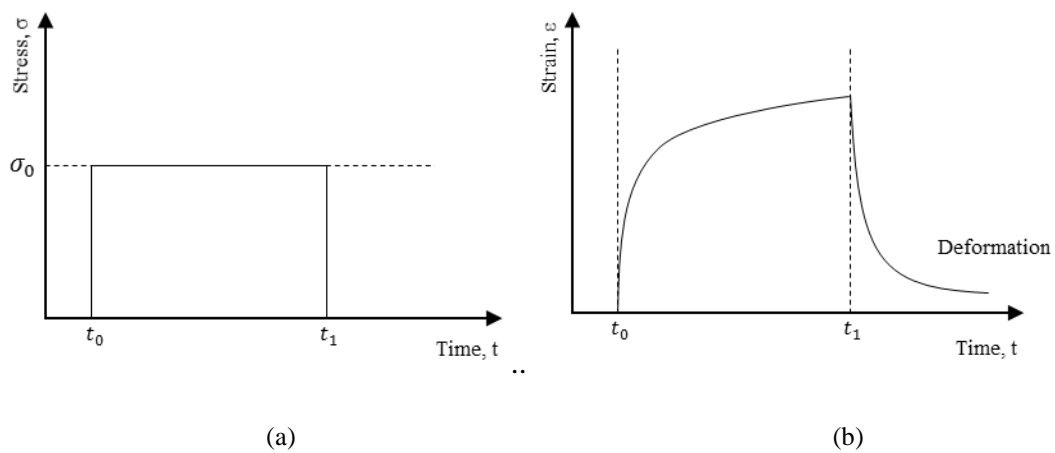


Figure 3-8 (a) Applied constant uniaxial load from  $t_0$  to  $t_1$  (b) Deformation response of material

The creep rupture is basically similar to a creep test with the exception that it is continued until the material fails. The basic information obtained from the stress rupture test is the time to failure at a given stress as shown in Figure 3-9. Based on that, a safe side stress can be determined. Below the limit which is safe to operate, provides the time requirement of the end use application [90].

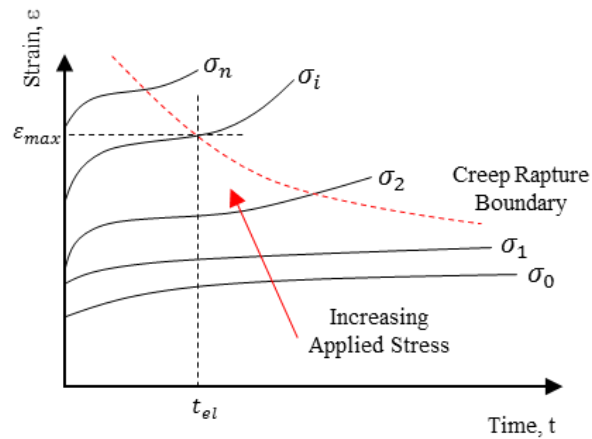


Figure 3-9 Creep rupture envelope and expected material life [90]

### 3.5.1. Elastomer Design

Design with plastics can be divided into two categories, design for strength and design for stiffness. The strength of a component is limited by the yield strength and rupture resistance of the material from which it is made. A creep rupture envelope given in Figure 3-9 can be obtained from creep test. For an expected life time, the maximum stress,  $\sigma_{max}$  allowed can be decided from the creep rupture envelope line. Design for stiffness with creep curves proceeds by establishing the maximum strain acceptable  $\epsilon_{max}$ , thereby establishing a horizontal line on the creep diagram correspondingly. The expected lifetime  $t_L$  of the part is also determined, and the maximum stress permissible is found on the creep curve at the intersection of these two lines [90]. Time dependence of the mechanical response in a so called quasi-linear viscoelastic model is described by using time dependent coefficients in the strain energy potential [45]

### 3.5.2. Linear Viscoelasticity

Let constant stress,  $\sigma_i$  are to be applied to a viscoelastic material and time dependent strains,  $\epsilon_i$  are to be recorded as given in Figure 3-10. Before each constant loading is

applied, assume that the load is fully removed and material is let to recover its original position [90].

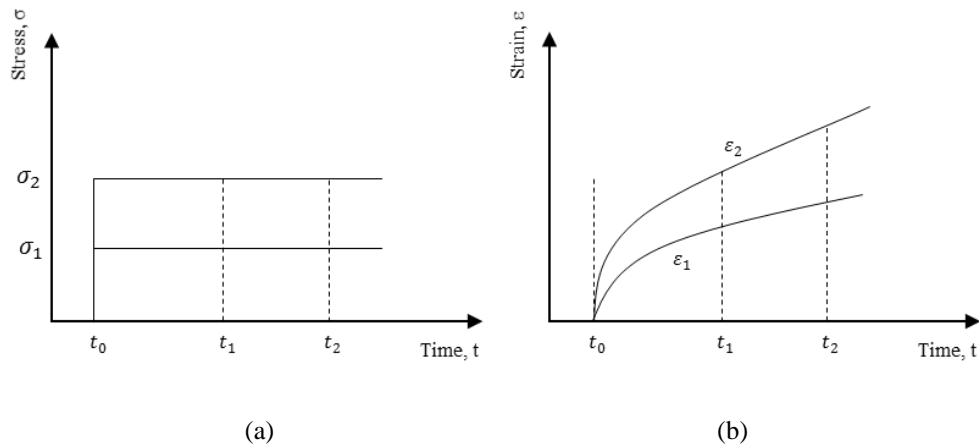


Figure 3-10 Viscoelastic creep response (a) Applied constant stress,  $\sigma_i$  (b) Observed strain,  $\epsilon_i$

If the stress-time and strain-time curves given in Figure 3-10 are replotted to form a strain-stress curve as given in Figure 3-11, for each applied loading,  $\sigma_i$ , there will be a strain deformation,  $\epsilon_i$  for each time,  $t_i$  which will be a straight line.

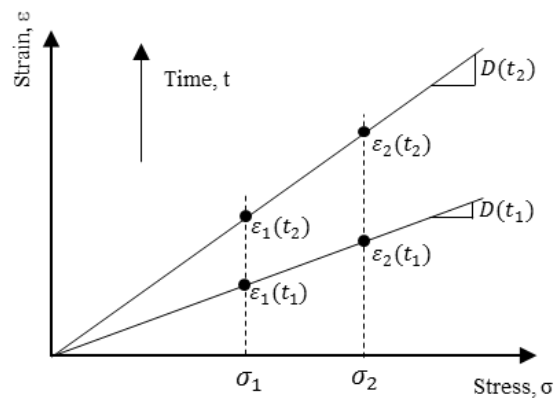


Figure 3-11 Applied constant loading,  $\sigma_i$  versus the strain deformation,  $\epsilon_i$

At a particular time  $t_1$  and  $t_2$ , following constant loading, the observed strains  $\varepsilon_1$  and  $\varepsilon_2$  are linear with the magnitude of corresponding stresses,  $\sigma_1$  and  $\sigma_2$  [90]. Then the stress strain relationship can be defined as given in eqn. (3.5-1) where the the slope is the constant time,  $t_i$  values. Thus, for any arbitrary time  $t_i$ , the strains encountered at two different stress levels can be expressed as presented.

$$\frac{\varepsilon_1(t_i)}{\sigma_1(t_i)} = \frac{\varepsilon_2(t_i)}{\sigma_2(t_i)} \quad (3.5-1)$$

For a creep test, *creep compliance function*,  $E_c(t)$  can be defined as given in eqn. (3.5-2) and expressed as the ratio of strain to stress at a certain time [90].

$$E_c(t) = \frac{\varepsilon(t)}{\sigma(t)} \quad (3.5-2)$$

This property is often characterized as *linear viscoelasticity*. In the linear range, the compliance is independent of stress, which means that the normalized compliance is identical whatever stresses are applied in the creep test ( $\sigma_1$ ,  $\sigma_2$  or other levels). The strain range where a specimen is considered linear viscoelastic can be determined by creep test [90]. The material is defined as nonlinear viscoelastic when these equalities defined in eqns. (3.5-1) and (3.5-2) are no longer valid. This phenomenon is sketched in Figure 3-12.

However, polymers generally exhibit linear viscoelastic property at low stresses such that the corresponding strain is below  $\sim 0.5 \times 10^{-2}$ . At higher stress levels, the material will assume nonlinear viscoelastic behaviors which will not obey the linear relation between stress and strain [90].

Linear viscoelasticity refers to a theory which follows the linear superposition principle, where the relaxation rate is proportional to the instantaneous stress [91].

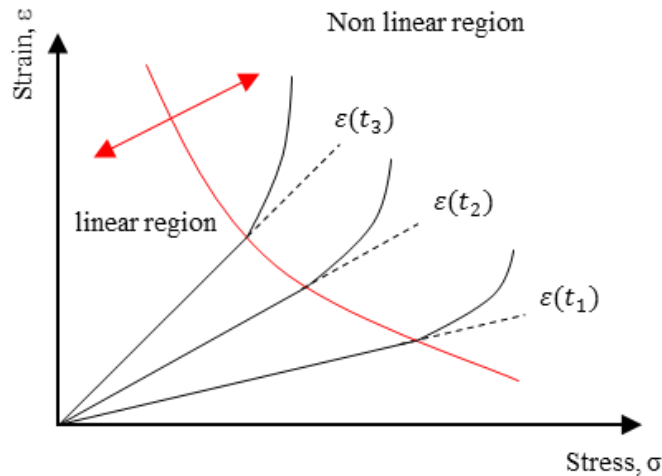


Figure 3-12 Linear-nonlinear transition of stress strain relationship with respect to different time levels [90]

The basis of small viscoelasticity is *Boltzmann superposition principle* [92], [93]. The principle assumes that “each loading step makes an independent contribution to the final state”. A viscoelastic material is said to be linear [93] if,

1. The stress is proportional to the strain at a given time as defined in eqn. (3.5-3). Where,  $c$  is a proportional constant.

$$\varepsilon[c\sigma(t)] = c\varepsilon[\sigma(t)] \quad (3.5-3)$$

The equation means that for a linear viscoelastic material, the creep compliance (or the relaxation function) is independent of the applied stress levels (or the strain levels). Thus, the compliance-time curves at different stress levels should coincide if the material is linear viscoelastic.

2. According to the definition of Boltzmann superposition principle, each loading step makes an independent contribution to the final deformation which can be obtained by the addition of these and indicates that the linear superposition principle holds and valid. Then, the linear viscoelastic response to a multiple step loading can be generalized in the integral form as given in eqn. (3.5-4).

$$\varepsilon(t) = E_{c,0}\sigma + \int_0^t \Delta E_c(t - \tau) \frac{d\sigma}{d\tau} d\tau \quad (3.5-4)$$

Where,  $E_{c,0}$  is defined as the instantaneous creep compliance,  $\Delta E_c(t - \tau)$  is the transient creep compliance,  $\sigma$  is the applied stress,  $\tau$  is a variable introduced into the integral in order to account for the history of the material. This integral equation is known as the *Heredity* or *Volterra integral*. It basically implies that the strain is depended on the stress history of the material under consideration [93].

### 3.5.3. Linear Viscoelastic Models

Different linear viscoelastic constitutive models can be constructed by superimposing springs and dashpots using them in serial and/or parallel as shown in Figure 3-13. The simplest forms are the *Maxwell Model* and the *Kelvin-Voigt Model* which consists of a Hookean spring and Newtonian dashpot connected in series and parallel is shown in Figure 3-13 (a) and (b). *Standard Linear Solid Model* consists of a combination of two springs and a dashpot [91]. *Generalized Maxwell Model* is a combination of Maxwell, Kelvin-Voigt and Standard Linear Solid Model and given in Figure 3-13 (c) [9], [91]. It is used as a base model for Prony series representation of stress relaxation function. In these models, spring is used to model the elastic response while the dashpot is used to model the viscous response of the material.

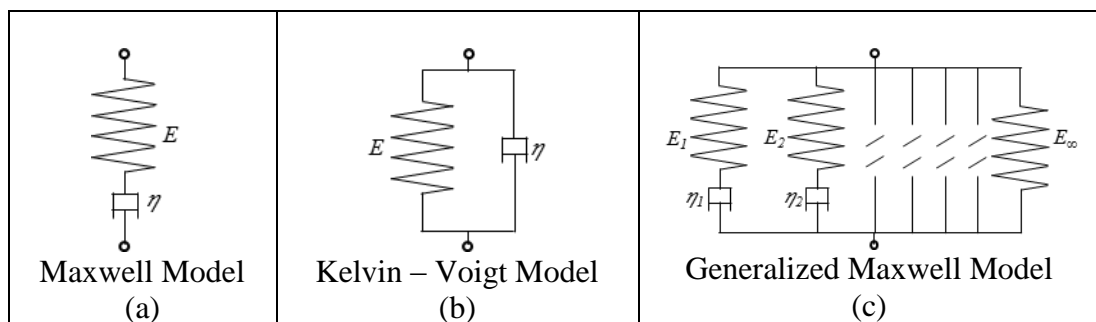


Figure 3-13 Constitutive elements to model viscoelasticity

The Maxwell model consist of a linear spring ( $\sigma = E\varepsilon_1$ ) and a linear dashpot ( $\dot{\varepsilon}_2 = \sigma/\eta$ ) in series where  $E$  is the Young's modulus and  $\eta$  is the viscosity [92, p. 338]. The rate of change in strain of the system is given by the equilibrium equation provided in eqn. (3.5-5).

$$\dot{\varepsilon} = \frac{d}{dt}(\varepsilon_1 + \varepsilon_2) = \frac{\dot{\sigma}}{E} + \frac{\sigma}{\eta} \quad (3.5-5)$$

This is the differential equation representation of the Maxwell model. If an applied step strain  $\varepsilon(t) = \varepsilon_0 H(t)$  is introduced to eqn. (3.5-5) where  $H(t)$  is the Heaviside step function, the closed form solution of this first order differential equation in terms of applied stress is given in eqn. (3.5-6).

$$\sigma(t) = \sigma_0 e^{\left(\frac{-t}{\eta/E}\right)} \quad (3.5-6)$$

Analogously, for a step strain input, the relaxation modulus can be given as in eqn. (3.5-7).

$$E_r(t) = E_{r,0} e^{\left(\frac{-t}{\eta/E}\right)} \quad (3.5-7)$$

The equation is also defined as a single Prony series term. Generalized Maxwell model is a rheological model. There is a free spring on one end and an arbitrary number  $N$  of Maxwell elements arranged in parallel [76, p. 298], [92, p. 340], [94, p. 98]. Then the effective stress relaxation modulus can be calculated to be as given in eqn. (3.5-8).

$$E_r(t) = E_{r,0} + \sum_{i=1}^N E_{r,i} e^{\left(\frac{-t}{\tau_i}\right)} \quad (3.5-8)$$

A linear viscoelastic model with a given Prony series is identical to a multi-network Maxwell model.

### 3.5.4. Modeling Linear Relaxation Behavior

Stress relaxation is defined as a gradual decrease in stress considering an applied deformation. In a relaxation test, the specimen's strain,  $\varepsilon_0$ , is held constant for a period of time while the stress is monitored. In a relaxation test, the time dependent stress response of material can be written as given in eqn. (3.5-9).

$$\sigma(t) = E_r(t)\varepsilon_0 \quad (3.5-9)$$

Where,  $E_r(t)$  is defined as the *stress relaxation modulus*. To develop a model capable of predicting the stress response due to an arbitrary applied strain history, it is relevant to decompose the strain history into sum of infinitesimal strain steps [92, p. 311].

$$\varepsilon(t) = \sum_{i=1}^{\infty} \Delta\varepsilon_i H(t - \tau_i) \quad (3.5-10)$$

Where,  $\Delta\varepsilon_i$  is the strain increment at time,  $\tau_i$ . The total stress response from applying this strain history can be obtained from superposition principle [92, p. 311] and given in eqn. (3.5-11).

$$\sigma(t) = \sum_{i=1}^{\infty} \Delta\varepsilon_i E_r(t - \tau_i) \quad (3.5-11)$$

This stress response can be written in integral form as the number of strain increments goes to infinity.

$$\sigma(t) = \int_{-\infty}^t E_r(t - \tau) \frac{d\varepsilon(\tau)}{d\tau} d\tau \quad (3.5-12)$$

Once the  $E_r(t)$  is determined, eqn. (3.5-12) can be used to predict the stress response due to any imposed strain history where  $\frac{d\varepsilon(\tau)}{d\tau}$  is the strain rate [92, p. 312], [93], [95].

The stress relaxation function,  $E_r(t)$  can be defined as in the form of Generalized Maxwell model as given in eqn. (3.5-13).

$$E_r(t) = E_{r,0} + \sum_{i=1}^N E_{r,i} e^{-(t/\tau_i)} \quad (3.5-13)$$

More commonly, the stress relaxation function,  $E_r(t)$  can be written as the normalized series expansion [92, p. 315] as presented in eqn. (3.5-14).

$$g_r(t) = \frac{E_r(t)}{E_{r,0}} = 1 - \sum_{i=1}^N g_i (1 - e^{-(t/\tau_i)}) \quad (3.5-14)$$

Where,  $g_R(t)$  is the *dimensionless relaxation modulus* and it is defined by a set of Prony series coefficients  $g_i$  and corresponding relaxation times,  $\tau_i$ . Using eqn. (3.5-13), the governing stress equation given in eqn. (3.5-12) can also be written in the form of Generalized Maxwell model is given in eqn. ) [45], [95], [96].

$$\sigma(t) = \sigma_\infty + \sum_{i=1}^N \sigma_i e^{-(t/\tau_i)} \quad (3.5-15)$$

Where,  $\sigma(t)$  is the time varying shear stress,  $\sigma_\infty$  is the long-term nominal stress,  $\sigma_i$  and  $\tau_i$  are the parameters which depend on the relaxation behavior and  $N$  is the number of Maxwell elements. Note that, the eqn. ) is a stress solution defined based on long-term nominal stress,  $\sigma_\infty$ .

The value of  $\sigma(t)$  at  $t = 0$ , which is called the initial shear stress,  $\sigma_0$ , can be found using eqn. ) as given in eqn. (3.5-16).

$$\sigma(t = 0) = \sigma_0 = \sigma_\infty + \sum_{i=1}^N \sigma_i \quad (3.5-16)$$

By substituting eqn. (3.5-16) into eqn. ), the time varying shear stress equation,  $\sigma(t)$  can be redefined based on initial shear stress,  $\sigma_0$  as given in eqn. (3.5-17).

$$\sigma(t) = \sigma_0 - \sum_{i=1}^N \sigma_i (1 - e^{-(t/\tau_i)}) = \sigma_0 g_r(t) \quad (3.5-17)$$

Where,  $g_r(t)$  is as defined in eqn. (3.5-14). Using the equation, the corresponding stresses,  $\sigma_i(t)$  can be determined for different applied constant strains,  $\varepsilon_i$ . According to the assumption of quasi-linear viscoelasticity, the stress relaxation function is independent of the magnitude of the deformation [45]. The first way to find the stress relaxation function is to normalize eqn. (3.5-17) with respect to initial shear stress,  $\sigma_0$  [96], [97] as given in eqn. (3.5-18).

$$g_r(t) = \frac{\sigma(t)}{\sigma_0} = \frac{\sigma_0 - \sum_{i=1}^N \sigma_i (1 - e^{-(t/\tau_i)})}{\sigma_0} \quad (3.5-18)$$

The Prony series coefficients,  $g_i$  can be obtained by dividing the stiffness of the individual springs stiffnesses,  $\sigma_i$  with the initial stiffness,  $\sigma_0$  as  $g_i = \frac{\sigma_i}{\sigma_0}$ . The rest of the unknown parameters can be found by parameter comparison [45, p. 27]. The second way to find the stress relaxation function is to normalize eqn. ) with respect to long-term nominal stress,  $\sigma_\infty$  [45, p. 39] as given in eqn. (3.5-19).

$$S_\infty(t) = \frac{\sigma(t)}{\sigma_\infty} = \frac{\sigma_\infty + \sum_{i=1}^N \sigma_i \cdot e^{-(t/\tau_i)}}{\sigma_\infty} \quad (3.5-19)$$

Normalization with respect to long-term nominal stress,  $\sigma_\infty$  is preferred when the initial stress value,  $\sigma_0$  is uncertain due to relaxation test conditions. In this method, the fading memory effect of the material is used. Eqn. (3.5-19) can also be written in terms of Prony series coefficients as defined in [45, p. 39].

$$S_\infty(t) = \frac{\sigma_\infty + \sum_{i=1}^N \sigma_i e^{-(t/\tau_i)}}{\sigma_\infty} = \frac{1 - \sum_{k=1}^N g_k + \sum_{k=1}^N g_k e^{-(t/\tau_k)}}{1 - \sum_{k=1}^N g_k} \quad (3.5-20)$$

$$S_\infty(t) = \frac{\sigma(t)}{\sigma_\infty} = \sum_{i=1}^N \frac{\sigma_i}{\sigma_\infty} e^{-(t/\tau_i)} = \frac{\sum_{k=1}^N g_k e^{-(t/\tau_k)}}{1 - \sum_{k=1}^N g_k}$$

The value of  $N$  can be obtained through experimental evaluation. Other parameters,  $\sigma_\infty$ ,  $\sigma_i$  and  $\tau_i$  can be deduced from a curve fitting algorithm. Plotting  $S_\infty(t)$  for all performed tests and using the average of  $S_\infty(t)$  plots and determine  $g_k$  and  $\tau_k$  where  $g_k$  and  $\tau_k$  can be obtained by coefficient comparison from parameters  $\sigma_\infty$ ,  $\sigma_i$  and  $\tau_i$ . In fact, the initial strain is applied over a short ramp of variable duration so that determination of the initial stress value is uncertain.

### 3.5.5. Modeling Linear Creep Behavior

Creep is a slow, continuous deformation of a material under constant stress. An instantaneous strain,  $\varepsilon_0$  proportional to the applied stress is observed after the application of stress and this is followed by a progressive increase in strain. The total strain as given in eqn. (3.5-21) at any instant of time is represented as the sum of the instantaneous elastic strain and the creep strain [93].

$$\varepsilon(t) = \varepsilon_0 + \varepsilon_c \quad (3.5-21)$$

*Creep compliance function*,  $E_c(t)$  can be defined as follows [95] as given in eqn. (3.5-22).

$$\varepsilon(t) = E_c(t) \cdot \sigma_0 \quad (3.5-22)$$

The creep compliance,  $E_c(t)$  at any instant of time is the sum instantaneous and creep states as provided in eqn. (3.5-23).

$$E_c(t) = \frac{\varepsilon_0}{\sigma_0} + \frac{\varepsilon_c}{\sigma_0} = E_{c,0} + \Delta E_c(t) \quad (3.5-23)$$

Where,  $E_{c,0}$  is defined as the instantaneous creep compliance and  $\Delta E_c(t)$  is the transient component of the compliance [93]. The resulting strain [92, p. 335] equation from applied stress is calculated by the eqn. (3.5-24).

$$\varepsilon(t) = \int_{-\infty}^t E_c(t - \tau_i) \frac{d\sigma(\tau)}{d\tau} d\tau \quad (3.5-24)$$

The transient creep compliance function,  $\Delta E_c(t)$  is often given in the form of a Power series or a Prony series expansion in viscoelastic modeling. The power law form of this function is defined as given in eqn. (3.5-25).

$$\Delta E_c(t) = E_1 t^n \quad (3.5-25)$$

Which is mathematically simple and has been found to provide an adequate prediction of short term creep behavior [93] and the Prony series form is defined as given in eqn. (3.5-26).

$$\Delta E_c(t) = \sum_{i=1}^N E_i \left(1 - e^{-\frac{t}{\tau_i}}\right) \quad (3.5-26)$$

Using the Prony series expansion, the resulting creep strain function will be as given in eqn. (3.5-27).

$$\varepsilon(t) = E_{c,0}\sigma + \sum_{i=1}^N E_{c,i}\sigma \left(1 - e^{-\frac{t}{\tau_i}}\right) \quad (3.5-27)$$

The use of Prony series is dominant over Power series. If a specimen is load free prior to the time  $t = 0$ , at which a stress  $\sigma_0 + \sigma(t)$  is applied, the strain at  $t > 0$  can be represented as follows [95],

$$\varepsilon(t) = E_{c,0}(t)\sigma_0 + \int_0^t E_c(t - \tau) \frac{d\sigma(\tau)}{d\tau} d\tau \quad (3.5-28)$$

Where,  $\frac{d\sigma(\tau)}{d\tau}$  is defined as the stress rate. To determine the stress state in a viscoelastic material at a given time, the deformation history must be considered. For linear viscoelastic materials, a superposition of hereditary integrals describes the time dependent response [95]. For linear elastic behavior, the relaxation modulus and creep compliances are interrelated and can be inverted to with each other by using convolution integrals [93], [98].

### 3.5.6. Nonlinear Viscoelasticity

If any of the conditions for linear viscoelasticity are no longer satisfied, the viscoelastic behavior is considered to be nonlinear. The degree of nonlinearity can be influenced by factors such as applied stress level, strain rate, and temperature [93].

Non-linear viscoelastic behavior encountered when the observed strain,  $\epsilon$  is large. A finite strain viscoelastic model may be derived by generalizing linear viscoelasticity in the sense that the 2<sup>nd</sup> Piola-Kirchhoff stress is substituted for engineering stress and Green-Lagrange strain is used instead of engineering strain [91].

The Bergstrom-Boyce approach is based on the generally accepted idea that elastomers act as if they were made from two superposed solids as given in eqn. (3.5-29) and sketched in Figure 3-14: one purely elastic and one viscous. Solid A is a purely elastic network of polymer chains while solid B is a plastic or viscous network connected in series with a second elastic network [87]. The resulting true stress on the material is the sum of the stresses acting on each network.

$$\sigma = \sigma_A + \sigma_B \quad (3.5-29)$$

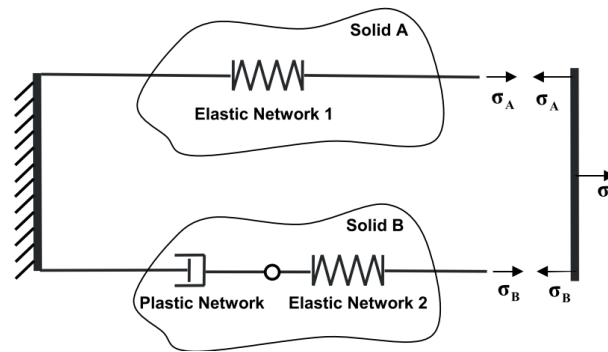


Figure 3-14 Bergström-Boyce Rheological Model [87]

For a quasi-linear viscoelastic material model, the time dependence of mechanical response can be described by using time dependent coefficients in the strain energy potential. Usually rheological models are used to model viscoelastic behavior of materials. These models involve elastic part to simulate recursive energy and inelastic parts to simulate the loss energy [77].

On the other hand, in-plane pre-straining and out-of-plane electrostatic activation induce a three-axial stress and deformation state in dielectric elastomer actuators. Under such circumstances hyperelastic-viscoelastic models derived from uniaxial tests are often inadequate for predicting the mechanical response [45]. The time-dependent mechanical response of dielectric elastomers can be described by using a quasi-linear viscoelastic model (QLV). In QLV model the material parameters in the strain energy potential are dependent on time but independent of the deformation. The time dependency of the material parameters can be expressed by using 4<sup>th</sup> order Prony series expansion of dimensionless relaxation modulus [49].

### 3.6. Force Balance

The electrostatic pressure or the Maxwell stress describes the behavior of charged bodies when a potential difference across the two electrode surfaces of the elastomer is subjected to an electric field as demonstrated in Figure 3-15. Electrostatic forces arise only at the interface between the electrodes and the elastomer. The elastomer behaves as a passive layer and no direct interaction occurs between electrical field and its mechanical properties.

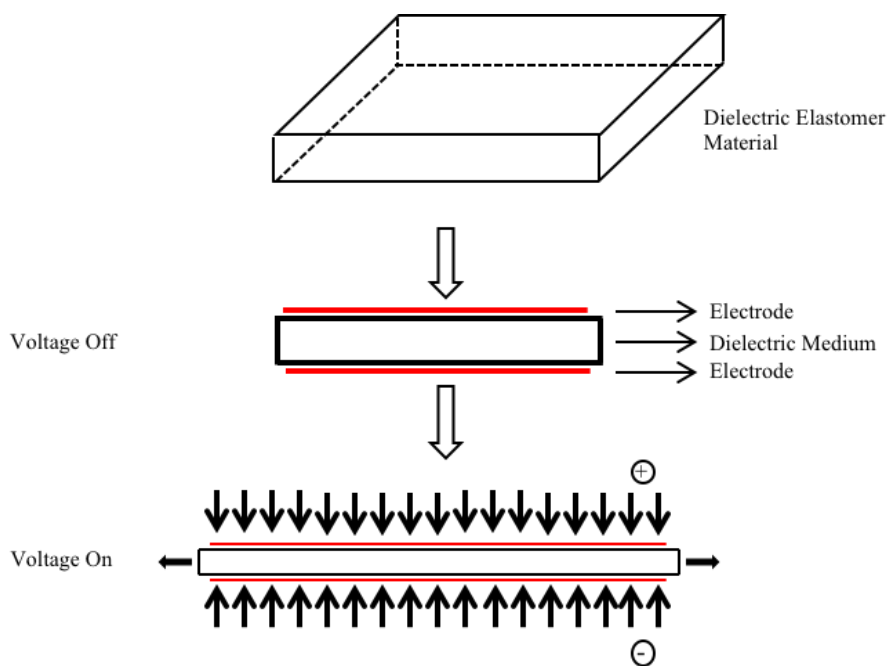


Figure 3-15 Schematic of the actuation response of dielectric elastomers

The electrostatic pressure or the Maxwell stress,  $p_{el}$ , acting on the insulating elastomer film can be calculated for a given applied voltage,  $V_{app}$  using the initial film thickness,  $z_0$  [7], [45], [46], [56], [59], [61], [70], [88] as given in eqn. (3.6-1).

$$p_{el} = -\epsilon_0 \epsilon_r \left( \frac{V_{app}}{z_0} \right)^2 \quad (3.6-1)$$

Where the free-space permittivity,  $\epsilon_0$  is equal to  $8.85 \times 10^{-12} \left(\frac{F}{m}\right)$ , and  $\epsilon_r$  is the relative dielectric constant of the elastomer,  $V$  is the applied electrical potential to the electrodes and  $z_0$  is the initial thickness of the polymer film.

The minus sign given in eqn. (3.6-1) indicates that the equivalent pressure is compressive. Due to the mechanical compression, the elastomer film contracts in the thickness direction and expands in the film's planar directions.

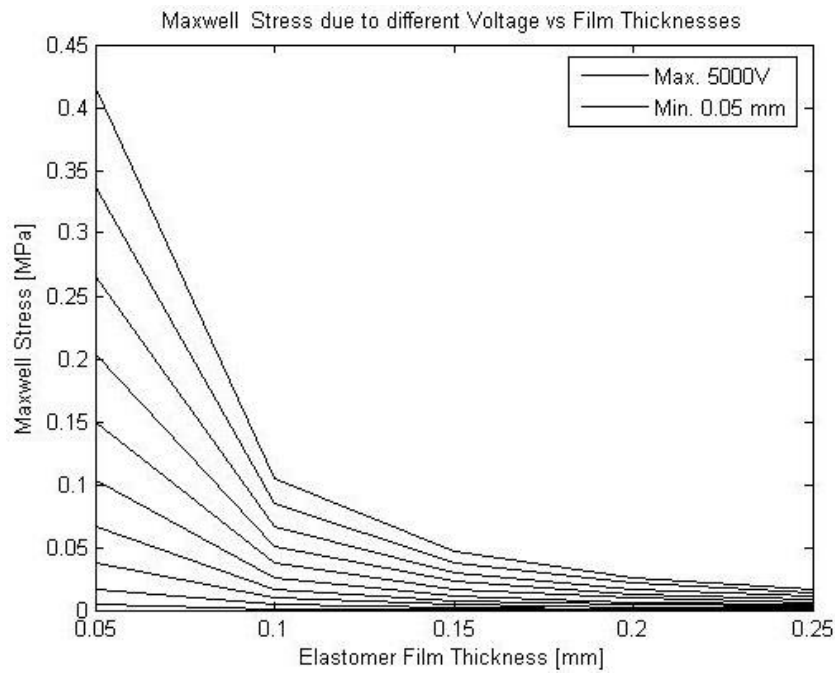


Figure 3-16 Change of Maxwell stress w.r.t. applied voltage and initial thickness

The Maxwell equation is valid for uniform electrical charge distribution on infinitely large electrodes and uniform film thickness and it is experimentally verified [60]. The equation provided is an approximation of the real film loading. A pull-in failure occurs when the film thickness falls below a certain threshold and the equivalent Maxwell pressure becomes always greater than the compressive stress of the elastomer film.



## **CHAPTER 4**

### **MATERIAL CHARACTERIZATION TESTS**

#### **4.1. Introduction**

Identification tests are required to observe the material and DEA mechanical properties which can be used in an effective actuator design. These tests are grouped mainly as material characterization tests and electromechanical tests. Material characterization tests are applied both to 3M's VHB 4905 and VHB 4910 materials. The electromechanical tests are performed on DEAs which are manufactured from VHB 4910 materials. All tests are performed at room temperature. All the presented test results are given as in raw data form. The comparisons are made for the same initial configured actuators unless otherwise specified.

#### **4.2. Material Characterization Tests**

Different kind of material characterization tests are available in literature. The tests are selected according to the desired use of material. In this study, uniaxial tension, quad lap shear and volumetric compression tests are performed for both 3M's VHB 4905 and VHB 4910 acrylic tape materials at METU Central Laboratory. All tests were performed using Zwick Roell (Z250) testing machine using proper mountings. According to the type of test, stress/strain or force/displacement results are recorded. The tests are performed at room temperature and defined test speeds.

#### 4.2.1. Uniaxial Tensile Tests

There are several standardized uniaxial tensile tests (i.e. ISO 37, ASTM D412 and DIN 53504) that can be used to determine stress-strain properties of vulcanized and thermoplastic rubbers which are also applicable to DE materials [22], [46], [65], [66], [87], [99], [100].

Uniaxial tension tests were performed according to the test matrix provided in Table 4-1. The test campaign is applied both to 3M's VHB 4905 and VHB 4910 tapes, separately. Initial Young's modulus, yield stress, failure stress and strain history were observed and recorded.

Table 4-1 Uniaxial tension test matrix

#	Applied Strain Value to each Specimen	Total Number of Test Specimen	Total Number of Repetition for each Specimen
1	%20	3	3
2	%50	3	3
3	%100	3	3
4	%20+	3	3
	%50+		3
	%100+		3
	Rapture		1
5	Direct Rapture	3	1

The procedure for uniaxial tension testing is quite simple. 30 dog bone shaped specimens (15 specimens for each VHB 4905 and VHB 4910) were cut considering at least 1/10 width to length ratio using a punch machine as given in Figure 4-1 (a) & (b). During specimen preparation, the use of oily paper was a good choice to bypass the sticky nature of the VHB tape material. Before each test, specimen's red liner was removed with a scalpel as shown in Figure 4-1 (c).

The specimen top and bottom ends were connected to the grips of testing machine as presented in Figure 4-2 (a). Undeformed gauge length of 20 mm was maintained for each specimen. Unfortunately, due to sticky nature of the material and the mounting of the specimen is made by hand, slight gauge length divergences observed which was unavoidable. For measuring the strain of the specimen during tensile testing, non-contact extensometer device cannot be used which was a better way of measuring the strain due that grips of extensometer damaged the specimen material. To start a uniaxial test, application of 0.030 N preload is programmed on testing machine. When the specimen is loaded with the preload, the uniaxial tensile test was started. All tests were performed with a 50 mm/min strain rate speed. The strain history was collected via the displacement of the machine strikers with a predefined zero position. The time history of the specimens' tension stress,  $\sigma(t)$  and strain,  $\varepsilon(t)$  were measured and recorded.

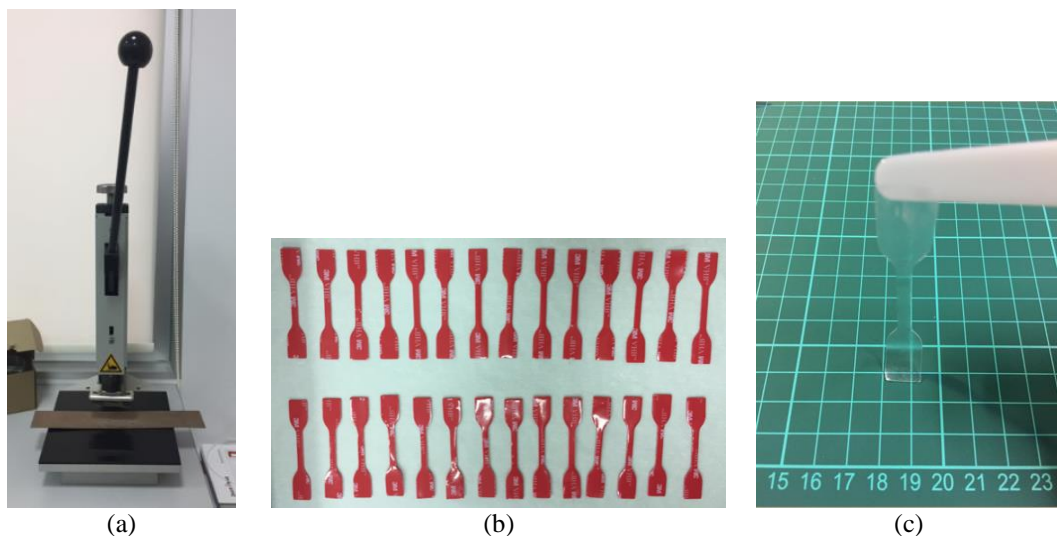


Figure 4-1 Specimen preparation for uniaxial tensile test (a) Punch machine (b) VHB 4905 and VHB 4910 specimens (c) Dog bone shaped and red liner removed specimen

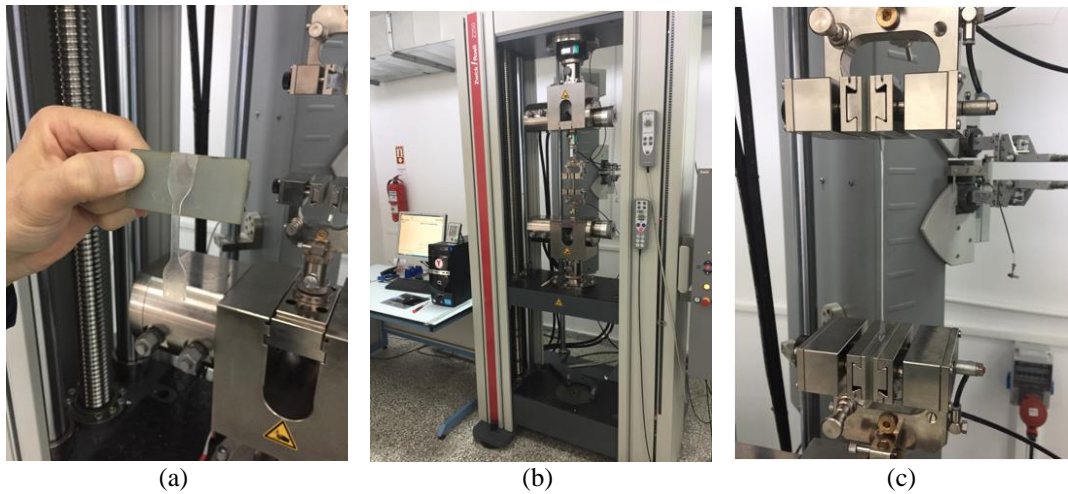


Figure 4-2 Uniaxial tensile testing (a) Mounting the specimen (b) Zwick testing machine (c) Elongation of material during testing

It has been shown in literature that normally a sample has to be strained at the same strain level minimum three times to overcome stress hardening effect [101]. Considering this fact, different testing scenarios were tried to simulate as tabulated in Table 4-1. For each test, three specimens were used. At the beginning the specimens were strained up to %20 strain, data recorded and the test was terminated. The specimen is not removed from the test machine and it is let to traverse its original starting gauge length position. Material was let to relax itself for five minutes. Following the relaxation, the material was loaded again with %20 strain. The test procedure repeated and finally, the specimen was loaded again with % 20 strain for the last time. After completion of testing, specimen removed from testing machine. This defined test scenario was applied to each three specimens individually. The same routine was also applied to %50 and %100 strain test.

A more combined testing scheme was performed by straining a specimen first %20 three times, then %50 for three times and then %100 again for three times following consecutively and finally specimen is forced to strain until rupture occurs. This test was aimed to observe the material in cyclic relaxation capability after different straining steps.

Last set of specimens were used to observe material behavior in direct rapture. No interval strains were applied and the material is forced to strain until rapture. In all tests, the stress and strain time history were recorded.

The results of these tests are given from Figure 4-3 to Figure 4-5 for 3M's VHB 4905 and VHB 4910 tapes. The presented time histories belong to the final data measure of each specimen. Note that, each specimen is tested three times for the same loading condition and the final history is taken into consideration. The presented raw stress level does not start from zero due that a preloading was used. In Figure 4-3 to Figure 4-5, the presented stress values are offset to start from zero.

In Figure 4-3 to Figure 4-5 it is shown that VHB 4905 and VHB 4910 material responses have slight differences. For low strain levels, these materials have no significant difference. As the strain level goes beyond %100, VHB 4905 material achieved higher stress values. In demonstrative application of this study, around %100 strain level and higher will be required. As seen from Figure 4-3 (a) and (b), frontier straining of material results in higher stress level for same straining. In Figure 4-5 (a) and (b), VHB 4910 material proves higher resistance to breakdown which is due to higher material thickness. Hyperelastic material modeling is focused on %100 straining and breakdown straining levels.

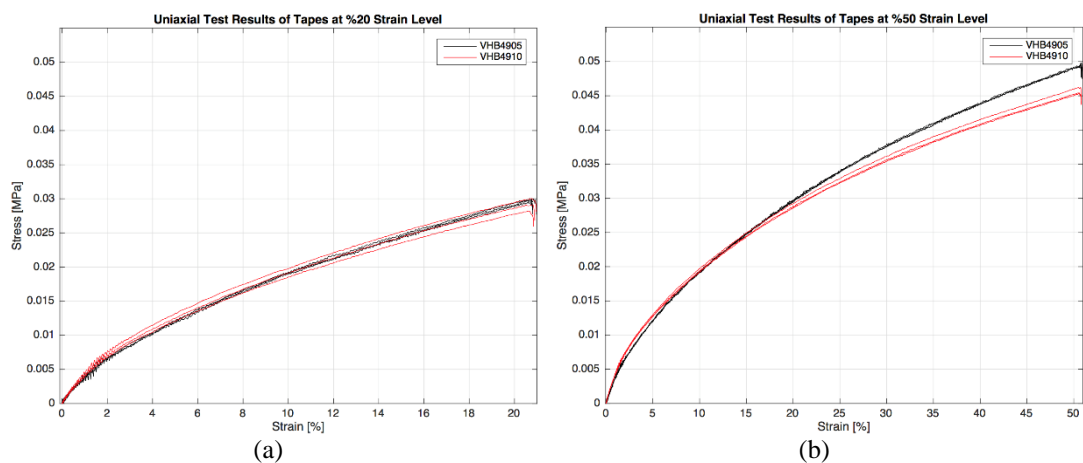


Figure 4-3 Uniaxial tension test results (a) %20 Strain level (b) %50 Strain level

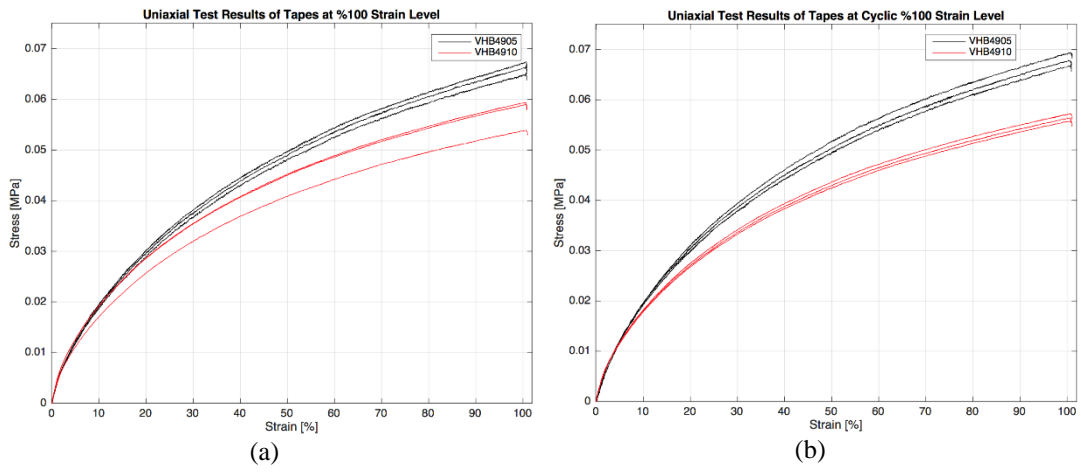


Figure 4-4 Uniaxial tension test results (a) % 100 Strain level (b) % 100 Strain level with cyclic loading

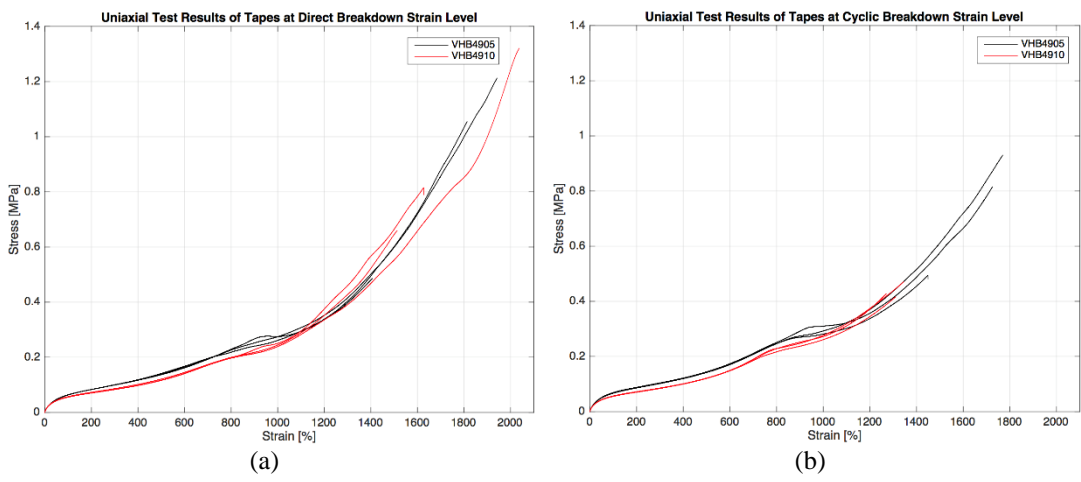


Figure 4-5 Uniaxial tension test results (a) Direct rapture (b) Rapture after cyclic loading

#### 4.2.2. Volumetric Compression Tests

Volumetric compression test shall be performed using a dilatometer by applying a true hydrostatic pressure in a viscous environment where viscous forces act equally in each outer plane of material in all directions. Measurements using this method are the most accurate but require more effort [81]. There is a simpler but an approximate way of conducting a volumetric compression test which involves applying stress to the sample in one direction only [81]. The main objective of the test is to calculate the bulk modulus. The initial slope of the resulting stress-strain function will be considered as the bulk modulus. This value is typically 2-3 orders of magnitude greater than the shear modulus [66, p. 45]. The similar test is performed in many researches [10, p. 43], [11], [101]. ASTM (2001) 'Standard no: D575-91', Standard Test Methods for Rubber Properties in Compression [11].

The main objective of a volumetric compression test is to measure the compressibility of the material. Bulk modulus of the material is obtained from the slope of the stress-strain curve. To perform the test, 40 disk shaped specimens were prepared with a 2 mm diameter and defined thickness (for VHB 4905, thickness is 0.5 mm and for VHB 4910 the thickness is 1.0 mm). These samples are lubricated with silicone oil and filled into test fixture forming a cylindrical final specimen geometry totally having 20 mm height. Three tests are planned for VHB 4905 and totally 120 disk shaped specimens were cut. This procedure is also repeated for VHB 4910 material and 60 disk shaped specimens were cut. The Zwick Roell (Z250) testing machine illustrated in Figure 4-2 (b) was also used for volumetric compression test. The test fixture was replaced with new grippers and compression test fixture. The testing speed was 0.5 mm/min.

The VHB 4905 and VHB 4910 samples were cut in circular shapes using a cutting punch shown in Figure 4-6 (a) and (b). The cutter knife is a special heat-treated apparatus manufactured to cut the samples. The knife edges designed to cut the specimens in a true cylindrical shape. The oily paper is used to store and protect the prepared specimen away from environment dust.

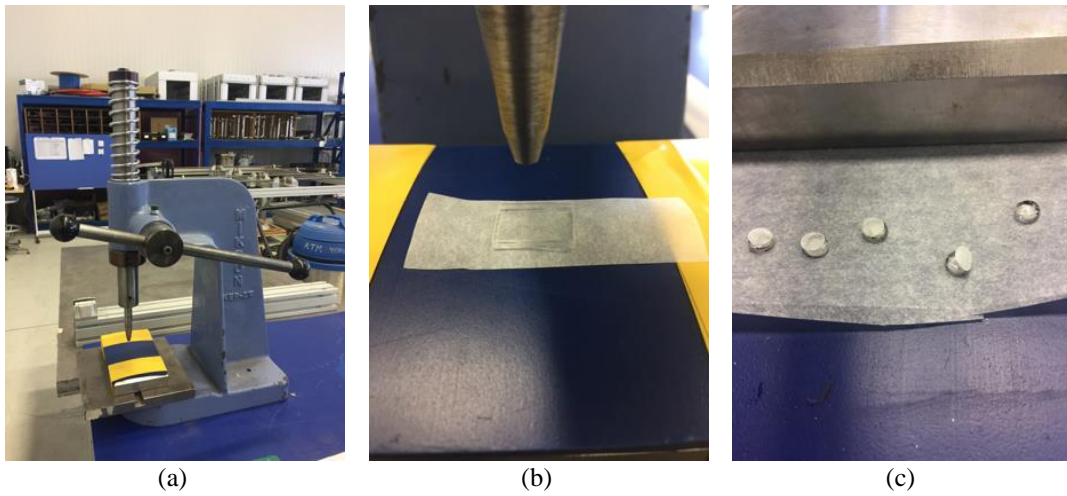


Figure 4-6 Volumetric compression test specimen preparation (a) Cutting punch (b) Cutting laminated tape with special knife (c) The circular shaped specimens

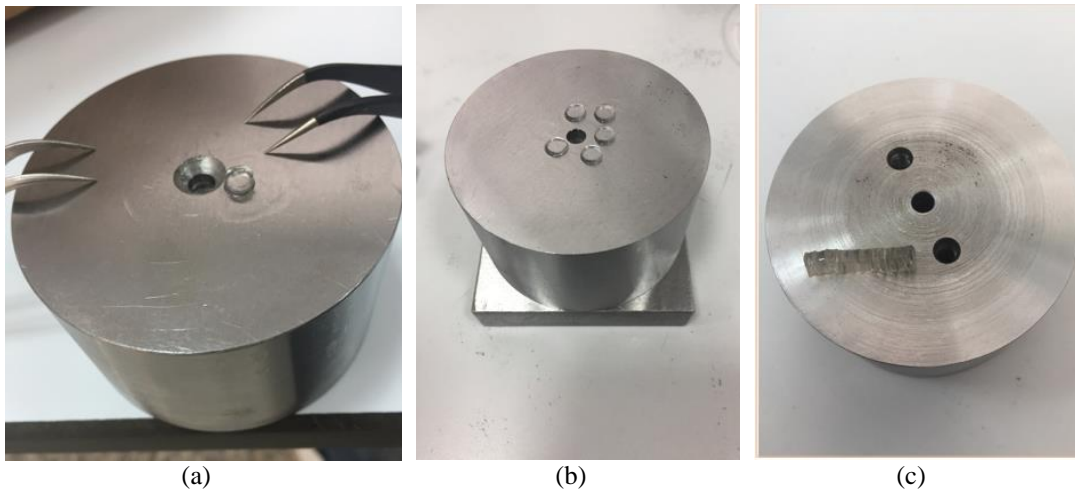


Figure 4-7 Volumetric compression test specimen stacking (a) Cut samples are stacked in the hole of fixture (b) Multiple samples are used to form the required thickness (c) Total number of samples stacked in fixture

Tool apparatus is in cylindrical form as given in Figure 4-7 (a). There is a deep and edge tapered cylindrical hole in the middle of the fixture. The prepared specimens were stacked through the hole one by one using silicone oil and tweezers. A great care should be taken to avoid the specimen twist while translating through the hole bottom point. For each test, 40 specimens were stacked for VHB 4905 and 20 specimens for VHB 4910 material. Total length of the filled specimens was 20 mm forming a long tubular specimen bundle for each material type as illustrated in Figure 4-7 (c).

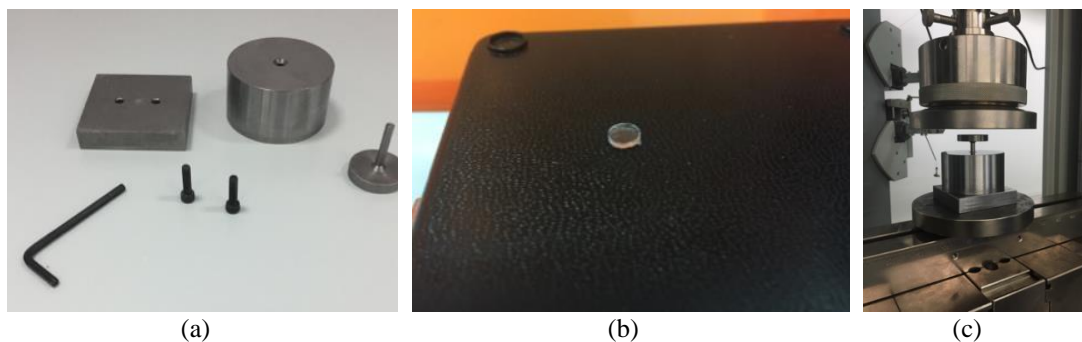


Figure 4-8 Volumetric compression test specimen fixtures (a) Test fixture (b) One cylindrical specimen (c) Fixture mounted on test machine

The test apparatus filled with specimens were mounted on the testing machine as presented in Figure 4-8 (c). The compression test was started from defined origin point and ended after 2 mm vertical travel of the punch head. The punch head displacement versus applied force history was monitored and recorded. It is advised to measure the height of the specimen bundle after testing is finished.

When the volumetric compression test started, a trial compression force was applied to force remove all voids inside test fixture for each specimen bundles. These compression trials were also monitored and recorded but not used in analyses. When a test finished, the specimen bundle was not removed from the test apparatus. The punch head was let to traverse to its original start position and the specimen bundle was let to relax for 5 minutes.



Figure 4-9 The Samples are removed from test fixture and then measured

After relaxation time finished, a second compression test was performed to same sample again up to 2 mm of vertical deflection and the force generated was recorded. This procedure was applied third time to the same specimen bundle and then removed.

In Figure 4-10, for material VHB 4910 and in Figure 4-11, for material VHB 4905, the results are shown. Note that the trial run results are not presented. According to results it is observed that the compressive force value is getting higher in each test.

The third and final experiments results on each three samples of VHB 4905 and VHB 4910 materials are also given in Figure 4-12 and Figure 4-13. The response of material to compression force outputs similar characteristics but it is seen that the applied maximum force values are different due to test conditions. The reason of this variation may be the hand stacking of samples to test fixture and unidenticality of test specimen bundles.

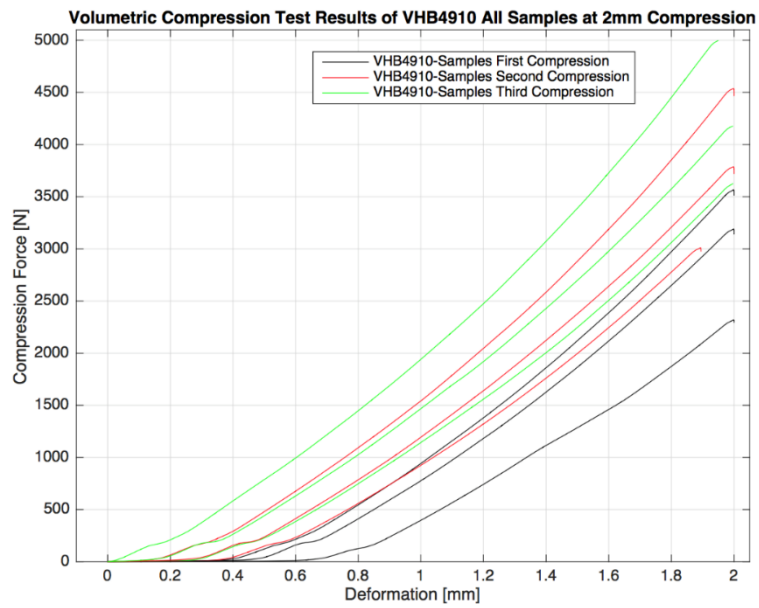


Figure 4-10 Volumetric compression test result of VHB 4910 specimen bundles (all trials)

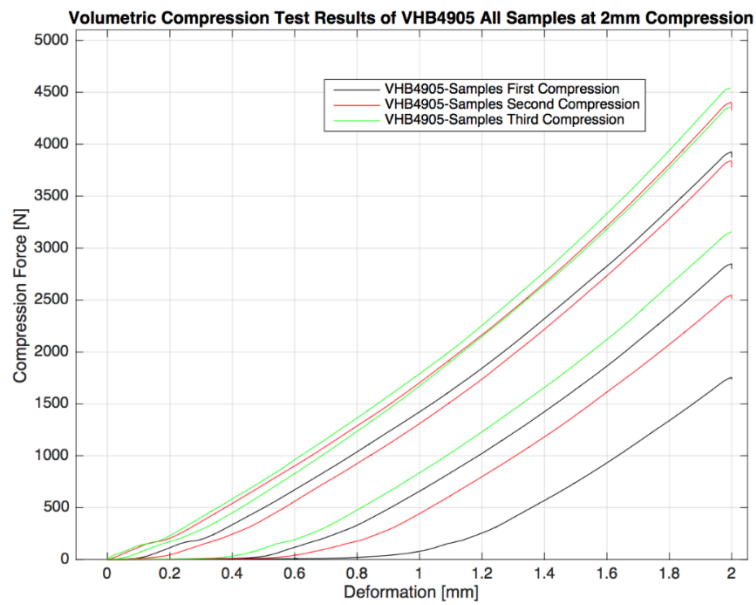


Figure 4-11 Volumetric compression test result of VHB 4905 specimen bundles (all trials)

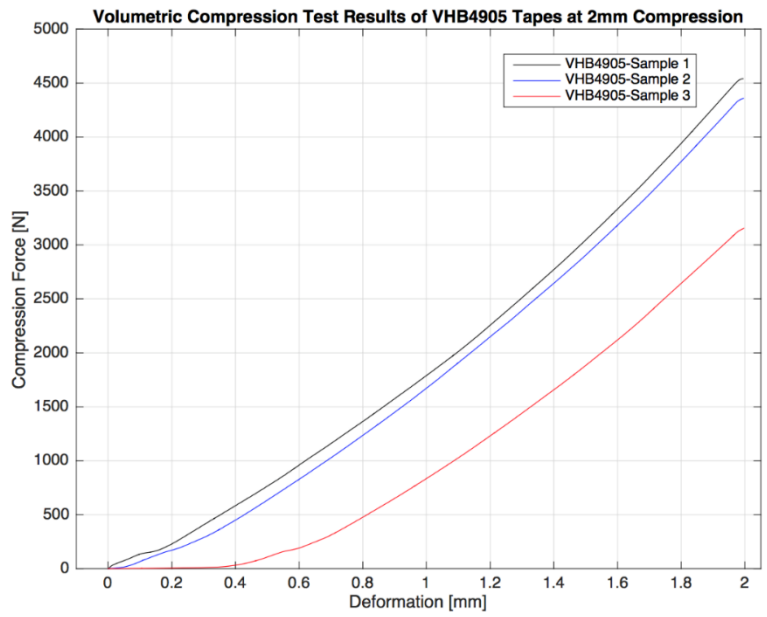


Figure 4-12 Volumetric compression test result of VHB 4905 specimen bundles

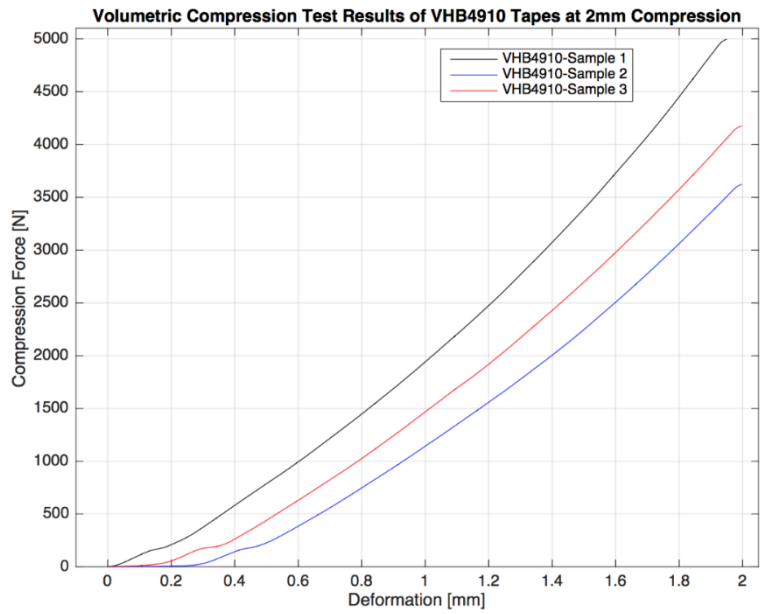


Figure 4-13 Volumetric compression test result of VHB 4910 specimen bundles

In Figure 4-14 the third trials of each sample of VHB 4905 and VHB 4910 materials are presented. In overall perspective, the samples exhibit similar compressive behavior and it is not possible to say one material shows superior response with respect to the other.

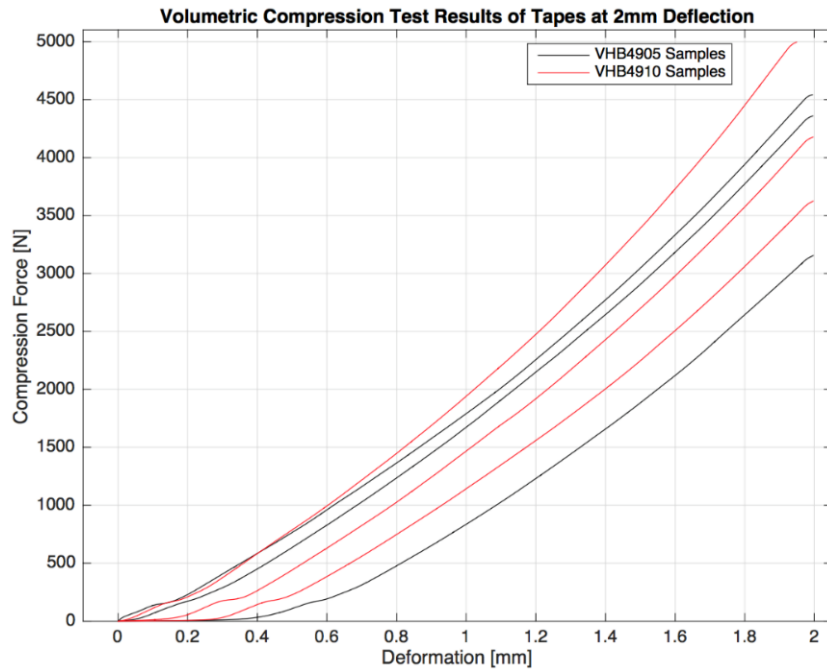


Figure 4-14 Volumetric compression test result of VHB 4905 & VHB 4910 specimen bundles - third trials

### 4.2.3. Quad Lap Shear Tests

The quad lap simple shear test is mainly used in bearing industry [66]. The test was performed using the Zwick Roell (Z250) testing machine as illustrated in Figure 4-2 (b). 20 metallic test apparatus bars as shown in Figure 4-15 (a) were manufactured to perform the quad lap shear test. The quad lap shear test was performed while the tapes were bonded on metallic test apparatuses. According to data sheet of VHB tape series [43], at room temperature, approximately 50% of ultimate bond strength will be

achieved after 20 minutes, 90% after 24 hours and 100% after 72 hours. Ultimate bond strength can be achieved more quickly by exposure of the bond to elevated temperatures (e.g. 66°C) for 1 hour. Thus, a heat chamber was used to bond the samples before testing. The quad lap shear test was performed with a tensile speed of 0.25 mm/sec.

The metallic bars were 100 mm in length and 20 mm in width. 10 of the bars' thicknesses were 10 mm and the rest 10 of them were 5 mm. 5 mm thick bars were used in the middle of the fixture as shown in Figure 4-15 (b). Thick bars were used to mount the fixture to test machine. All bars were manufactured in lathe and a slight surface roughness was maintained for best bonding.

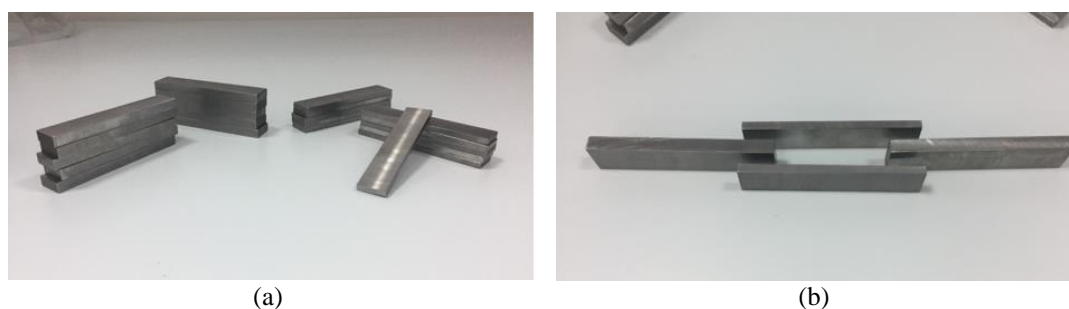


Figure 4-15 Text fixture preparation for quad lap shear test (a) Metal blocks (b) Test configuration

All VHB tapes have a width of 19 mm in a standard sample roll. These tapes were cut with a scalpel in 20 mm x 19 mm x 0.5 mm (for VHB 4905) and 20 mm x 19 mm x 1.0 mm (for VHB 4910) and bonded on thin metal bars first as shown in Figure 4-16 (a) then red liners on the films were removed and the thick metal bars were bonded. Totally three sets of test fixtures are prepared for each VHB 4905 and VHB 4910 tapes as given in Figure 4-16 (b).



Figure 4-16 Bonding for quad lap shear test (a) Bonding step (b) Completed test apparatus

Espec heat chamber was selected to heat the test fixtures given in Figure 4-16 (b). The heat chamber was heated to 66 °C and the test fixtures were let to rest an hour in chamber for best bonding strength.

When the bonding process was completed, the test fixtures were removed from the heat chamber and ready to test as given in Figure 4-18 (a). It was noticed that the transparent VHB tapes are turned in black color after heating process as can be observed from Figure 4-18 (b).



Figure 4-17 Heat chamber used to speed up bonding process

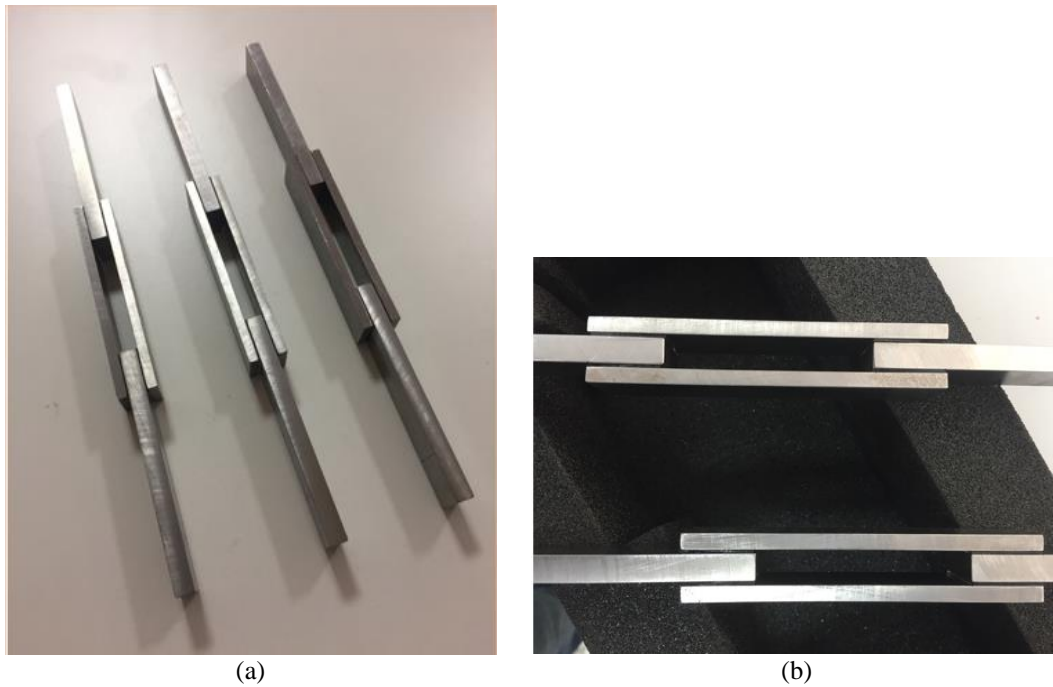


Figure 4-18 Bonded quad lap shear test fixtures (a) Bonded fixtures (b) Closer look to bond area

The prepared and bonded samples of VHB 4905 and VHB 4910 were mounted on the testing machine as presented in Figure 4-19 (a). The displacement and the force history of the test were monitored and recorded. Reader should note that the monitored displacement results are the sum of the displacement of the upper and lower bonded tapes thus the results should be divided into two to find single bond result. Also, the force output should be divided into two because the right and left bars of the test fixture transfer the total force. This has to be taken into consideration while processing the test history. At a certain time, the VHB tapes' shear response was visible during test as shown in Figure 4-19 (b). The tests were let to continue until the rapture breakdown occurs as illustrated in Figure 4-19 (c). The test results are provided in Figure 4-20 to . In (a), (c) and (e) VHB 4905 and in (b), (d) and (f) VHB 4910 sample results are presented. Each sample is subjected to tensile loading resulting in shear deformation.

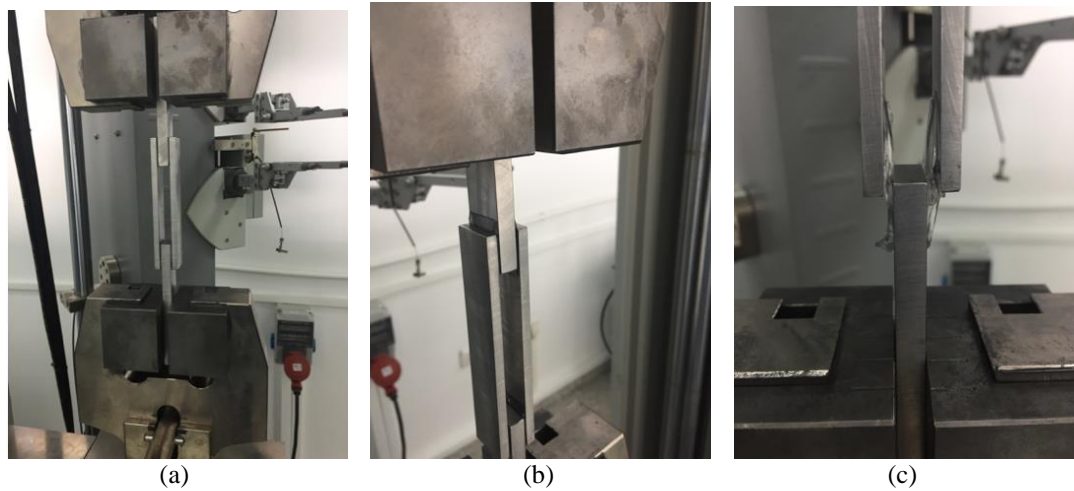


Figure 4-19 Quad lap shear test (a) Test fixtures are mounted on the testing machine  
 (b) Peel off starts (c) Complete rapture

The applied force [N] and observed displacement,  $d$  [mm] were recorded. The amount of shear  $k = d/h$  where  $d$  is the displacement of the outer bar with respect to fixture base and  $y$  is the thickness of the specimen is calculated. For VHB 4905 and VHB 4910 materials, thickness,  $h$  is a known parameter ( $h = 0.5 \text{ mm}$  and  $1.0 \text{ mm}$ ). For each sample, when the shear deformation was reached to 2 mm, the test was terminated and the test fixture moved to its original start position. The same loading scheme was applied four times including a five minutes of relaxation time between each testing. The relaxation time means the time where material recovers its original shape. As seen from , for both VHB 4905 and VHB 4910, the maximum shear strength was achieved in the last fourth trial. VHB 4905 presented higher shear stress value than VHB 4910 for the same testing conditions. In the fifth trial, test was not stopped at 2 mm travel and the material was let to peel completely until breakdown occurs. Complete peel off breakdown results of specimens are given in Figure 4-21. The test was terminated when one of the four tapes removed from its bonded surface and it was assumed that breakdown was observed.

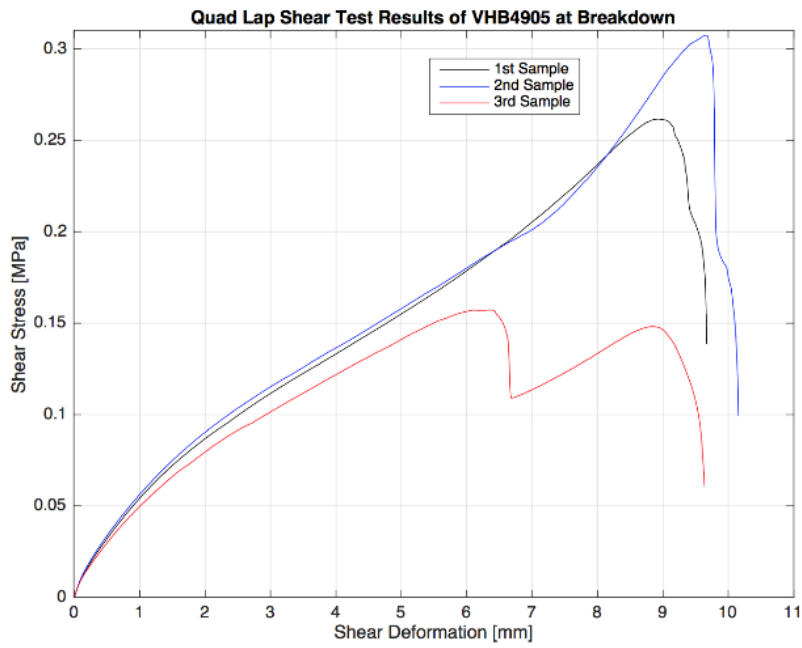


Figure 4-20 Quad lap shear test results of VHB 4905 at breakdown

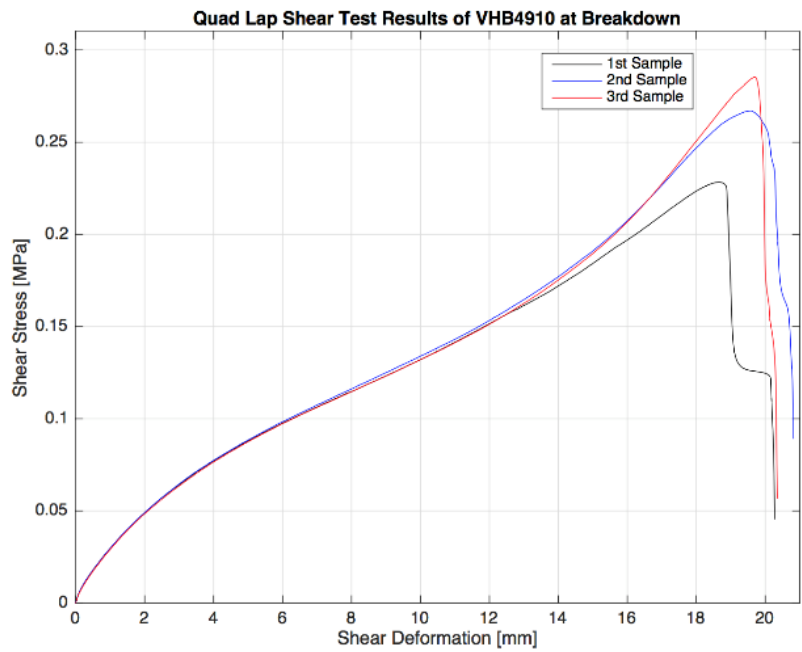
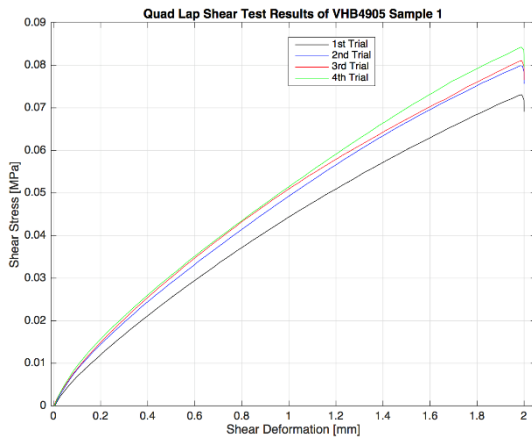
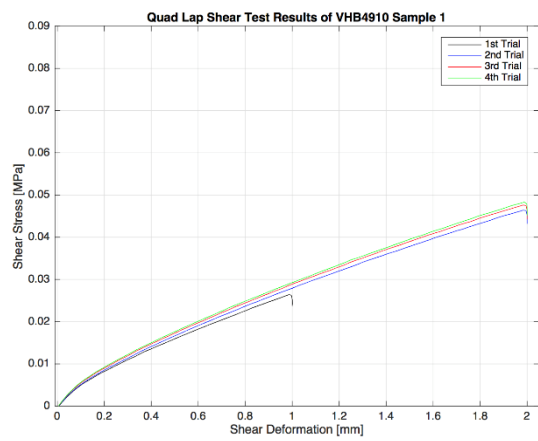


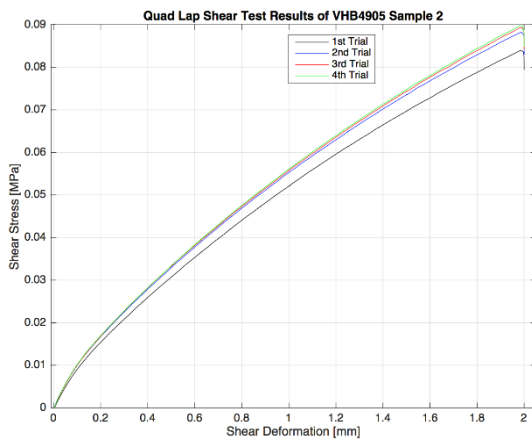
Figure 4-21 Quad lap shear test results of VHB 4910 at breakdown



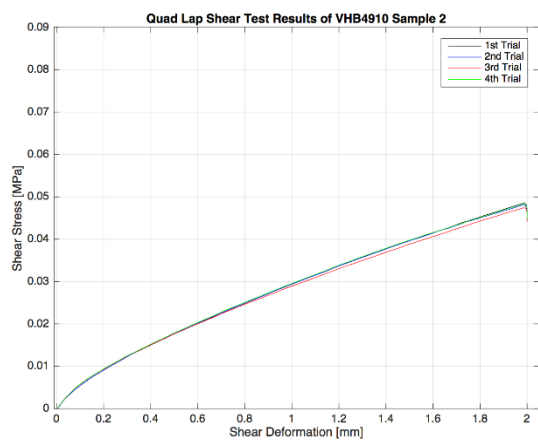
(a)



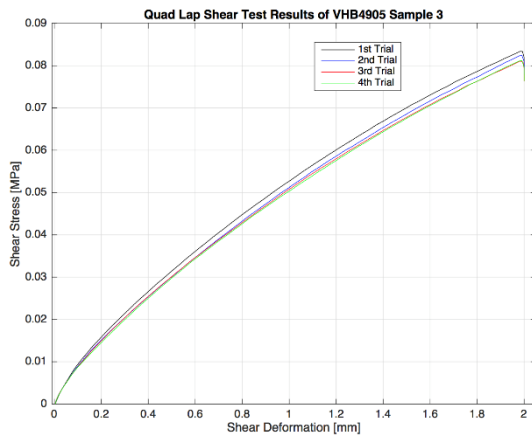
(b)



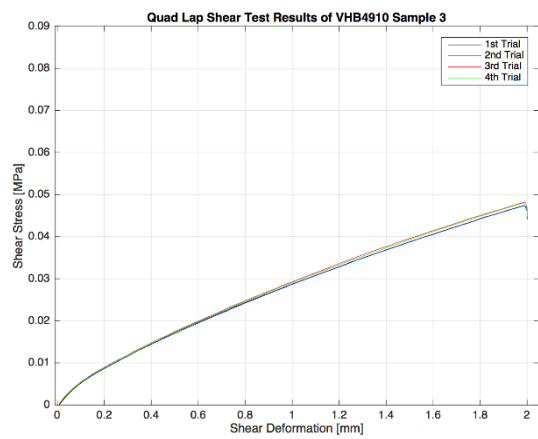
(c)



(d)



(e)



(f)

Figure 4-22 Quad lap shear test results (a) VHB 4905 sample 1 (b) VHB 4910 sample 1 (c) VHB 4905 sample 2 (d) VHB 4910 sample 2 (e) VHB 4905 sample 3 (f) VHB 4910 sample 3

#### 4.2.4. Creep and Relaxation Tests

Standard viscoelastic material experiments like creep and stress relaxation are convenient to study material response. These tests provide good accuracy for long times like hours to days but less accurate at shorter times (seconds and less) [100].

Creep tests are performed by holding a specimen at a constant tensile stress and measuring the resulting strain,  $\epsilon$  as a function of time. Similarly, relaxation tests are performed by holding a specimen at a constant tensile strain and measuring the resulting internal stress,  $\sigma$  as a function of time.

Creep and relaxation tests of VHB 4905 and VHB 4910 materials are performed using Dynamic Mechanical Analysis (DMA) module given in Figure 4-23 (a) at METU Central Laboratory. Pyris Diamond Dynamic Mechanical Analyzer shown in Figure 4-23 (b) performed the creep and relaxation test campaign.

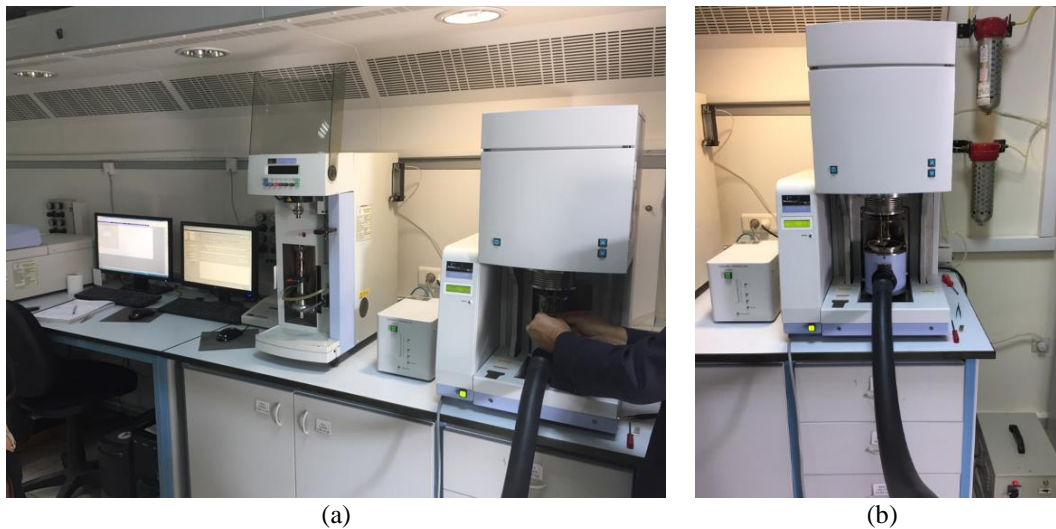


Figure 4-23 Creep and relaxation testing (a) Test environment (b) Pyris diamond dynamic mechanical analyzer

The geometry of the creep and relaxation test samples were same and cut in 40 mm x 5 mm in length and width dimensions. The thickness of the specimens was 0.5 mm for VHB 4905 and 1.0 mm for VHB 4910. 18 samples are prepared, removed from its red liner and kept in oily paper as shown in Figure 4-24. Due to Dynamic mechanical analyzer displacement range limits and its force application constraints, creep test was performed at 50 mN, 100 mN and 150 mN for VHB 4905, 100 mN, 200 mN and 300 mN for VHB 4910. Relaxation tests were performed for 1250, 2500 and 5000 microstrains for all samples. All creep and relaxation tests were started at 5000 microstrains gauge length corresponding to 5 mm of free sample length. Here it should be clarified that the original samples' length was 40 mm but the effective testing length was 5 mm as presented in Figure 4-25 (a). The extra portions of the sample length were used for grip connections as illustrated in Figure 4-25 (b).



Figure 4-24 Creep and relaxation test samples

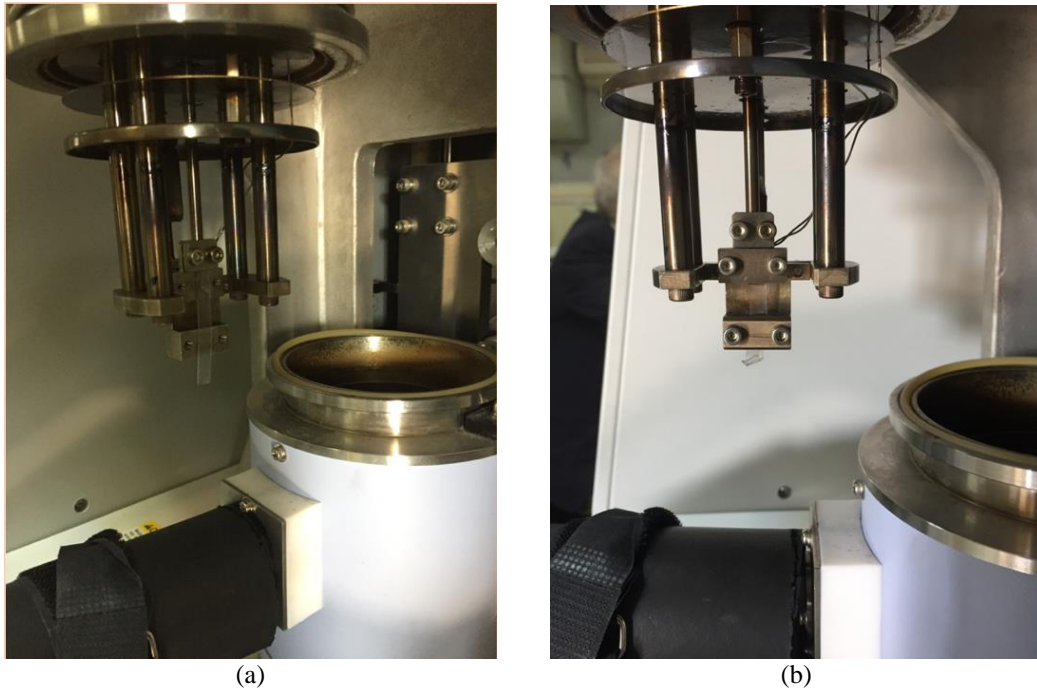


Figure 4-25 Creep and relaxation test sample mounting (a) Each sample was fixed on DMA (b) Metal covers were screwed and rest of the sample was not used.

At the beginning of creep tests, the results are recorded for 1800 seconds. Unfortunately, It was understood that the time was not sufficient to get a steady response and the recording time was increased to 2400 seconds in the next runs. Finally, 3000 seconds of recording was agreed for the final tests. The deduced duration was applied to both creep and relaxation experiments.

In Figure 4-26 (a), (c) and (e), VHB 4905 creep results for 0.05 N, 0.10 N and 0.15 N and in Figure 4-26 (b), (d) and (f), VHB 4910 creep results for 0.10 N, 0.20 N and 0.30 N are presented. The strain history was recorded for a duration of 3000 seconds. Same plot scale is applied for the test results as given in Figure 4-26 to provide an exact sense of material behavior to reader. At the end of the tests, it was seen that the creep response of the material did not settle which are all given in Figure 4-26.

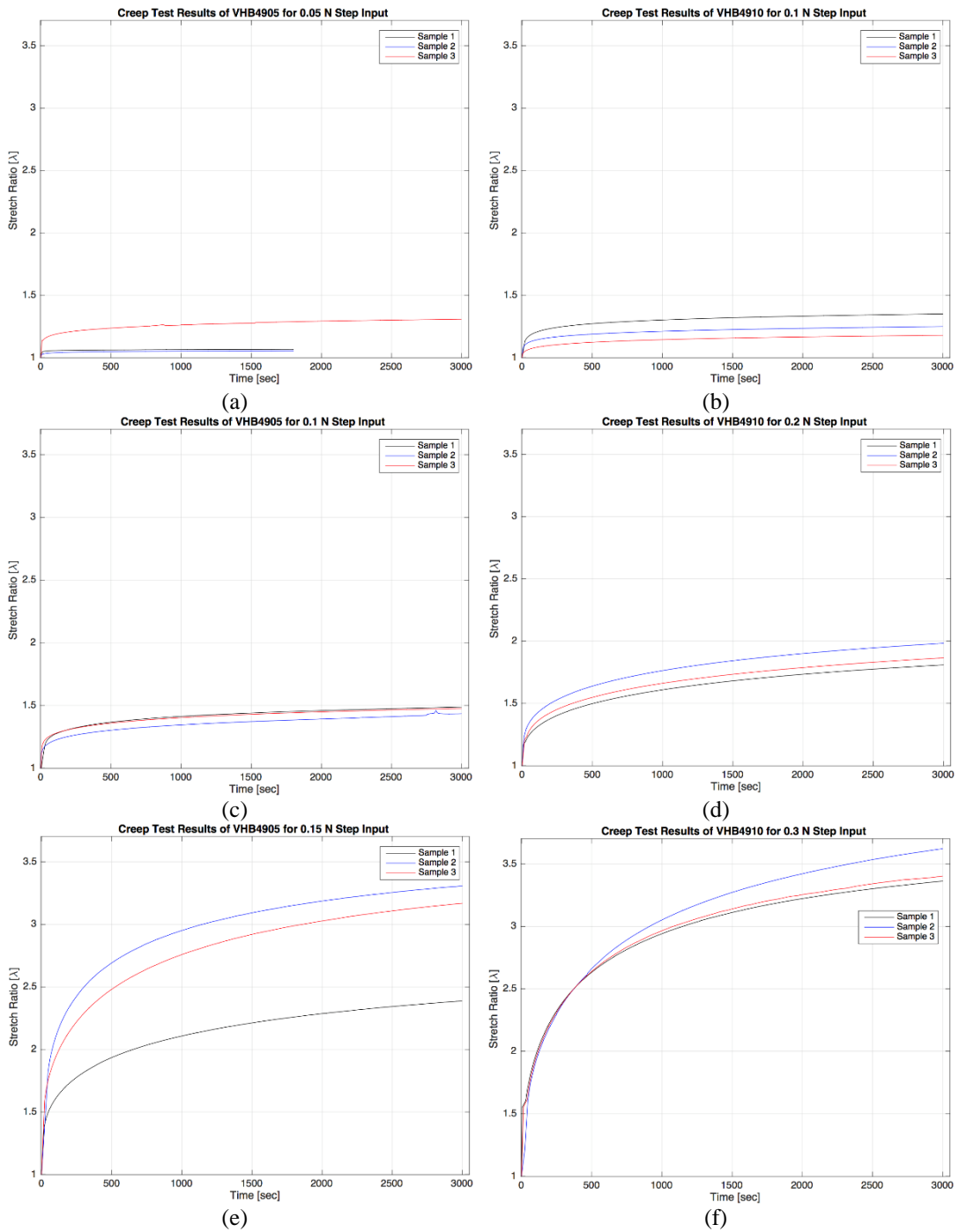


Figure 4-26 Creep test results (a) VHB 4905 at 0.05 N step input (b) VHB 4910 at 0.10 N step input (c) VHB 4905 at 0.10 N step input (d) VHB 4910 at 0.20 N step input (e) VHB 4905 at 0.15 N step input (f) VHB 4910 at 0.30 N step input

In Figure 4-27 the overall results of applied constant uniaxial tension results are provided.

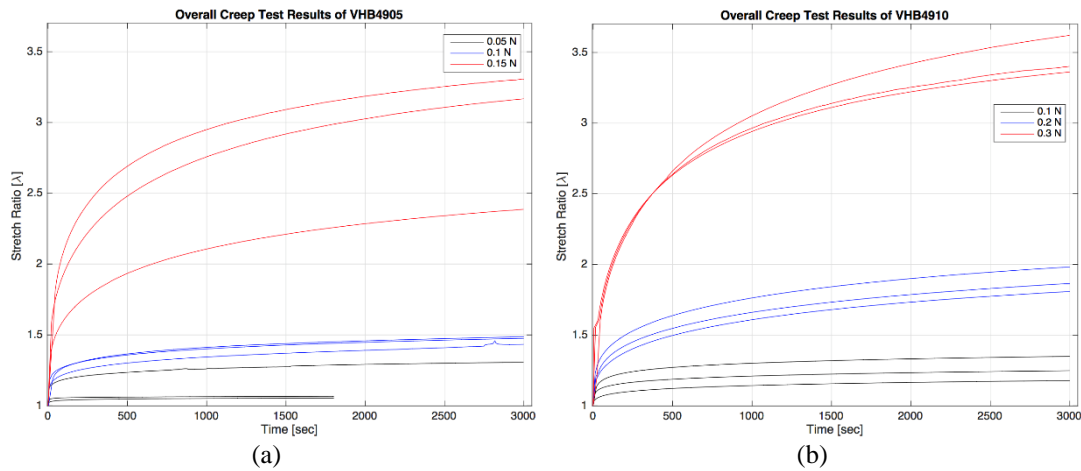


Figure 4-27 Creep test results (a) Overall results for VHB 4905 material (b) Overall results for VHB 4910 material

In Figure 4-28 (a), (c) and (e) VHB 4905 material response to 1250, 2500 and 5000  $\mu$ strain step input results are presented. Similarly, in Figure 4-28 (b), (d) and (f) VHB 4910 material response to same step inputs are presented. All relaxation tests are performed for 3000 seconds. The results of the relaxation tests are more uniform according to creep tests. VHB 4905 material presents more residual stress according to VHB 4910.

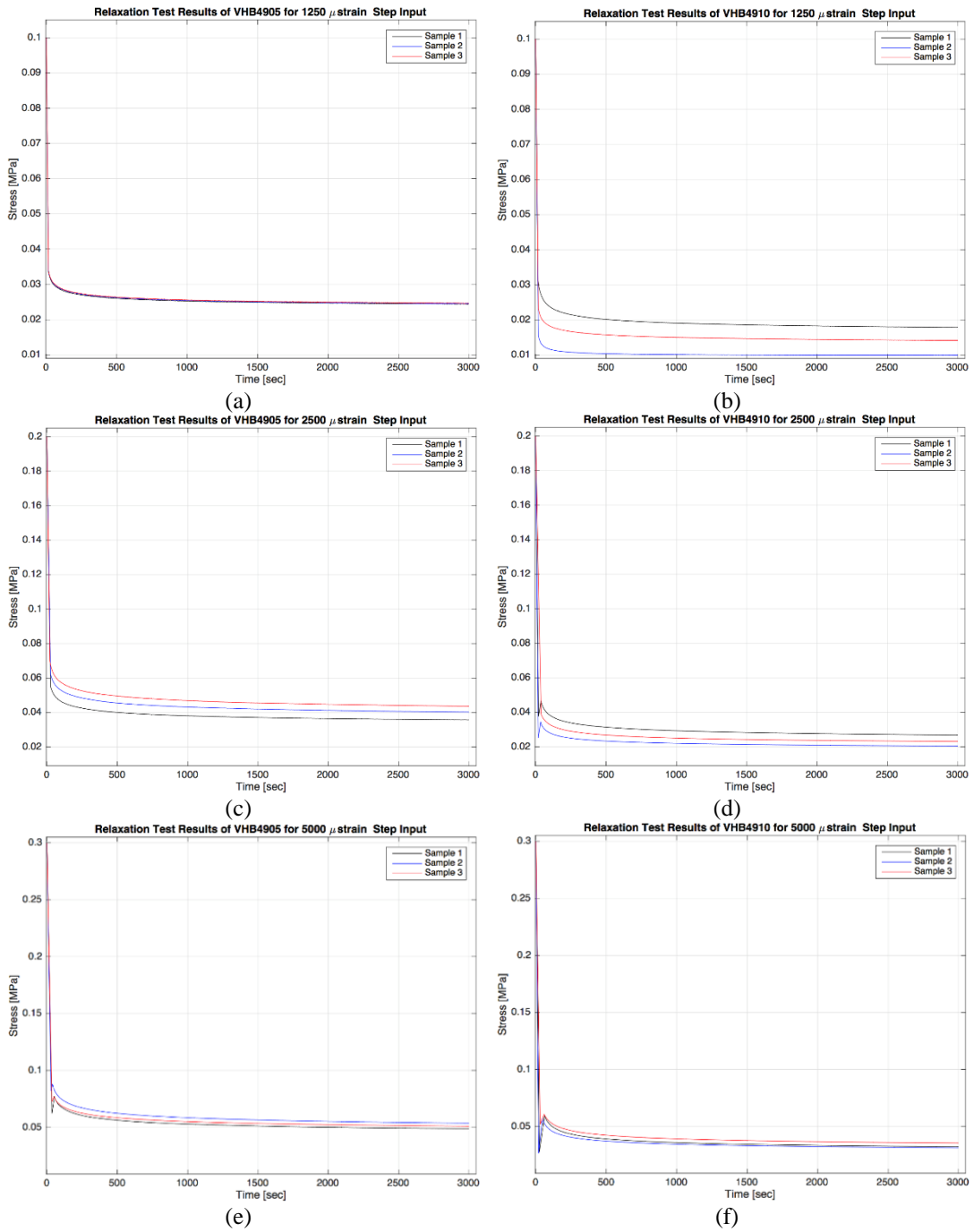


Figure 4-28 Relaxation test results (a) VHB 4905 at 1250  $\mu$ Strain step input (b) VHB 4910 at 1250  $\mu$ Strain step input (c) VHB 4905 at 2500  $\mu$ Strain step input (d) VHB 4910 at 2500  $\mu$ Strain step input (e) VHB 4905 at 5000  $\mu$ Strain step input (f) VHB 4910 at 5000  $\mu$ Strain step input



## CHAPTER 5

### ELECTROMECHANICAL TESTS

#### 5.1. Introduction

In Chapter 4, the VHB materials were subjected to various preliminary tests to define their stand-alone parameters. The tested materials were used as they are obtained from the manufacturer. Unfortunately, using those obtained parameters directly for an actuator design is not appropriate. The stiffness effect of pre-stretching, carbon black application, reinforcement strips, and actuator construction materials strongly effect the design prospect which all should be considered while designing a DEA. The preliminary tests will help to understand the change of material behavior in case of actuator tailoring. On the other hand, a DEA can be designed in multiple forms. The design can be in different shapes of different configuration options including various stacking models. In this study, linear DEAs are constructed. Single layer and double layer actuators are studies in electromechanical tests which all present different set of actuator parameters. The manufacturing of these DEAs are defined in detail in Chapter 5.2. This chapter will focus on the electromechanical test setup design and manufacturing.

#### 5.2. DEA Manufacturing

3M's VHB 4905 and VHB 4910 acrylic film tapes are commercially available in rolled form with a maximum of 1140 mm and 1180 mm widths. They are sticky in both sides. The length of the material has no limit. The material parameters announced by the manufacturer are given in Table 2-3. According to literature, it has been shown that the standard thickness of VHB tape materials are very high to generate efficient force/voltage values. The thickness of the material has to be thinned to decrease the

required amount of voltage potential. The film as supplied (VHB 4910) has a thickness of 1.0 mm, which is far too thick for an actuator. Decrease in thickness of the material can be achieved by pre-stretching. By pre-stretching the material in planar directions, the thickness can be decreased and the smaller amount of voltage potential can be used to get the same actuator force and strain result. As the volume of the material is constant, the pre-stretch in planar directions will result on thickness reduction.

The final application of the DEA is designed to work on an trailing edge of 3D wing concept. The actuation direction of DEA is design to be uniaxial. Although both VHB 4905 and VHB 4910 materials are tried in all manufacturing steps, it is observed that VHB 4910 material is superior with respect to VHB 4905 in terms of handling. Demonstrative DEAs are manufactured from VHB 4910 material.

Various planar pre-stretches are considered. The pre-stretch in length direction and width direction does not need to be equal namely equi-biaxial. As long as equi-biaxial pre-stretched DEAs are tested, the unequibiaxial pre-stretches are also tried. The length direction of DEA is always considered as the actuation direction. The width direction which is perpendicular to length direction is set with a fixed pre-stretch.

Pre-stretching VHB tapes can be achieved in many ways. Stretching by hand or using an apparatus are both applicable. Unfortunately, uniform and extended pre-stretches cannot be achieved by hand. The use of a fixture tool is essential. In this study, stretching of the material is made by a square scissor aluminum apparatus as given in Figure 5-1. The inner square of the scissor mechanism is designed to be 100 mm x 100 mm and it can extend up to 500 mm x 500 mm in planar directions. The head of bolts used in scissor mechanism is selected to be significantly large to ease the sticking the material on while increasing the stick area.

VHB tapes are purchased in rolled shape and originally covered with its red liner protective coating. The raw material is 1180 mm in width and 5 m in length for VHB 4910 and 1140 mm in width and 3 m in length for VHB 4905 which needs to be cut in smaller dimensions for actuator manufacturing trials given in Figure 5-2.



Figure 5-1 Prestretching scissor mechanism

Special blades are required to precisely cut the tapes in shape. If one cut a 100 mm x 100 mm VHB material and fix it on the scissor mechanism, he can stretch the material up to five times in planar directions. On the other hand, using a square cut tape to manufacture a DEA is not a must. Different amount of pre-stretches can be applied in both length and width directions. The scissor mechanism works well for all cut dimensions except the ones where any one dimension is less than 100 mm which is a case mostly experienced. In that case a hand pre-stretch is required to adhere the material first on scissor mechanism considering required dimensions, then stretching the scissor mechanism to desired level can be accomplished. By stretching the film 4 times in each direction the thickness drops to  $1.0 \text{ mm} / 4^2 = 63 \text{ } \mu\text{m}$ , which is excellent for actuator purposes.



(a)



(b)

Figure 5-2 (a) 3M's VHB tapes raw roll form (b) Cut of VHB tapes for actuator manufacturing

The scissor mechanism is only used to stretch the material to defined level but to keep the tape at that stretch size and work on it requires the use of Kestamid frames. The tapes are strongly and easily stick on the Kestamid frames. Frames in different sizes are manufactured to try different pre-stretched actuators. The ability to stretch the tape to desired dimensions and constraining at that dimension has a great flexibility. The sizes of pre-stretching Kestamid frames used are given in Table 5-1.

Table 5-1 Prestreching frame dimensions

<b>Code</b>	<b>X (inner) Dimension</b>	<b>Y (inner) Dimension</b>	<b>Width Dimension</b>	<b>Thickness Dimension</b>	<b>Type</b>
1	100 mm	100 mm	10 mm	10 mm	Square
2	200 mm	200 mm	10 mm	10 mm	Square
3	300 mm	300 mm	10 mm	20 mm	Square
4	400 mm	400 mm	10 mm	20 mm	Square
5	50 mm	100 mm	10 mm	10 mm	Rectangle
6	50 mm	200 mm	10 mm	10 mm	Rectangle
7	100 mm	200 mm	10 mm	20 mm	Rectangle
8	100 mm	300 mm	10 mm	20 mm	Rectangle

The stretched VHB tape on frame (Code 2) is given in Figure 5-3. The red liner illustrated demonstrates the initial dimension of the material.

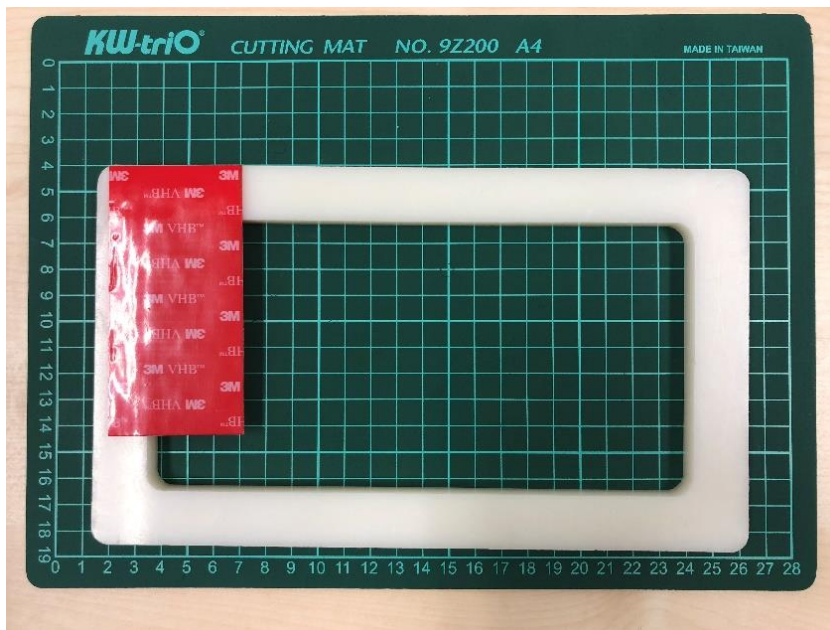


Figure 5-3 100 x 200 mm keastamid stretching frame and VHB band strip

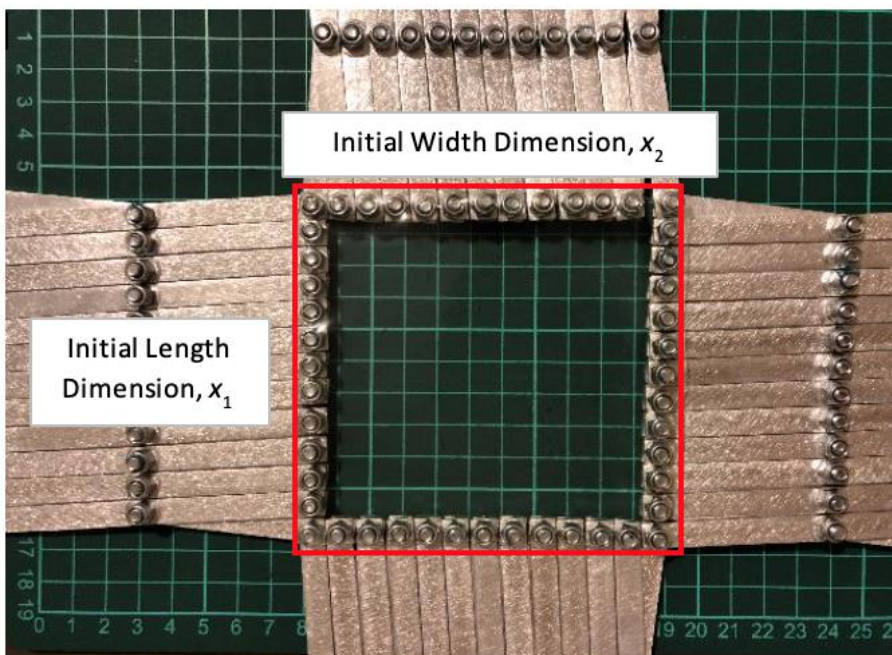
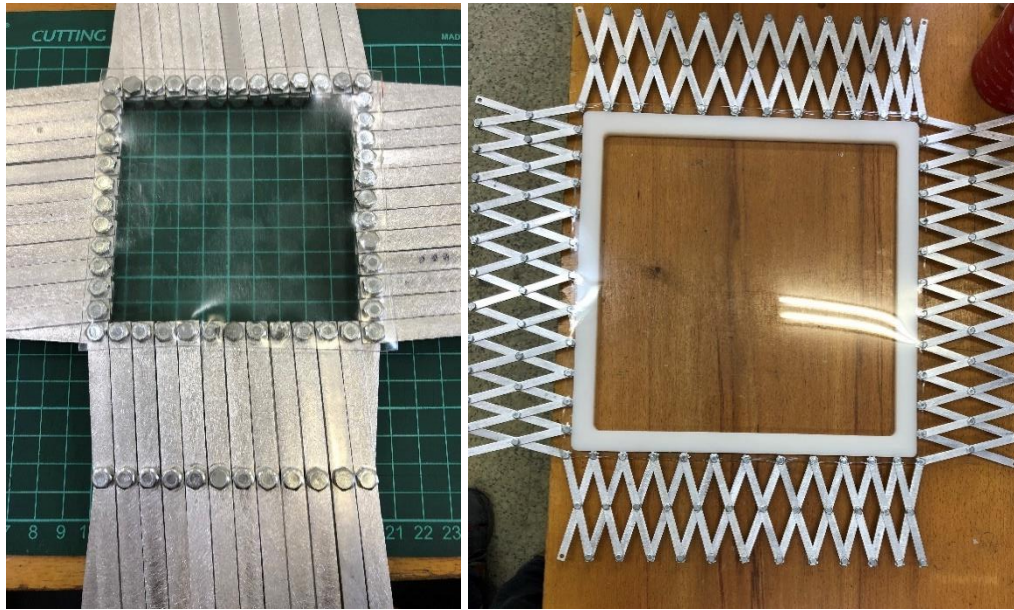


Figure 5-4 Stretched VHB tape on scissor mechanism



(a)

(b)

Figure 5-5 (a) 100 x 100 mm VHB Band stretched on scissor stretching mechanism  
 (b) 400 x 400 mm Kestamid stretching frame and stretched VHB band on it using scissor mechanism

When the stretching to the frame is completed the VHB tape is adhered on the Kestamid frame applying hand pressure by using oily paper and then VHB tape is detached from the scissor mechanism. While working with the VHB tapes, it is observed that oily paper and its original red liner are best non-sticking tools to work with. Reinforcement masks by a paper band should be applied to the edges of frame to avoid tearing of the stretched film.

The VHB tape is very sticky in nature due to its manufacturing purposes thus it is ready to emit any kind of dust particles in the air. The room conditions should be dust free for best performance. The carbon black smearing procedure should be performed quickly which will be defined next. After completing the stretching of the VHB tape on the frame, the carbon black should be applied on both sides (top and bottom) of the

material. The carbon black used is the Akzo Nobel's KetjenBlack EC-600JD as illustrated in Figure 5-6 which provides excellent carbon nano particle sizes.



Figure 5-6 Ketjenblack aggregated dust particles

On the other hand, the particle sizes of the Ketjenblack is as aggregated in packing. Prior to application, the carbon black should be squeezed to decrease the as is state of particle size. This can be done squeezing the particles between two spoons. Care should be taken for the fluttering particles and mask should be used. After handling ideal carbon black particle size, it is ready to smear on the stretched material. Also, Nyogel 756P conducting grease is tested as an electrode material is shown in Figure 5-7. Due to oily nature of Nyogel, a thin spatula is used to smear on VHB tape. Before smearing the carbon black on VHB tape, the use of a masking stencil should be introduced. If it is not used, the carbon dust particles flow on every part of the material especially the defined DEA edge borders which negatively affects the performance as

creating sparking areas at the edges. The electrode material should not be applied too close to the edges otherwise edge arcing will ruin the performance of the actuator.

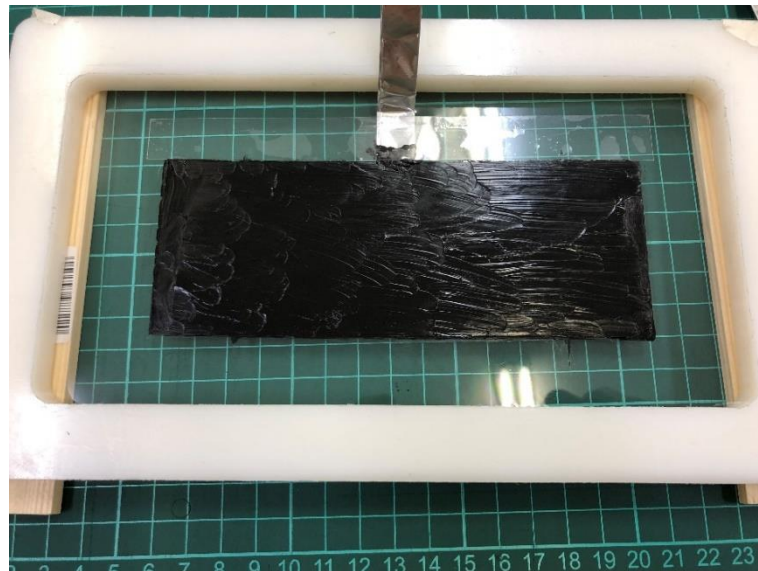
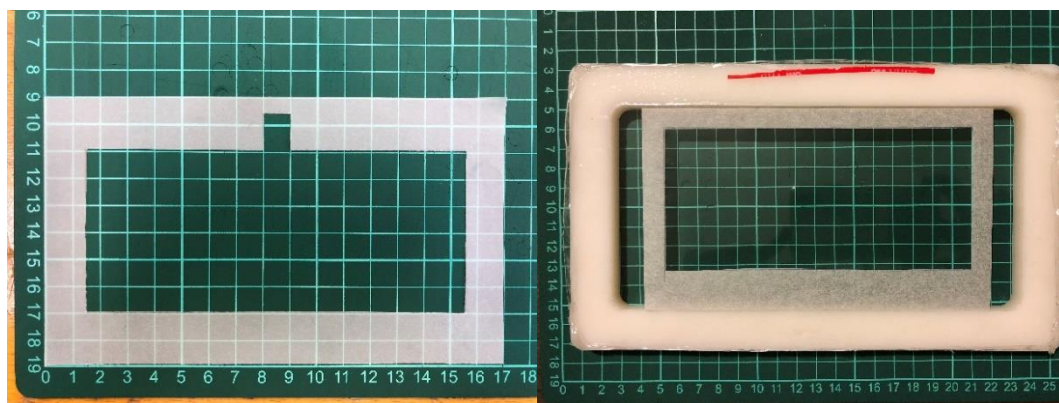


Figure 5-7 Nyogel 756P carbon grease application

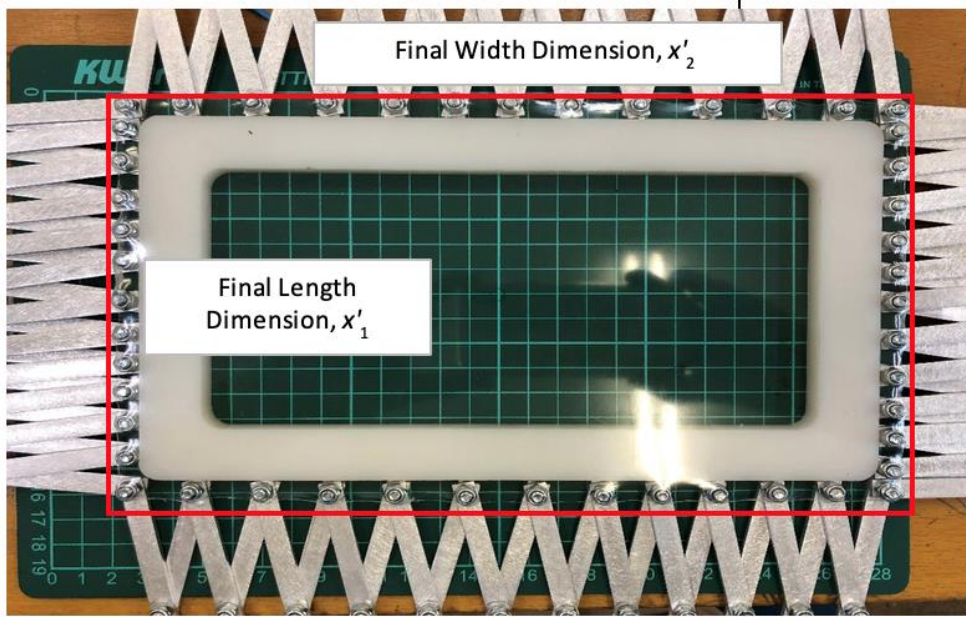
A stencil should be prepared to avoid this effect and apply the carbon black precisely in desired shape and area. Oily paper or VHB tapes' red liner can be cut in desired shape to use as a stencil. Both well sticks on the VHB tape and easily removed. But, new stencil should be used for each new actuator manufacturing as the carbon black is accumulated at the edges. It is experienced that there is a better way of manufacturing stencil for multi time use which is replacing the stencil material with acetate paper. The acetate paper is stiffer according to oily paper to avoid mini gaps at the edges however it sticks on the VHB tape resulting in fatal tears of pre-stretched material. To avoid sticking, the acetate paper shall be covered by 3M's VHB 5490 tape which provides excellent frictionless contact surface. The stencil design using oily paper is given in Figure 5-8. While designing a stencil, the area of carbon black should be well defined including the electrode application regions. For better performance, the electrode application region should be well isolated from the rest of

the carbon black area. This pattern is applied to the opposite side of the stretched VHB tape as well. Care should be taken not coincide the electrode application locations. The stencil shown has a 160 mm x 55 mm in width and length dimension excluding the electrode region. This is applied on a 4 x 4 pre-stretched VHB tape.



(a) (b)  
Figure 5-8 Oily paper masking stencil

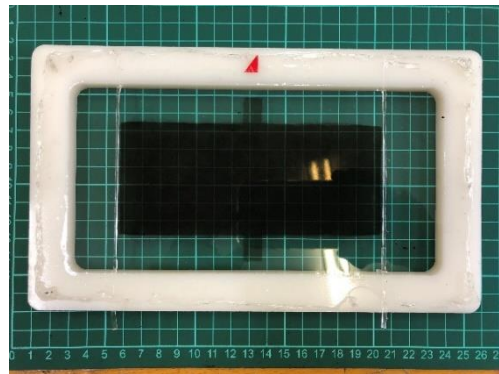
Carbon black can be smeared while the stencil is located on the pre-stretched material with a smooth and soft paint brush. The electrode application regions should be clearly visible which are illustrated on Figure 5-9. Brushing in length direction rather than width direction performed well. When the carbon black smeared on the both sides of the tape, it is not ready to be removed from the stretching frame. It can easily be torn due to high internal stress. Before removal, reinforcements should be applied. The upper and bottom edges of the actuator both on two sides should be stiffened. This can be done using acetate strips (15 mm x 165 mm works fine). The acetate strips can be glued and located on the tape. The glue material should be selected among fast drying ones.



(a)



(b)



(c)

Figure 5-9 Applied carbon black on stretched VHB tape

On the other hand, right and left-hand sides of the actuator on both sides (the edges of the carbon black area) are still weak to remove from DEA the frame. 2 mm in width and 20 mm in length strip VHB materials (VHB 4905 is used when VHB 4910 is selected as DEA) should be cut and stick on both edges at the both sides of the material by pre-stretching as shown in Figure 5-9 (b) & (c). The electrical conductivity can be accomplished by sticking aluminum strips (copper tapes can also be used) in 10 mm x 100 mm dimension to each electrode location (upper and lower parts). Finally, the regions where acetate strips are glued should be stiffened. Wooden strips, Kestamid strips or acrylic rigid strip bars can be used. Using a cutter knife, the actuator is ready to be removed from the pre-stretching frame. The final actuator can be obtained as given in Figure 5-10.

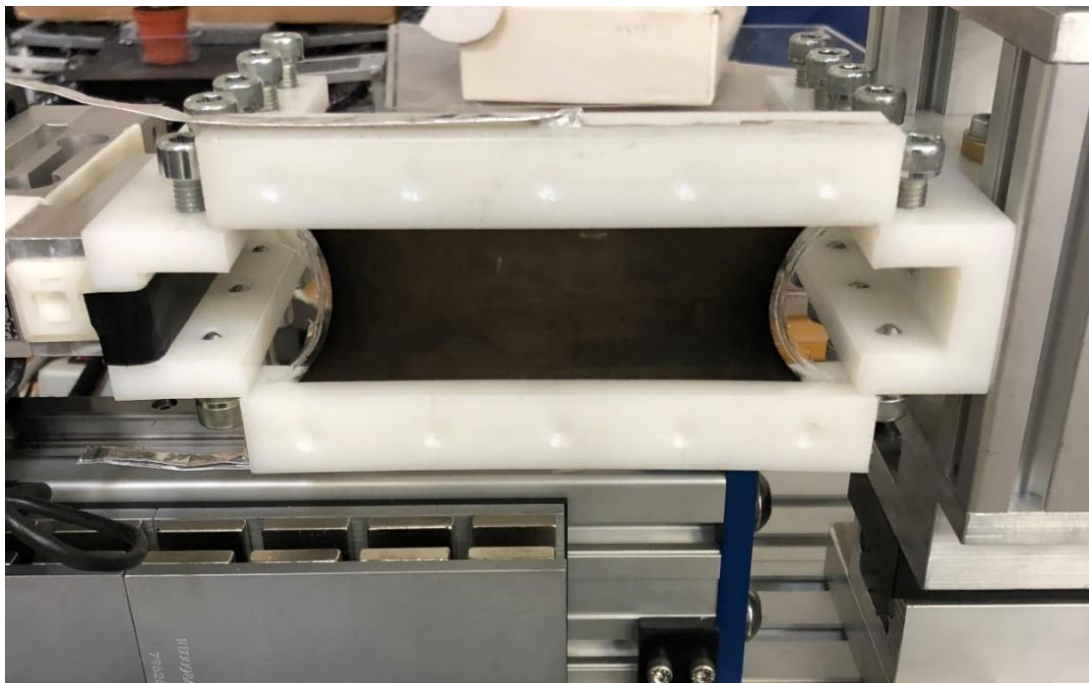


Figure 5-10 Final DEA

### **5.3. Hardware and Software Design**

Four tests are designed to evaluate the performance of DEAs in electromechanical test campaign. These are DEA relaxation, blocking force, creep and voltage induced creep tests.

In relaxation tests, the DEA performance will be monitored according to applied stretch and the generated residual stress will be observed. As the stretch ratio gets higher, the generated residual stress in increased on DEA.

In blocking force experiment, it is aimed to relax the DEA to a defined stretch position and apply a certain amount of voltage on it. It is expected that the applied voltage will decrease the internal stress and when the voltage is removed, there will be an internal force generation. The force observed will depend on the configuration of the DEA.

In creep test, the DEA will be loaded by a constant force and the actuator is expected to stretch to balance the applied force. The amount of stretch will depend on the applied force and actuator configuration.

In voltage induced creep test, it is intended to observe the stretch response of the actuator when voltage is applied while actuator is loaded by the creeping force. The effect of voltage on actuator will be monitored.

To perform these tests, a linear translation stage (SRS-012-04-030-01-F100) and its motion controller (DMC-30011) from H2W Technologies is selected. The linear stage can travel 305 mm unidirectionally with a maximum of 133 N continuous force. It is equipped with 1-micron linear encoder (LM 13) and powered by a brushless linear motor. The controller of the linear stage is a single axis motion controller and uses 32 bit RISC processor. The motion controller operates stand alone or can be networked to a PC via ethernet. It supports two analog inputs and outputs. The linear stage is equipped with a Xenus digital servo drive XTL-230-18.

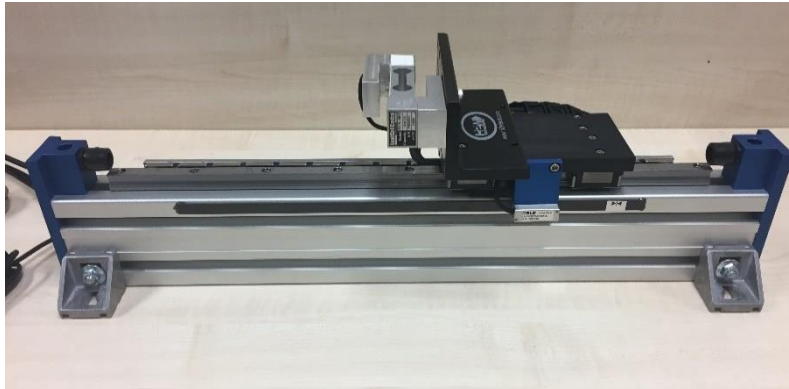


Figure 5-11 Linear translation stage from H2W



Figure 5-12 ESP4 – 100 N (10 kg) load cell is mounted on Linear Stage



Figure 5-13 Linear translation stage and its controller unit

For the testing purposes, a load cell (ESP4 – 100N) is mounted on the linear stage. The signal conditioning is performed by OM-19 load cell conditioner. The complete set of linear stage unit is presented in Figure 5-11 to Figure 5-13. Unfortunately, the linear stage as it is delivered cannot be used for planned tests. Grippers to hold the DEA and a stiffing structural unit is required to adopt the system. A non-conducting (due to high voltage application) structural bracket apparatus which can be adjusted in horizontal and vertical directions is designed and manufactured for the linear stage is given in Figure 5-14 to Figure 5-16.

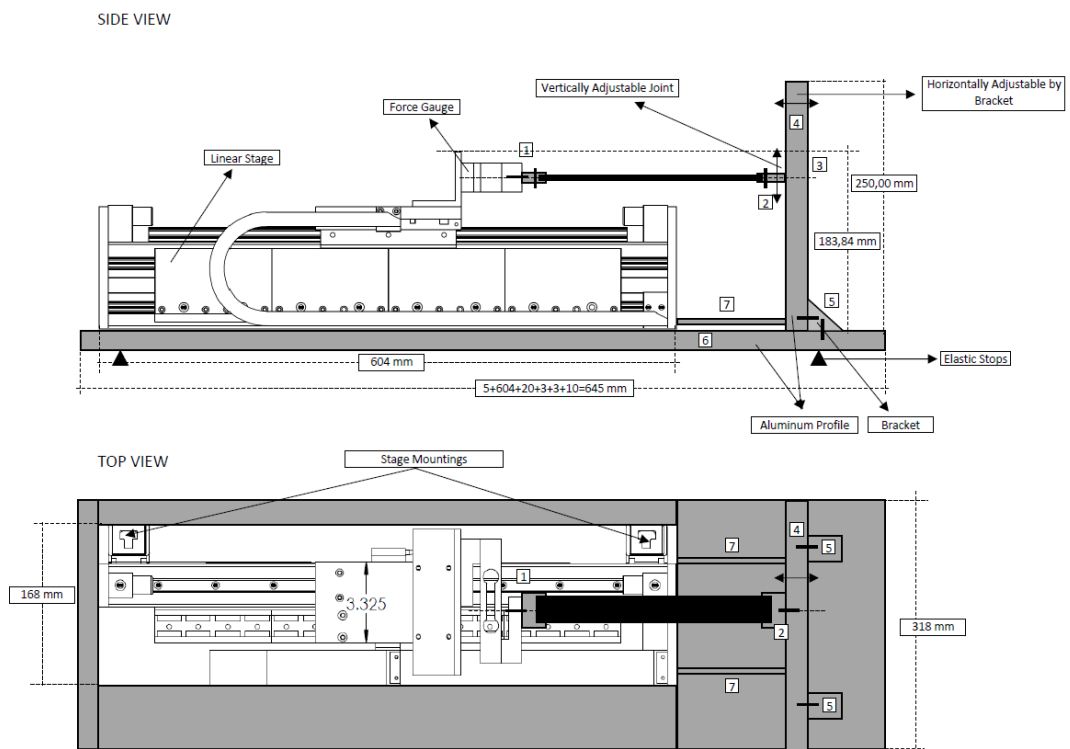


Figure 5-14 Linear stage fixture and actuator holder design

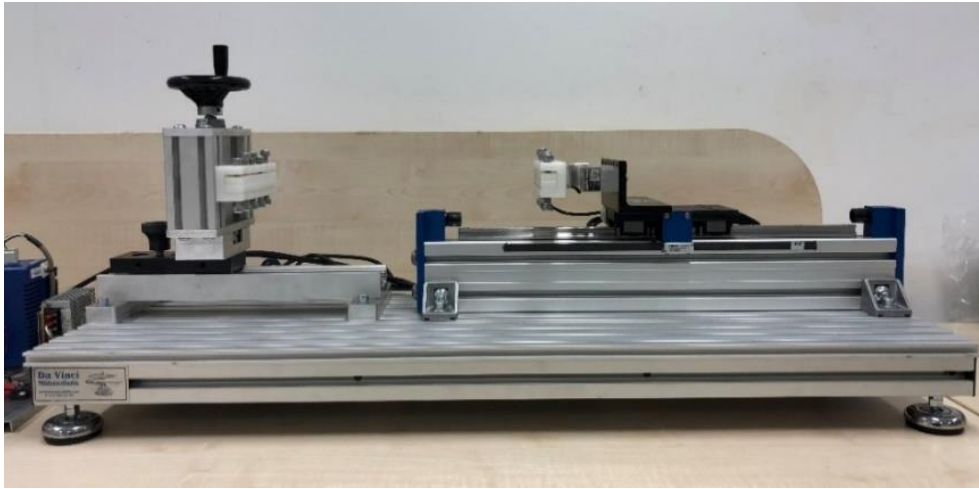


Figure 5-15 Linear stage fixture and actuator holder manufacturing and installation



Figure 5-16 Linear stage fixture design detail view

The manufactured DEAs will be tested squeezing between Kestamid bars using top and bottom screws as presented in Figure 5-16. The linear stage is capable to stretch the actuator in one direction. During tests, the actual length of the DEA in actuation direction, the applied force and voltage is recorded as the controller controls the driving motor of the linear stage and transmits the received force and position information to computer. The high Voltage Amplifier TREK Model 10/10B-HS is used to generate high-speed high voltage to system. It is capable of precise control of output voltages with 0 to  $\pm 10$  kV DC voltage. It is also possible to monitor the applied voltage and ampere values using the controller unit of linear stage. For blocking force and voltage induced creep tests, controller applies the required amount of voltage on DEA. The structural design of the electromechanical test setup is given in Figure 5-17.

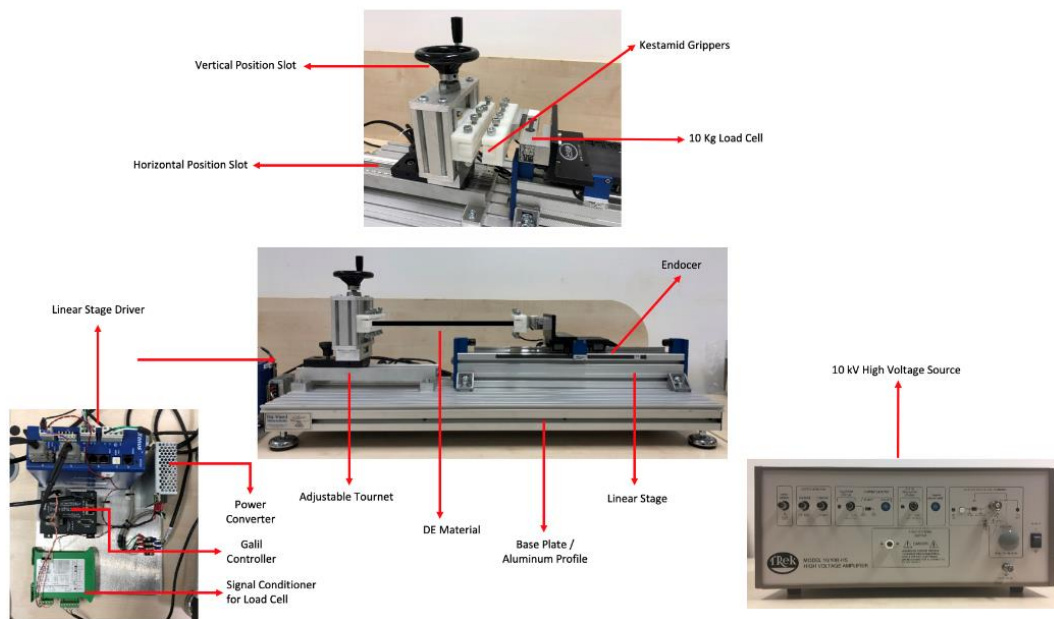


Figure 5-17 Schematic definition of structural electromechanical test components

When the DEA is mounted on the electromechanical test setup, the direction of motion of the linear stage is assumed to actuation direction,  $\lambda_1$  and the width direction,  $\lambda_2$  is kept constant as defined in Figure 5-18. The manufactured DEA is fixed to linear stage by the screws. Great care should be taken to align the actuator and the load cell to avoid undesired moment effects.

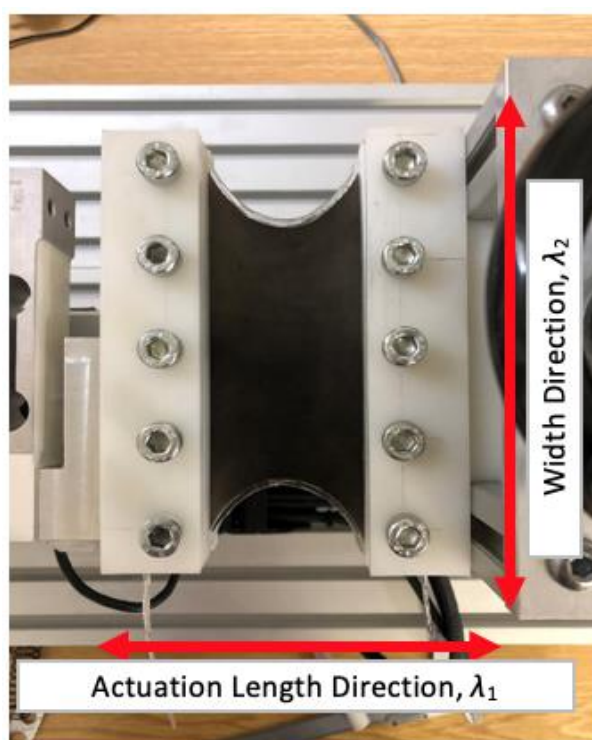


Figure 5-18 Installation direction definitions of DEA

#### 5.4. Software Design

Galil Motion controller DMC 30011 is programmed with a Galil tools software. The communication is well satisfied between the software and controller via ethernet protocol using Windows based platform. According to each type of test, related Galil controller codes are manually generated.

Basically, all four tests require, displacement control and read all other parameters or force control and read all other parameters. For relaxation tests, displacement control is performed. DEA is quickly stretched to an user defined position and kept constant for a certain amount of time. The DEA's initial and final positions and the force data are recorded throughout the test. In blocking force experiment, the base relaxation procedure is maintained and voltage is applied. User defined constant force is applied on the DEA starting from the start position and kept constant during creep test using a force controller. As the DEA responds in strain to applied force, the starting and ending position of the actuator are also recorded. For voltage induced creep test, the same routine applied for creep test is used. After a certain amount time, desired voltage is applied using high voltage amplifier by controller.

The position, force and applied voltage histories are all recorded throughout the tests. The control design of the system developed in Galil tools software is illustrated in Figure 5-19. The wiring diagram and the details of the codes are given in Appendix A & B.

The generated Galil codes are designed according to the data transfer schematics of the electromechanical test system is given in Figure 5-20.

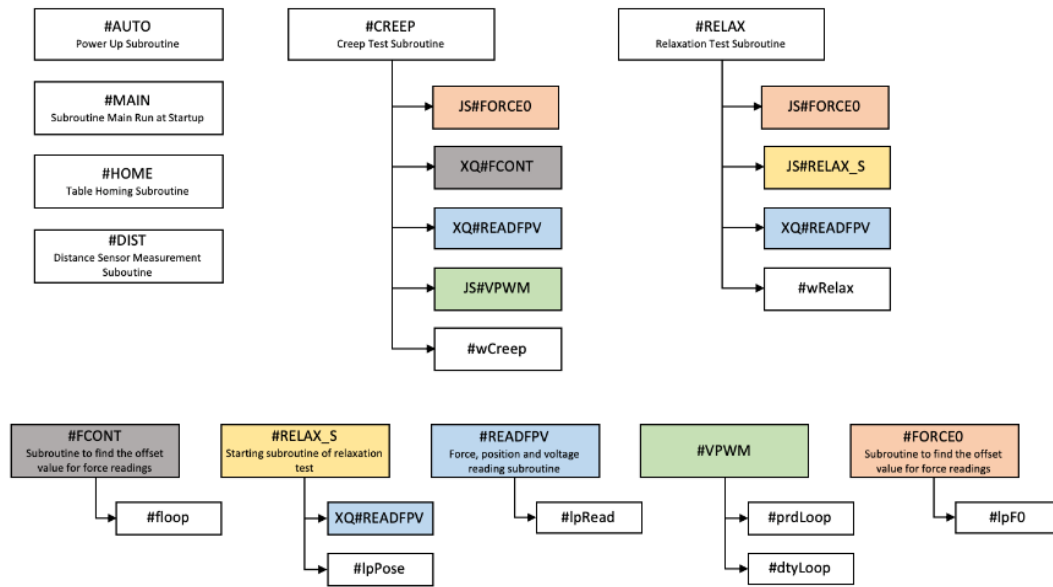


Figure 5-19 Schematic definition of logic of generated Galil control codes

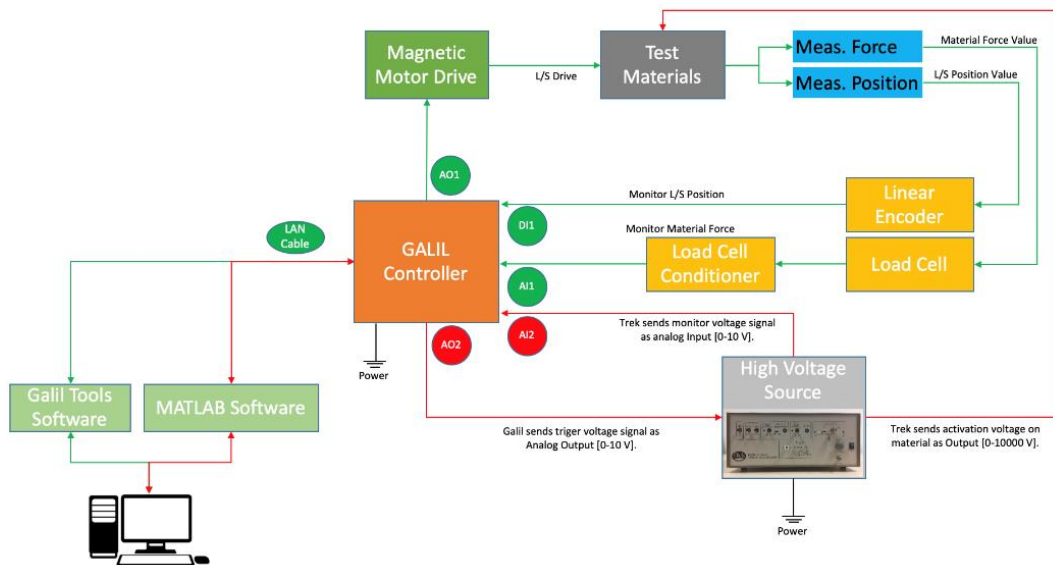


Figure 5-20 Schematic definition of logic of electromechanical test components

All Galil codes are first compiled on Galil tools software and test directly on the system. When the controller tests are completed, a Matlab GUI is constructed to operate controller from a standalone computer capable to input all user defined parameters input to controller and monitor desired output results. The Matlab GUI connects to GALIL via wireless IP communication. The opening screen of GUI is as given in Figure 5-21. The opening screen maintains connection to Galil controller and guides user to desired test sub module. Three sub modules are designed as GUI to perform related tests which are presented in Figure 5-22 to Figure 5-24.

For the relaxation test GUI given in Figure 5-22, the initial DEA start position and ending position are required inputs. The duration of the relaxation test, linear stage's begin and ending speeds and accelerations can be defined using the GUI. The test data resolution can be adjusted.



Figure 5-21 Matlab GUI opening screen to connect Galil controller

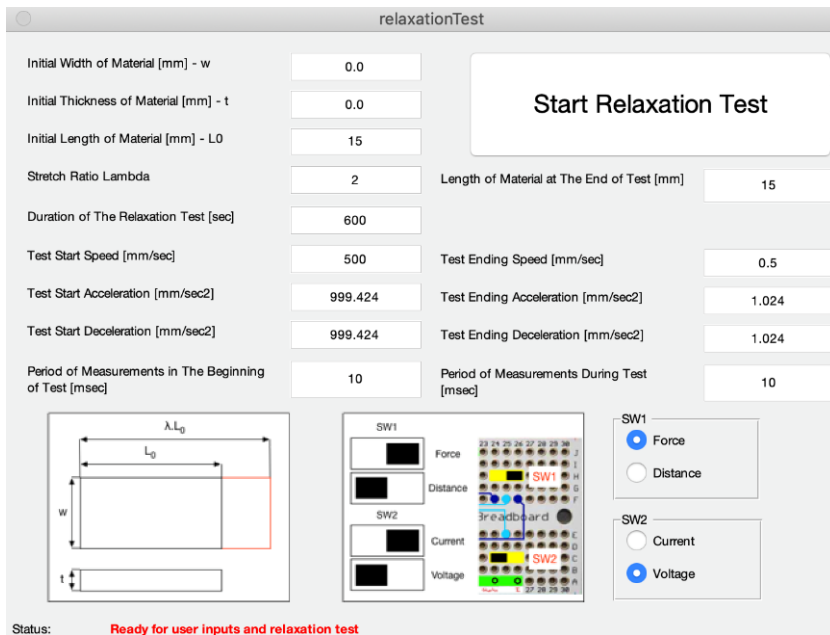


Figure 5-22 Matlab GUI relaxation test module

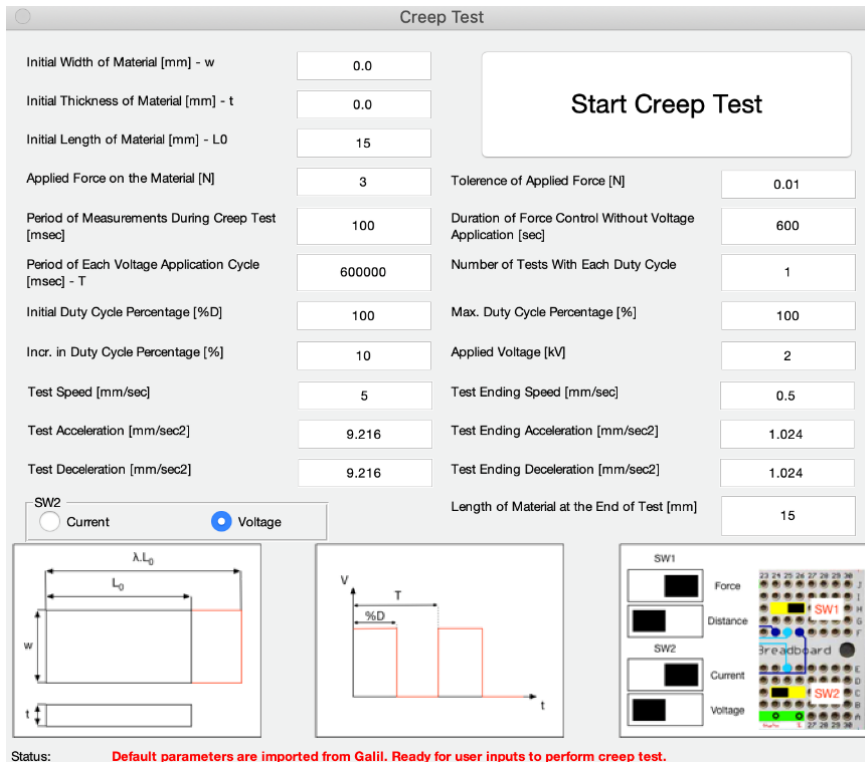


Figure 5-23 Matlab GUI creep test module

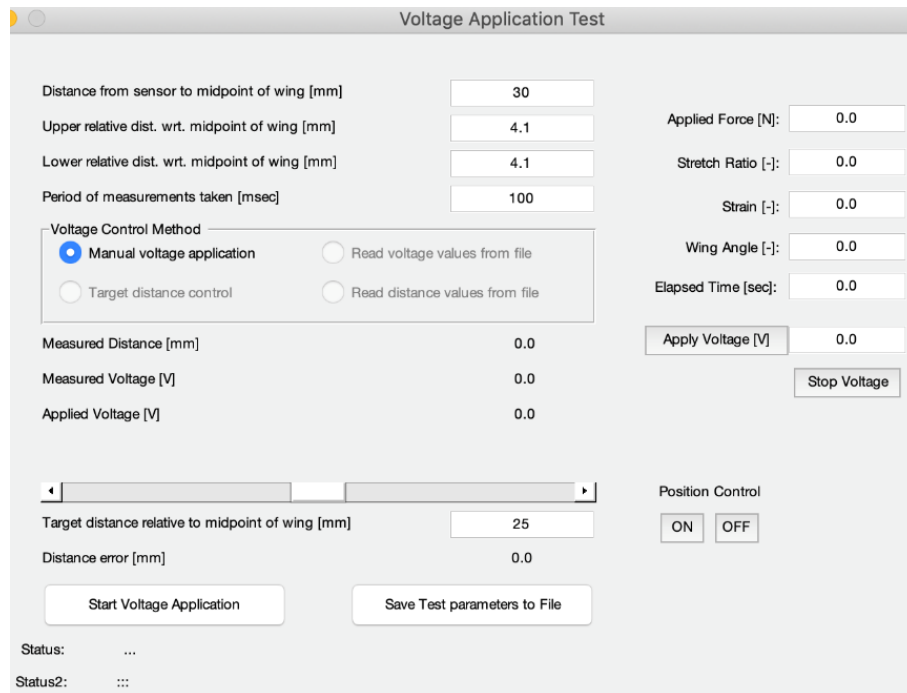


Figure 5-24 Matlab GUI voltage application test module

For the creep test GUI module given in Figure 5-23, the similar DEA and linear stage parameters can be configured. As only creep test can be performed, also cyclic voltage application is possible to define.

The final module is the voltage application GUI as given in Figure 5-24. It is possible to control the DEA as installed on the wing structure. The module inputs the displacement laser sensor data and computes the error to rotate the trailing edge according to desired position. The module also supports manual voltage input to installed DEA. The concept, design and implementation of the wing structure will be defined in next chapters.

## **5.5. Effect of Pre-stretching on Design**

Pre-stretching of the DEAs improves their actuation performance and can be done in planar directions. The aim of pre-stretching is to decrease the thickness of the elastomer material and increase the applied voltage effect with reduced voltage input. Individual pre-stretches can be set in length and width directions according to desired performance level.

When the DEA released from the initial strainer frame, the pre-stretch in width and length direction remains constant and can be used as it is. However, in the scope of this study, the pre-stretch in width direction is kept fixed while the pre-stretch in length direction is not forced to be fixed (free to counteract) and it is free to return to its initial unstretched dimension due to material internal stress. The stretchability of the material in length dimension will be used as the actuation stretch and will be considered as a free control variable which will depend on the applied load and voltage on the material.

During tests, various initial length and width pre-stretch combinations are manufactured as DEA. The carbon black is smeared on the actuator while its pre-stretched in both directions at the strainer frame. Whatever pre-stretch is applied in longitudinal direction at design level, it is set free and used as a control parameter during in all actuation tests. As it can be seen from Figure 5-18, the actuator is installed to linear stage in the direction of the free length while the width is kept constant. Different length stretches are applied by linear stage to learn the capabilities of the DEA.

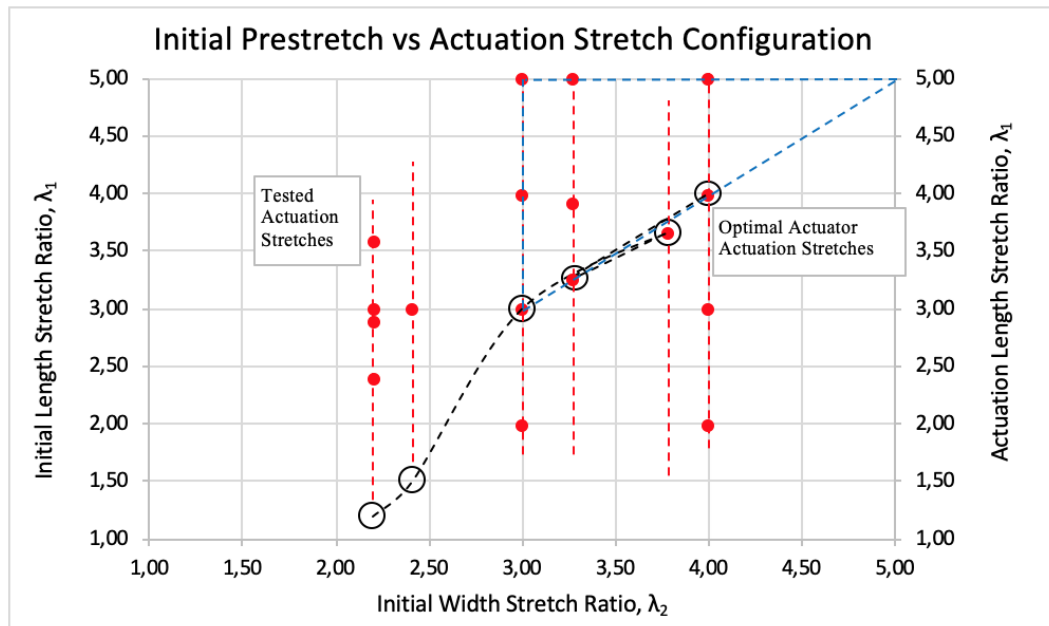


Figure 5-25 DEA manufacturing and activation chart

More than hundred different pre-stretch configured DEAs are manufactured. As presented in Figure 5-25, blank circles indicate the initial pre-stretches in length and width directions of the manufactured DEAs. The DEAs are all mounted on the linear stage at a minimum possible length stretch position. Using linear stage, the manufactured DEAs are activated to predefined stretches for testing purposes which are indicated by red dots. It is observed in the tests that starting from the initial width stretch ratio,  $\lambda_2 = 3$ , maximum length stretches up to  $\lambda_1 = 5$  are the most durable DEAs. The region bounded by blue triangle can be used to design maximum performance actuators. The results of blocking force experiments support the outcome of the observation which will be detailed next.

## 5.6. DEA Relaxation Tests

The DEA relaxation test experiments are performed as the same way defined in Chapter 4.2.4. In material characterization relaxation test, the material is used as it is

delivered from the supplier. However, in electromechanical relaxation tests, the VHB tape material is first stretched to predetermined level, then carbon black is smeared on both sides and reinforcement is applied. As a result, the theoretical design of the two relaxation tests are same but the used material designs are different. A sample DEA is presented in Figure 5-26. This actuator is pre-stretched  $\lambda_1 = 3.93$  in length (actuation) direction and  $\lambda_2 = 4.02$  in width (fixed) direction on the strainer frame. After it is released, the width (fixed) pre-stretch is still  $\lambda_2 = 4.02$  (as it is constrained on the stiffner frame) and the length (actuation) prestretch is returned back to its original dimension 32 mm where  $\lambda_1 = 1$ .

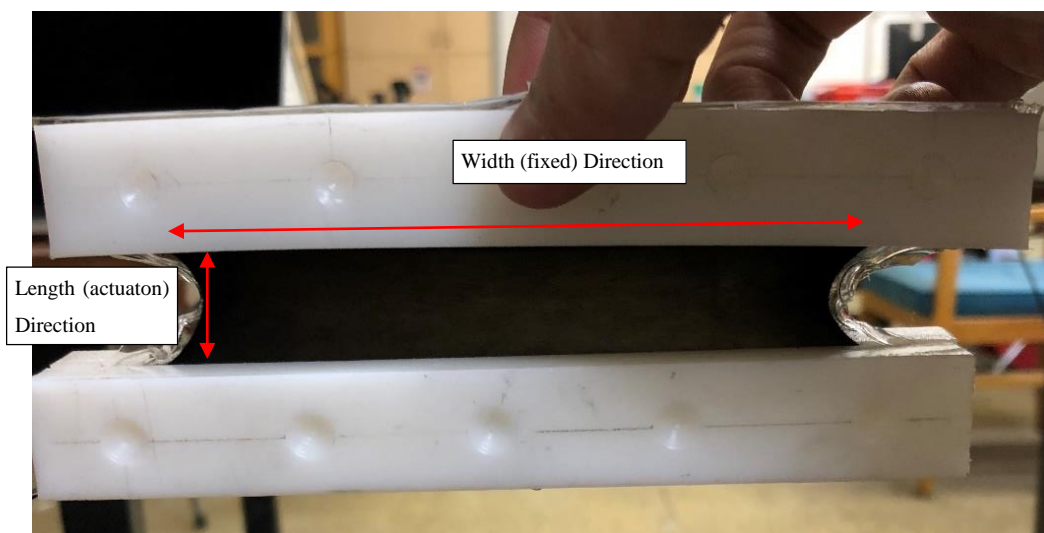


Figure 5-26 A Sample of a manufactured DEA

After installing the DEA to linear stage as given in Figure 5-27, any desired actuation pre-stretch can be applied (theoretically it is up to linear stage's maximum travel distance) to actuator for testing purposes. The actuation stretches illustrated in Figure 5-25 are applied for relaxation test experiments. The shape of the DEA in relaxation test is given in Figure 5-28. This actuator is stretched up to  $\lambda_1 = 5$ . Beyond that stretch level, most of the actuators are torn out during testing.

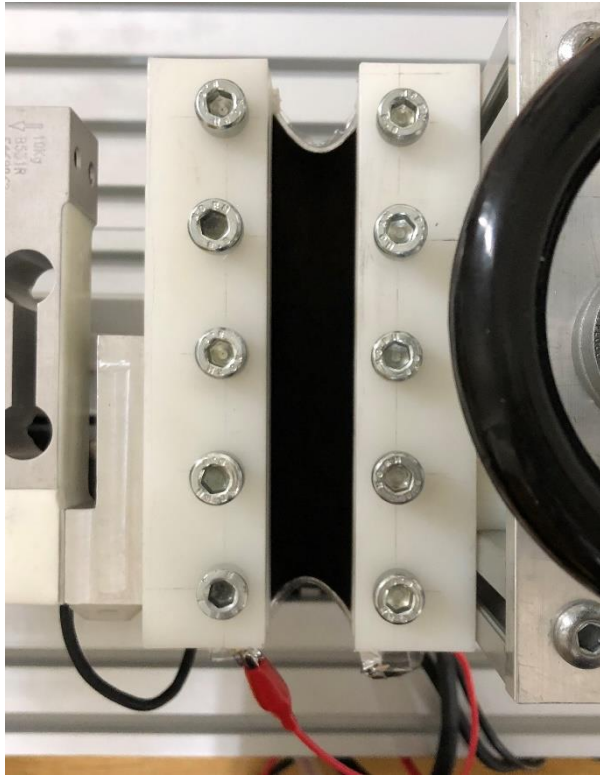


Figure 5-27 DEA installed to test bench

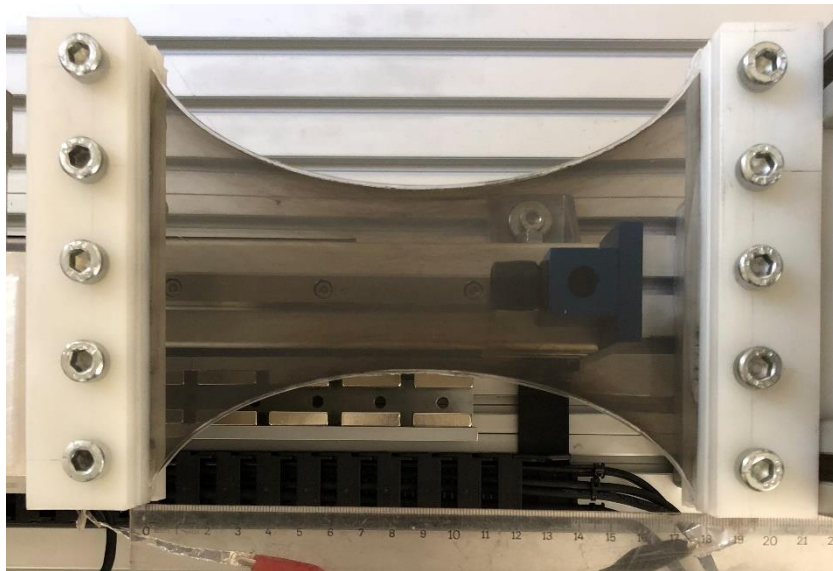


Figure 5-28 DEA shape in relaxation test

After preliminary tests, two kind of relaxation tests are performed. One of them is the short time relaxation tests which is let to run 600 seconds after stretching. The second one is the long run test which is let to run 3600 seconds. All tested actuators are installed to test bench at 150 mm which is equal to  $\lambda_1 = 1$  and the tests are performed upto 675 mm which is equal to  $\lambda_1 = 4.5$ . The test results are as presented in Figure 5-29. After 600 seconds, the maximum observed force for  $\lambda_1 = 4.5$  is equal to 3.52 N. This force is the one that is trying to recover the DEA to its initial rest position.

In long run test, the test is performed for  $\lambda_1 = 1.5, 2.5$  and 3 stretch ratios and the results are given in Figure 5-30. The maximum force for  $\lambda_1 = 3$  is equal to 1.55 N where for the same stretch, the maximum force was equal to 1.71 N at 600 seconds.

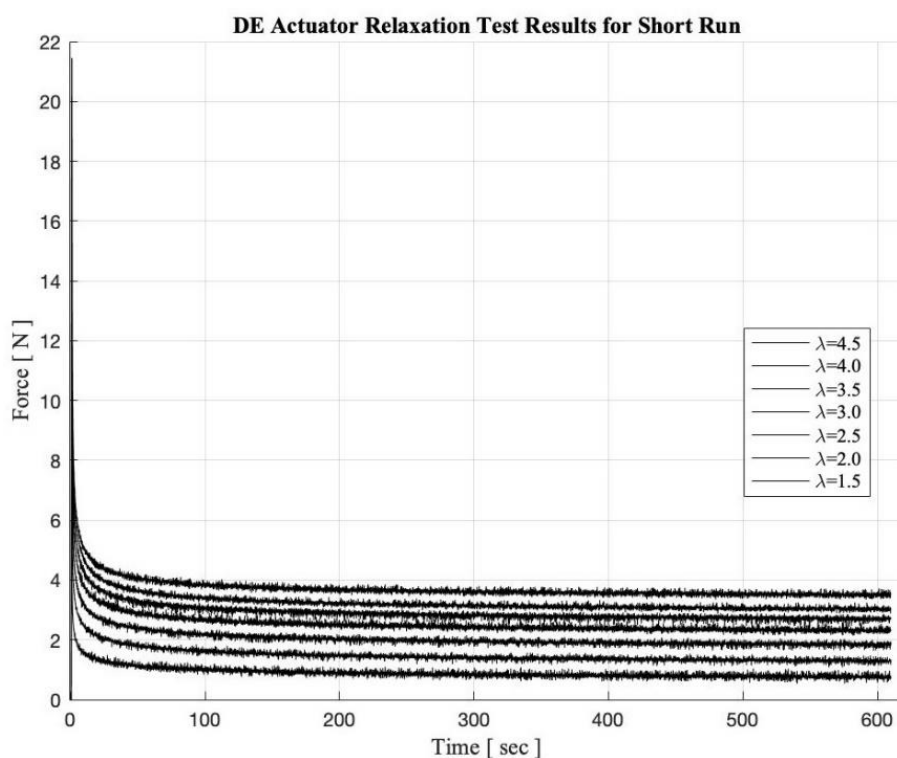


Figure 5-29 Single layer DEA relaxation test results for short run

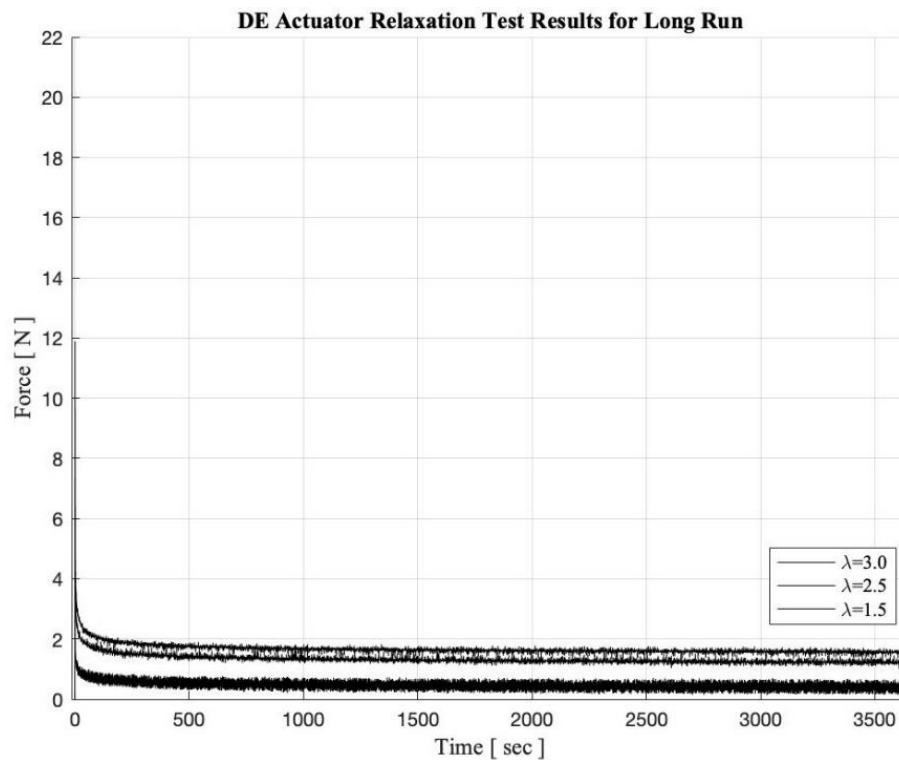


Figure 5-30 Single layer DEA relaxation test results for long run

On the other hand, the elastomeric materials exhibit Mullins effect which is a mechanical response encountered in filled rubbers in which the stress-strain curve depends on the maximum loading previously encountered. It is an instantaneous and irreversible softening of the stress strain curve that occurs whenever the load increases beyond its all-time maximum value. When the load is less than a prior maximum, nonlinear elastic behavior prevails. The Mullins effect is not modeled in the scope of this study but shown as a result of applied relaxation tests. The DEA is loaded with increasing constant stretch ratios and then the tests are reperformed for the same stretching and the effect of stress softening is shown in Figure 5-31 and the resulting force difference is given detailed in Figure 5-32.

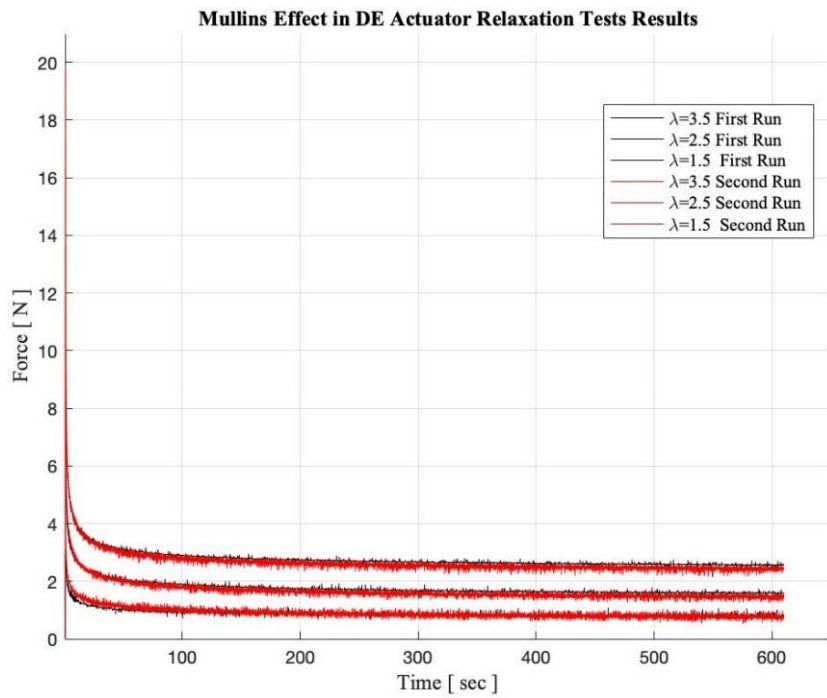


Figure 5-31 Mullins effect observed on relaxation test results for single layer DEA

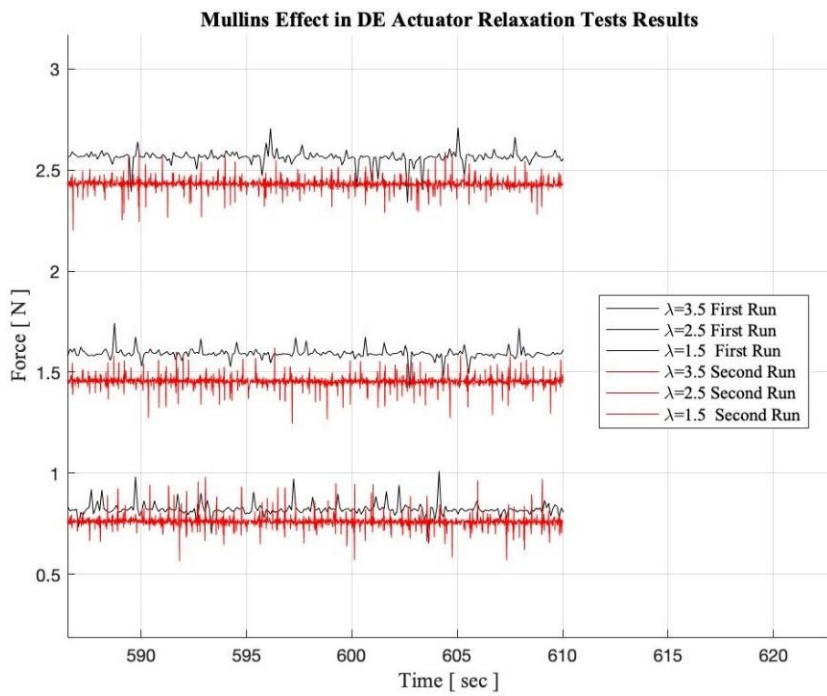


Figure 5-32 Mullins effect encountered in DEA relaxation tests - detailed

The relaxation tests are also performed for double layered DEAs. For a stretch ratio of  $\lambda_1 = 3$ , the double layered actuator resulted in 3.26 N force at the end of 600 seconds of relaxation test as presented in Figure 5-33 while the single layered DEA for the same stretch ratio encountered a force value of 2.30 N. Doubling the actuator layer did not doubled the resulting force value but performed a more durable behavior. The manufacturing conditions and the higher stiffness of the double layer smeared carbon black between the layers affected the results.

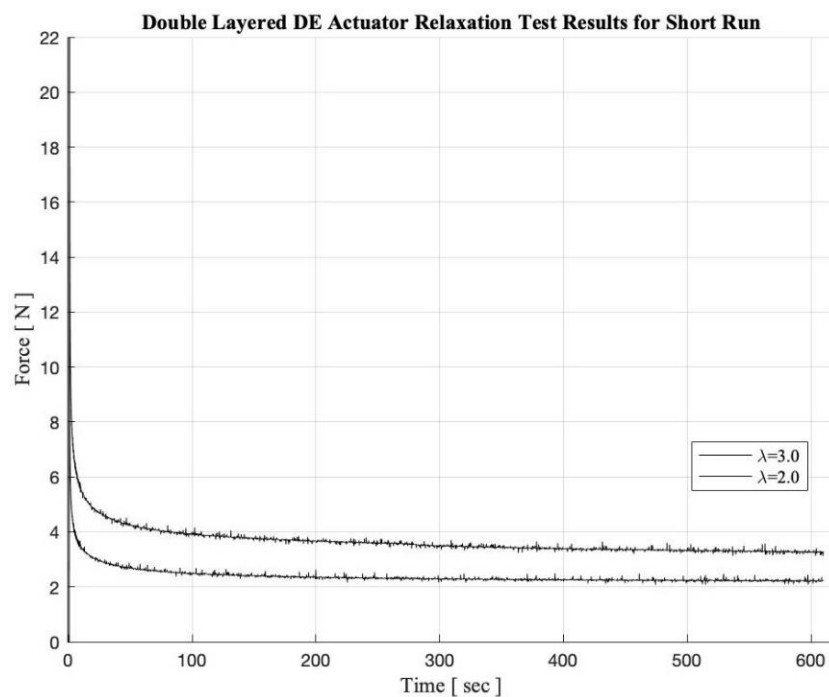


Figure 5-33 Double layer DEA relaxation test results for short run

### 5.7. DEA Blocking Force Tests

In a blocking force experiment, DEA stretched to a predetermined amount and electric field is applied. As the strain is constant in the test, the force generated due to relaxation is in the decreasing form as experienced in Section 4.2.4. Whenever a voltage potential is applied on the DEA, this creates a Maxwell stress on the stretched

elastomer and results in a rapid force reduction observed in longitudinal actuation direction. The force effect of the applied voltage potential creates a counter force in actuation direction (effect is observed in planar directions but only the effect in actuation direction is considered) which is opposite to current state of internal force occurred as a result of relaxation. When the voltage potential is removed, the force effect diminishes and the elastomer continues to its relaxation behavior. This test provides us to examine the effect of voltage while a DEA is being loaded. Different stretches are applied to DEA on linear stage and different voltages are applied at certain stretches.

In Figure 5-34, a DEA sample which is stretch to  $\lambda_1 = 4.4$  is presented. It is exposed to electric field up to 4.8 kV. First the DEA let to relax for 600 seconds then a certain constant voltage is applied on the actuator for 300 seconds starting from 900V. After voltage is removed, the actuator is let to continue relaxation another 300 seconds and DEA is again exposed to electric field. There is an apparent force difference encountered in each different voltage application. The magnitude of the force difference is in line with the magnitude of the applied voltage application. As the applied voltage gets higher, the force also increases.

Many tests are performed with different pre-stretches and varied electric fields. The force results (in grams) of these tests are as given in Figure 5-35. As the thickness of the DEA decreases, the output force of the actuator increases for the same applied electric field as expected. The maximum obtained force value from a single layer actuator with 3.93 stretches in both length and width directions gives the maximum force output of 187 gr at 3900 Volts. The minimum stretch of 1.2 in both length and width directions give the minimum force output of 51 gr at 7712 Volts.

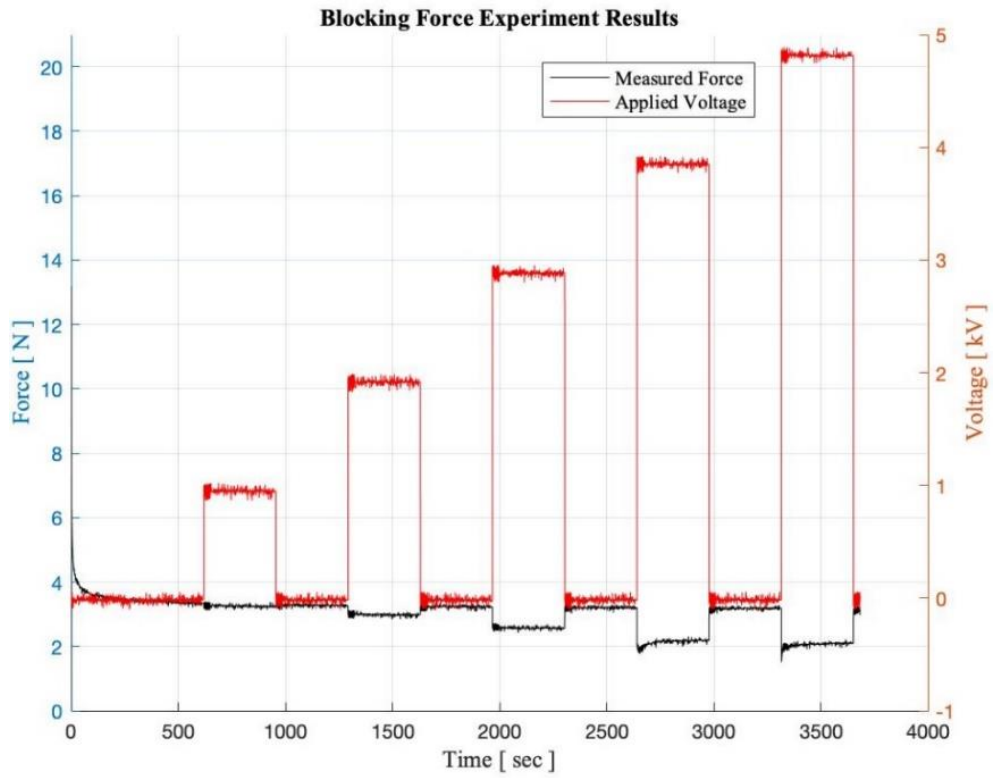


Figure 5-34 Blocking force test

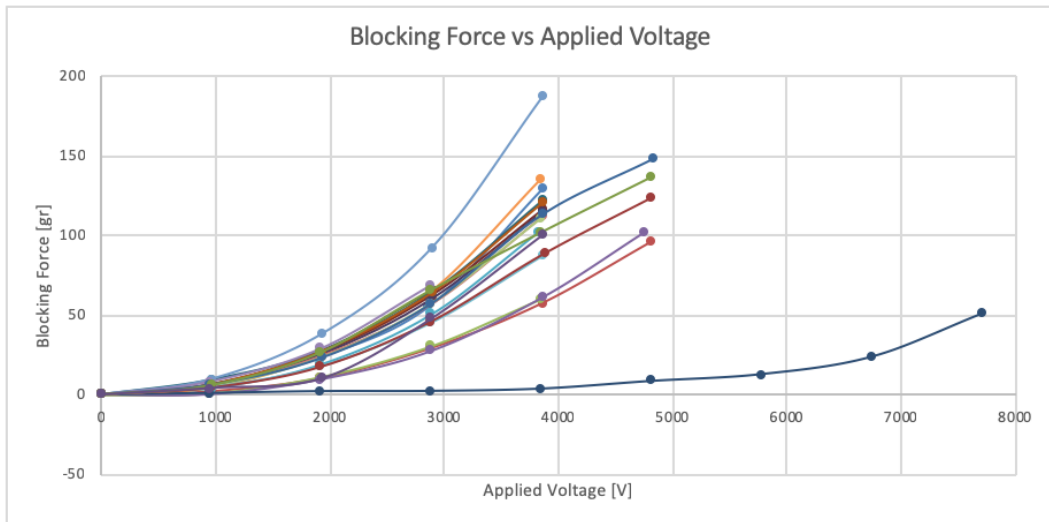


Figure 5-35 Single layered DEAs blocking force results

## 5.8. DEA Creep Tests

The DEA creep test experiments are performed as the same way defined in Chapter 4.2.4. Different force values are applied to both single and double layered actuators. The maximum creep force applied on a single layer DEA was 1.7 N and 5.5 N for double layered DEA. Beyond that forces, DEAs failed to operate. The creep tests are performed using the same initial pre-stretched actuators. All DEAs are located to linear stage at same grip distance which is 15 mm and equivalent to  $\lambda_1 = 1$ . When the constant creep load is applied, the stretching of the DEA is recorded and the results are presented in Figure 5-36. Maximum stretch ratio,  $\lambda_1 = 2.76$  is observed. Some of the creep tests (0.90 N, 1.10 N and 1.30 N) last for 1200 seconds to observe long time reaction response which are presented in Figure 5-37. Also, as performed for DEA relaxation test, Mullins effect on creep response is studied and the results are as given in Figure 5-38 for 2.1, 2.3 and 2.5 N creep forces.

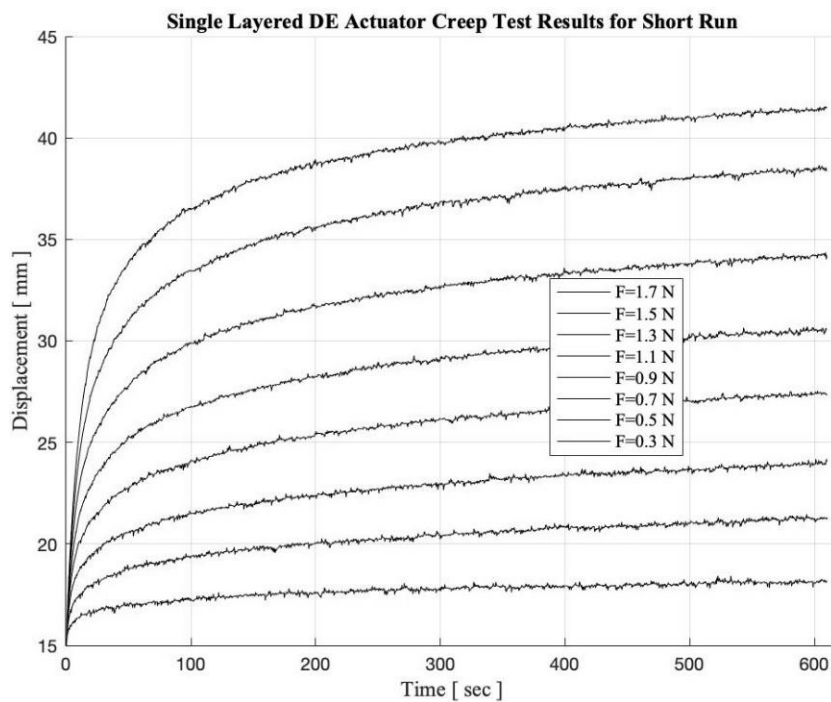


Figure 5-36 Single layered DEAs creep test results for short run

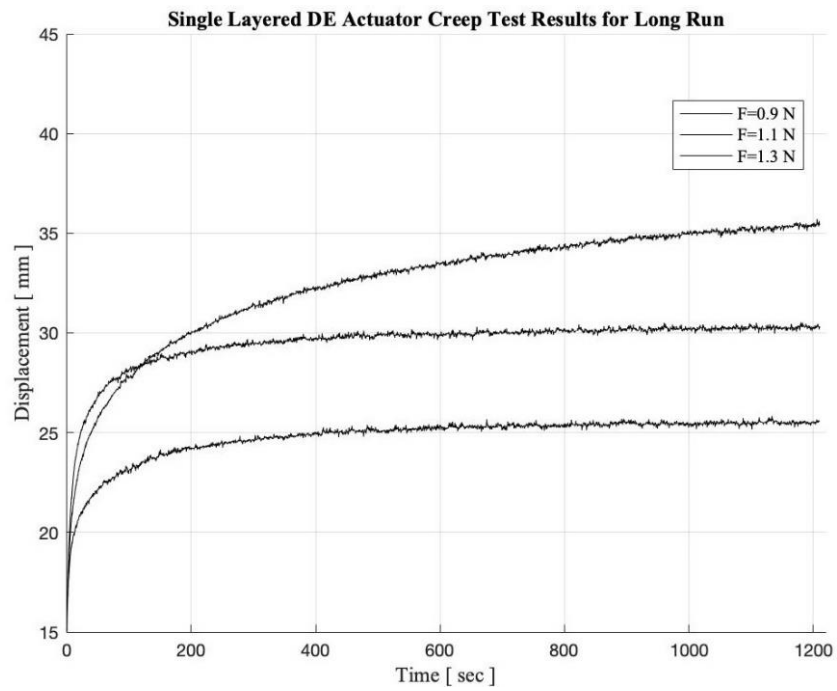


Figure 5-37 Single layered DEA creep test results for long run

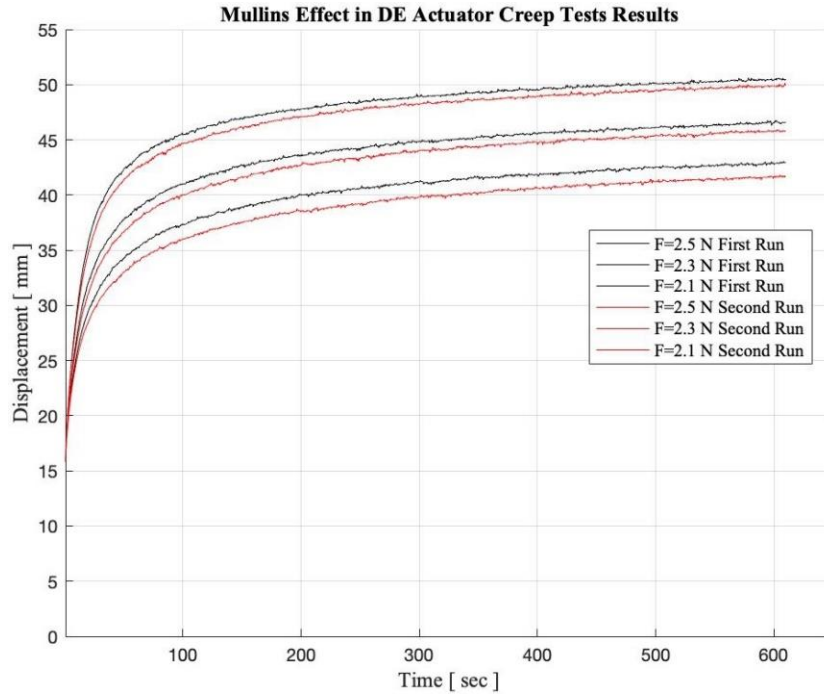


Figure 5-38 Mullins effect observed on creep test results for single layer DEA

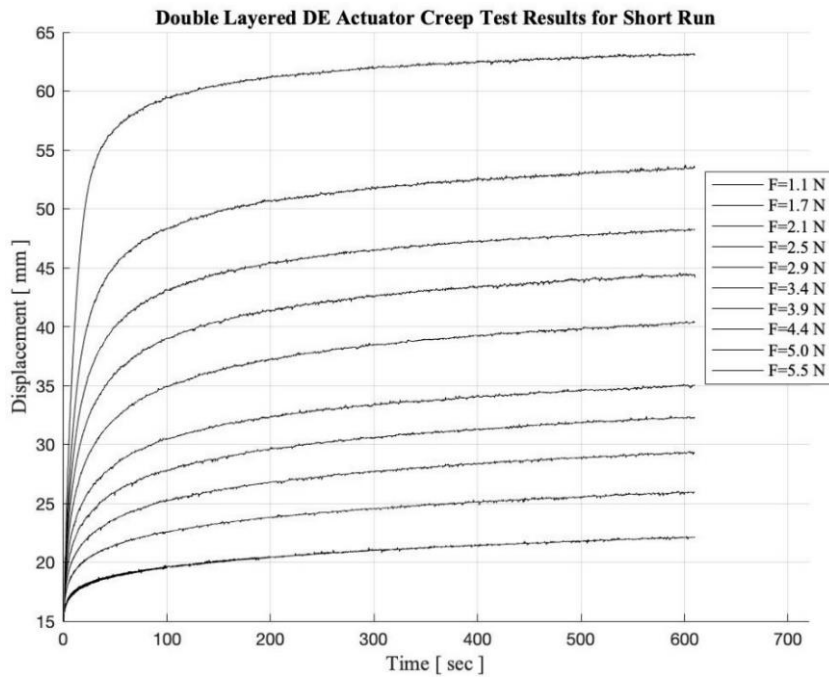


Figure 5-39 Double layer DEA creep test results for short run

### 5.9. DEA Voltage Induced Creep Tests

DEA configuration is also tested to study voltage effect. All the voltage induced tests are performed while the DEA is creeping. The tests are applied both for single layer and double layer configured actuators. First the DEA is let to creep under a certain amount of load for a pre-determined duration. The creep duration is selected as 600 seconds nominally but different durations are also considered. Applied force value is selected different for single and double layered actuators. DEA is loaded by 1.10 N creep force and the displacement outcome is recorded for 600 seconds as presented in Figure 5-40.

The applied voltage levels are presented in Figure 5-41. Reader should note that, the exact voltage value input by user is not the exact output of the high voltage amplifier. There is a minor voltage gap occurs between the input and output. As given in Figure 5-41, the given input voltage to DEA is 3.0 kV while the applied output voltage is

measured to be 2.87 kV. Throughout the study, it is calculated that there exists %4 reduction in actual applied output voltage with respect to theoretical applied input voltage.

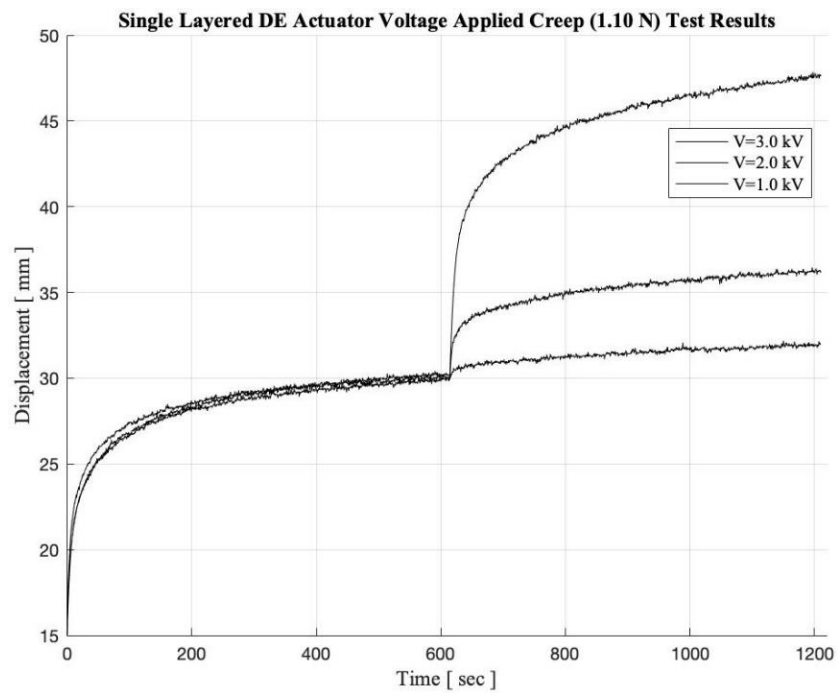


Figure 5-40 Single layer DEA voltage induced creep test results

The voltage induced tests are performed for various applied creep loads. For the same DEA, the 2 kV applied voltage creep results are presented in Figure 5-42. The displacement results for creep loads of 0.90 N, 1.10 N and 1.30 N are given. Voltage induced creep tests are also performed for double layered DEAs. The results are given Figure 5-43 and Figure 5-44.

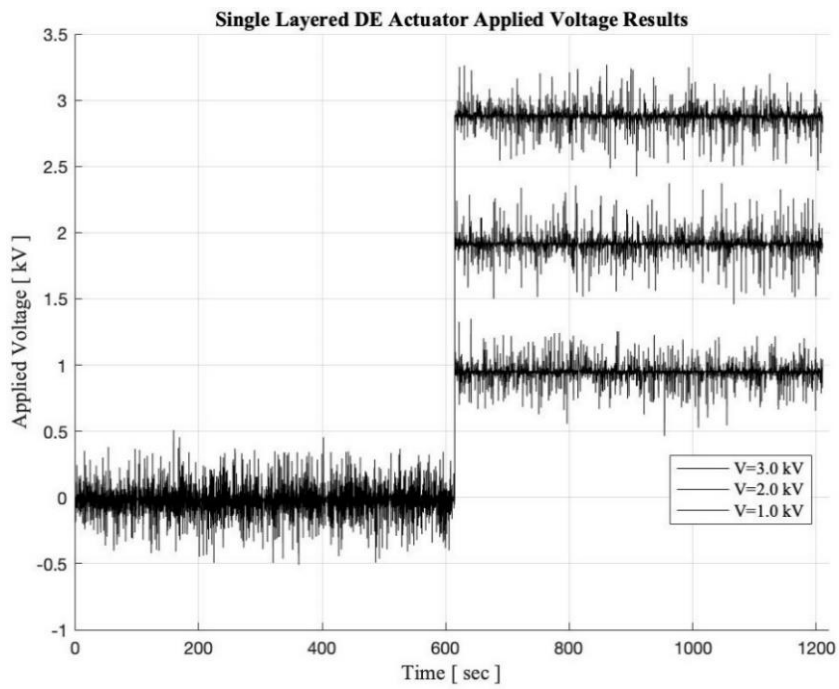


Figure 5-41 Single layer DEA applied voltage levels

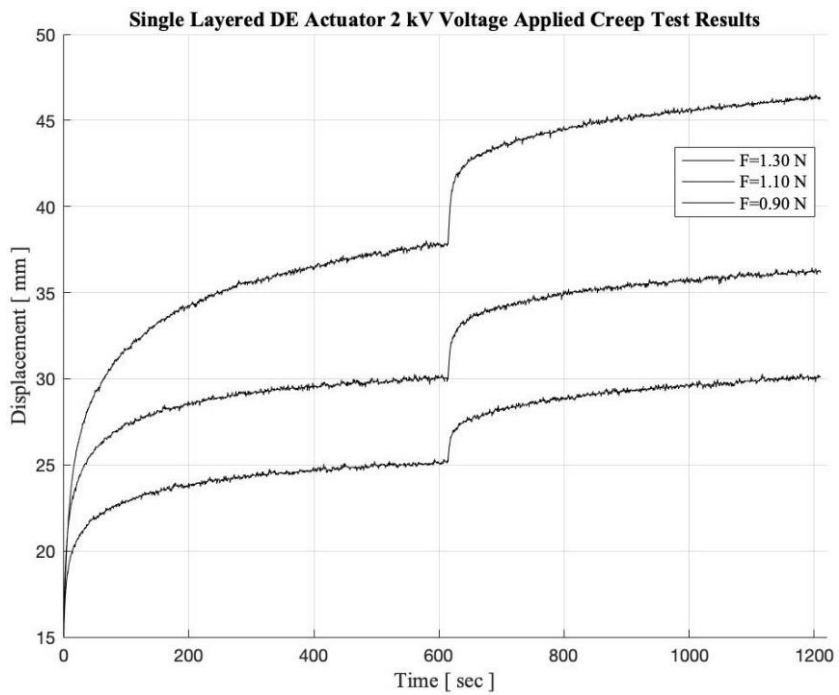


Figure 5-42 Single layer DEA 2kV applied voltage results at various creep loads

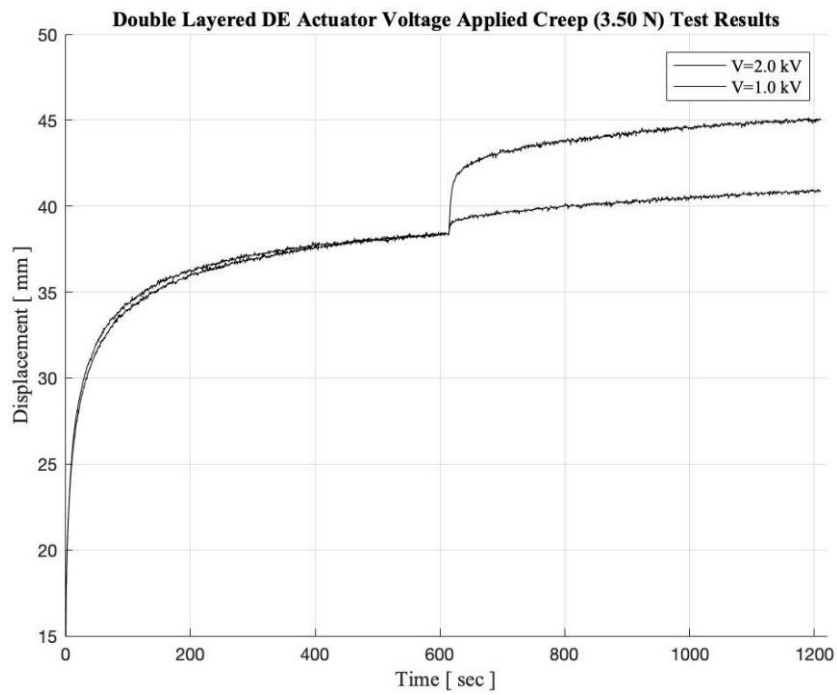


Figure 5-43 Double layer DEA voltage induced creep test results

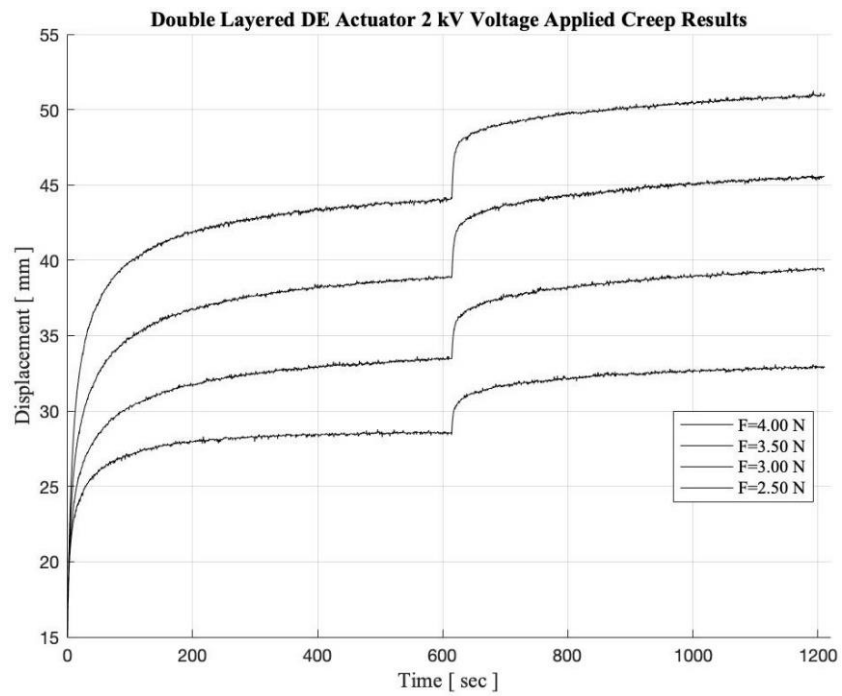
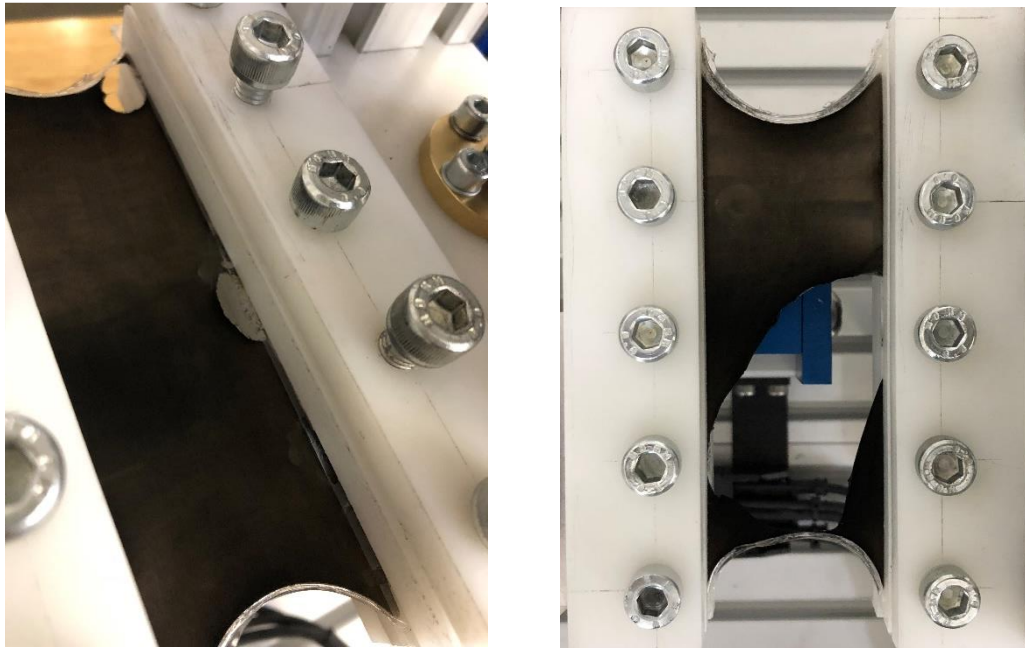


Figure 5-44 Double layer DEA 2 kV applied voltage results at various creep loads

### 5.10. Observed Failure Modes

While DEA is in actuation, various failure modes are observed. One of the fatal of them is the edge arcing which can be defined as the electrical sparks jumps occurred through upper surface to lower surface or vice versa as presented in Figure 5-45. The edge arc can be observed when DEA is high voltage activated. On the other hand, no high voltage is required. If the carbon black smeared edge is manufactured without a predetermined edge smear dimension tolerance, the sparks can jump easily. Thus, sufficient amount of place should be maintained to avoid arcing. Even with small amount of voltage is applied, edge arcing can happen. The sufficient edge tolerance shall be minimum 1.5 mm as experienced. As given in Figure 5-45 (b), the edge arc may result in total DEA loss but local burned areas may also observed as presented in Figure 5-45 (a). If this is the case, the DEA can continue to work and transfer load with reduced amount. Note that, the edge arcing may not need to happen at the edges only. When the DEA thickness is extremely decreased, the infused carbon black in elastomer tape let the sparks transmit through material itself and let burns the material. Meanwhile, the electrode locations are highly risky regions where material is thinned enough and high electric field is maintained. One example can be seen Figure 5-45 (a).

Another failure mode is observed when the DEA is set free after a long action time. This failure is not fatal. The actuator is capable to work with a minor loss of efficiency. The DE material shapes in a wavy form at the DEA support edges as illustrated in Figure 5-46. The failure vanishes as the DEA released unloaded for a sufficient time. It is observed that the time required is not less than one minute.



(a)

(b)

Figure 5-45 Edge arcing failure mode

The final mode observed in the tests is the DE crimping. The failure is occurred when the thickness of the DEA in action gets extremely thin. The failure is sketched in Figure 5-47 (a) and (b) for different test samples. This failure mode highly depends on the applied voltage. When the voltage is high, the carbon black particles are forced to aggregate to form a random wavy form. The relation between the carbon black size and voltage is not analyzed. The performance of DEA drops which may be considered a limit on applied voltage level. When the high voltage is decreased, the crimping failure diminishes and the DEA continues to work expectedly. If one tries to increase the high voltage omitting the failure, the DEA fails.



Figure 5-46 Edge waviness at DEA supports



(a)

(b)

Figure 5-47 Face crimping failure mode

## CHAPTER 6

### MATHEMATICAL MODELING OF MATERIAL AND DEA

#### 6.1. Introduction

In previous chapters, the manufacturing steps of DEA is detailed, the performed material and electromechanical tests are outlined. For the application of DEA in proposed 3D model concept, the test data obtained should be well suited to mathematical models. This may be achieved by dividing the design phase into two. The first part is the modeling solely the material itself and the second part is the modeling of DEA Maxwell stress effect on actuation strain.

Multi parameter curve fitting optimization is studied to obtain hyperelastic and viscoelastic material parameters. Hyperelastic material models namely Mooney-Rivlin, Ogden and Yeoh models are adopted and compared to each other to evaluate the best fitting strain energy function model. Linear viscoelastic response is modeled using Prony series and the related strain energy function model parameters are determined. Moreover, a more robust approach of modeling viscoelasticity that would be straight forward in real time applications are also defined.

#### 6.2. Assumptions

Throughout this parameter optimization studies and mathematical modeling of material and DEAs, the following assumptions are valid; It is assumed that the electrostatic pressure is applied by the carbon black electrodes and considered to be constant and uniform during actuation on every point of the actuator. The carbon black dust particles are uniformly distributed and no thickness variation on actuator exists. Electromechanical coupling is only occurred due to electrical forces. No mechanical

constraint exists on electrodes and they are fully compliant with the dielectric elastomer material. The elastomeric material is isotropic and incompressible. There exists no DEA thickness variation across actuation area. The applied pre-stretch withstands as designed in planar directions and remains unchanged while in actuation. The stiffeners (rigid and soft ones) that are used to increase the reliability and stiffness of the DEAs are a complete part of its mechanical behavior. The dielectric constant (relative permittivity) of the material is used as its given in related data sheet and assumed to be constant during DEA actuation. No specific dielectric constant measurement is made. Most of the DEAs are manufactured using VHB 4910 materials. DEA manufacturing trials using VHB 4905 materials are also performed but it is observed that the manufacturability of a DEA using VHB 4910 is much confident and easy with respect to VHB 4905 material. Thus, all the mathematical models are developed using VHB 4910 material test data unless otherwise specified. The geometric variations of DEA during actuation is omitted. The temperature effect is neglected and room temperature is considered for all tests. The calculated parameters are truncated after three digits where appropriate.

### **6.3. Adjusting Raw Test Data**

The recorded stress-strain or force-displacement response of DEA is in raw data form. Raw test data include the test start and end states which needs to be extracted. Data cannot be used in any parameter identification or mathematical model as is. How to adjust a data is well defined in [102, p. 75].

In general, hyperelastic material models assume zero stress start value when the strain is zero. Unfortunately, in actual test environments, it is not always the case. The measured strain or stress shall not start from the origin because of manual installation of DEA to test bench or due to test requirements (like defining an average of stress level to start a force-controlled test). The recorded strain and stress test data has to be shifted to origin to well suit to proposed mathematical models. Note that, this axial

shift changes the apparent gauge length and original cross section area. The method to shift the measured strain value to origin is detailed below and sketched in Figure 6-1.

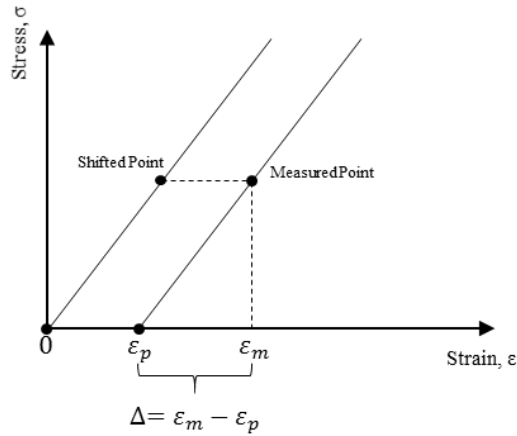


Figure 6-1 Shifting the measured strain value to origin

Let  $L$  is the original/assumed length of the test sample and  $L_0$  is the actual starting length (as installed on test bench) of test sample. The actual length,  $L_0$  is the sum of the original length,  $L$  and the divergency encountered in strain measurement which is defined in eqn. (6.3-1).

$$L_0 = L + L\varepsilon_p \quad (6.3-1)$$

Where,  $\varepsilon_p$  is defined as the divergency of initial strain value. As the test starts, the material's actual length,  $L_1$  is continuously measured by the test module. The real strain of the material,  $\varepsilon$  which is different than the measured raw strain,  $\varepsilon_m$  can be calculated using the eqn. (6.3-2).

$$\varepsilon = \frac{\Delta L'}{L'} = \frac{L_1 - L_0}{L_0} = \frac{(L + L\varepsilon_m) - (L + L\varepsilon_p)}{L + L\varepsilon_p} = \frac{\varepsilon_m - \varepsilon_p}{1 + \varepsilon_p} \quad (6.3-2)$$

Analogously, method to shift the measured stress value to origin is defined below and sketched in Figure 6-2.

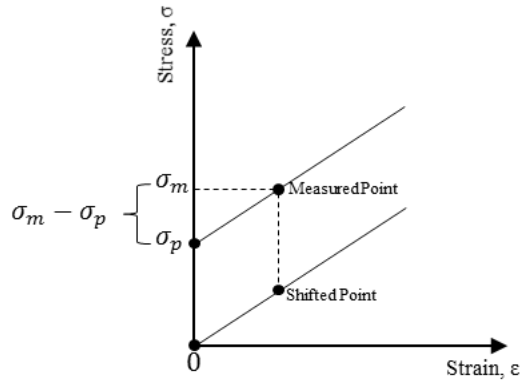


Figure 6-2 Shifting measured stress value to origin

The stress value shifting to origin is not straight forward as strain shifting. Let a volume of a material,  $V$  is constant and equal to  $V = LA$  where  $L$  is the original/assumed length and  $A$  is the original/assumed cross sectional area of the test sample. If the assumed length,  $L$  is not the installation length of the material and equals to actual length,  $L_0$ ; assuming that the volume is constant, the actual cross section area,  $A_0$  should not be equal to assumed cross section area,  $A$  and needs to be redefined as given in eqn. (6.3-3).

$$V = LA = L_0A_0 = L(1 + \epsilon_p)A_0 \quad (6.3-3)$$

Then, rewriting actual cross section area,  $A_0$  in terms of assumed cross section area,  $A$  results in,

$$A_0 = \frac{A}{1 + \epsilon_p} \quad (6.3-4)$$

According to new cross section,  $A_0$  one can calculate an updated stress value,  $\sigma_0$  which is given in eqn. (6.3-5) where  $F$  is the applied force during test and  $\sigma$  is the original/assumed stress value.

$$\sigma_0 = \frac{F}{A_0} = \frac{F}{\frac{A}{1 + \varepsilon_p}} = \sigma(1 + \varepsilon_p) \quad (6.3-5)$$

In eqn. (6.3-5), the term  $(1 + \varepsilon_p)$  can be considered as a stress reduction factor. The shifted value of the measured stress value can be calculated as given in eqn. (6.3-6),

$$\sigma = (\sigma_m - \sigma_p)(1 + \varepsilon_p) \quad (6.3-6)$$

Where,  $\sigma_m$  is the measured raw stress value and  $\sigma_p$  is the divergency in raw stress value observed in stress plots. Reader should note that both divergencies in strain,  $\varepsilon_p$  and stress,  $\sigma_p$  are the minimum values of the measured strain,  $\varepsilon_m$  and stress,  $\sigma_m$ .

On the other hand, there are irregularities and unexpected data measurement points in raw test data. Due to rapture of test samples, instant stress and/or force value decreases are observed. These instant stress and/or force decrease points are removed to fit to theoretical model with low error values.

When test data is recorded, due to sampling frequency, different level of noise are available on data. In material characterization tests, even if the sampling frequency is selected to be the same, not exactly the same number of data points are collected from the tests. For an example, in %100 strain uniaxial testing, a test sample has recorded by 120 data points while the other sample has recorded 130 data points. For optimization purposes, the number of data array of each sample is set to be same with proper truncation. When required, minimum number of data points for a bunch of test is determined and all sample data points are adjusted accordingly.

## 6.4. Curve Fitting Procedure

Non-linear least squares curve fitting methods are applied to fit theoretical models to experimental data. All test data is adjusted to be used in curve fitting. Matlab's *lsqcurvefit* function with Levenberg-Marquardt algorithm, *fminsearch* function with Nelder-Mead minimization method [103] and curve fitting tool box are used to solve the least square error functions where appropriate. The flow chart of curve fitting procedure is sketched in Figure 6-3.

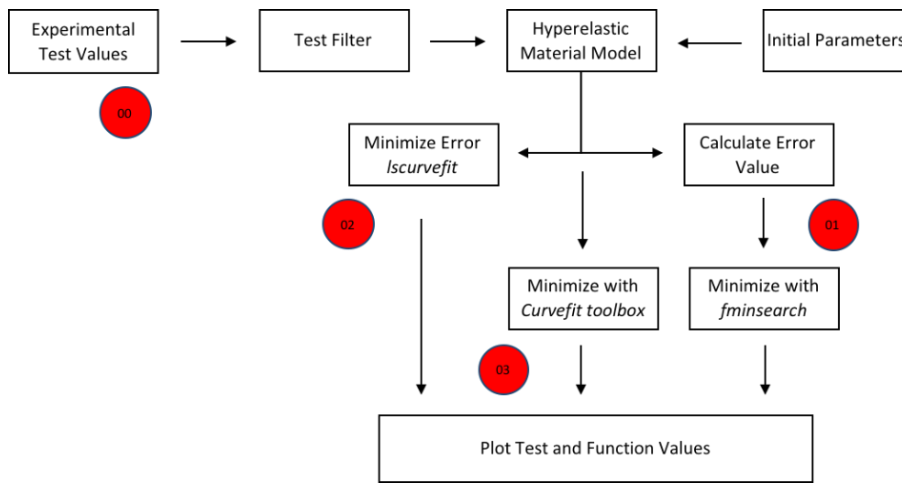


Figure 6-3 Curve fitting procedure

The objective function of the non-linear least squares model is given in eqn. (6.4-1).

$$\min E: \sum_{i=1}^n w_q \left( \sum_{j=1}^m ((f_q)_i - (\sigma_q)_i)^2 \right) \quad (6.4-1)$$

Where,  $w_q$  is identifies the weighting function related to different experiments. If there is no experiment data to weigh then  $w_q$  has to be set to unity. On the other hand, if a specific type of experiment needs to be emphasized,  $w_q$  can be set larger with respect

to others.  $m$  represents the number of the experiment data for each type of experiment.  $(f_q)_i$  is the theoretical value which is to be calculated by hyperelastic equations and  $(\sigma_q)_i$  is the value obtained from experiments. For multi purpose optimizations which will be required to find coefficients of models (if more than one test type is used to optimized at the same time) the eqn. (6.4-2) can be used.

$$\begin{aligned} \min E : e_T + e_P + e_B \\ \min E : \sum_{i=1}^{n_T} \left( (f_q)_i - (\sigma_q)_i \right)^2 \\ + \sum_{j=1}^{n_P} \left( (f_q)_j - (\sigma_q)_j \right)^2 + \sum_{k=1}^{n_B} \left( (f_q)_k - (\sigma_q)_k \right)^2 \end{aligned} \quad (6.4-2)$$

Where,  $e_T$ ,  $e_P$  and  $e_B$  denote the error functions related to different optimization sub routines. The error functions are taken as the squared difference between experimental and theoretical values of stress.  $E$  is defined as the global error function.  $n_T$ ,  $n_P$  and  $n_B$  are defined as the number of experimental points considered. The solution is considered optimum when its global error is small.

## 6.5. Material Modeling

The uniaxial tensile, volumetric compression and quad lap shear test are performed to model material itself and justify some of the assumed material mechanics. The performed tests results are presented in Chapter 4. The raw test data is adjusted as to use in modeling purposes. Mooney-Rivlin, Yeoh and Ogden strain energy function models are theoretically presented in Chapter 3.4 and used to fit to test results. The best fitting model is advised. All material tests are performed for VHB 4905 and VHB 4910 materials. However, as VHB 4910 material is selected to use in DEA manufacturing due to its ease of handling, the material modeling is performed

considering VHB 4910 material results. VHB 4905 material modeling is not performed and assumed that it will show similar mechanical behavior with VHB 4910.

### **6.5.1. Uniaxial Tension Modeling**

Uniaxial test data is presented in Chapter 4.2.1. Tests are made at various strain levels and three samples are used at each level. Each test resulted in similar mechanical behavior. Modeling is not performed for each tested strain level. Matlab m file scripts are created for curve fitting purposes and the %100 strain response of the material is considered.

All test data are collected as engineering stress vs engineering strain. The raw test data are adjusted. Three hyperelastic material models which are Mooney-Rivlin, Yeoh and Ogden are considered. These models are a function of stretch ratios so the engineering strain values of raw test data are converted accordingly.

While optimizing the hyperelastic material parameters for uniaxial tensile tests, eqn. (3.4-19) is used for Mooney – Rivlin energy function, eqn. (3.4-30) is used for Ogden Strain energy function and eqn. (3.4-47) is used for Yeoh Strain energy function. Though the numerical optimization algorithms search for local minimum, initial start point values are provided for the optimization routines. Each unique initial start point value resulted in different hyperelastic coefficients. Due that, the optimization routine is adjusted to search the minimum error value by trying various initial start points to conclude on confident parameter sets.

Three samples are used to perform %0 to %100 strain uniaxial tension tests. For each sample, the uniaxial test is performed three times. In the first cycle, the sample is subjected to tension load up to %100 strain and let to recover its original position by moving the gauge to its start point. The sample is let to relax for 5 minutes. In the second cycle, the sample is subjected to tension load up to %100 strain again and let to relax for another 5 minutes. The test is reperformed for the third and last time using

the same procedure. The recorded test data obtained in the last cycle is used for parameter optimization. The optimization is let to run for all three samples strain history records. The algorithm searched to find the best fit that minimizes the error function considering all three test results.

Both `fminsearch` and `lscurvefit` function routines are used and best fit is presented. The objective function used to minimize the error is given in eqn. (6.5-1).

$$\begin{aligned} \min E: \sum & \left( (f_q)_1 - (\sigma_q)_1 \right)^2 + \left( (f_q)_2 - (\sigma_q)_2 \right)^2 \\ & + \left( (f_q)_3 - (\sigma_q)_3 \right)^2 \end{aligned} \quad (6.5-1)$$

Where,  $E$  is the total error to be minimized,  $(f_q)_i$  is the theoretical hyperelastic stress equation value to be calculated and  $(\sigma_q)_i$  is the value obtained from experiments. Curve fitting results (using `fminsearch` algorithm) of the hyperelastic material models are presented in Figure 6-4 to Figure 6-7. While curve fitting, the initial start point is not pre-introduced to search algorithm, a user defined interval [-5,5] for each parameter is set and Matlab is let to evaluate the best initial starting point of each parameter that minimizes the overall fit error. On the other hand, the uniaxial tension tests were not limited to %100 strain level. Longer stretch values were tried in the test campaign. According to the test results presented in Figure 4-5 (b), the material was let to strain up to break point for cyclic straining case. When all the results are evaluated, it is seen that approximately %1300 strain is obtained without breaking for each sample. The material model fitting is also applied for the most stretching test campaign also. The optimized parameter sets of the material models for both %100 strain and %1300 strain levels are tabulated in Table 6-1. The results of curve fitting to test results are given in Figure 6-7. Matlab simulations to find the best initial start point run more than a hour.

Based on parameter optimization results for %100 uniaxial tension strain level, Ogden strain energy function model fits well to the test curves better than Yeoh model. Unfortunately, Mooney-Rivlin model did not fit well to test results. The same curve fitting methodology can be adapted for other strain levels.

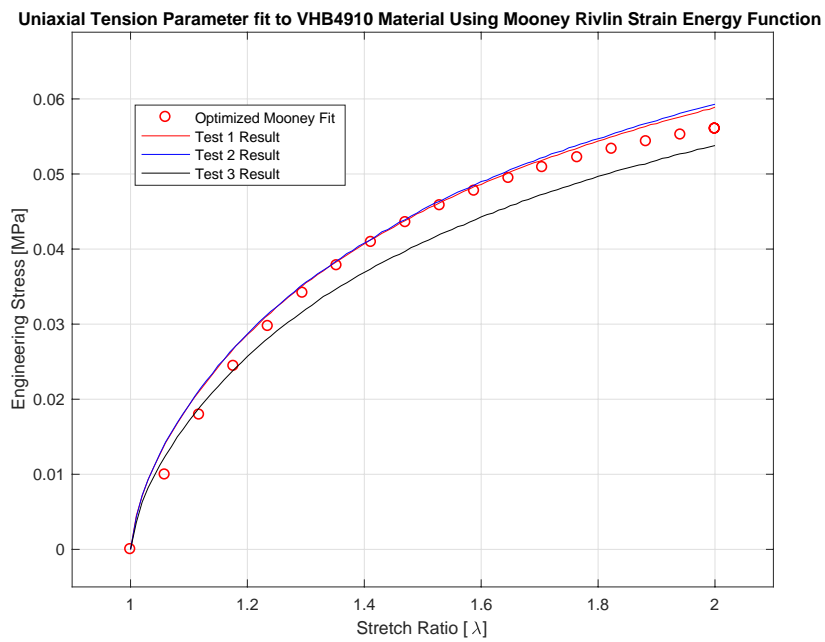


Figure 6-4 Mooney-Rivlin model fit w.r.t. three uniaxial test at %100 strain

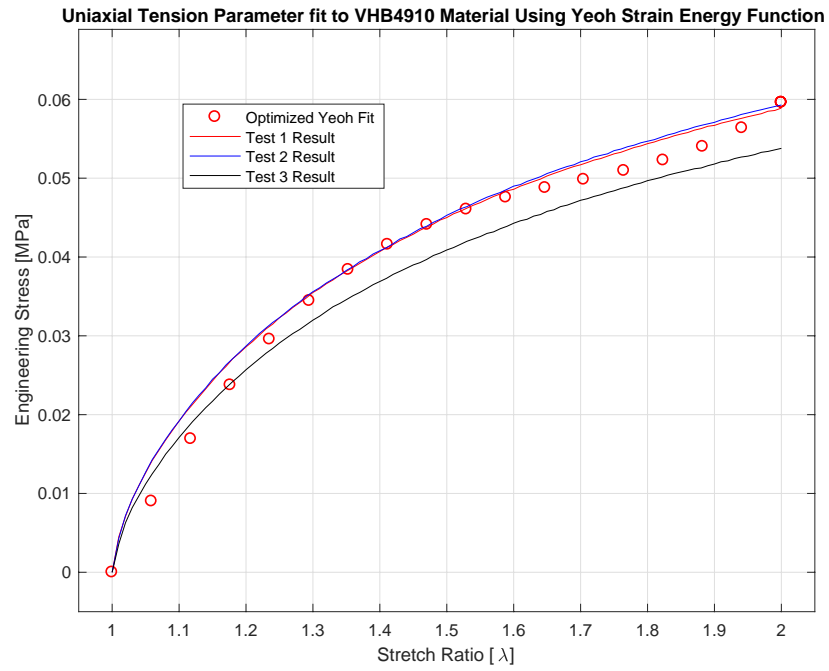


Figure 6-5 Yeoh model fit w.r.t. three uniaxial test at %100 strain

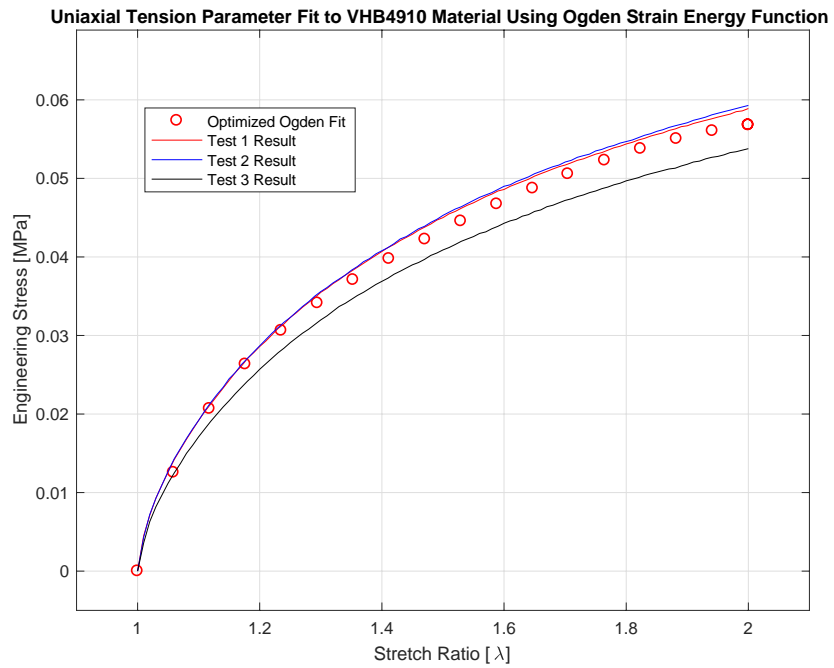


Figure 6-6 Ogden model fit w.r.t. three uniaxial test at %100 strain

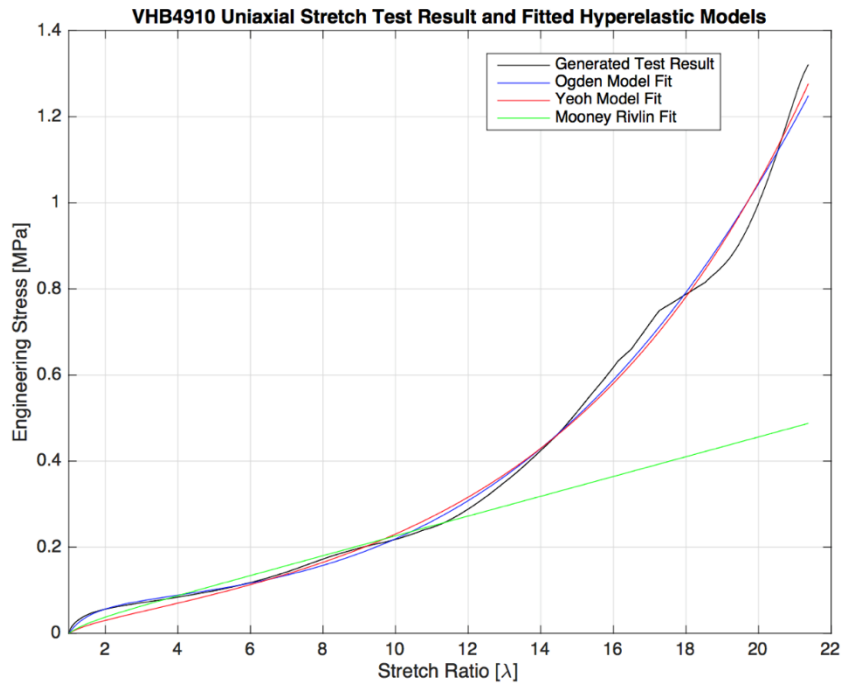


Figure 6-7 Curve fitting results of hyperelastic material models to %1300 strain

Table 6-1 Optimized hyperelastic material model parameters at %100 and %1300 strain levels for uniaxial test

Strain Energy Function Model	Parameter	%100 Strain Value	%1300 Strain Value
Mooney-Rivlin model	$C_{10}$ [MPa]	$4.678 \cdot 10^{-4}$	$131.769 \cdot 10^{-4}$
	$C_{01}$ [MPa]	$310.760 \cdot 10^{-4}$	$-83.556 \cdot 10^{-4}$
	$ R^2 $	$16.584 \cdot 10^{-4}$	0.816
	Initial Start Point	[-1, 5]	[4, 2]
Ogden model	$\mu_1$ [MPa]	$-135.699 \cdot 10^{-4}$	$-777.808 \cdot 10^{-4}$
	$\alpha_1$	4.408	-0.986
	$\mu_2$ [MPa]	$-333.696 \cdot 10^{-4}$	$-60.298 \cdot 10^{-4}$
	$\alpha_2$	-7.160	-5.123
	$ R^2 $	$11.820 \cdot 10^{-4}$	0.223
Yeoh model	Initial Start Point	[0, -2, 0, -4]	[0, -1, 0, -2]
	$C_{10}$ [MPa]	$271.249 \cdot 10^{-4}$	$106.018 \cdot 10^{-4}$
	$C_{20}$ [MPa]	$-59.105 \cdot 10^{-4}$	$0.064 \cdot 10^{-4}$
	$C_{30}$ [MPa]	$11.290 \cdot 10^{-4}$	$0.001 \cdot 10^{-4}$
	$ R^2 $	$20.896 \cdot 10^{-4}$	0.408
	Initial Start Point	[5, 2, -2]	[-3, 1, 2]

### 6.5.2. Quad Lap Shear Modeling

Quad lap shear test is kind of simple shear test that is intended to be observed on each side of the test apparatus. During simple shear tests, the amount of shear,  $k$  was calculated from the measured displacement of the specimen in the transverse direction and the original thickness of the specimen. The force applied on the end clamps are divided into two to encounter the force applied on a single tension line. Also, the measured deformation involves the upper and lower parts of the test setup which should be halve before considering the results in analysis. The shear stress is evaluated as  $F/A$ , where  $F$  is the measured shear force by the load cell and  $A$  is the area of the cross section of stucked part of the material. Note that in simple shear, it is assumed that the shear area remains unchanged. The experimentally measured shear stress is compared to the predictions of the hyperelastic model and the material parameters are adjusted to provide good parameter fits. Matlab's `fminsearch` algorithm is used in the same methodology as performed in uniaxial tension test. The initial start points are again not predefined. The interval of initial start points is provided to solver and the best initial start point is determined by optimization.

The quad lap shear tests were performed up to the pre-determined shear deformation. Following the completion of tests, the samples are let to shear up to breakdown point for capability study. The deformations which are larger than materials original thickness is not considered in modeling. The reason of that is the shear plane loses its efficiency and deformation states start to violate material behavior [104], [105]. For VHB 4910 materials, the shear deformation up to 1 mm is considered (as the material thickness is 1.0 mm) and for VHB 4905 materials, the shear deformations up to 0.5 mm is considered (as the material thickness is 0.5 mm). The results of VHB 4910 are presented to be in consensus with the rest of the study.

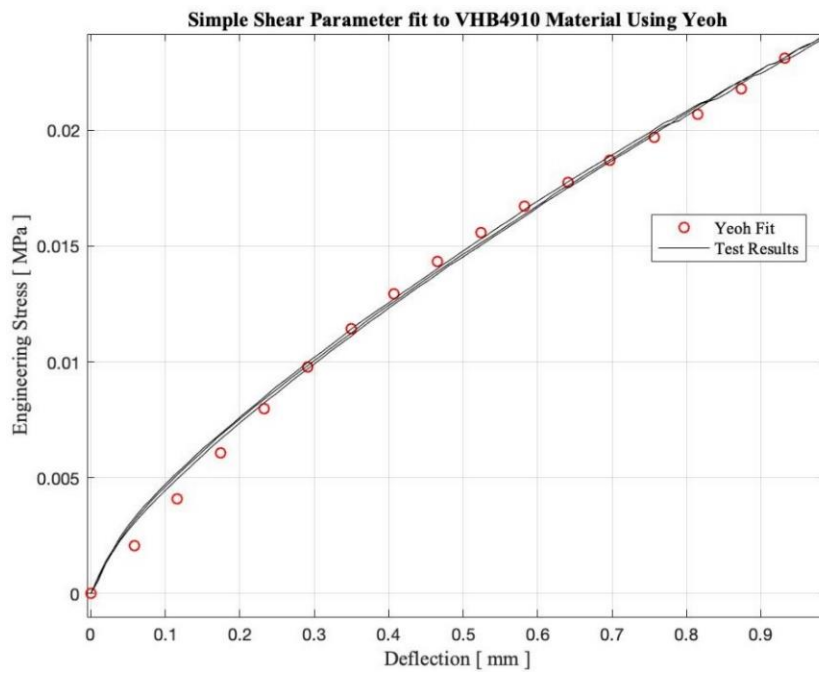


Figure 6-8 Curve fitting of Yeoh model to k=1 mm shear deformation

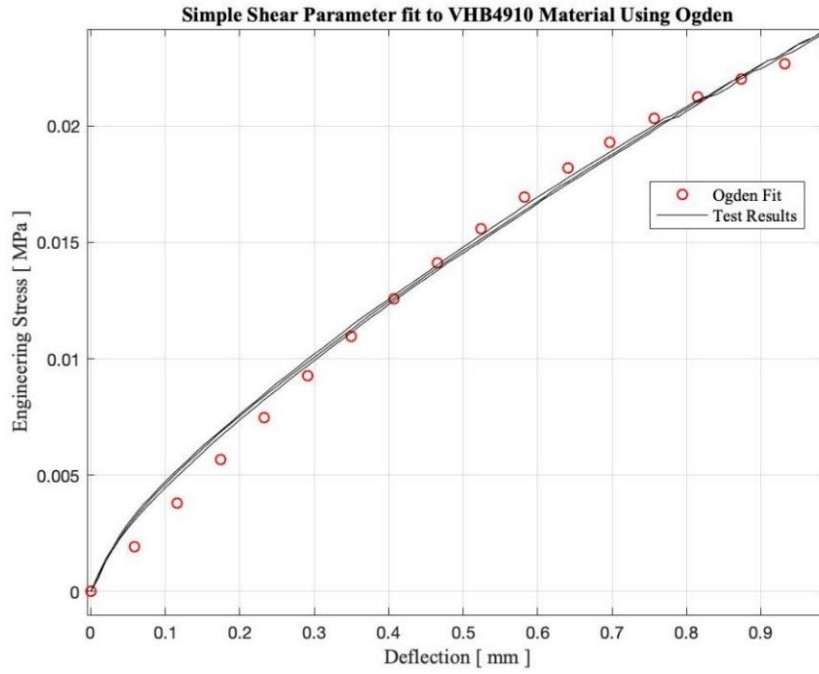


Figure 6-9 Curve fitting of Ogden model to k=1 mm shear deformation

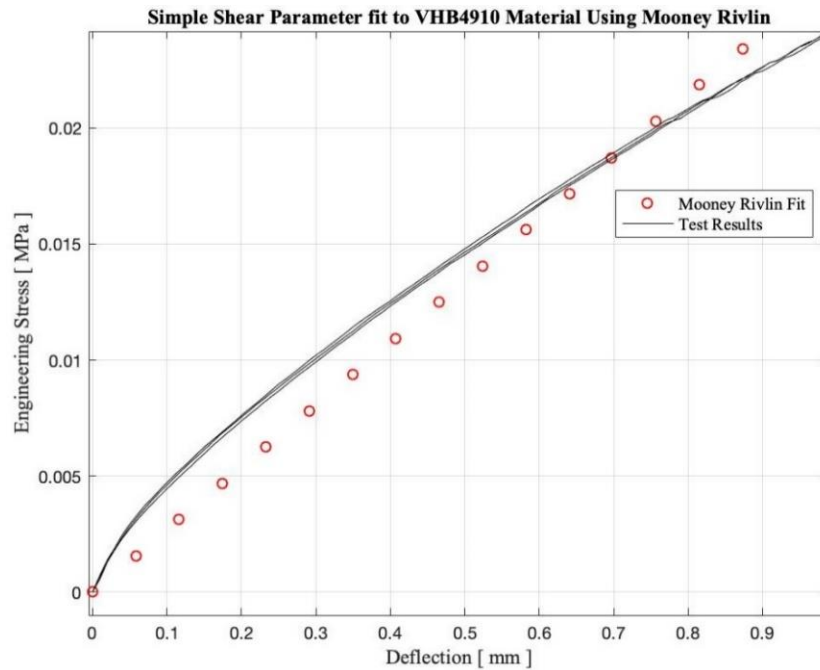


Figure 6-10 Curve fitting of Mooney-Rivlin model to  $k=1$  mm shear deformation

The curve fitting algorithm calculated the hyperelastic material coefficients as tabulated in Table 6-2 and the results are plotted in Figure 6-8 to Figure 6-10 for each strain energy model. The shear stress component of the strain energy functions as given in eqn. (3.4-20) for Mooney-Rivlin, eqn. (3.4-32) for Ogden and eqn. (3.4-49) for Yeoh are considered throughout the optimization process. The calculated shear moduli of the VHB 4910 material are determined using the same functions and the optimized coefficients assuming  $k = 1$  and are provided in Table 6-3. All models resulted in similar shear behavior and values are close to each other.

Table 6-2 Optimized hyperelastic material model parameters using Quad-Lap shear test

Strain Energy Function Model	Parameter	Value
Mooney-Rivlin model	$C_{10}$ [MPa]	1.39224
	$C_{01}$ [MPa]	-1.37884
	$ R^2 $	$6.93230 \cdot 10^{-4}$
	Initial Start Point	[1, 1]
Ogden model	$\mu_1$ [MPa]	5.766
	$\alpha_1$	$-141.185 \cdot 10^{-4}$
	$\mu_2$ [MPa]	-5.733
	$\alpha_2$	$1599.915 \cdot 10^{-4}$
	$ R^2 $	$1.388 \cdot 10^{-4}$
	Initial Start Point	[-5, -5, -5, -1]
Yeoh model	$C_{10}$ [MPa]	$177.541 \cdot 10^{-4}$
	$C_{20}$ [MPa]	$-62.330 \cdot 10^{-4}$
	$C_{30}$ [MPa]	$24.191 \cdot 10^{-4}$
	$ R^2 $	$0.7307 \cdot 10^{-4}$
	Initial Start Point	[3, 1, -2]

Table 6-3 Estimated shear modulus of VHB 4910 material

Shear Stress	Mooney-Rivlin model	Yeoh model	Ogden model
$\sigma_{12}$ [MPa]	0.0268	0.0251	0.0235

### 6.5.3. Volumetric Compression Modeling

The quasi-volumetric compression test results of both VHB 4905 and VHB 4910 are given in Section 4.2.2 in raw test output format. The test data were in force [N] versus displacement [mm] and involves high plunger effects that are encountered at the beginning of the test. The plunger effect is eliminated by data adjusting and the variables are converted to stress [MPa] and volume ratio, J [-]. The volumetric equations of the strain energy functions which are given in eqns. (3.4-22), (3.4-50) are used in curve fitting procedure. Matlab's fminsearch algorithm (also lscurvefit algorithm) is performed. The optimization results obtained from fminsearch are presented. To run the optimization procedure, user defined initial start point interval is introduced and the algorithm constructed concluded the best initial start point itself.

For calculating the bulk modulus,  $K$  of the material, literature offers different approaches. The calculation of bulk modulus using uniaxial tension test for various strain energy functions are available [10], [104]. The bulk modulus,  $K$  can be calculated using eqn. (6.5-2) in case where volumetric compression is performed.

$$K = \frac{2}{D_1} \quad (6.5-2)$$

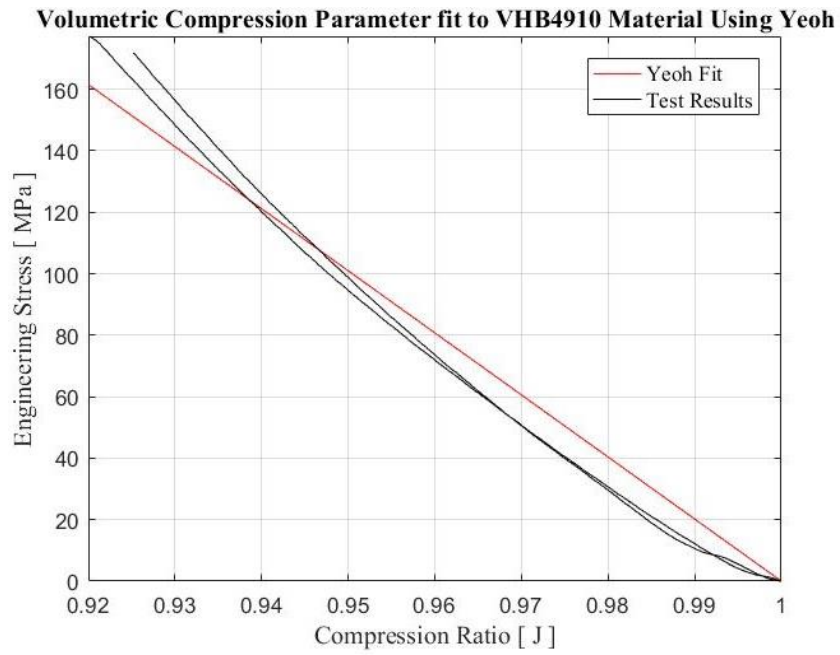


Figure 6-11 Curve fitting of Yeoh model compression deformation

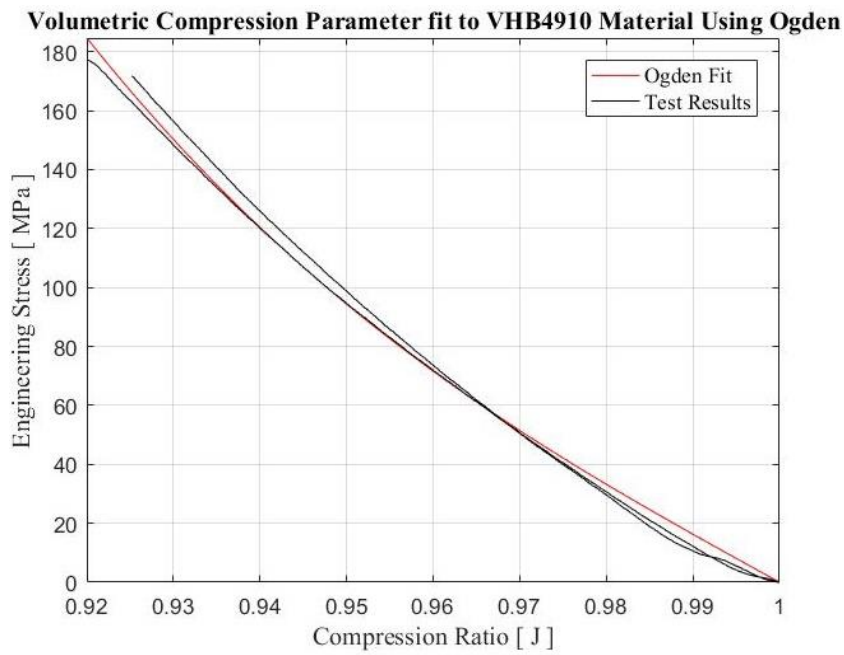


Figure 6-12 Curve fitting of Ogden model compression deformation

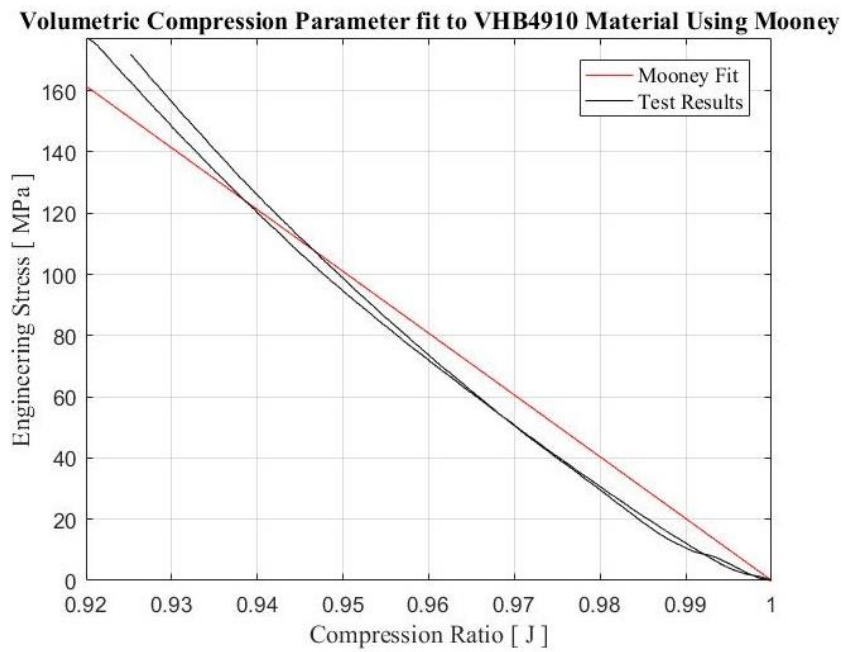


Figure 6-13 Curve fitting of Mooney-Rivlin model compression deformation

Table 6-4 Optimized hyperelastic material model parameters for compression test

Strain Energy Function Model	Parameter	Value
Mooney-Rivlin model	$D_1$ [1/MPa]	0.00099
	$ R^2 $	6.96
	Initial Start Point	[1.7]
Ogden model	$D_1$ [1/MPa]	0.0123
	$D_2$ [1/MPa]	0.0003
	$ R^2 $	9.06
	Initial Start Point	[0.8, 1.9]
Yeoh model	$D_1$ [1/MPa]	0.0123
	$D_2$ [1/MPa]	0.0003
	$D_3$ [1/MPa]	-30.527
	$ R^2 $	9.01
	Initial Start Point	[1, 0, -1]

The estimated deviatoric hyperelastic material parameters,  $D_i$ 's are tabulated in and the results are presented in Figure 6-11 to Figure 6-13. Using the calculated  $D_i$ 's, estimated bulk modules are given in Table 6-8. On the other hand, the bulk modulus can also be estimated without any parameter optimization by calculating the initial slope of the stress-deflection curve of the related test. By doing so, the estimated bulk modulus is about 1600 MPa. Mooney-Rivlin model performs the closest estimate to test evaluated bulk modulus.

Table 6-5 Estimated bulk modulus of VHB 4910 material

Bulk Modulus	Mooney-Rivlin model	Yeoh model	Ogden model
$K$ [MPa]	2020.20	162.60	162.60

The Poisson ratio,  $\nu$  of the material can be calculated using the estimated bulk modules and the calculated shear modules which are provided in Table 6-3 using eqn. (6.5-3). The calculated Poisson ratio related to each strain energy potential is given in Table 6-6. It is convenient to conclude that the material incompressibility assumption is valid

$$\nu = \frac{3K - 2G}{6K + 2G} \quad (6.5-3)$$

Table 6-6 Estimated Poisson ratio

Poisson Ratio	Mooney-Rivlin model	Yeoh model	Ogden model
$\nu$	0.499	0.499	0.499

#### 6.5.4. Relaxation and Creep Modeling

Relaxation and creep test were performed using DMA test machine and the results were presented in Section 4.2.4. For both tests, due to test machine capabilities, not a uniform sampling frequency was encountered. The tests were started at  $t = 0$  but the initial data record time were actualized at around  $t = 16$  seconds. Thus, the stress values at  $t = 0$  cannot be captured. But, sufficient data are collected to model both relaxation and creep responses. These experiments can be used to fit to determine the Prony series function coefficients. Although, There are numerius methods for determining these coefficients from relaxation and/or creep data [95], the best method to analyze the material behavior was defined in Section 3.5. Many nonlinear viscoelastic models have been formulated in literature, but Fungs's theory of quasi-linear viscoelasticity (QLV) is probably the most widely used one due to its relative simplicity [106]. A material is quasi-linear viscoelastic when the relaxation function  $E_r(t)$  is independent of imposed elongation in the relaxation test. The material creep and relaxation tests were performed using a predetermined speed. It is known from literature that the stiffness of a soft material increases with the loading velocity [106]. The model fitting result are given according to the defined strain rate and quasi-linear viscoelasticity assumption holds. Different strain rates may be tried and non-linear viscoelastic modelling may be considered.

For both creep and relaxation tests, related force,  $F$  [N], time,  $t$  [sec] and displacement,  $l$  [mm] data were recorded. These values are converted to engineering

stress,  $\sigma$  [MPa] when appropriate. The raw test data is adjusted for modelling purposes and VHB 4910 material results are selected to be presented throughout the study.

In a relaxation test, the engineering stress can be defined as  $\sigma(t) = E(t)\varepsilon$  where  $E(t)$  is the time dependent elastic modulus. The engineering stress,  $\sigma(t)$  recorded in the test can be stated as used in eqn. ). The reason of using the eqn. ) is the lack of initial  $\sigma(t) = \sigma_0$  value. On the other hand, the  $\sigma(t) = \sigma_\infty$  is a known parameter. The parameters  $\sigma_\infty, \sigma_i$  and  $\tau_i$  values shall be determined by means of curve fit. Matlab's lscurvefit function is used in parameter optimization. Levenberg-Marquardt method is applied and presented the best results. In the relaxation tests of the material three strain levels, namely %25, %50 and %100 were tested. Note that the sample used in the tests were 5 mm in length dimension (so as the testing dimension) and %100 straining will result in 10 mm final sample length. For each test, the initial start points assigned to all variables for the optimization algorithm is selected to be zero. The number of Maxwell elements,  $N$  should be determined based on the duration of the test. The value of  $N$  is selected as less than or equal to  $\log\left(\frac{t_{max}}{t_{min}}\right)$  [96] which indicates  $N = 3$  in this test campaign. Test fit results are given in Figure 6-14 and the resulting parameter set is given in Table 6-7.

Table 6-7 Optimized parameter sets from material relaxation tests

Parameter	%25 Strain	%50 Strain	%100 Strain
$\sigma_\infty$ [MPa]	175.56 $10^{-4}$	261.06 $10^{-4}$	175.56 $10^{-4}$
$\sigma_1$ [MPa]	88.81 $10^{-4}$	84.87 $10^{-4}$	88.81 $10^{-4}$
$\tau_1$ [sec]	31.57	185.79	31.57
$\sigma_2$ [MPa]	46.82 $10^{-4}$	67.38 $10^{-4}$	46.82 $10^{-4}$
$\tau_2$ [sec]	192.172	1335.45	192.17
$\sigma_3$ [MPa]	32.21 $10^{-4}$	208.50 $10^{-4}$	32.21 $10^{-4}$
$\tau_3$ [sec]	1327.81	32.09	1327.81

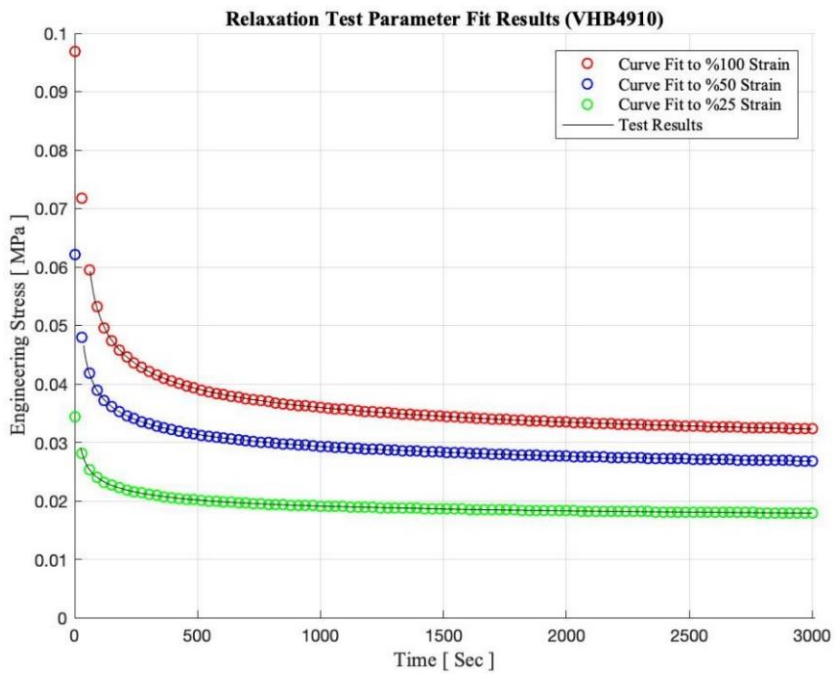


Figure 6-14 Material relaxation results with applied curve fitting

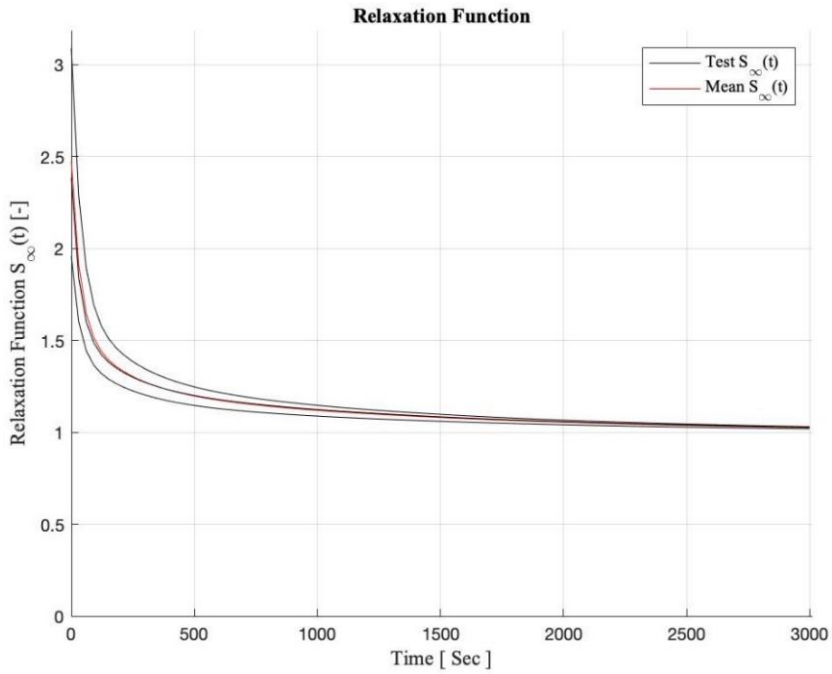


Figure 6-15 Material relaxation functions,  $S_{\infty}(t)$

For a linear material model, the relaxation functions,  $S_{\infty}(t)$  should be independent of the applied strain which are plot in Figure 6-15. This can be validated using the equation given in eqn. (3.5-19) which is in normalized basis. The relaxation function  $S_{i,\infty}(t)$  for each test which are in good consensus and the mean relaxation function,  $S_{\infty}(t)$  are given in Figure 6-15. The mean relaxation function,  $S_{\infty}(t)$  can be used to determine the Prony series coefficients by parameter comparison based on the mathematical equality given in eqn. (3.5-20). The fit results are given in Figure 6-16.

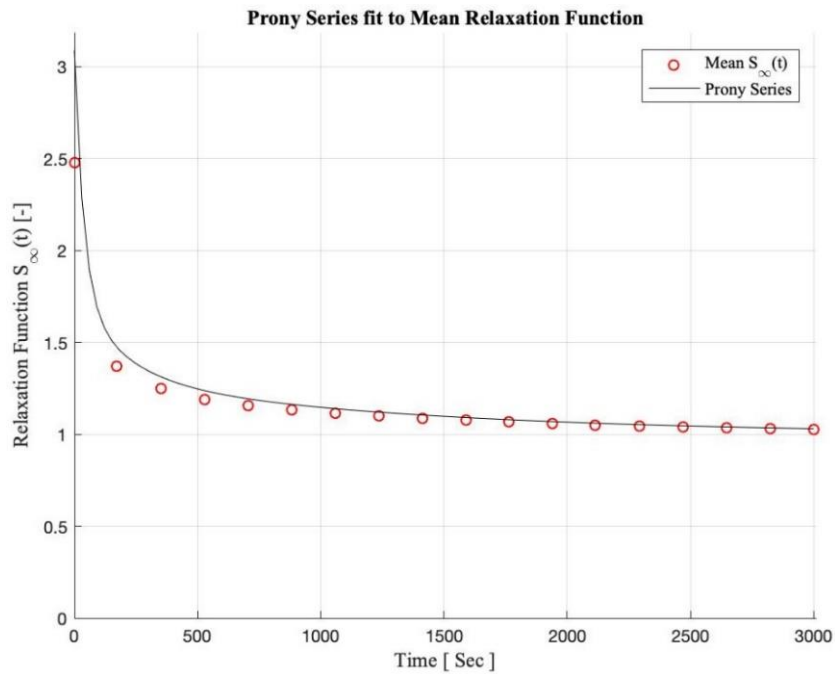


Figure 6-16 Prony series fit to mean relaxation function,  $S_{\infty}(t)$

The Prony series function is a dimensionless relaxation modulus that is defined in eqn. (3.5-14). The Prony series function shall start from 1 and vanish at the infinity while the plot given in Figure 6-16 does not. The reason of that is the Prony series are fitted according to coefficient comparison. The actual Prony series result with appropriate mapping to eqn. (3.5-14) is provided in Figure 6-17.

The Prony series fit function parameters are given in Table 6-8. Substituting eqn. (3.5-14) into eqn. (3.5-13), is the time dependent elastic modulus,  $E(t)$  can be calculated accordingly.

Table 6-8 Optimized parameters of Prony series fit function

Parameter	$g_1[-]$	$\tau_1[\text{sec}]$	$g_2[-]$	$\tau_2[\text{sec}]$	$g_3[-]$	$\tau_3[\text{sec}]$
Value	0.35	34.61	0.10	1309.41	0.14	189.39

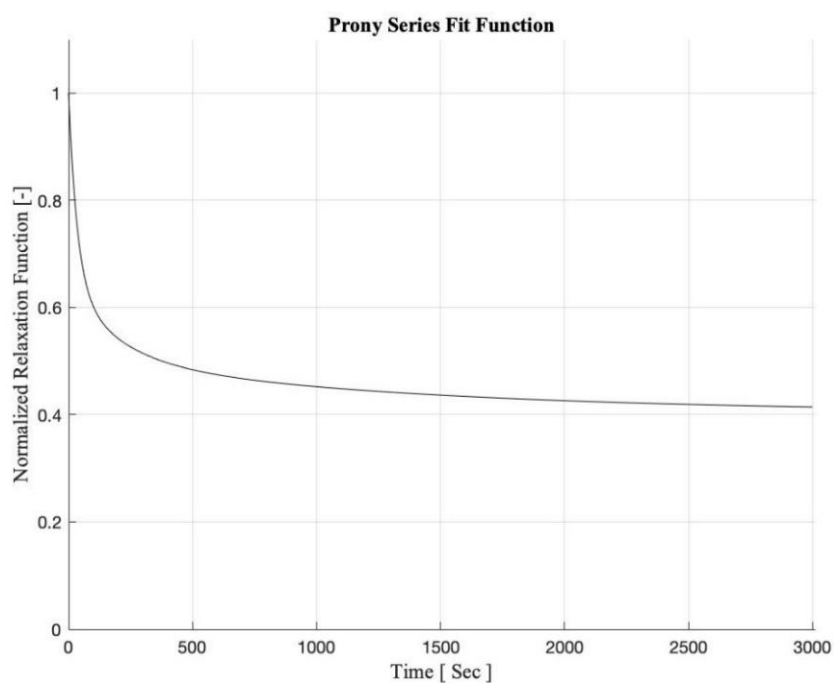


Figure 6-17 Prony series fit function for material relaxation test

The stress relaxation of the VHB 4910 tape according to the applied constant strains can be also verified using strain energy functions. Strain energy functions are given in eqn. (3.4-47) for Yeoh, eqn. (3.4-30) for Ogden and eqn. (3.4-19) for Mooney-Rivlin for the calculation of uniaxial tensile stress. The dimensionless relaxations modulus,

$g_r(t)$  can be applied on the hyperelastic material coefficients which indicates that they can be described with the so called Prony series [45], [107].

The material parameters,  $C_{ij}^R$  for Polynomial and Yeoh strain energy potential models can be written as given in eqn. ) as a time function.

$$C_{ij}^R(t) = C_{ij}^0 \cdot \left( 1 - \sum_{i=1}^N g_i (1 - e^{-(t/\tau_i)}) \right) = C_{ij}^0 f(t) \quad (6.5-4)$$

Where,  $C_{ij}^0$  is the instantaneous elastic response,  $g_i$  and  $\tau_i$  characterizes the relaxation behavior, determined from uniaxial test and  $f(t)$  is the relaxation function. At  $t = 0$ ,  $C_{ij}^0$  will be equal to  $C_{10}$ ,  $C_{20}$  and  $C_{30}$ . For Ogden model material parameters can be defined as given in eqn. ).

$$\mu_i^R(t) = \mu_i^0 \cdot \left( 1 - \sum_{i=1}^N g_i (1 - e^{-(t/\tau_{ri})}) \right) = \mu_i^0 f(t) \quad (6.5-5)$$

The hyperelastic model coefficients needs to be solved using the eqn. (3.5-16) at  $t = 0$  and nominal engineering stresses,  $\sigma_0$  shall be determined for different stretch ratios. Unfortunately, not enough test results are obtained to deduce experimental stress vs stretch ratio curve in this study. So, it is not possible to construct the initial stress,  $\sigma_0$  and stretch ratio plot and curve fit for hyperelastic model coefficients. On the other hand, the Prony series coefficients are already solved and provided in Table 6-8 and the initial hyperelastic model coefficients ( $C_{ij}^0$  and  $\mu_i^0$ ) shall be obtained optimizing for the whole available test results using eqns. ) and ). Matlab's fminsearch algorithm is used with variable initial start points.

In Figure 6-18 and Figure 6-19, the goodness of fit for each of the optimized strain energy function using the Prony series values tabulated in Table 6-8. The Mooney-Rivlin strain energy function did not fit well to relaxation test results and it is not presented. summarizes the initial coefficients that are best fit to experimental results

using the strain energy functions. It should be noted that hyperelastic material coefficients are evaluated using the available relaxation function results. This method can be used in case if there is insufficient test data available.

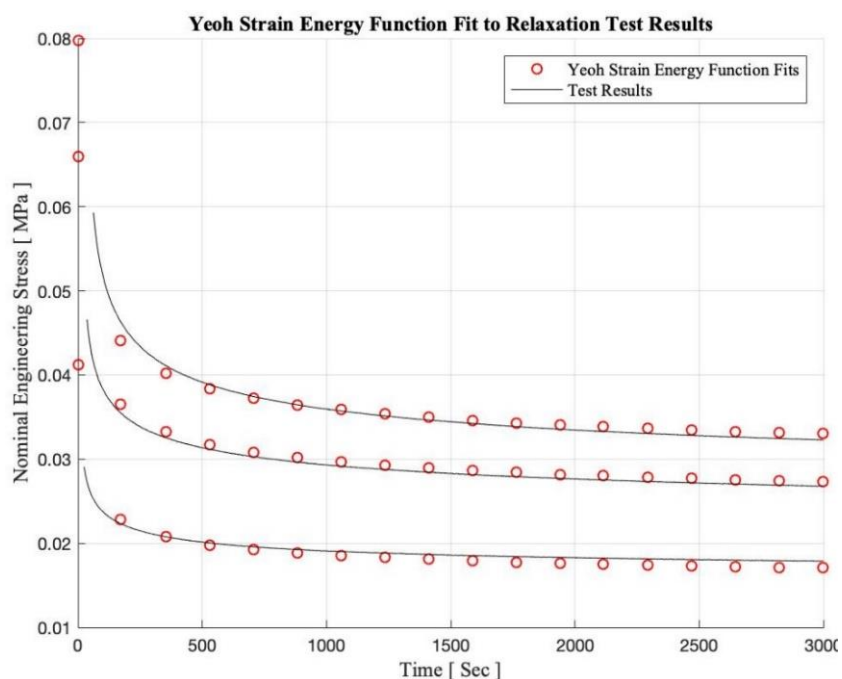


Figure 6-18 Yeoh strain energy function fit to material relaxation test

In a creep test, the strain can be defined as  $\varepsilon(t) = E_c(t)\sigma_0$  where  $E_c(t)$  is the time dependent creep compliance as defined in eqn. (3.5-22). The strain,  $\varepsilon(t)$  as given in eqn. (3.5-27) which is recorded in the creep test can be restated as given in eqn. ).

$$\varepsilon(t) = \varepsilon_0 + \sum_{i=1}^N \varepsilon_i \left(1 - e^{-\frac{t}{\tau_i}}\right) \quad (6.5-6)$$

Table 6-9 Hyperelastic material properties obtained from relaxation test

Energy Potential	Parameter	Unit	Value	Initial Start Point	Error, R <sup>2</sup>
Yeoh model	$C_{10}$	[MPa]	0.0344	[0, -2, -1]	0.00177
	$C_{20}$	[MPa]	-42.230		
	$C_{30}$	[MPa]	28.151		
Ogden model	$\alpha_1$	[-]	11.931	[0, 4, -4, -2]	0.00053
	$\mu_1$	[MPa]	$-0.063 \cdot 10^{-4}$		
	$\alpha_2$	[-]	-5.143		
	$\mu_2$	[MPa]	$-632.891 \cdot 10^{-4}$		
Mooney-Rivlin model	$C_{10}$	[MPa]	$-0.134 \cdot 10^{-4}$	[-5, -2]	0.15514
	$C_{01}$	[MPa]	$160.944 \cdot 10^{-4}$		

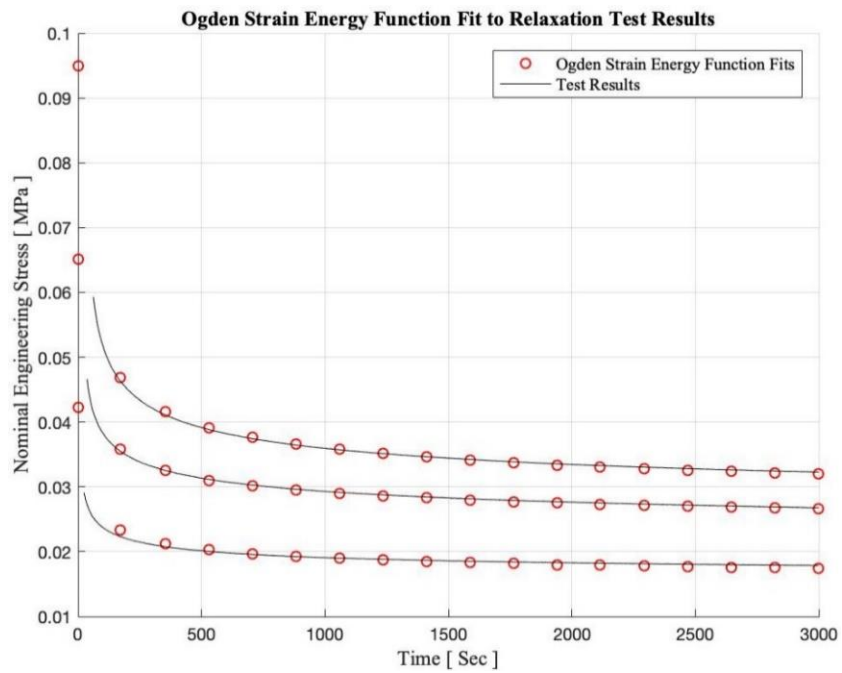


Figure 6-19 Ogden strain energy function fit to material relaxation test

The parameters  $\varepsilon_0$ ,  $\varepsilon_i$  and  $\tau_i$  values shall be determined by means of a curve fit. Note that, the creep response of the material starts from initial rest position that indicates the first term,  $\varepsilon_0$  will be zero. Matlab's `lscurvefit` function is used in parameter optimization. Levenberg-Marquardt method is applied and presented the best results. In creep tests, three constant force levels (100 mN, 200 mN and 300 mN) were applied to VHB 4910 material and the strain history recorded. The samples used in the tests were selected to be less than 5 mm in length dimension (so as the testing dimension) due that when it creeps under a constant force, the sample shall extend more than %100 strain. For each test, the initial start point of all variables for the optimization algorithm is selected accordingly. The number of Maxwell elements,  $N$  is again determined based on the duration of the test which is  $N = 3$ . Test fit results are given in Figure 6-20 and the resulting parameter set is given in Table 6-10.

Table 6-10 Optimized parameter sets from material creep tests

<b>Parameter</b>	<b>100 mN</b>	<b>200 mN</b>	<b>300 mN</b>
$\varepsilon_1$ [-]	0.144	-2.687	-4.348
$\tau_1$ [sec]	6.585	-3373.85	-3938.08
$\varepsilon_2$ [-]	0.274	0.375	-0.671
$\tau_2$ [sec]	1530.38	517.75	37.091
$\varepsilon_3$ [-]	0.151	0.381	-0.913
$\tau_3$ [sec]	143.33	19.404	472.289

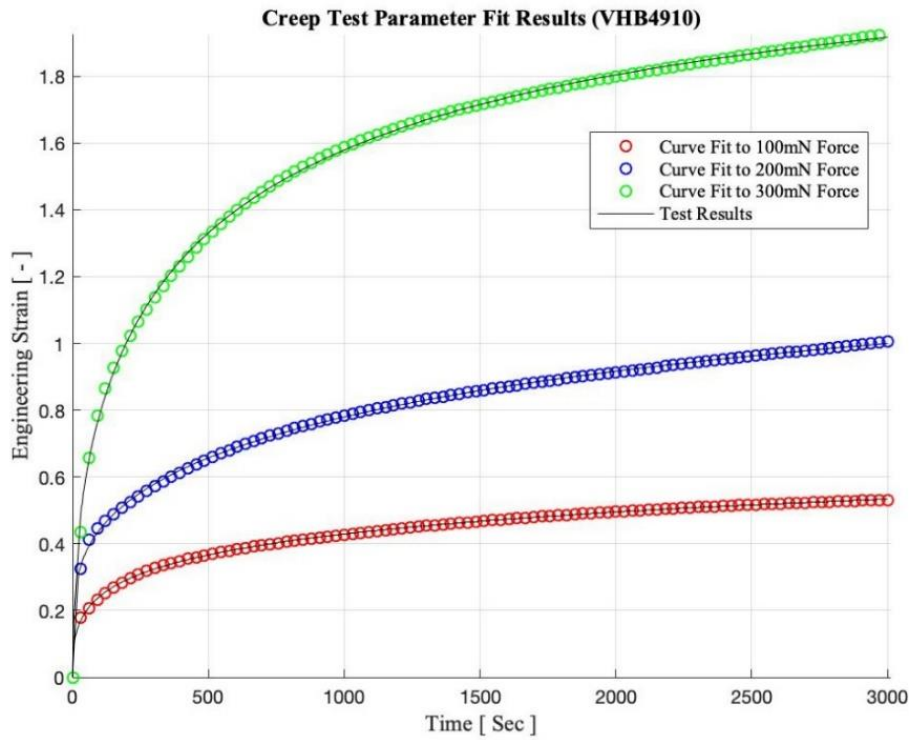


Figure 6-20 Material creep curve fitting results

For a linear material model, the creep compliance functions,  $S_{i,c}(t)$  should be independent of the applied input force as encountered relaxation modulus. The results of creep compliance functions of each test according to eqn. (6.5-7) and the mean creep compliance function are plotted in Figure 6-21. The mean creep compliance function can be used to determine the Prony series coefficients by parameter comparison based on the mathematical equality given in eqn. (3.5-20). The fit results are given in Figure 6-16.

$$S_c(t) = \frac{\varepsilon(t)}{\sigma_0} \tag{6.5-7}$$

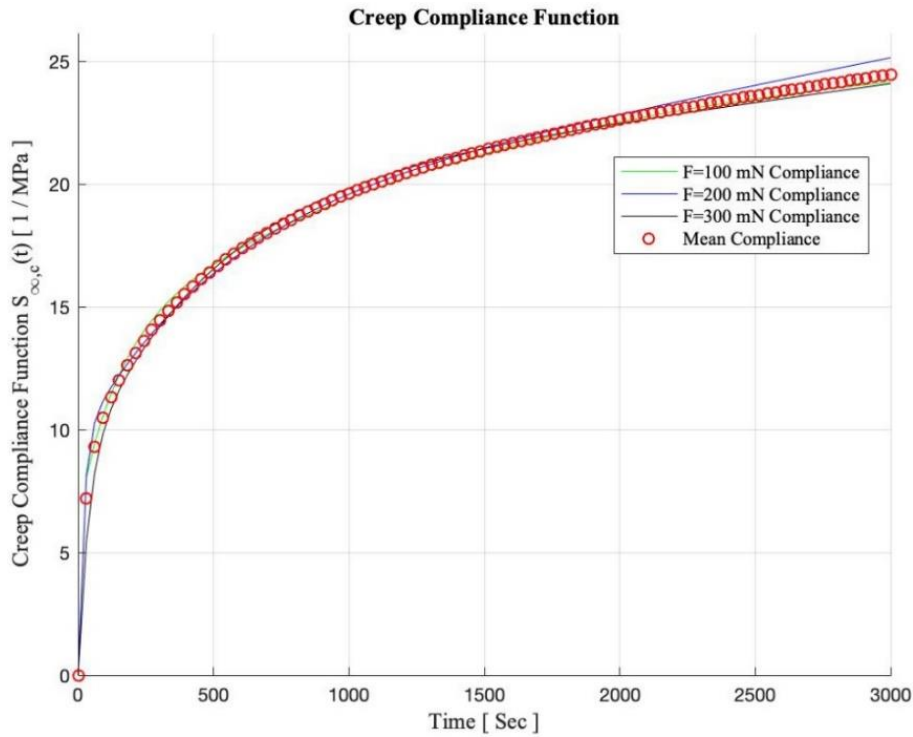


Figure 6-21 Material creep compliance functions  $S_{\infty,c}(t)$

The normalized creep compliance function,  $S_{c,n}(t)$  can be computed as given in eqn. (6.5-8). As long as the initial start point of normalized creep compliance,  $S_0$  is equal to zero, the normalization is performed using  $S_{\infty}$ .  $S_{\infty}$  depends on the duration of the performed test which is equal at  $t = 3000$  seconds. The Prony series fit function and its related parameters are given in Figure 6-22 and Table 6-11.

$$S_{c,n}(t) = \frac{S_{c,mean}(t)}{S_{\infty,mean}} \quad (6.5-8)$$

Table 6-11 Optimized parameters of Prony series fit function

Parameter	$g_1[-]$	$\tau_1[s]$	$g_2[-]$	$\tau_2[s]$	$g_3[-]$	$\tau_3[s]$
Value	-0.434	38.767	-0.559	996.014	0.001	-1089.96

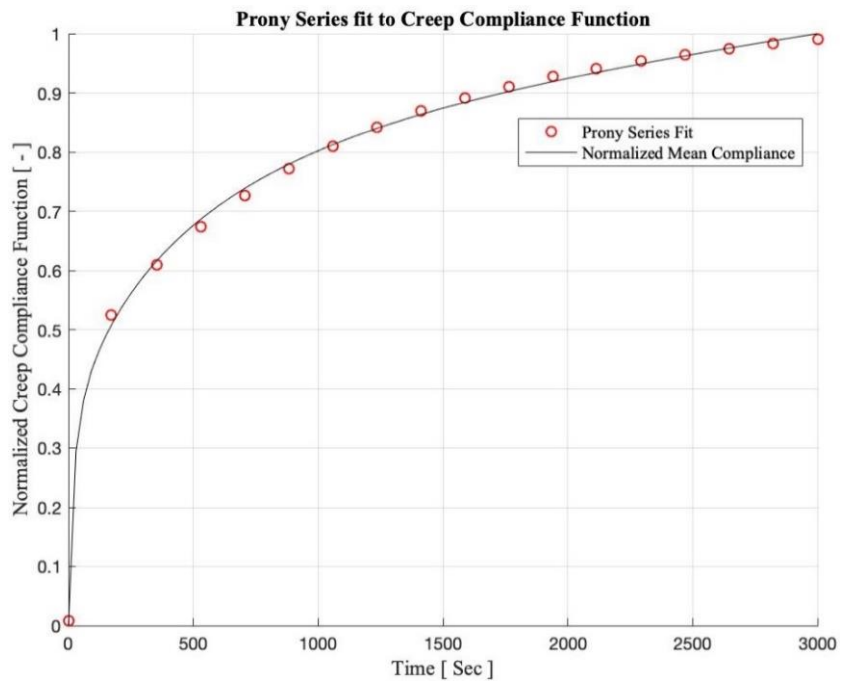


Figure 6-22 Normalized creep compliance functions  $S_{\infty,c}(t)$

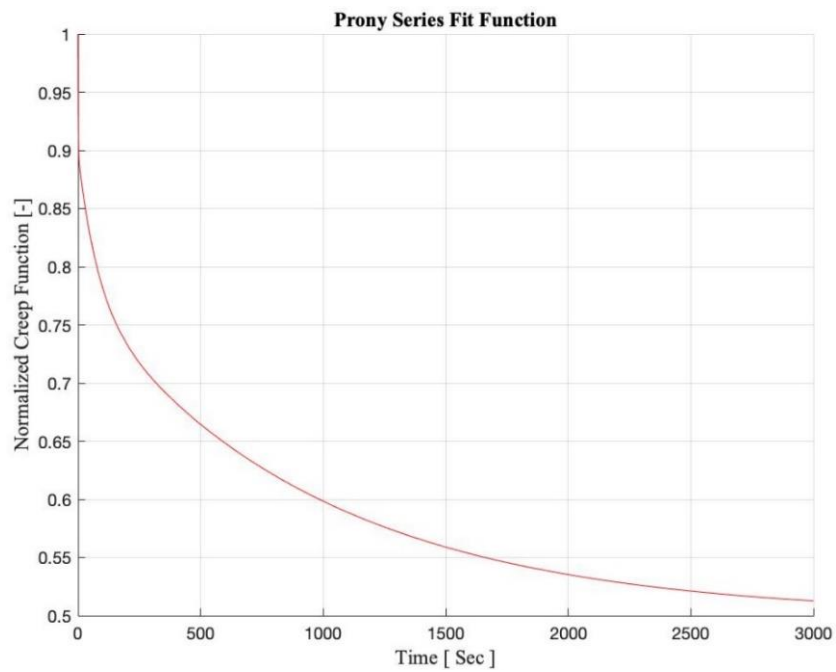


Figure 6-23 Prony series fit function used in creep analysis

Using the eqn. (3.5-27), the below given eqn. (6.5-9) can be written where  $\varepsilon_0$  will be zero due to the test conditions.

$$\varepsilon(t) = \varepsilon_0 + \sum_{i=1}^N \varepsilon_i \left(1 - e^{-\frac{t}{\tau_i}}\right) \quad (6.5-9)$$

Analogously adopting eqn. (6.5-8) to the eqns. (3.5-17) and (3.5-18), the dimensionless Prony series function can be calculated using eqn. (6.5-9). After determining the coefficients, the final Prony series function will be in the form given in eqn. (6.5-10).

$$\frac{\varepsilon(t)}{\varepsilon_\infty} = \frac{\varepsilon_0 + \sum_{i=1}^N \varepsilon_i \left(1 - e^{-\frac{t}{\tau_i}}\right)}{\varepsilon_0 + \sum_{i=1}^N \varepsilon_i} = \frac{1 + \sum_{i=1}^N g_i e^{-\frac{t}{\tau_i}}}{1 + \sum_{i=1}^N g_i} \quad (6.5-10)$$

$$g_r(t) = \frac{S_c(t)}{S_\infty} = 1 + \sum_{i=1}^N g_i e^{-\frac{t}{\tau_i}} \quad (6.5-11)$$

Finding the hyperelastic material coefficients in creep state is cumbersome. While using the uniaxial tension equations given in eqn. (3.4-47) for Yeoh, eqn. (3.4-30) for Ogden and eqn. (3.4-19) for Mooney-Rivlin, it should be noted that the given stress equations are in terms of stretch ratios,  $\lambda_i$ . Deriving and solving these equations in terms of stress is not easy and practical. Meanwhile the hyperelastic terms are also a time function as defined in eqn. (6.5-10) and eqn. (6.5-11). To present the creep compliance of these strain energy functions, an alternative approach is studied. Matlab scripts are written to calculate stress output results using the stretch ratio history (already recorded in the tests as strain) and the computed Prony series. The calculated stress is optimized using the applied engineering stresses which are already known. If it is tried to solve the stress output of the strain energy functions with the stretch ratio and applied Prony series, it is possible to find a particular hyperelastic material coefficient. However, in this study, all tests (all applied forces) are used in a single optimization routine to find

the best hyperelastic material coefficients that are best fit to all tests. This procedure is performed for all strain energy functions individually. As long as the applied engineering stress are assumed to constant, using the optimized hyperelastic coefficients, the constant stresses should be validated.

The results of the optimization routine is provided in Figure 6-24 to Figure 6-26. The applied constant engineering stresses are well fitted to strain energy functions. The hyperelastic coefficients are calculated with a multi optimization procedure that will result in best fitting hyperelastic material coefficients which are tabulated in Table 6-12.

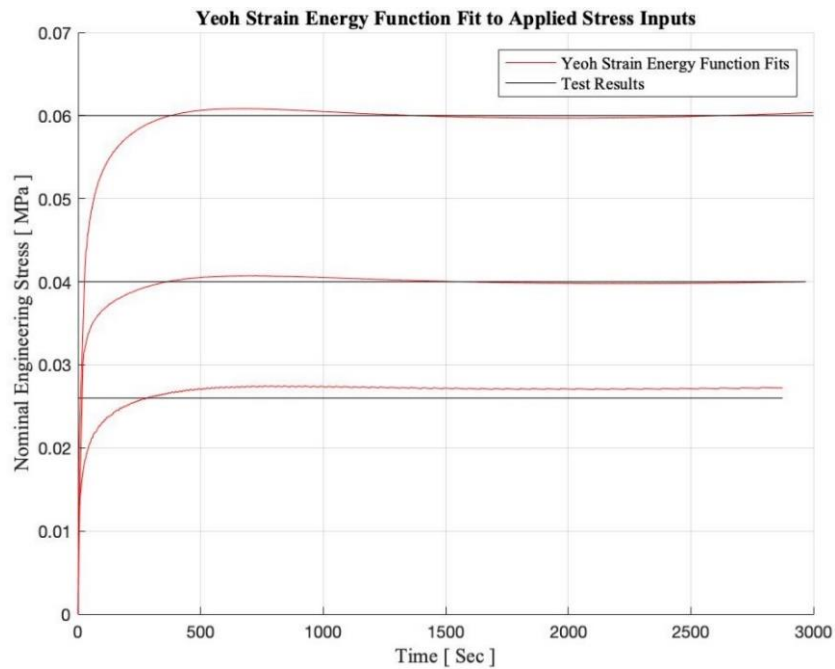


Figure 6-24 Yeoh strain energy function fit to material creep test

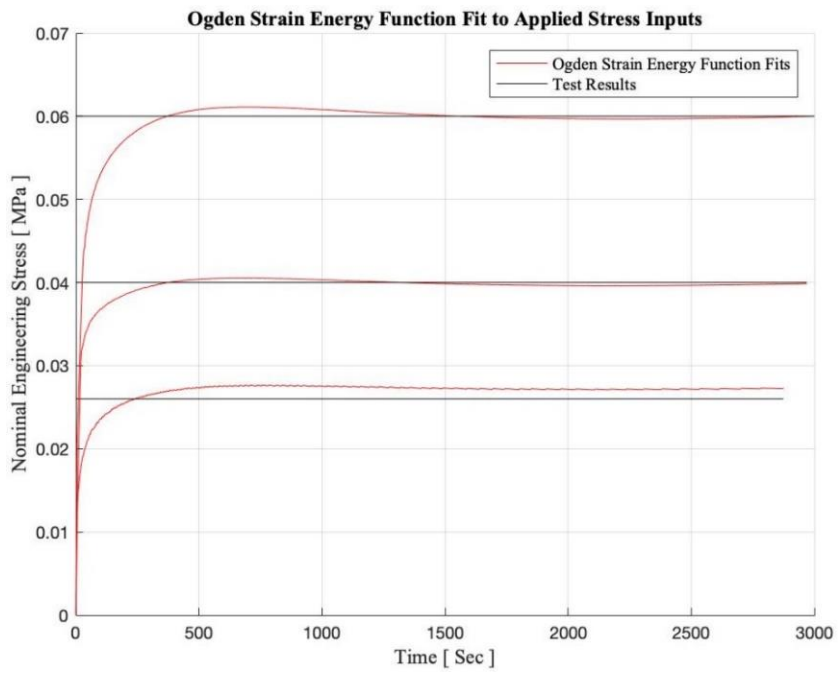


Figure 6-25 Ogden strain energy function fit to material creep test

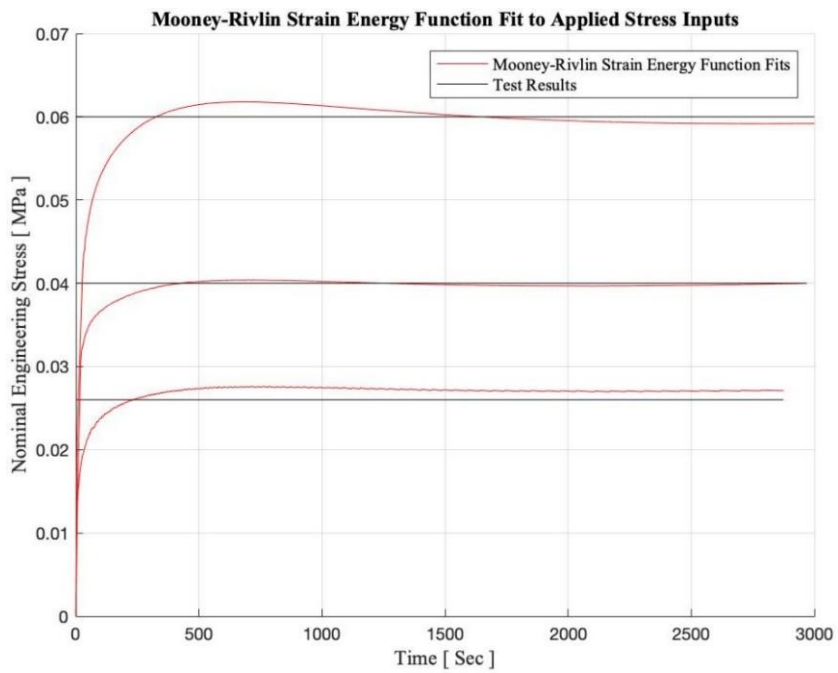


Figure 6-26 Mooney-Rivlin strain energy function fit to material creep test

Table 6-12 Hyperelastic material properties obtained from creep test

Energy Potential	Parameter	Unit	Value	Initial Start Point	Error, R <sup>2</sup>
Yeoh model	$C_{10}$	[MPa]	0.025	[3, -5, -2]	0.0157
	$C_{20}$	[MPa]	$-8.747 \cdot 10^{-4}$		
	$C_{30}$	[MPa]	$0.588 \cdot 10^{-4}$		
Ogden model	$\alpha_1$	[-]	1.423	[0, 5, 0, 4]	0.01586
	$\mu_1$	[MPa]	$739.618 \cdot 10^{-4}$		
	$\alpha_2$	[-]	7.329		
	$\mu_2$	[MPa]	$0.142 \cdot 10^{-4}$		
Mooney-Rivlin model	$C_{10}$	[MPa]	$169.685 \cdot 10^{-4}$	[4, 4]	0.0161
	$C_{01}$	[MPa]	$106.546 \cdot 10^{-4}$		

## 6.6. DEA Creep Response Modeling

In Chapter 6.5, the material modeling of VHB 4910 tape is presented. The material used in the analyses was in its raw form. Neither pre-stretch nor reinforcement was applied on the material. It is demonstrated that the hyperelastic and viscoelastic material models are well suited to observed test results. However, to use the VHB tape as a DEA, a manufacturing process should be applied including pre-stretching, reinforcements and carbon black smearing. As a result of these modifications, the material behavior will be changed and the previously presented mathematical models has to modified. Some of the outcomes of preliminary raw material studies will not be used further more. These are volumetric compression and quad lap shear results which are used to validate material incompressibility. The intended application of DEA is to use it on a 3D model of a trailing edge that can camber to certain angles. To perform such a motion, it is considered that creep phenomenon will be dominant in actuation. Due that the hyperelastic creep models are simplified when DEA modeling.

A Matlab GUI is created to ease the DEA parameter analysis as presented in Figure 6-27. In this GUI, user can input more than one raw material DEA test data and analyze

it for further use. On the other hand, GUI can perform force and voltage application analyses including material modeling. The capabilities of GUI will be detailed in the next.

The creep responses that are presented in Chapter 5.8 are studied in the first run. The tests were performed using the linear stage and the results were recorded for further analysis. The test results are in raw form as presented in Figure 6-28. The raw data includes the deformation of DEA with respect to applied load history, load sensor measurements and applied voltage if there is any. The data parts which are recorded at the end of the test are truncated from raw data and are not used in analysis. All creep tests are performed with zero voltage input. Unfortunately, the controller generated artificial random voltage signals while data transmission while there is no voltage application on DEA. These voltage readings in creep tests are omitted.

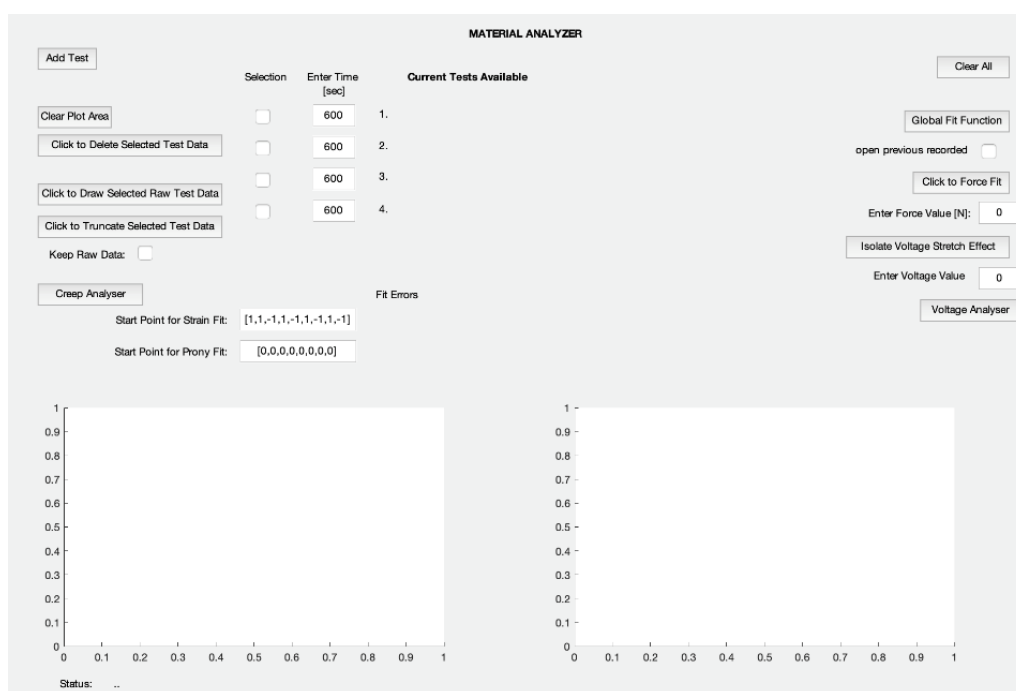


Figure 6-27 Matlab GUI for DEA analysis

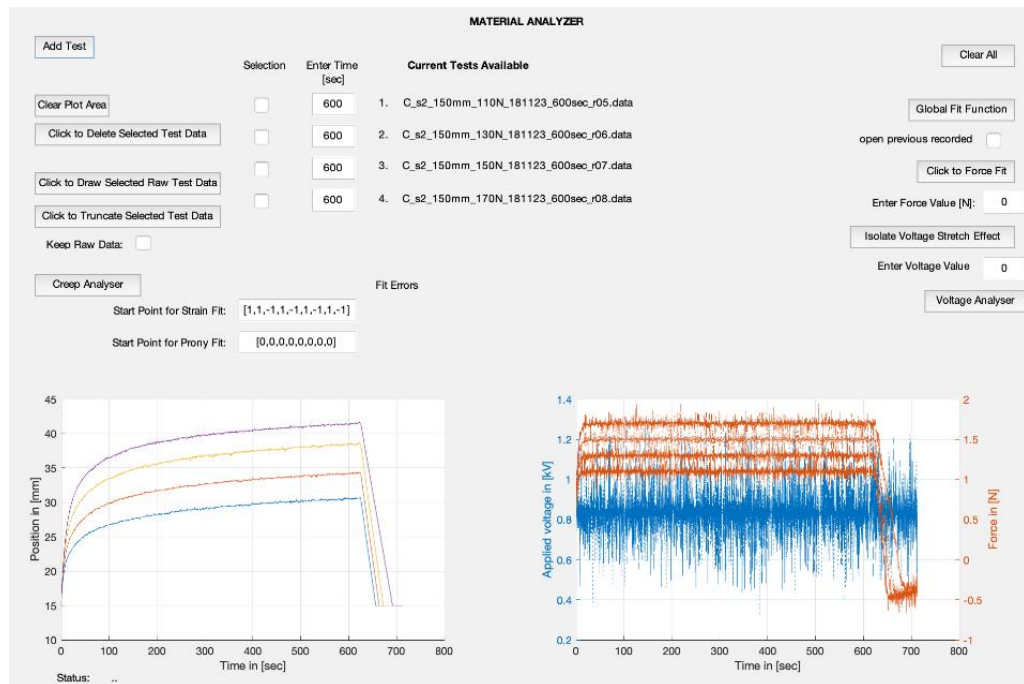


Figure 6-28 Extraction raw creep DEA test data for DEA analysis

In all tests, if otherwise is not stated, DEAs are single layered and manufactured from VHB 4910 tape material. All the pre-strains are selected to be 4 x 4 in all length and width directions (55 mm x 55 mm initial cut dimensions) while manufacturing. For the demonstration purposes, all the below given derivations and plots are performed using the results of 1.10 N, 1.30 N, 1.50 N and 1.70 N creep loadings. The creep tests data are collected for 610 seconds. All DEAs are mounted to linear stage manually and  $l_0 = 15 \text{ mm}$  gap is maintained (unprestretched length dimension) between the clamping edges. The 15 mm gap is measured by a caliper gage. Procedure of testing is summarized as defined; The DEA is clamped from one end and the other end is set free to react to applied constant creep load. The encoder of the linear stage measured DEA unidirectional elongation [mm] with respect to the clamped edge, the force sensor measured the applied force [N] and controller measured the applied voltage [kV] where this information is provided from high voltage amplifier where appropriate. The sampling frequency was 10 Hz. For creep analysis, the uniaxial DEA

elongation is converted to strain,  $\varepsilon_1$  and stretch ratio,  $\lambda_1$ . The width and thickness dimensions as well. The force value is input as a constant parameter during creep tests. However, the data recorded from the force sensor was noisy. The mean value,  $F_m$  of the force sensor output is calculated and used throughout the analysis. Engineering stress,  $\sigma_{eng}$  is given in eqn. (6.6-1) that is the mean force divided by the initial cross section area,  $A_0$ . The initial cross section area,  $A_0$  is the perpendicular to the uniaxial loading direction.

$$\sigma_{eng} = \frac{F_m}{A_0} \quad (6.6-1)$$

The linearity of the material itself was previously studied and presented in Section 6.5.4 with the provided relaxation and creep compliance functions given in Figure 6-15 and Figure 6-22. When DEA is considered it is required to check the linearity using eqn. (3.5-1) and eqn. (3.5-2). The stress values observed in the tests are calculated and corresponding strain values are plotted in Figure 6-29. The blue lines pass through the same time instance points. The time lines have a constant slope which indicates that the DEA is linear.

The creep compliance functions,  $E_c$  which is defined in eqn. ) are selected to use rather strain energy functions, to ease the computation time required for control and real time actuation demonstrations. It is computed as given in eqn. ) for actual and predicted test results.

$$E_c(t) = \frac{\varepsilon(t)}{\sigma_0} \quad (6.6-2)$$

All creep compliance functions,  $E_c$  are normalized as presented in eqn. ) with respect to their maximum values encountered during a creep test.

$$E_{c,n}(t) = \frac{E_c(t)}{E_{c,\infty}} \quad (6.6-3)$$

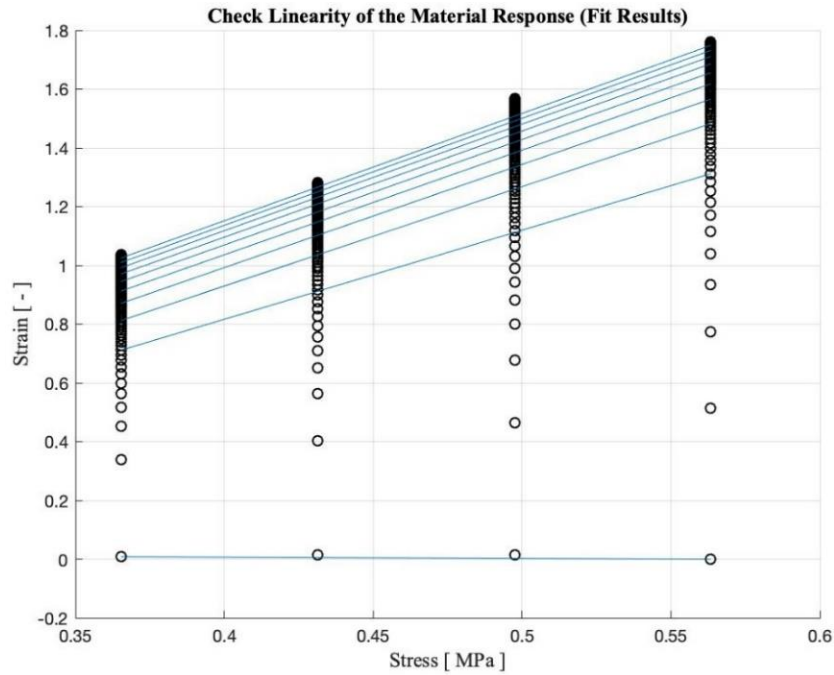


Figure 6-29 Linearity check of DEA

The output strain,  $\varepsilon(t)$  history of creep tests are fit to a curve which is defined in eqn. (6.6-4) using Matlab's `lscurvefit` function with Levenberg-Marquardt solver. The GUI solver is capable to solve solution for  $N = 2, 3$  and 4. Best fit solution for strain predictions are obtained at  $N = 4$  which is slightly better than  $N = 3$  with the initial start point,  $X_0 = [1, 1, -1, 1, -1, 1, -1, 1, -1]$ . The mean square error,  $R^2$  is 0.102. The parameter values,  $\varepsilon_\infty$ ,  $\varepsilon_i$  and  $\tau_i$  are not tabulated for each optimized test because for each different test, new set of variables can be calculated and these values are not global. But the estimated strain history fit well to test strain results as presented in Figure 6-30.

$$\varepsilon(t) = \varepsilon_\infty + \sum_{i=1}^N \varepsilon_i e^{-\frac{t}{\tau_i}} \quad (6.6-4)$$

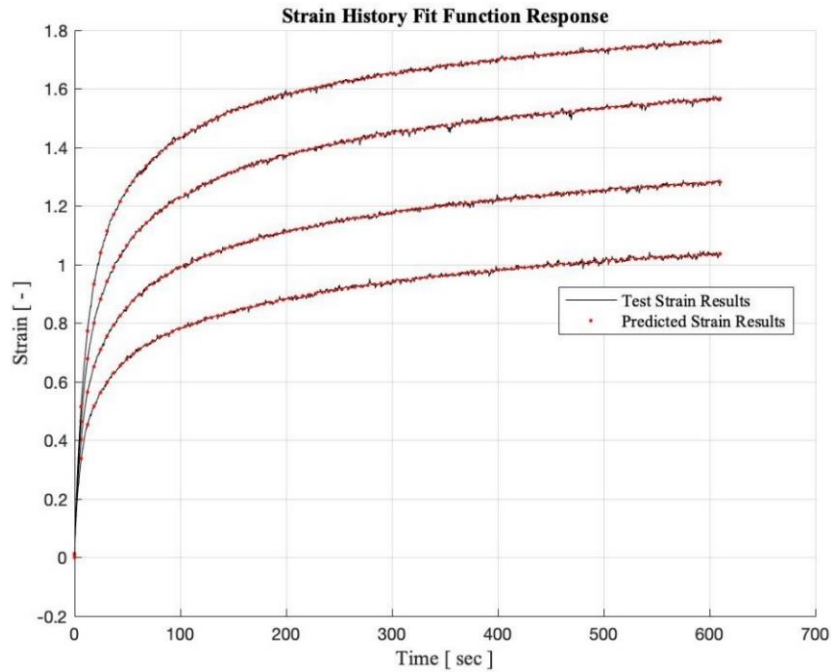


Figure 6-30 Creep test strain outputs of DEA and its estimated values

As long as the strain is predictable so the stretch ratios. Once the strain values are fit to a function then it is easy to obtain other functions such as, estimated stress, estimated creep compliance and normalized creep compliance. Using eqn. (6.6-4), the normalized estimated creep compliance can be well fitted to a so called Prony series where the used form is given in eqn. (6.6-5). The GUI can try up to five term Prony series and outputs the best results using Matlab's lscurvefit function with Levenberg-Marquardt solver. The initial start point of the solver is  $X_0 = [0,0,0,0,0,0,0,0]$  where a best fit is found at  $N = 4$ . The mean square error,  $R^2$ . The normalized compliances of tests and estimations including the Prony series fit function are given in Figure 6-31.

$$g_r(t) = 1 + \sum_{i=1}^N g_i e^{-\frac{t}{\tau_i}} \quad (6.6-5)$$

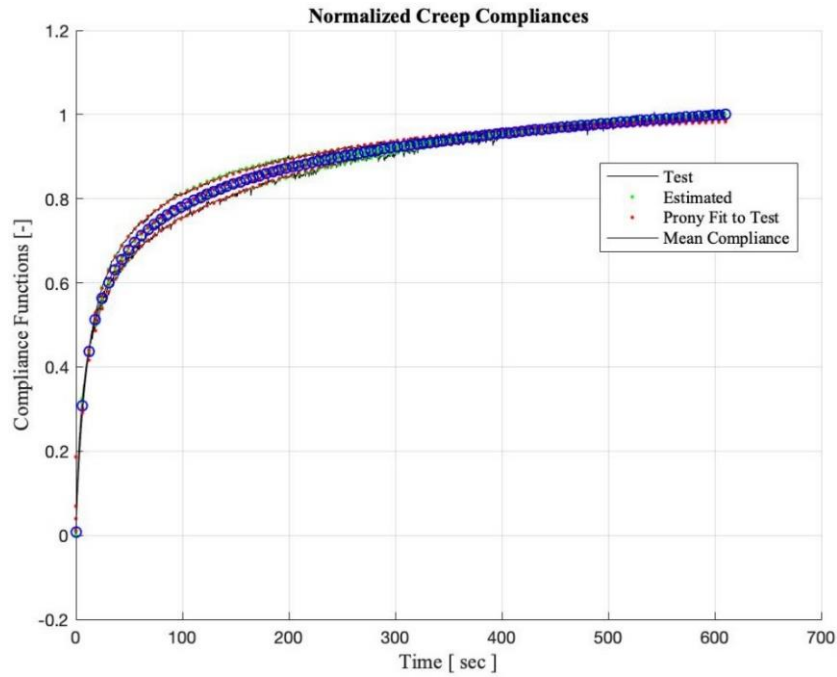


Figure 6-31 Normalized test creep, means and predicted compliances

According to the needs in trailing edge design of 3D model wing, a relation between creep compliance,  $E_{c,\infty}$  and applied force,  $F_{app}$  is required. For every applied force loading there exist a unique compliance response which will yield to a common creep compliance DEA response as presented in Figure 6-31. The applied force and the corresponding creep compliance is somehow related. If one tries to plot the end point of creep compliance,  $E_{c,\infty}$  (the maximum value) with respect to the applied force,  $F_{app}$ , It will be concluded that there is almost a linear relationship which is given in Figure 6-32. When all the creep parameters are estimated by mathematical modeling, it is possible to compute any DEA predicted creep strain,  $\varepsilon_p(t)$  that can be given as given in eqn. ) where normalized estimated creep compliance,  $E_{c,n}(t)$ , estimated creep compliance end value,  $E_{c,\infty}(t)$  and estimated applied stress,  $\sigma_{e,0}$ . The actual test strains results can be replicated using eqn. ) as given in Figure 6-33.

$$\varepsilon_p(t) = E_{c,n}(t) \cdot E_{c,\infty}(t) \cdot \sigma_{e,0} \quad (6.6-6)$$

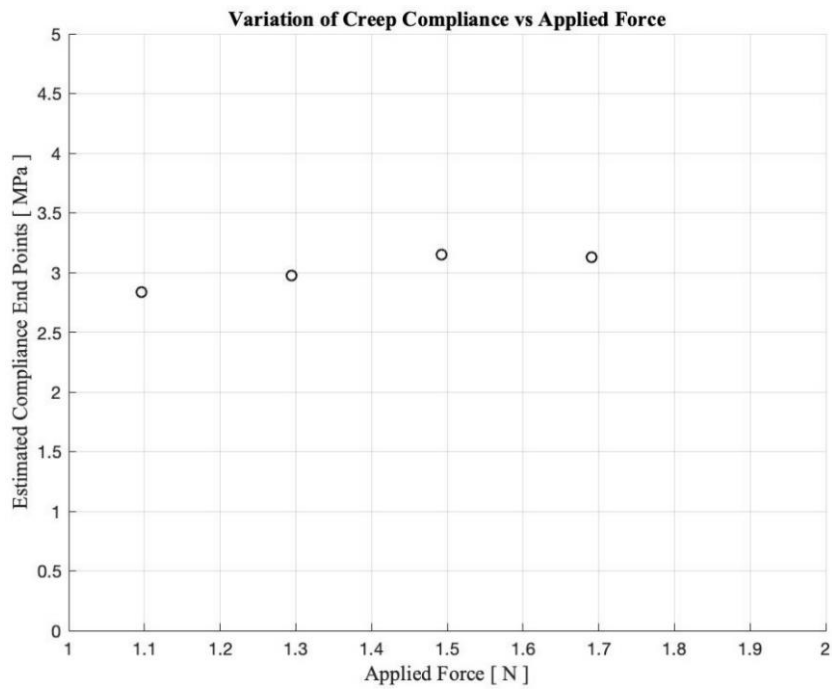


Figure 6-32 Variation of creep compliance end point vs applied force values

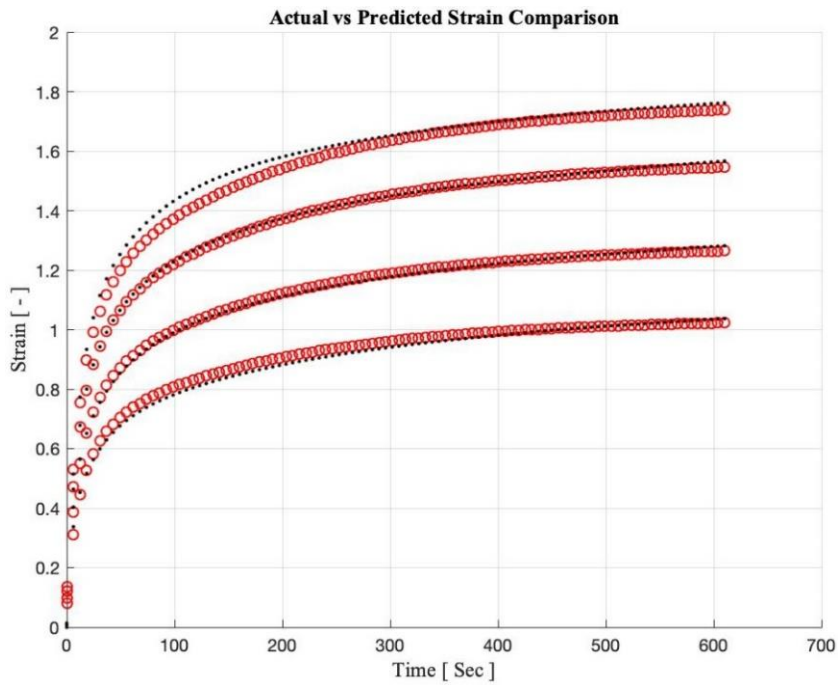


Figure 6-33 Actual test strain results and their predicted strain results

As long as the above given calculations are performed for the step applied four different constant force loadings, the same procedure is repeated for all single layered DEAs. The normalized creep compliance results of each test are provided in Figure 6-34 which are in good consensus with the optimized Prony series fit function (indicated with red line). Meanwhile, the applied constant force and the creep compliance end values are plotted on Figure 6-35. The linearity is validated as previously presented in Figure 6-32. On the other hand, the Mullins effect was previously introduced and the implications were presented in Chapter 5.6. The DEA creep tests are also performed more than one considering the Mullins effect. The related normalized creep compliances and Prony series fit are given in Figure 6-36. Force and final creep compliance variation is provided in Figure 6-37.

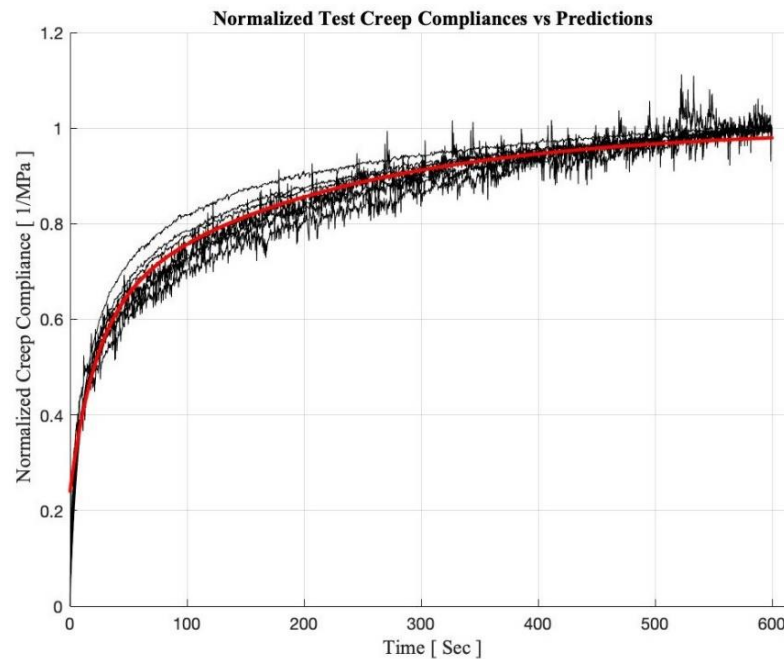


Figure 6-34 Normalized test creep compliances of all test (first run) and predictions

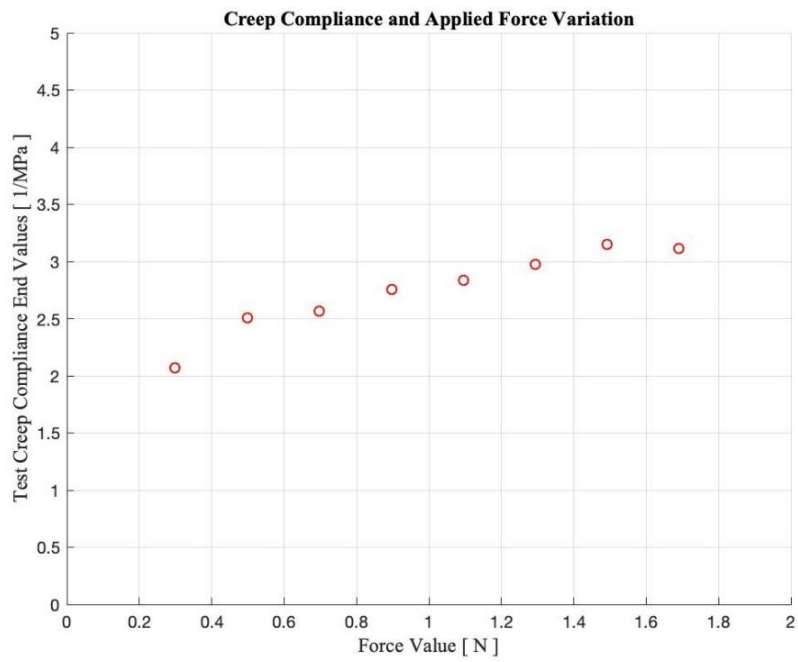


Figure 6-35 Test creep compliances' final values (first run) and applied loads

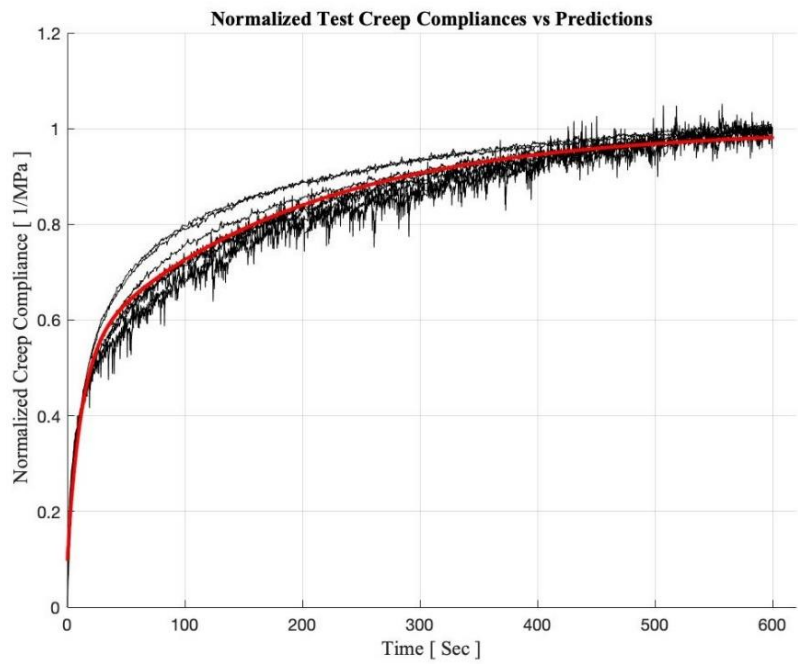


Figure 6-36 Normalized creep compliances of all tests (second run) and predictions

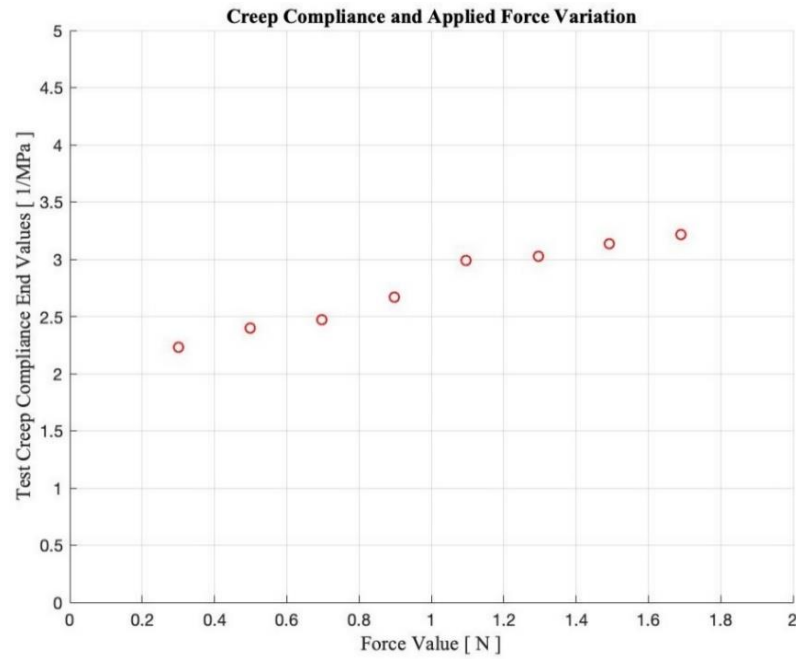


Figure 6-37 Test creep compliances' final values (first run) and applied loads

In Figure 6-35 and Figure 6-37, the creep compliance end points and applied force value variation are provided. It is apparent that a stress softening occurs on material such that for the same force loading the material exerts enlarged strain results. So, it is possible to conclude that the Mullins effect still hold true for DEA as in the actuator form. The material response provided in Figure 6-37 is more convenient in modeling of DEA modeling. This phenomenon can be repeated for third or more times but reader should note that the effect of stiffness decrease will much more limited. Endurance tests shall be performed for final DEA behavior including a fatigue point of view. As a result, the DEA's creep compliance end points interrelated to applied force by means of a polynomial function which is obtained by Matlab curvefit toolbox. The estimated function is given in eqn. (6.6-7) and the resulting DEA length simulation using engineering stress is given in Figure 6-38.

$$E_{c,\infty}(t) = -0.09966F_{app}^3 + 0.01509F_{app}^2 + 1.034F_{app} + 1.868 \quad (6.6-7)$$

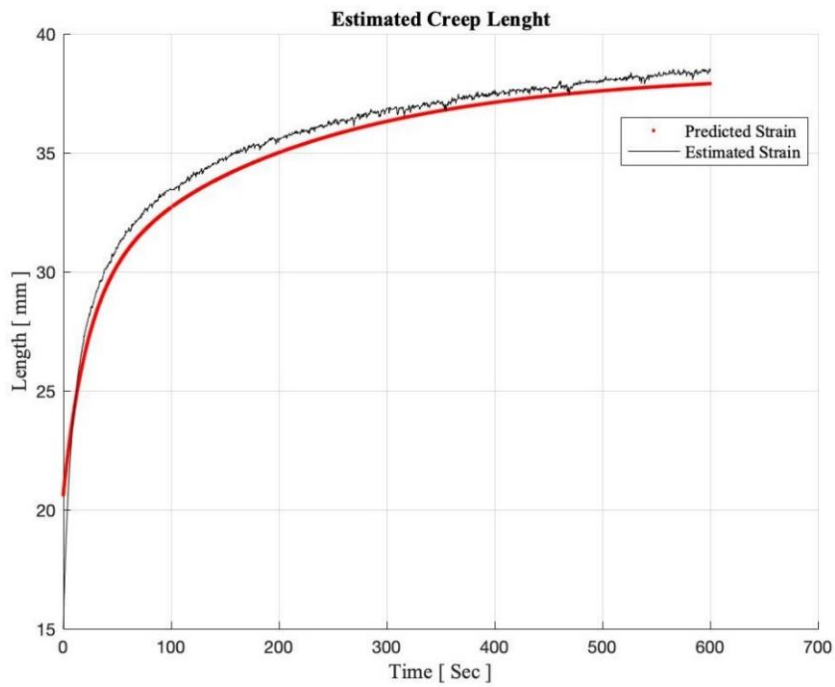


Figure 6-38 DEA creep simulation

The DEA creep tests are performed at 600 seconds simulation time. However, long term simulations are also tested. Maximum test duration is selected for one hour (1h). One hour long run tests are not performed for all DEAs. The DEA creep results for 1.10 N and 1.50 N constant step loads are given in Figure 6-39.

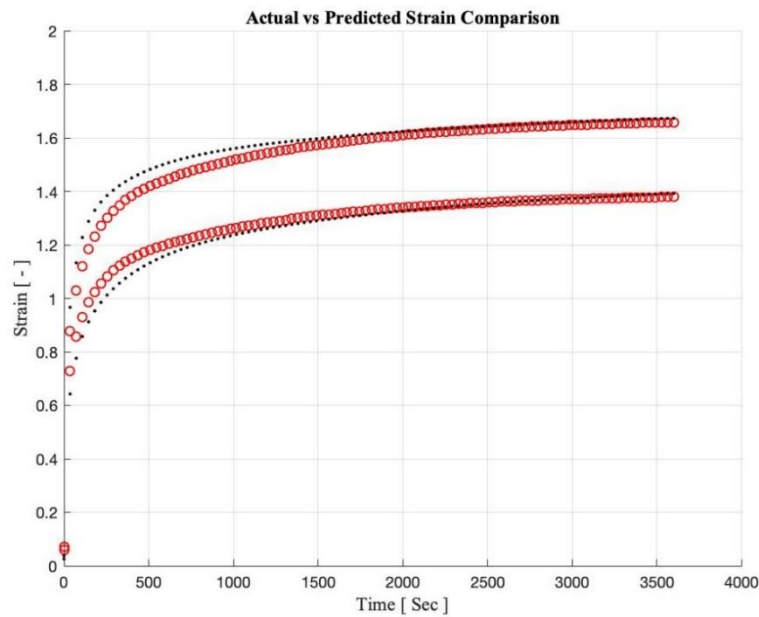


Figure 6-39 DEA creep simulation for long run

### 6.7. DEA Voltage Induced Creep Response Modeling

The Maxwell force effect is the driver for DEA actuation. The response of DE film to applied voltage is experimentally verified. Tests are performed with different constant step input loads and various high voltage is exerted. When the applied loading is increased, the DE film thickness decreases as well even without electric potential. Thus, the response of the DEA dramatically increases with high applied loading and high voltage potential. All DEAs are manufactured from 3M's VHB 4910 material and first tested in order to obtain mechanical response which is summarized in Section 6.6. The voltage induced creep tests are performed as defined in Section 5.9. The approach conducted throughout the study is as follows; creep the DEA for a certain amount of time (usually 10 minutes of creep time is allowed) then apply constant step voltage potential for sufficient time (10 minutes of voltage potential is allowed). All the DEAs are pre-stretched four by four in length and width directions equi-biaxially. The thickness of DEAs is very small and no more than 3 kV is applied. For demonstration purposes, the DEA that is loaded by a constant creep load of 0.90 N

and applied constant high voltages (1, 2 and 3 kVs) are presented. The other DEA voltage induced test results will be provided when appropriate. Note that the prescribed applied voltage potentials are theoretical values that are input to high voltage amplifier by the controller. The actual applied voltage value is smaller than the theoretical value by a reduction factor of %4 (as calculated). Matlab GUI is designed also for DEA analysis for voltage induced creep test as illustrated in Figure 6-40. The deflection response of the tip of creep loaded DEA is given in the left axes and the applied voltage is presented in the right axes.

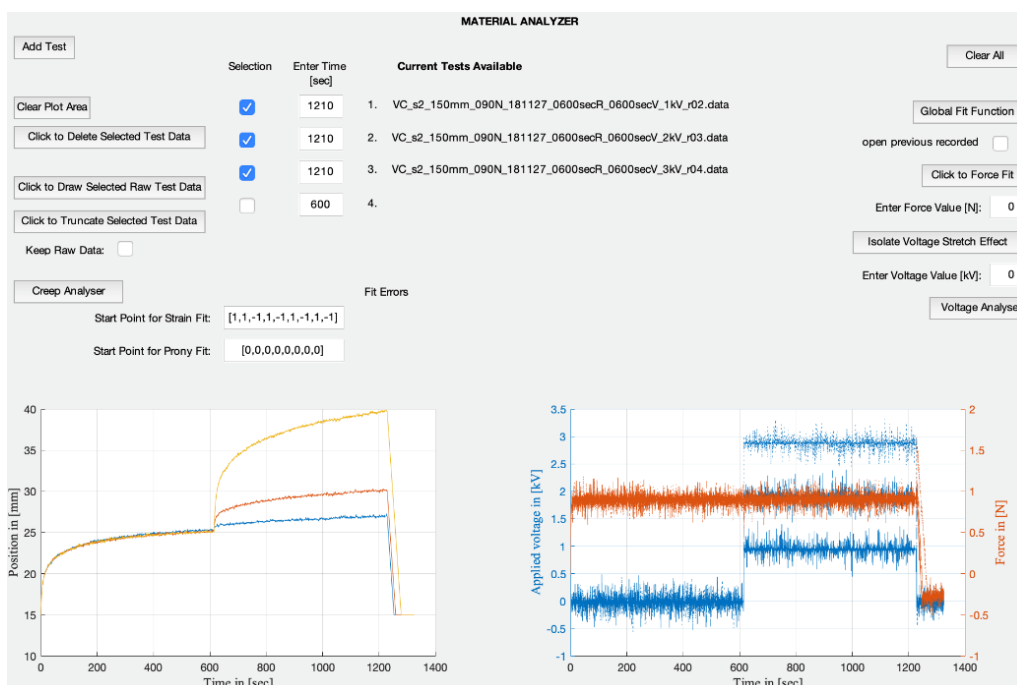


Figure 6-40 Material analyzer run for voltage induced creep test

The response of the DEAs can be split into two. First part involves the solely creep behavior and the second part involves both the creep behavior and the voltage induced creep behavior. Thus, to analyze a voltage induced creep response of a DEA, first the application time of the voltage potential should be well defined. One may doubt that

the voltage application time is certain but he should note that controller time clock is slightly different than actual computer time. The controller and computer clock difference is so small and even assumed to be same in whole analysis but on the other hand, this small amount of difference is significantly important when the time of voltage application is considered. Because if the split was not made properly, the pre-determined voltage application timing would not be the exact activation time and it would result considerable amount of effect while computing the average applied voltage values. The data split analysis is given in Figure 6-41. The GUI continuously computes the next ten data points' mean value and compares the result with the current data value. For the first part of the DEA response, no significant applied voltage mean is expected. But for the second part, there is a high difference between the computed mean applied voltage and the mean observed at the first response part. The intersection of the first and second responses will be the data point that will be used in whole voltage induced creep analysis.

Following the determination of the intersection point, the whole DEA test response data can be split into two. Following the separation, the resulting DEA response can be simulated as given in Figure 6-42. Note that for ease of understanding, the maximum voltage (3 kV) value are used for presenting.

The solely creep response of the DEA can be analyzed as previously described in Section 6.5.4. The creep part may fit to a creep compliance function and a mathematical model can be developed. The test data in the hyperelastic creep response is used to calculate related Prony series coefficients and using the fit data, the extended hyperelastic creeping behavior of the DEA is predicted as illustrated in Figure 6-43 for the voltage induced creep region. The DEA material continues to creep to infinity. The one-hour creep response of DEA as previously given in Figure 6-39 validates that the creep response of material does not settle to a steady state response. Whenever the voltage potential is applied on the DEA, there will be already continuing creep behavior which can be splitted from DEA response to conclude on solely voltage response of the DEA.

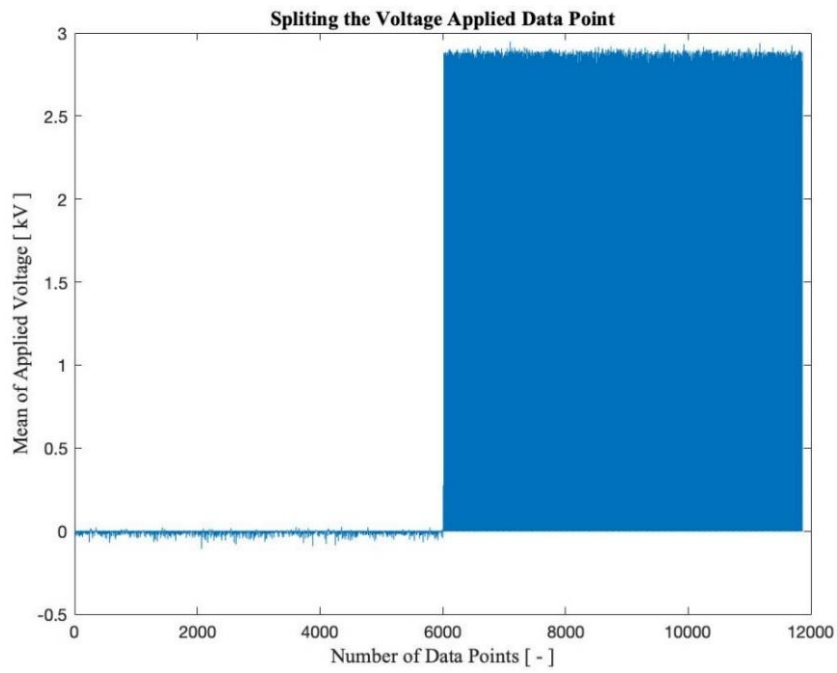


Figure 6-41 Detemination of data split point for DEA response

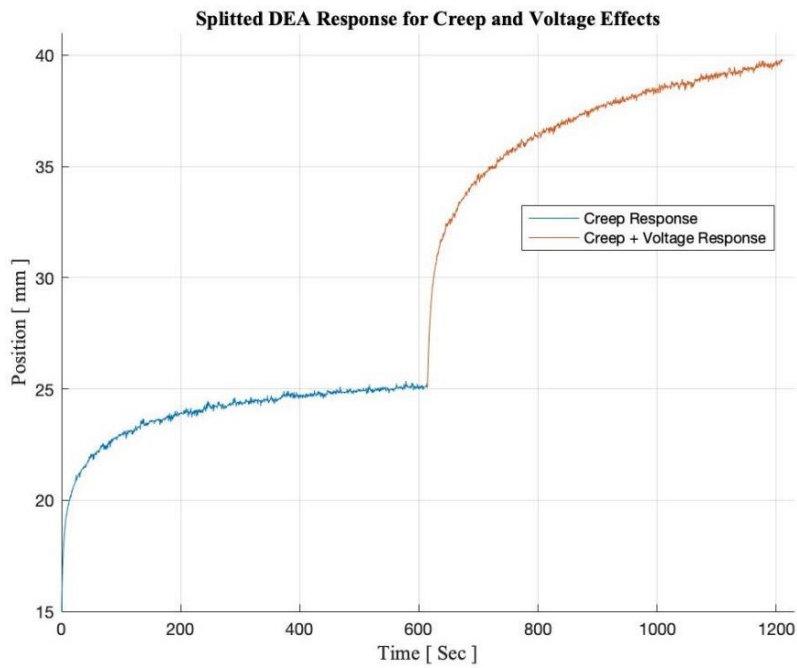


Figure 6-42 Splitted DEA response

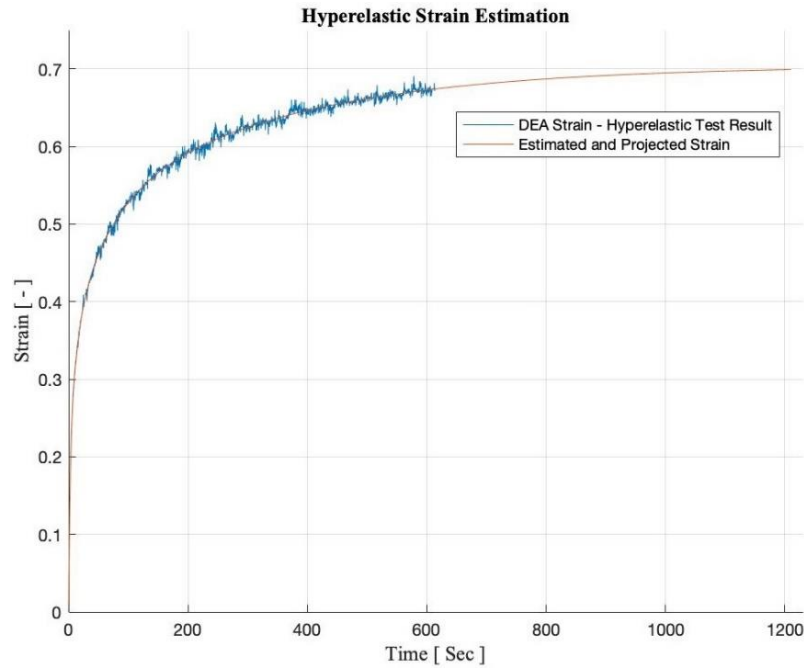


Figure 6-43 Predicted DEA hyperelastic response

The total response of DEA is as given in Figure 6-42 which involves the both the creep and the voltage induced responses. The isolation of voltage induced response can be obtained subtracting the long term hyperelastic creep response from voltage induced response. The resulting creep strain that is solely belongs to voltage effect is given in Figure 6-44. This creep response can be modeled by using the eqn. (3.6-1) where the free-space permittivity,  $\epsilon_0$  is equal to  $8.85 \times 10^{-12} \left(\frac{F}{m}\right)$ , and  $\epsilon_r$  is the relative dielectric constant of the elastomer and assumed to be 4.7,  $V_{app}$  is the applied electrical potential to the electrodes and equals to 3 kV and finally the  $z_0$  is the initial thickness of the polymer film. It should be noted that the given eqn. (6.7-1) can be used for thickness calculation where  $\lambda_1$  should be equal to the stretch ratio that is calculated from Figure 6-43 (the last test observed and stretch converted value,  $\lambda_p$ ) and  $\lambda_2$  is equal to four.

$$z_0 = \lambda_3 = \frac{1}{\lambda_2 \lambda_1} = \frac{1}{4\lambda_p} \quad (6.7-1)$$

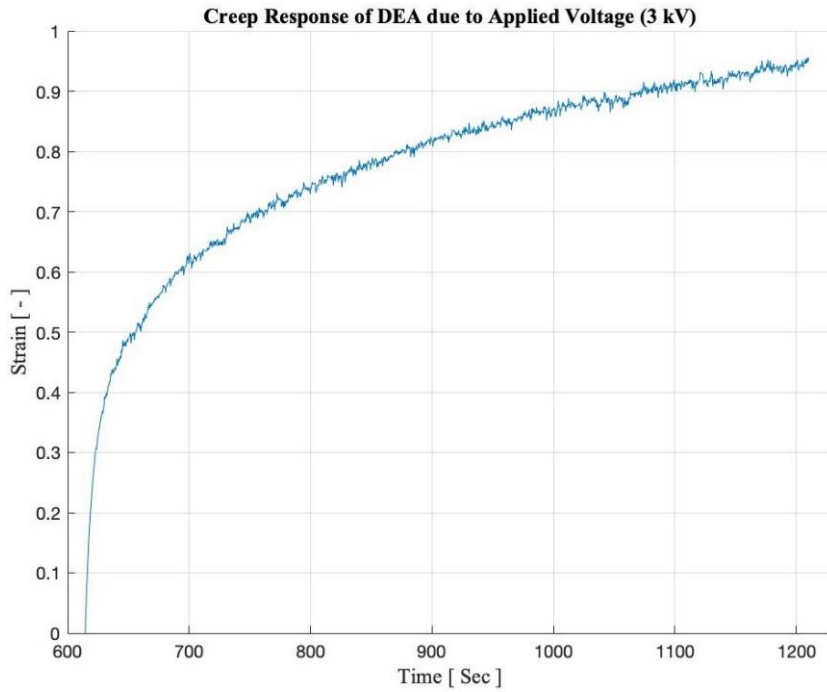


Figure 6-44 DEA creep response due to applied voltage input

The voltage induced creep response as given in Figure 6-44 has a different creep compliance than hyperelastic creep compliance. The voltage induced creep compliance can be found using the equation given in eqn. (6.7-2).

$$E_{c,v}(t) = \frac{\varepsilon_v(t)}{p_{el}} = \frac{\varepsilon_v(t)}{-\varepsilon_0 \varepsilon_r \left(\frac{V}{z_0}\right)^2} \quad (6.7-2)$$

Where,  $V$  is the mean of the applied voltage potential and  $z_0$  is the initial thickness of the elastomer. The resulting normalized creep compliance due to applied voltage is given in Figure 6-45 and its related Prony series fit function is plotted in Figure 6-46.

Analogously as given in eqn. (6.6-7), similar approach is used and the voltage induced creep response is predicted as presented in Figure 6-47.

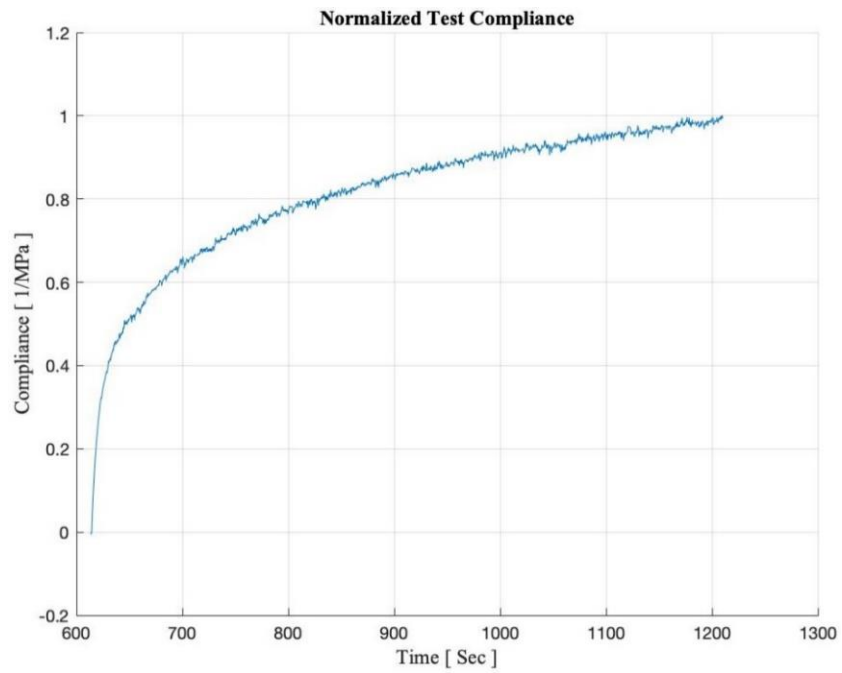


Figure 6-45 DEA normalized creep compliance due to applied voltage input

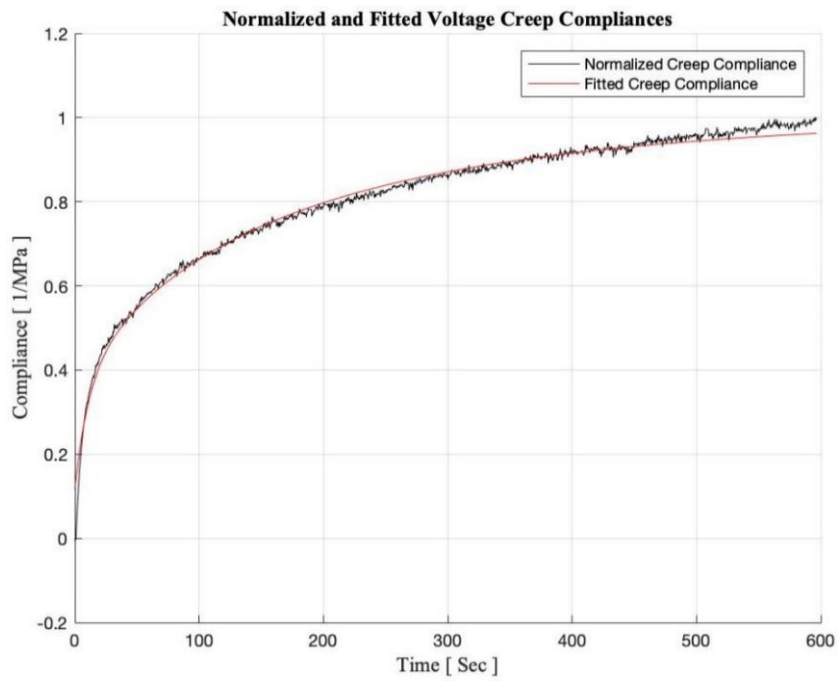


Figure 6-46 DEA normalized creep compliance fit to Prony series

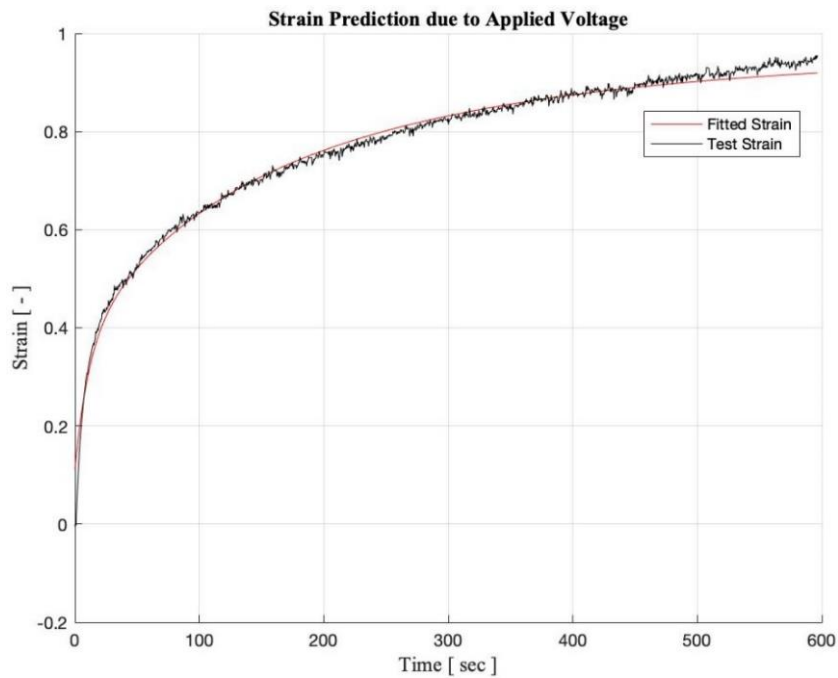


Figure 6-47 DEA voltage induced strain prediction

Both hyperelastic and voltage induced strain responses may be plot together as given in Figure 6-48. The total response of DEA is a combination of two compliances. The results shown in Figure 6-48 is a response for 3 kV applied voltage. The given response will be in the same characteristics for other applied voltage levels. As long as the normalized compliances fit in one the output will vary according to pre-strech and dimensions of the DEA.

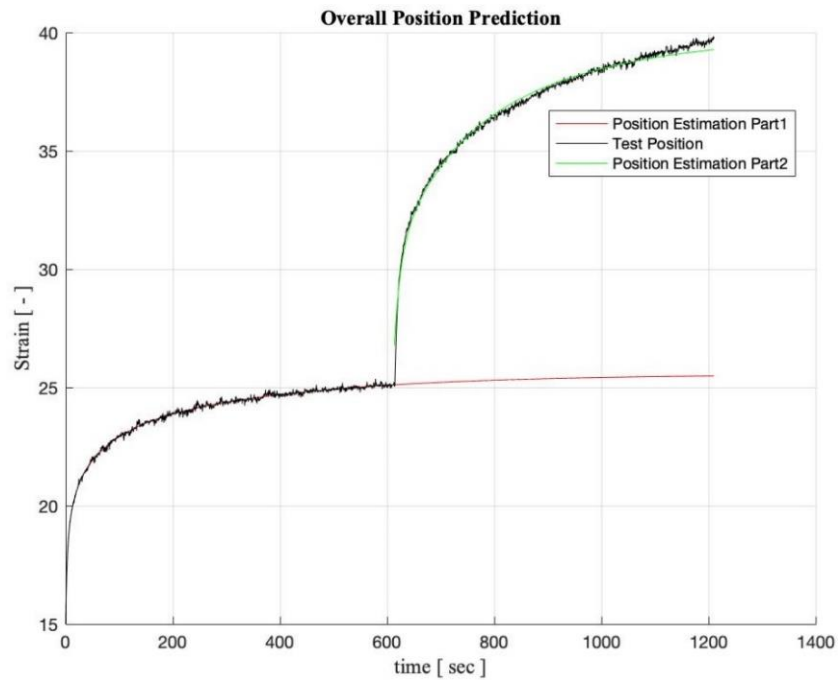


Figure 6-48 DEA voltage induced overall strain prediction

Meanwhile, DEA responses are grouped together to ease of understanding. In Figure 6-49, the complete list of grouping is presented. For a DEA in action, Figure 6-49 (a), (b) and (c) illustrates the strain responses for different applied voltages (hyperelastic effect removed) for different applied constant creep loads. Note that for 1.30 N, 3 kV applied voltage is tried many times but unfortunately, the tested DEAs are failed. So the related results are not given. On the other hand, Figure 6-49 (d), (e) and (e) presents

the results in the reversed order. For each applied voltage level, the effect of the applied creep response is presented in the figures. As seen from Figure 6-49 (a), (b) and (c), the tested minimal voltage (i.e. 1 kV) has minor effect on DEA while the applying 3 kV performs more than twice the effect the 2 kV. It is clear that the applied voltage do not have a linear effect on DEA strain response. Contrarily, it is observed that there is a linear relation between applied creep load for the same applied voltage level strain outputs.

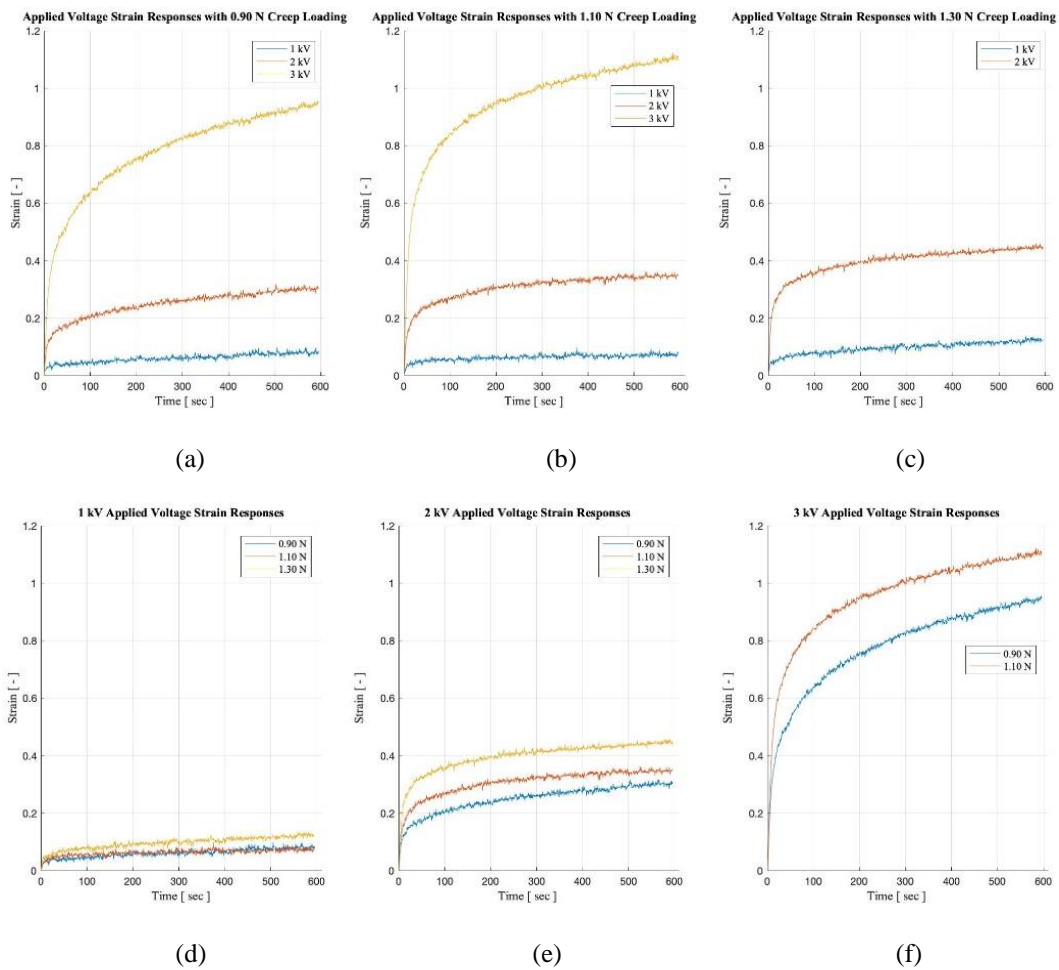


Figure 6-49 DEA voltage induced and creep loaded strain results

It is apparent that the DEA results in higher strain responses with the applied high voltages but the applied creep loading has a linear and small effect considered to applied voltage level. The maximum observed strain values and the corresponding applied voltage values are also plot on a single graph as given in Figure 6-50. It is apparent that there is a polynomic relation between the maximum observed strain and the applied voltage.

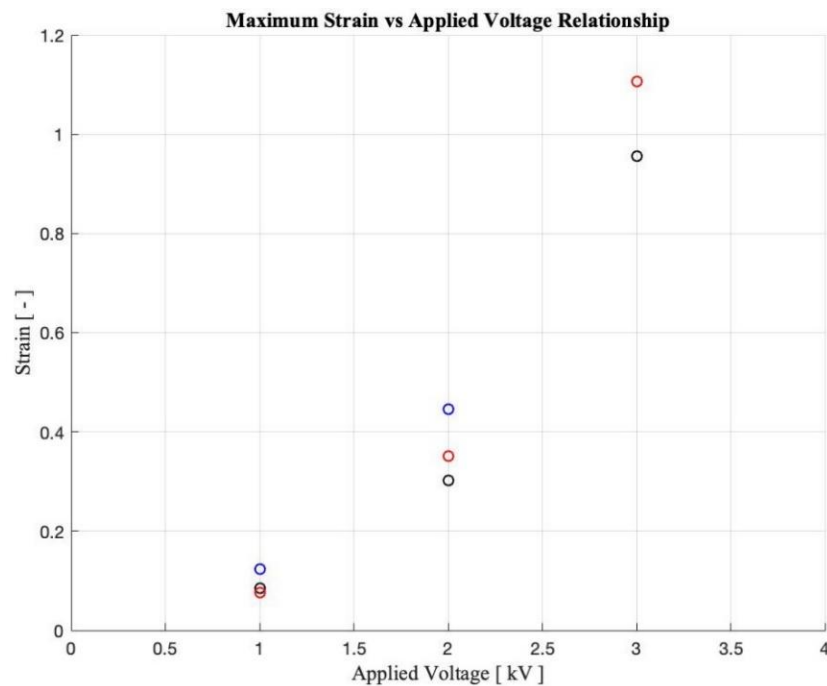


Figure 6-50 DEA applied voltage and observed maximum strain results

In Figure 6-51 (a), (b) and (c), the variation of the normalized strains is given with respect to the applied voltage levels for each applied creep loading. Also, in Figure 6-51 (d), (e) and (f) this also given in the reversed order where the normalized strains are given with respect to the applied creep loading for each applied voltage potential. Meanwhile, the Prony series fit to normalized strain is also given in Figure 6-51 (b) where the results show good agreement with the tests results. It is shown that the

responses in terms of applied voltage and creep loading are sufficient for modelling. The applied voltage versus the measured compliance end force diagram is given in Figure 6-52. The relation can be defined using the equation given in eqn. (6.7-3).

$$F(v) = 0.04687v^3 - 0.041v^2 + 0.06953v - 1.661 \cdot 10^{-16} \quad (6.7-3)$$

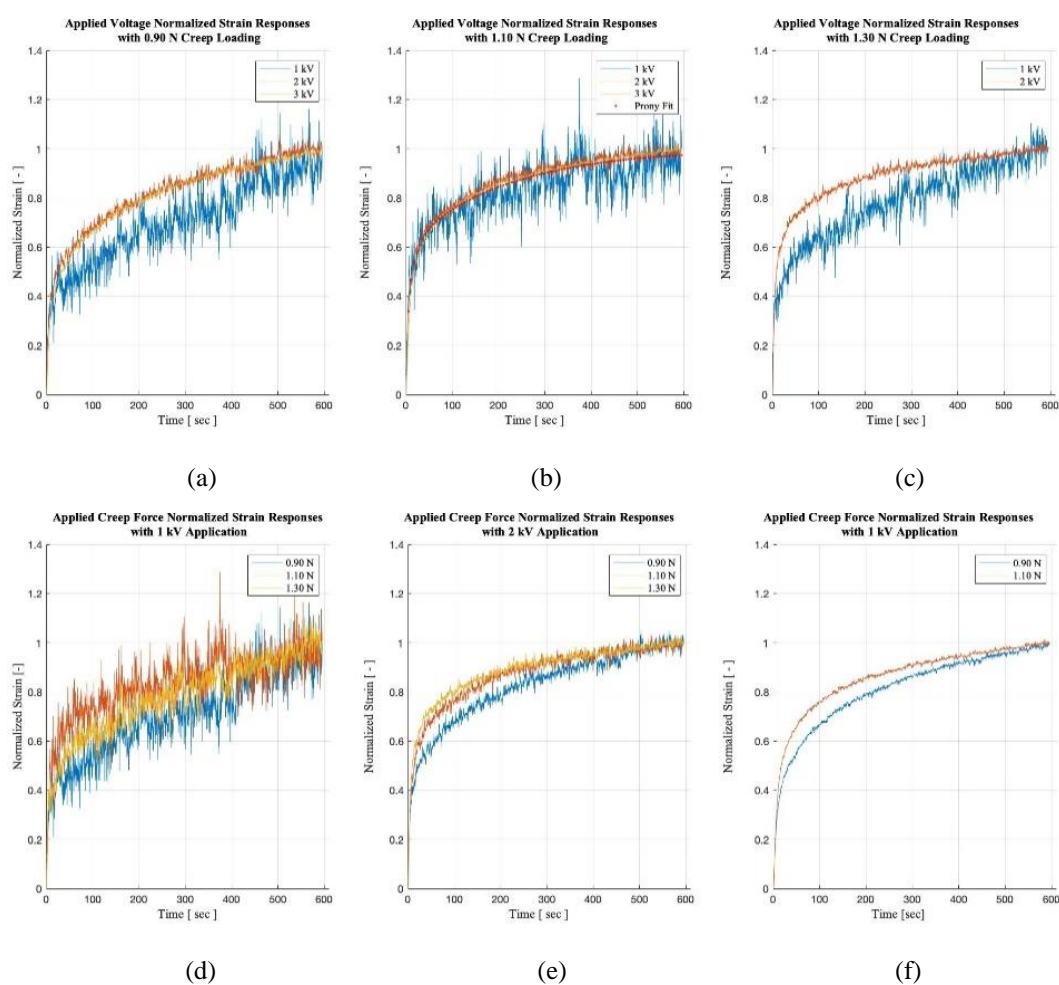


Figure 6-51 DEA voltage induced and creep loaded normalized strain results

The equation provided in eqn. (6.7-3) is obtained using Matlab's Curve Fit Toolbox using the plot given in Figure 6-52. The relation can be used to predict the strain results using just the applied creep loading force (1.1 N is presented) and the applied voltage.

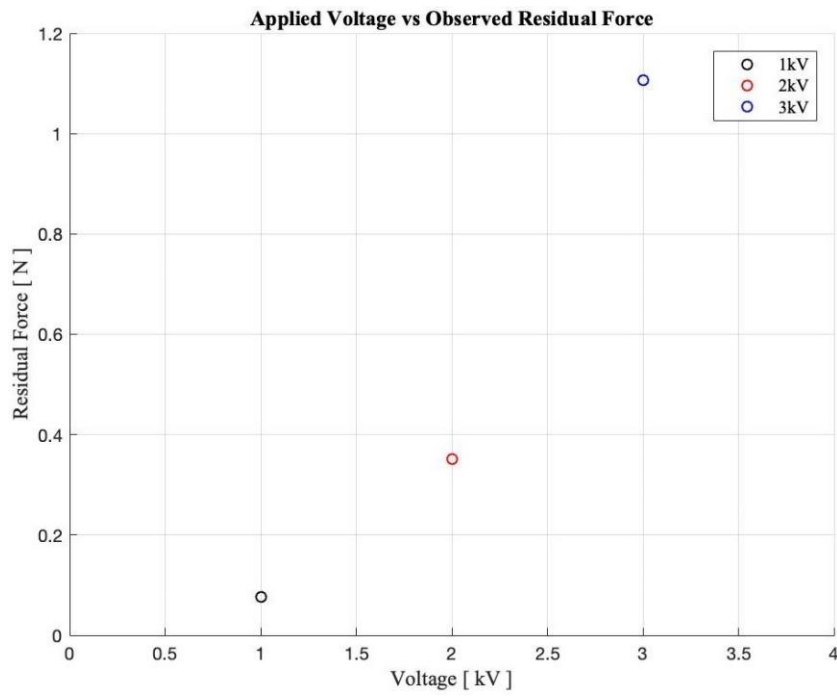


Figure 6-52 DEA applied voltage and residual force relation



## CHAPTER 7

### APPLICATION TO 3D MODEL TRAILING EDGE

#### 7.1. Introduction

The DEA has been tested and mathematically modeled in previous chapters. It is observed that DEA fits to mathematical models but the generated force is relatively low. Note that this low load level is due to use of a single DE layer and the design of the DEA (actuation area and actuation procedure). The use of DEAs today aircrafts is considered to be an emerging topic in the near future. The DEAs can be used where small force generation is acceptable. On the other hand, aviation is a industry where reliability and safety comes first. So, the use of any DEA on aerial vehicles needs to be studied carefully and exhaustively to satisfy reliability and safety concerns. Meanwhile, the current technology of DEAs is not sufficient to cover environmental effects (hot, wet conditions and bird/lightning strike) that an aircraft is subjected to. Thus, the use of a DEA shall be designed to operate within the interior shell. In this chapter, a 3D model trailing edge which is powered by a DEA to provide camber actions is constructed. The developed 3D model is a demonstrative concept design which will be outlined below.

#### 7.2. Trailing Edge Design

The trailing edge of an aerodynamic surface is located at its rear edge. The airflow is separated between the trailing edge and leading edge. 4-digit NACA airfoil 6520 is selected for the shape of the wing cross section and the end %20 portion is considered as its trailing edge. The shape of the NACA 6520 airfoil is defined by the eqn. (7.2-1) where,  $c$  is the chord length ( $c = 1$  is assumed so not shown in equation),  $x$  is the

position along the chord from 0 to  $c$ ,  $y$  is the thickness at the given value of  $x$  and  $t$  is the maximum thickness as a fraction of chord.

$$y = \frac{t}{0.2} [0.2969\sqrt{x} - 0.1260(x) - 0.3516(x)^2 + 0.2843(x)^3 - 0.1036(x)^4] \quad (7.2-1)$$

The  $x$  and  $y$  are defined as the local axis with the nose of the airfoil as the origin of the axis. The first digit of NACA profile specifies the maximum camber in the percentage of the chord, the second digit indicates the position of the maximum camber in tenths of chord and the last two digits provides the maximum thickness of the airfoil in percentage of chord. The schematic view of the described airfoil is given in Figure 7-1.

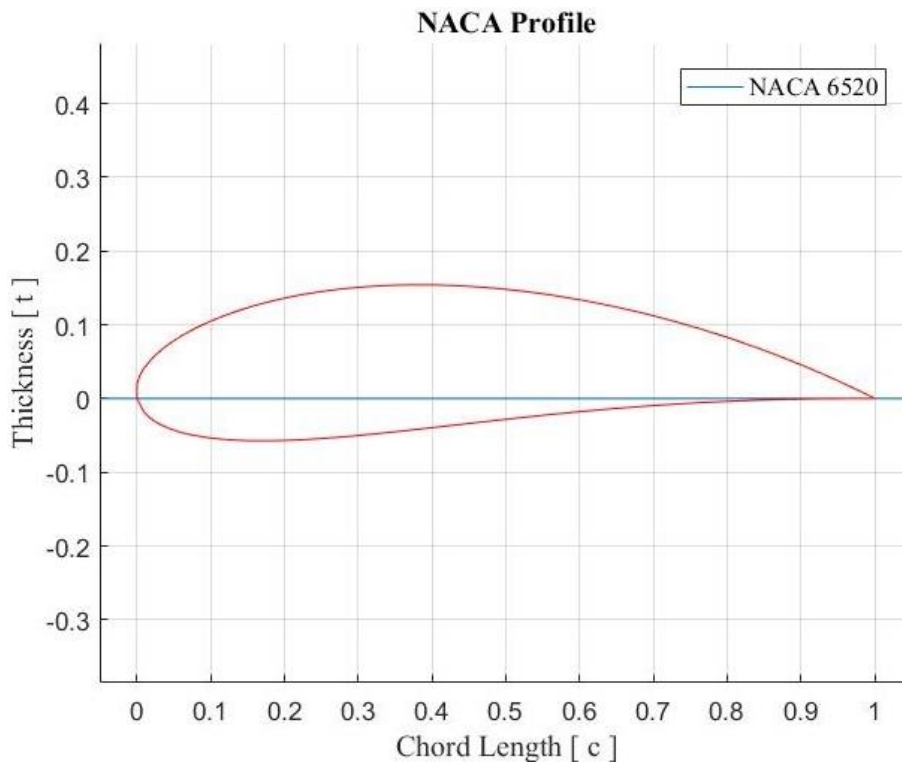


Figure 7-1 Cross section view of NACA 6520 profile

The part between  $c = 0.8$  and  $c = 1.0$  is design as the trailing edge. According to the desired final geometry, the view given in Figure 7-1 can be scaled up. The 3D model design of the airfoil is set to a chord length of 600 mm. The final concept design including the trailing edge addressing is given in Figure 7-2.

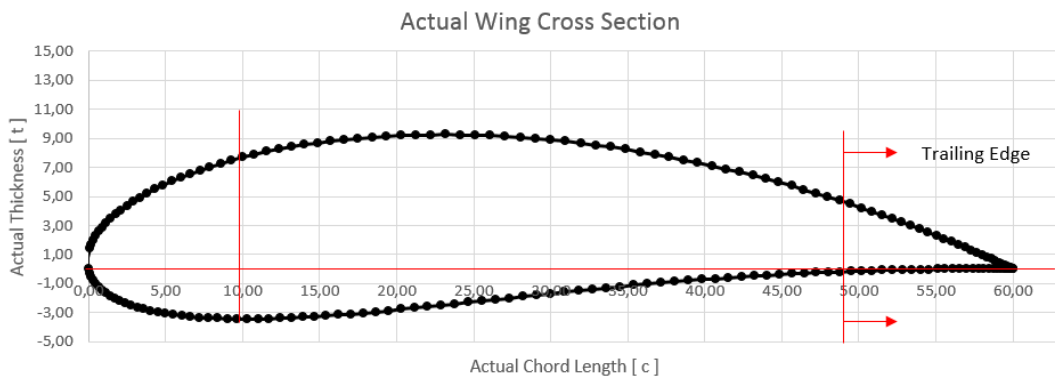


Figure 7-2 3D Model cross section view of NACA 6520 profile including trailing edge location

The aerodynamic surface of the 3D model is designed in CATIA v5 R21. The inner structure of the wing structure is modelled as to support the outer profile by means of T shaped spar designs. The trailing edge is separately modelled and connected to the rest of the profile by a C spar. The final design of the demonstrative wing section is given in Figure 7-3.

The numbered items 1, 2 and 3 are T shaped spar designs. Items 2 and 3 are used for structural stiffening in vertical and horizontal directions. Item 3 is used for wing nose integrity. Item 1 is used both as a structural stiffener and DEA a backup. Item 4 is simple curvilinear element to form the aerodynamic surface. Item 9 consist of four stiffening panels. Two of them located at the bottom and two of them at the top. These panels are design to have stringers to increase stiffness. Item 5 is the trailing edge.

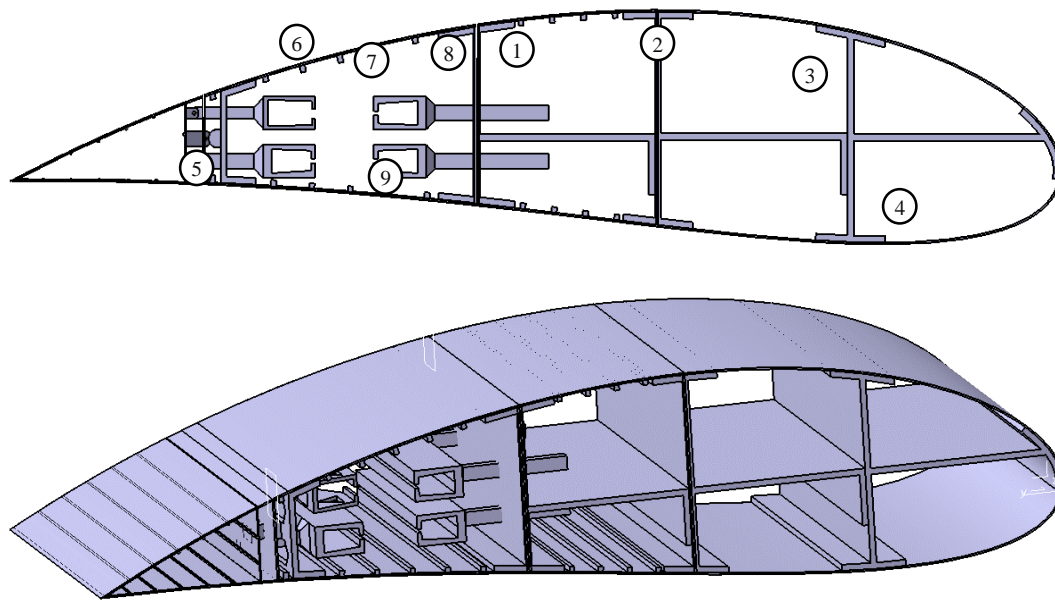


Figure 7-3 3D Model of the wing structure

It has a shell model and also involves stringers. It is connected to item 6 which is a C spar by means of simple joints. Items 7 and 8 are the base mountings to DEAs. The DEA end parts are designed to assemble to the items. Item 8 can be located to the pin holes available at item 8 and the position can be adjusted to tune DEA boundary condition. Meanwhile, item 7 is also connected to item 5, the trailing edge by means of simple joints. The simple illustration is given in Figure 7-4. The design is also valid for the DEAs that will be located at the bottom. The idea behind the design is to active the upper DEA and camber the trailing edge about C spar interface line. The DEA at the lower side can be used to de-camber the trailing edge also. Two DEAs may work simultaneously to rotate the trailing edge to the desired angle position. Note that the width of the 3D model is 240 mm.

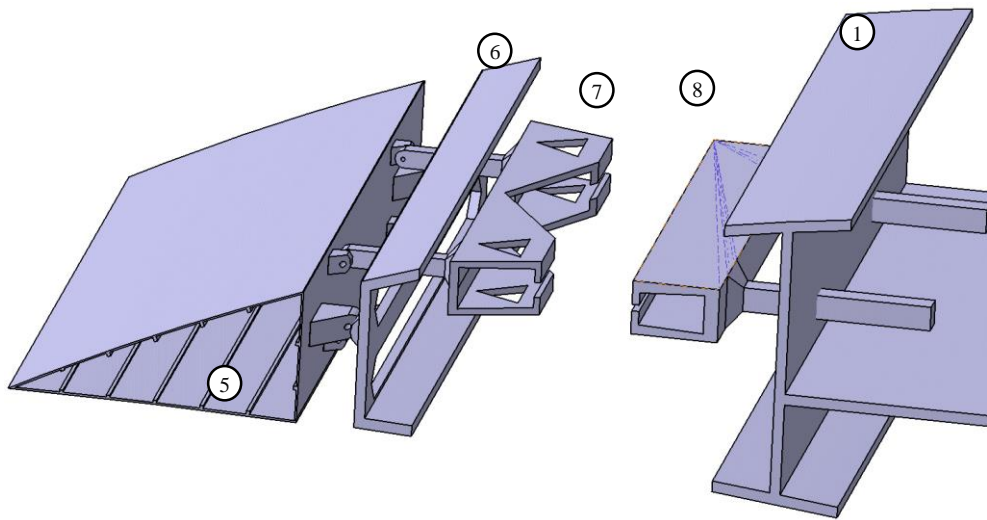


Figure 7-4 3D Model trailing edge installation

The DEA has capable to actuate with low force levels where weight reduction is a serious concern in 3D model design. The trailing edge, item 5, is in a shell form with stiffeners in it and the outer design fits to aerodynamic surface. Item 5 is capable to camber around C spar connection line. The C spar, item 6, has rectangular holes in it as can be seen in Figure 7-4. The DEA active clamp, item 7, is weight optimized. The unnecessary geometric features are cut out. The trailing edge connection is given in Figure 7-5.

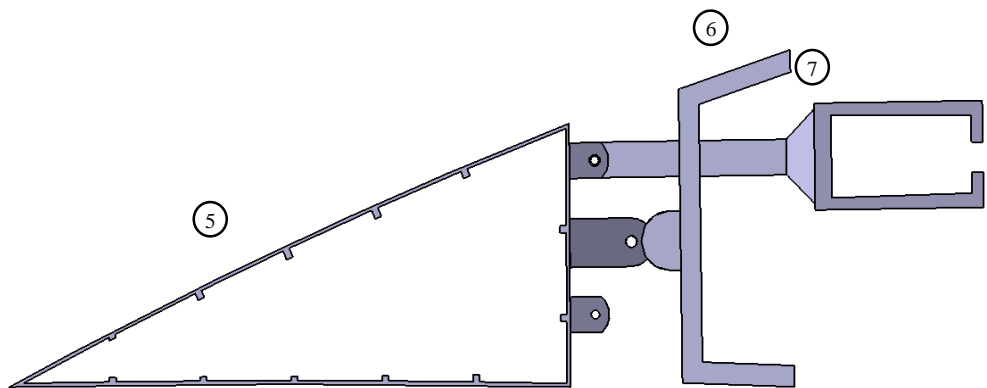


Figure 7-5 3D Model trailing edge connection

### 7.3. Draft Model for Actuation

A balsa wood semi-model of the wing section is constructed. The reason of using a wooden structure is to validate the CAD design and identify the design faults. It is a cheap, easily formable and can be found in any hobby market in different dimensions. Fret saw and sandpaper are enough to cut and shape the balsa wood in desired shape. A super glue provides sufficient bonding strength while assembling the parts. The semi-model without an aero surface but with double DEA installed function simulator wing prototype is sketched in Figure 7-6.

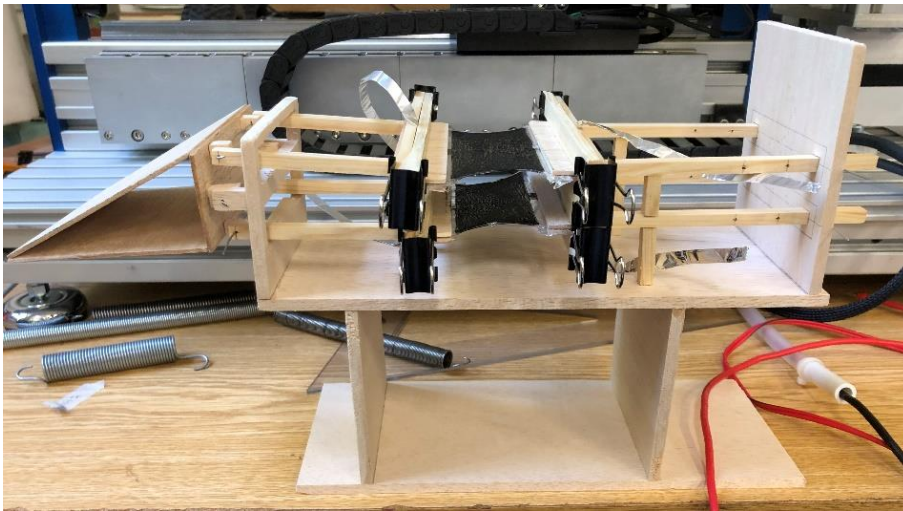


Figure 7-6 Prototype wooden functional model

DEAs for use in the model are manufactured as illustrated in Figure 7-7. These single layered DEAs have 45 mm length in actuation direction and 80 mm width in fixed support direction. Both carbon black and conducting grease electrodes are applied. The miniaturized DEAs installed to wing prototype as given in Figure 7-8. DEAs are attached to designed model via clamps. When the installation is complete the DEAs length was equal to pre-stretch dimension and apparently forced to tear. In original trials, twelve hours later it was observed that the DEAs both on the upper side and

lower side were torn. Multiple DEAs are therefore manufactured to understand possible failures and circumstances before production of 3D wing model. Due that the T spar, item 1 presented in Figure 7-3 is introduced to the original design. The DEAs are let to camber the trailing edge easily. Total force exerted on DEA was 12 gr for plywood trailing edge and 14 gr for clamp support. Two weigh bars (Delrin bars with 28 gr of each) are loaded on the wing to increase the applied force for capability analysis. Wiring route and additional assumptions are determined and tested. Maximum applied voltage potential of 4kV is loaded on both upper and lower DEAs.

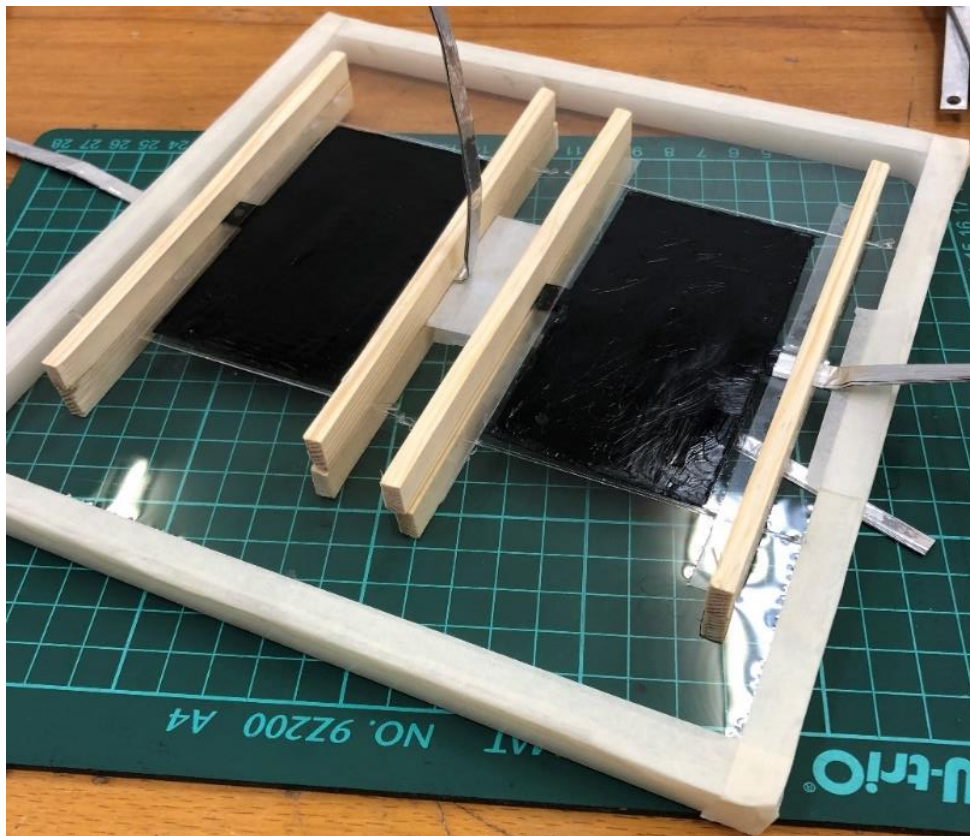


Figure 7-7 DEAs for prototype model

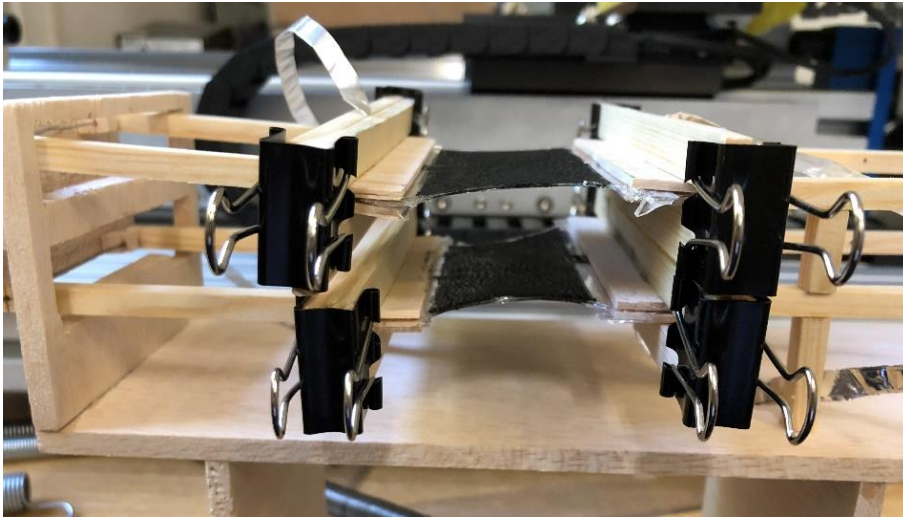


Figure 7-8 Installation of DEAs to prototype model

#### **7.4. 3D Printing and Installation**

Following the finalization of the DEA activation simulations and design validations/corrections, CAD model is updated accordingly. The 3D model of the wing section cannot be manufactured using conventional techniques due to its small and complex geometric features. However, the 3D additive manufacturing technology provides a solution. The main parts CAD drawings of the wing section are all optimized considering manufacturing constraints. Each item part is manufactured by an Ultimaker 3 Extended additive manufacturing machine as given in Figure 7-9 available at METU, Mechanical Engineering Department. Cura 3.1.0.6 software is used to modify and fine tune the items' CAD data. The software communicates with the bench via network. PLA (Poly lactic acid) which has a smooth finish and considerable strength for such a design is the selected 3D printing material. The machine nozzle has a 0.4 mm printing capability which means that the thicknesses of multiples of 0.4 mm has a superior structural integrity. Otherwise, spongy structure is observed within the printed item.



Figure 7-9 3D printing machine

The 3D items, manufactured base of the wing, installation of displacement laser sensor and carbon reinforced plies are installed at Turkish Aerospace Inc. as illustrated in Figure 7-10. The 3D parts are glued and screwed to each other. All sharp edges and aerodynamic surfaces are grinded. The trailing edge is mounted to the hinges located at the two sides of the C spar as given in Figure 7-11 (a). The joint alignment is performed and great care is taken not to cause any kind of stress concentration and friction. The DEA clamp, item 8 (previously given in Figure 7-3) support rods are addressed on the web of I spar in Figure 7-11 (c). The web is drilled for both upper and lower clamps. The clamp rods are also drilled equally with every ten millimeters to ease the adjustment of the clamp as illustrated in Figure 7-11 (d) & (e). This adjustment is required to manually stretch the DEA to a desired level when additional stretch ratio with its related relaxed force. Upper and lower DEA clamps do not touch each other with DEA loaded. The trailing edge is designed to camber and de-camber as sketched in Figure 7-11 (d). On the other hand, as can be seen in Figure 7-10, there

is a skin missing part of the 3D wing model. The missing aerodynamic surface part is formed with two plies of CFRP as provided in Figure 7-11 (e). Thin CFRP can easily be deformed for the designed shape.

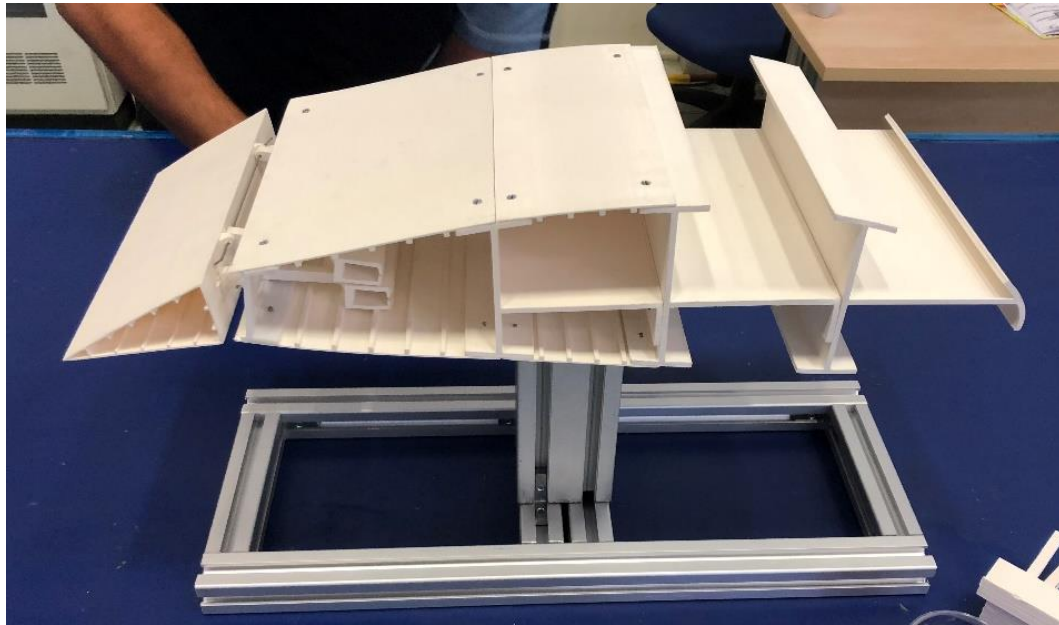


Figure 7-10 Installed 3D manufactured items



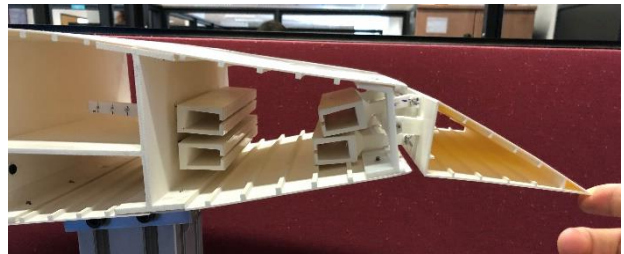
(a)



(b)



(c)

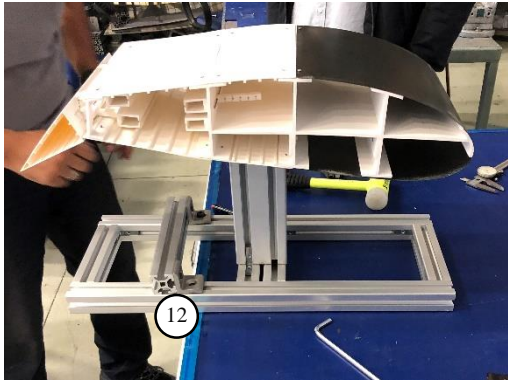


(d)



(e)

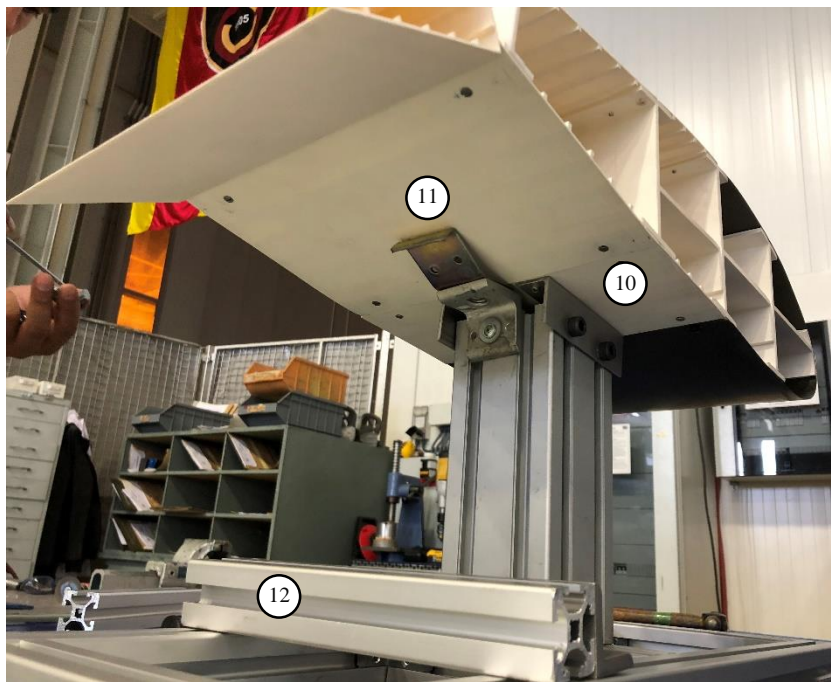
Figure 7-11 Installation details



(a)



(b)



(c)

Figure 7-12 Installation details – sensor mounting

For the designed and installed wing structure, a rigid aluminum frame is manufactured to use as a base frame as illustrated in Figure 7-11 (e) and Figure 7-12 (c). The metallic structure is considered rigid with respect to 3D model wing. Model is connected to vertical metal support via adjustable bolts as illustrated in Figure 7-12 (c), item 10. These adjustable fasteners help to position the angle of attach of the wing. Meanwhile, a support bended thin sheet metal is bolted to vertical stiffer frame as item 11 given in Figure 7-12 (c). Following the installation, it is observed that the back of the model wing cannot sustain wing rigidity so a support element is used and contact is introduced to avoid bending of wing lower panel.

According to the designed test scenario, a displacement sensor is needed to measure the trailing edge deflection. DEA in action will result in camber and de-camber of the trailing edge however the laser sensor will measure the linear vertical translation of the trailing edge in a limited measurement interval. Due that, the sensor needs to be installed as close as to the root of the trailing edge. So, the sensor is mounted on a 5 mm metallic plate as illustrated in Figure 7-12 (b). The plate is installed on a second vertical aluminum strut. The metallic support of the sensor is adjustable in vertical position by screws on vertical strut and the vertical strut which is mounted on to a horizontal strut given in Figure 7-12 (a) & (c) namely item 12. Horizontal strut is capable to traverse along horizontal direction. As a result, the displacement sensor is designed to translate both in horizontal and vertical directions.

The displacement sensor is a laser displacement sensor of Keyence (LK-G32) which is capable to measure  $1/10000$  mm within 7 mm measuring range. On the other hand, the sensor shall be located to a point where the measured object is at least 25 mm far from the laser source. These limitations of the sensor is need high adjustability capabilities when DEA is in action.

### 7.5. Installation of DEA to 3D Model Wing

Following the installation of the 3D model, a single layer DEA is manufactured from VHB 4910 tape. It is initially cut in 55 mm x 55 mm dimensions and pre-stretched 4 times in both length and width directions. The DEA is coated with carbon black and stiffening is sustained at the edges. The wooden sticks are glued to increase support. The final active carbon coated area is 55 mm in length and 140 mm in width direction as illustrated in Figure 7-13.

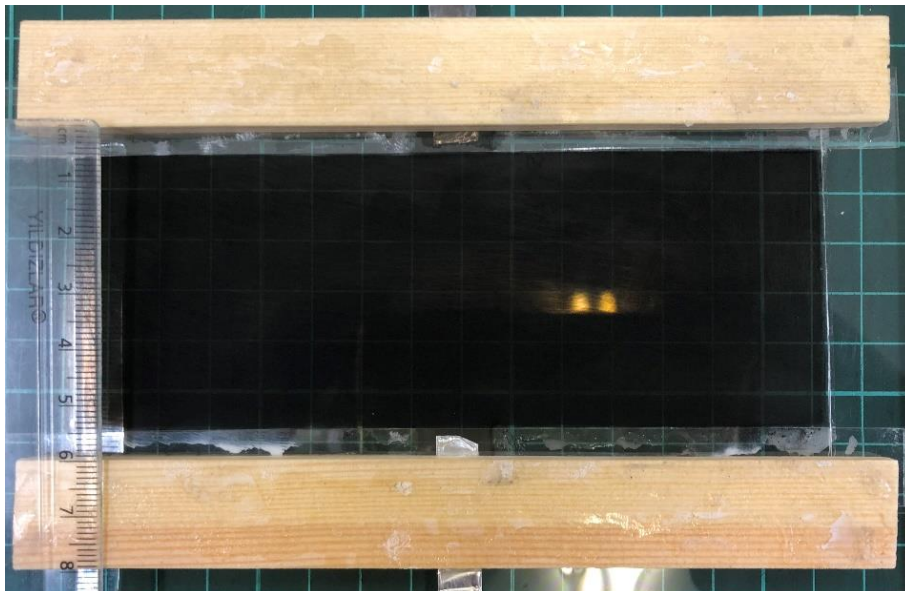


Figure 7-13 DEA actuator

The manufactured DEA is cut from the frame. The measured mass of DEA is about 41 gr. including the wooden supports. The installation of DEA to 3D wing model is given in Figure 7-14 and Figure 7-15. Meanwhile, the grippers to mount the DEA which are clearly shown in Figure 7-15 weighs about 28 gr. The grippers are designed for weight optimization and capable to mechanically locking the DEA. Many 3D printed trailing edges design is tried to decrease the weight.



(a)

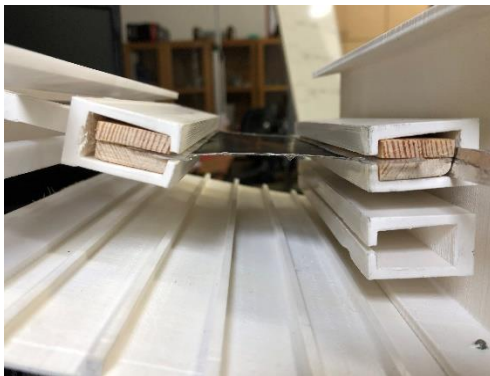


(b)



(c)

Figure 7-14 DEA installed trailing edge configuration



(a)



(b)

Figure 7-15 DEA installation

The first 3D printed model of the trailing edge was 95 gr which has a 2 mm shell thickness, the final 3D printed trailing edge weigh about 46 gr. with 0.6 mm shell thickness. Although the DEA can lift all trailing weights as demonstrated on the test, due to the installation of trailing edge, the moment exerted has higher final force on DEA.

The stretch ratio of DEA can be adjusted using the gripper's support position. The DEA as installed and shown in Figure 7-15 has a stretch ratio of four. When the DEA is mounted between the grippers, the counter force generated by DEA naturally lifts the trailing edge as illustrated in Figure 7-14 (c). When the voltage potential is applied, the elongation of DEA will camber and de camber the trailing edge. Note that in Figure 7-14 (b), the installation of laser displacement sensor is set close to the trailing edge root location to measure the minor angular changes as vertical displacements.

## 7.6. Mathematical Modeling of DEA and Trailing Edge

The mathematical modeling of the trailing edge is limited by the static validation of the applied loads. As sketched in Figure 7-16, the trailing edge connection to DEA is presented in wireframe form. The red lined plot indicates the de-cambered position of the trailing edge with respect to angle,  $\theta$ . The mass of the wing,  $m_w$  and the sum of the masses of linkage element and DEA support,  $m_s$  are lumped at theoretical center of gravity positions. The center of gravity and related geometrical properties are obtained from CATIA software. The elastic force,  $F_E$  exerted by DEA is as illustrated in Figure 7-16. For the sake of simplicity, the elastic force,  $F_E$  is assumed to be horizontally guided where the internal DEA force as generated when installed is sufficient enough to hold the assumption true. The minor deflections due to joint is omitted within the calculations.



The position vector from joint,  $O$  to the center of gravity of support linkage can be defined in eqn. (7.6-3).

$$\begin{aligned}
 \vec{r}_{o,s} &= \vec{r}_{o,b} + \vec{d} \\
 \vec{r}_{o,s} &= \vec{r}_{o,b} + [d\cos\beta(\vec{i}) - d\sin\beta(\vec{j})] \\
 \vec{r}_{o,s} &= [(b-c)\cos\theta + a\cos(90-\theta) + d\cos\beta](\vec{i}) \\
 &\quad + [(c-b)\sin\theta + a\sin(90-\theta) - d\sin\beta](\vec{j})
 \end{aligned} \tag{7.6-3}$$

The position vector from joint,  $O$  to the end of support linkage where the elastic force,  $F_E$  acts can be defined in eqn. (7.6-4).

$$\begin{aligned}
 \vec{r}_{o,e} &= \vec{r}_{o,b} + (\vec{d} + \vec{e}) \\
 \vec{r}_{o,e} &= \vec{r}_{o,b} + [(d+e)\cos\beta(\vec{i}) - (d+e)\sin\beta(\vec{j})] \\
 \vec{r}_{o,e} &= [(b-c)\cos\theta + a\cos(90-\theta) + (d+e)\cos\beta](\vec{i}) \\
 &\quad + [(c-b)\sin\theta + a\sin(90-\theta) - (d+e)\sin\beta](\vec{j})
 \end{aligned} \tag{7.6-4}$$

Due to the constraint motion of DEA in direction,  $i$ , the following eq. (7.6-5) holds.

$$\sin\beta = \frac{[(c-b)\sin\theta + a\sin(90-\theta)] - g}{(d+e)} \tag{7.6-5}$$

For static equilibrium, total moment given in eqn. (7.6-6) shall be satisfied. The parametric dimensions required for vector calculations are given in Table 7-1.

$$\begin{aligned}
 \vec{M} &= \sum_{i=1}^n \vec{r}_i \times \vec{F}_i \\
 \vec{M} &= \vec{r}_i \times \vec{F}_i = \vec{r}_{o,cg_w} \times \vec{F}_w + \vec{r}_{o,s} \times \vec{F}_s + \vec{r}_{o,e} \times \vec{F}_s
 \end{aligned} \tag{7.6-6}$$

Where, trailing edge mass including the joint element masses is  $m_w = 49 \text{ gr.}$  and the support element including one of the DEA support member masses, is  $m_s = 48.5 \text{ gr.}$

Table 7-1 Dimension parameters of the trailing edge connection

Dimension	Value [mm]	Dimension	Value [mm]
c	15.65	a	15.10
l	12.16	b	4.00
f	17.45	d	20.00
e	5.00	g	5.00

For the analysis purposes, the kinematics of trailing edge (solely frictionless and without manufacturing defects assumption) is modelled in Matlab. The motion of the trailing edge using the parameter set given in Table 7-1 with respect to applied angle theta,  $\theta$  is provided in Figure 7-17. Note that the angle,  $\theta = 0$  is the trailing edge is parallel to ground and given in black color and the angle,  $\theta = 45$  position of the system is given in red color.

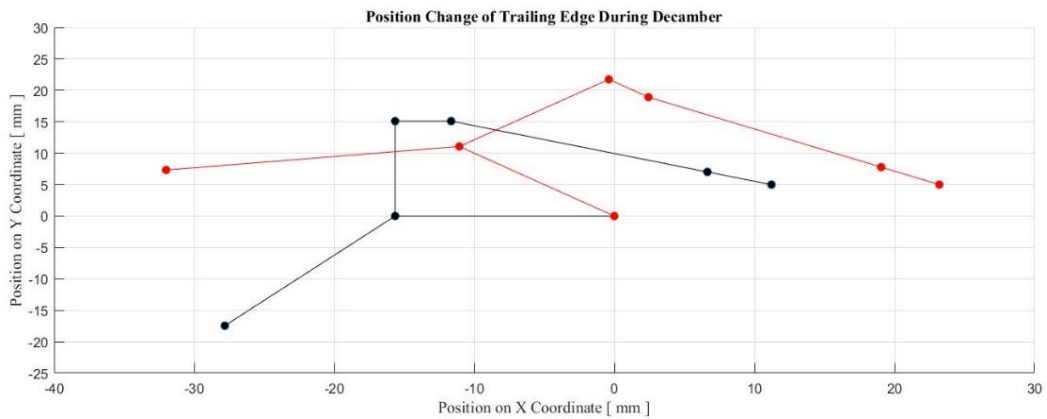


Figure 7-17 Kinematic illustration of trailing edge on Matlab

According to the kinematics of the trailing edge mechanism, a static moment analysis performed. The known parameters are the trailing edge and the support element's mass and the elastic force,  $F_E$  is unknown. The static balancing values of DEA force,  $F_E$  is solved for each angle,  $\theta$ . It should be noted that due to rotational motion, the moment of weight about pivot point,  $O$  is not constant. As the trailing edge cambers, the

moment balance varies. The moment distribution of joint elements are provided in Figure 7-18. While maintaining the total moment balance equal to zero, the variation of the joint elements are calculated. To counter balance the trailing edge moment, the support element and DEA works together. Support element is a natural moment generator in the system. The moment due to DEA is illustrated in the figure with red color which is a function of the angle,  $\theta$ .

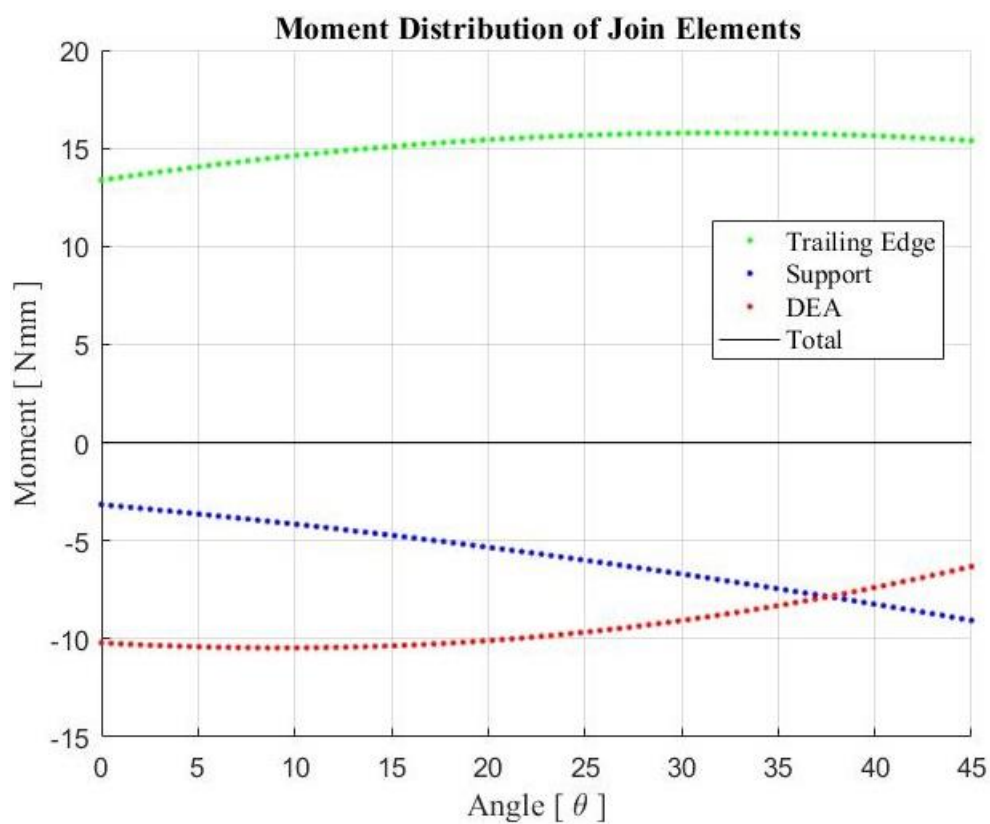


Figure 7-18 Moments generated due to trailing edge rotation

When the required DEA moment to balance the trailing edge at the specified angle,  $\theta$  is converted to required force needs to be sustained in the system, the resulting force levels are obtained and presented in Figure 7-19.

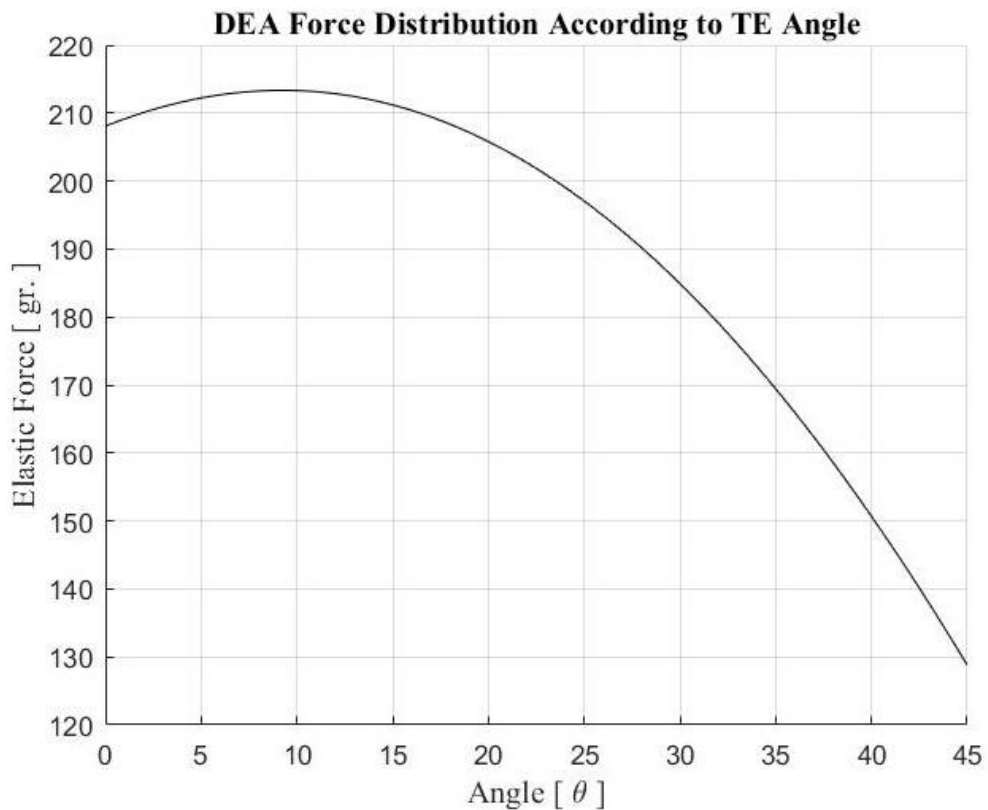


Figure 7-19 Required DEA force according to trailing edge angle,  $\theta$

Note that the force required on DEA is very sensitive to system design and will be affected from equipment design. The required force of DEA does not provide an idea what kind of DEA shall be used. On the other hand, the required amount of stretch can be adjusted to maintain this force. In Figure 7-20, according to the design geometric parameters of the trailing edge mechanism, the required stretch variation with respect to trailing edge rotation is provided. The given force and stretch ratio values highly affected from the initial pre-stretch and DEA design geometries.

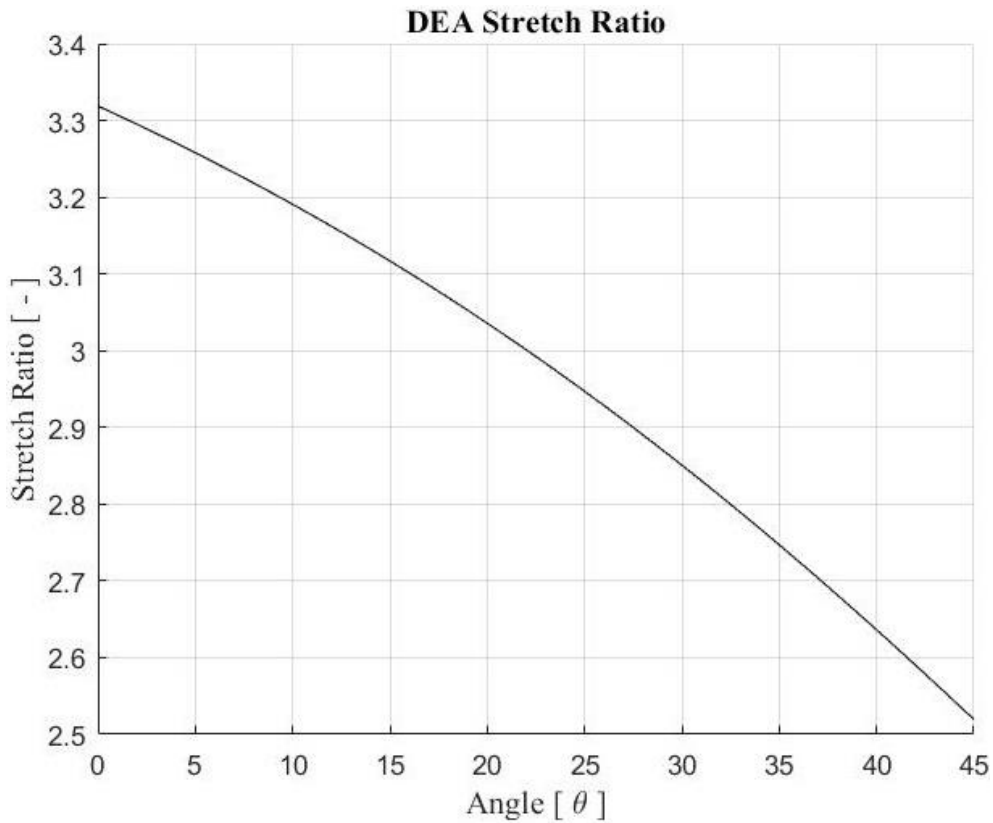


Figure 7-20 Required DEA Stretch Ratio according to Angle,  $\theta$

Considering the above given information, it is possible to say that a 4 x 4 pre-stretched single layer DEA can sustain the required force at the limit levels. The required stretch ratio is close to the design stretch levels.

### 7.7. Simulation and Control

Galil controller is used in real time simulations. Galil controller's one of analog output is set for high voltage application. Also, the controller's analog input is reserved for high voltage applied voltage reading. The high voltage amplifier, TREK Model 10/10B-HS, has the capability of output the applied voltage and current as a control signal. The processing of applied current may lead the researcher for various self-

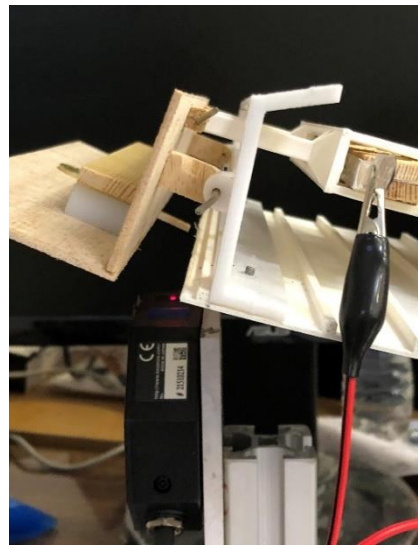
sensing applications. In the scope of this study, the wiring to read applied current value is maintained but was not used.

The Matlab software is used to design an interface between Galil controller and PC. For control purposes, the user is able to send and receive commands using Galil tools library deployed in Matlab.

The laser displacement sensor is mounted under the trailing edge. Due to limited measurement range and installation constraints, a fin (thin smooth wooden part) is attached to the bottom of the trailing edge as illustrated in Figure 7-21 (a) & (b). To measure the large span of the rotation angle using the vertical displacement, the use of fin is essential. The laser sensor outputs between 9.28 V and -9.48 V at the top and bottom measurement points. As long as the output voltage is linear with the measured distance as experienced, however, it is noticed that the angle of rotation of the trailing edge is not linear with the sensor output. The geometric sketch is fin, trailing edge and the sensor is given in Figure 7-22. Due to rotational motion, the large rotation angle is should be estimated with small vertical displacement results. In Figure 7-22, red continuous line through point,  $n$  indicates the sensor measurement direction. When the trailing edge rotates, the point,  $n$  translates to point,  $n'$ . The distance of point,  $n'$  to the initial base line of the trailing edge is denoted by,  $W$  which is larger than the actual sensor measuring point. The actual sensor measuring point is  $d$  distance far away from the initial base line of the trailing edge.



(a)



(b)

Figure 7-21 Sensor positioning and fin attachment

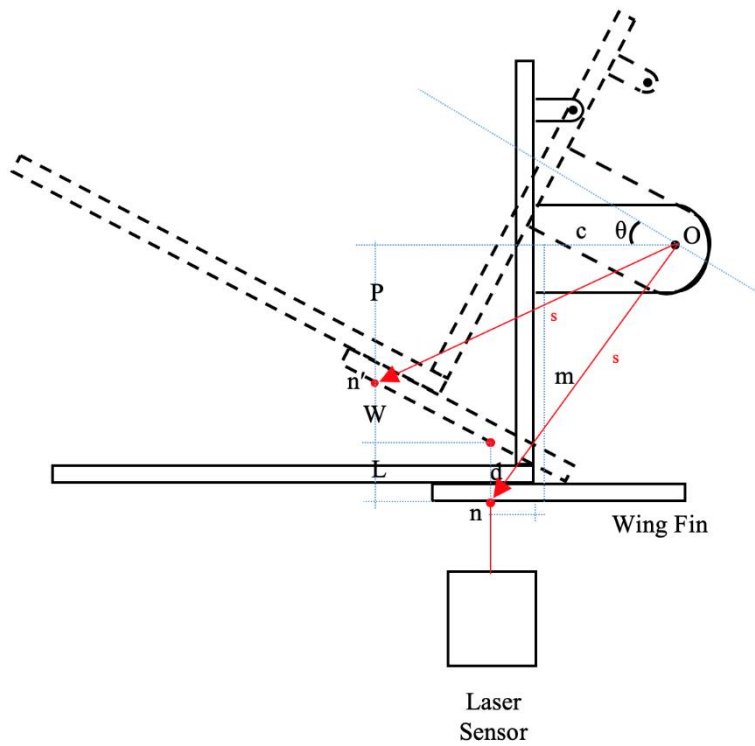


Figure 7-22 Sketch of sensor and fin position

The point,  $n$  rotates about point,  $O$  which is the trailing edge connection to C spar. The length,  $P$  is the distance of point,  $n$  with respect to the line passing through point,  $O$ , while the vertical lengths,  $W$  and  $L$  denotes the lengths from point,  $n'$  to current sensor position and to base line of the trailing edge. The following mathematical interperations applies.

$$W = m - d - P_j \quad (7.7-1)$$

Where,  $P_j = [(c + n)\sin\theta - m\cos\theta]$  denotes vertical distance.

$$K = P_i - (n + c) \quad (7.7-2)$$

Where,  $P_i = [(c + n)\cos\theta + m\sin\theta]$  denotes vertical distance. So, analogously,

$$\tan\theta = \frac{W}{K} = \frac{m-d-P_j}{P_i-(n+c)} \quad (7.7-3)$$

No explicit solution exists for the eqn. (7.7-3). Thus, the above given equations are numerically solved by assigning value to angle,  $\theta$  in the range of 0 to 45° to find corresponding sensor read distance,  $d$  which is given in Figure 7-23.

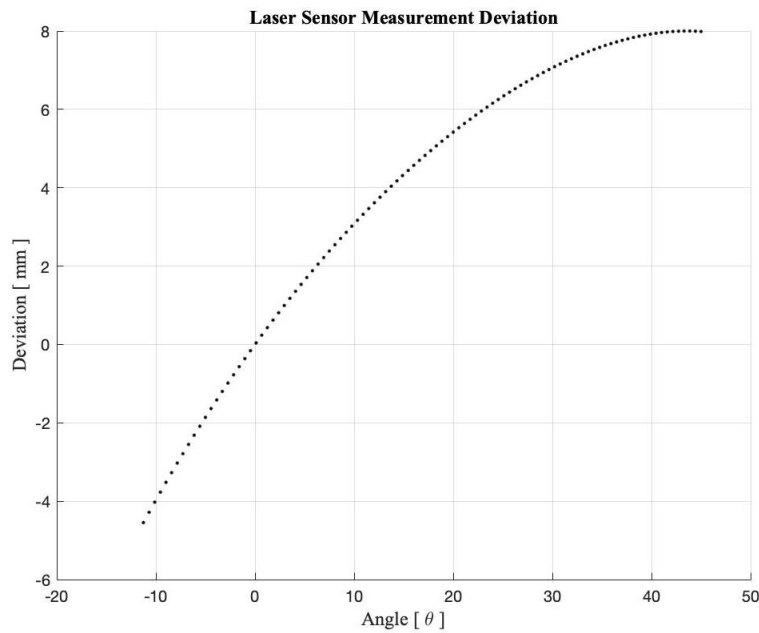


Figure 7-23 Sensor measurement vs angle deviation

Using Matlab, a GUI is scripted to run the simulation of the trailing edge as presented in Figure 7-24. Using the GUI, high voltage can be manually to DEA with a horizontal scroll bar. The scroll bar can sustain DC high voltage either in 1 kV or 100 V step inputs. To ease the installation of the laser sensor and able to study different angle spans, the sensor initial read position is set as a variable. The period of measurement is a user defined parameter where sensitivity is required. On the other hand, high data transmit frequencies both increase the noise and computational effort which results in poor performance while plotting the responses. It also possible to apply constant DC high voltage using the GUI. The applied voltage level on DEA is also feedback to GALIL controller to monitor the applied DC voltage input to DEA.

Using the laser sensor measurement, a target distance relative to the wing position can be set and the GUI computes the relative error which can be used in control purposes. The voltage application module of GUI is structured in outlined in Figure 7-25.

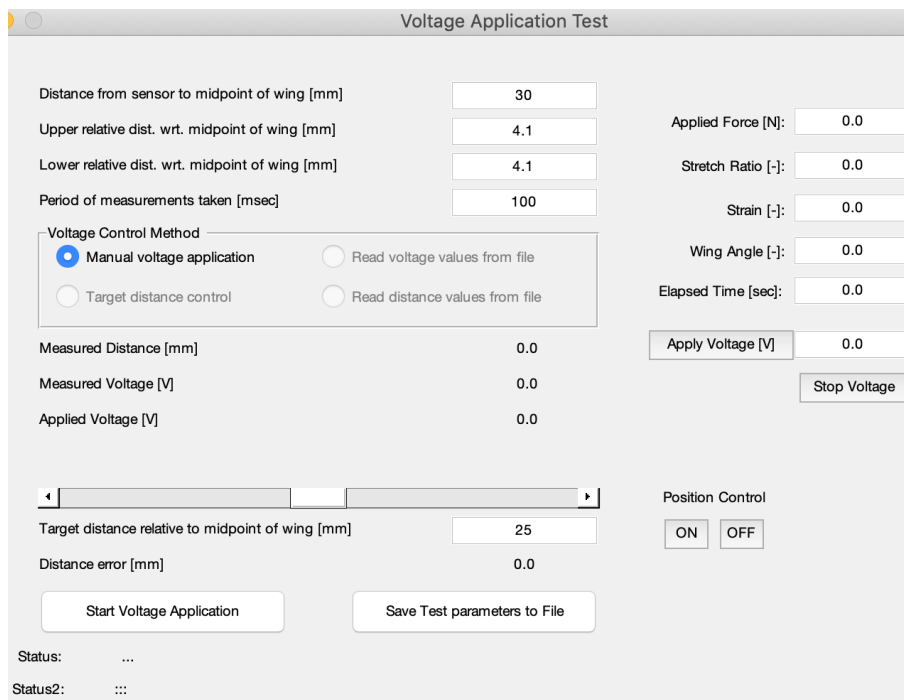


Figure 7-24 Matlab GUI for real time simulation

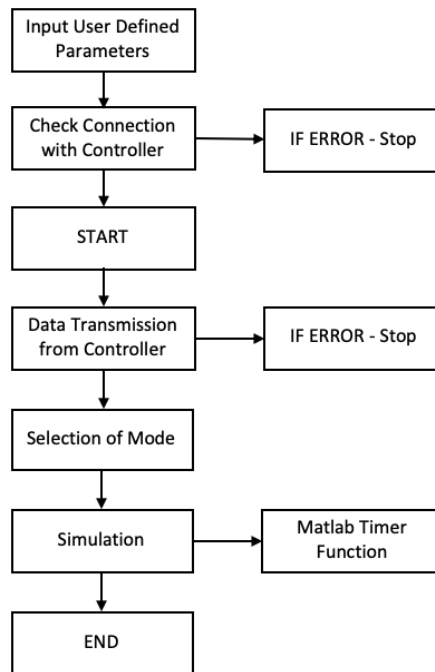


Figure 7-25 Structure of voltage application module

It should be worth noting that the main objective of this exercise is to demonstrate DEA can be used in a controlled environment rather than the development of a sophisticated control algorithm. Therefore, a relatively simple closed loop position control is applied and the mathematical models of DEA is in line with the trailing edge motion.

The control scheme includes the followings as well; the displacement sensor measures the position of the trailing edge. The measured distance is converted to angle,  $\theta_{cur}$  using the eqns. (7.7-1) to (7.7-3). The error,  $\Delta\theta$  between the reference,  $\theta_{ref}$  and the measured angle,  $\theta_{cur}$  is computed. The control of the DEA is sustained by a Proportional controller. The applied control block diagram is as given in Figure 7-26. The gain of the proportional controller,  $K_p$  is selected as 0.1 to prevent damage to the DEA during operation.

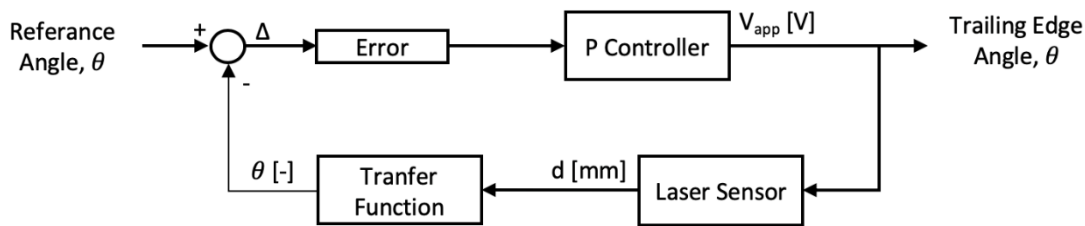


Figure 7-26 Control block diagram

In proportional control, the current stretch ratio,  $\lambda_{cur}$  and the target stretch ratio,  $\lambda_{tar}$  of the DEA are both calculated using the measured angle,  $\theta_{cur}$  and reference angle,  $\theta_{ref}$ . The applied voltage,  $V_{app}$  is determined by the controller. After the high voltage is applied, new error angle value,  $\Delta\theta$  is obtained and the procedure is continued until the error angle,  $\Delta\theta$  is bounded within a predefined limit. As the DEA continues to creep, the applied voltage value is adjusted accordingly.

As given in Figure 7-25, the GUI involves Matlab timer function which is used in real time applications. A single timer function is used to execute all the tasks. The modules of the timer function are illustrated in Figure 7-27.

The timer function communicates with GALIL controller and transmits the controller time,  $t_c$ , applied DEA voltage,  $V_{app}$  and the laser sensor voltage,  $V_{sen}$  data. The received data is converted to processible vector arrays.

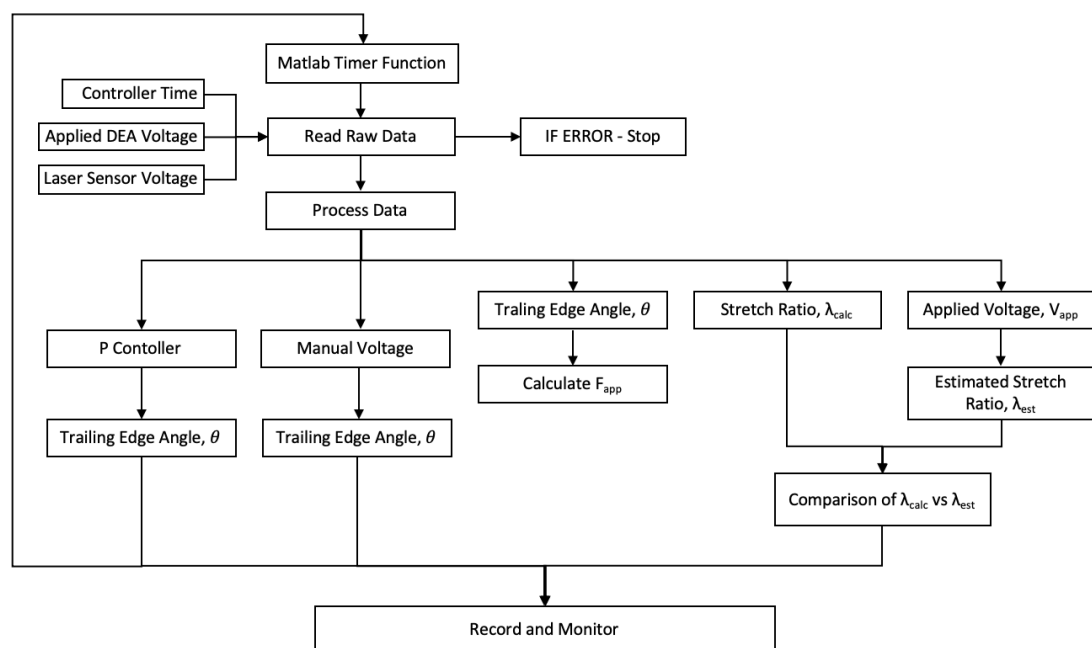


Figure 7-27 Main execution tasks of the GUI voltage module

On the other hand, due to test setup's geometric limitations, it is not possible to use a force gauge attached to the DEA. The load on the DEA during actuation cannot be determined in real time. Additionally, the stretch ratio of the DEA can only be estimated since it is impossible to measure DEA strain during high voltage application. As a consequence, the creep DEA model cannot be used directly. Meanwhile, a slight downwards deflection at the connection of the DEA to the support element is

observed. Friction exists at the joints of the assembly due to manufacturing and installation uncertainties. The effect of these parameters is assumed to be small and neglected.

It is previously shown in Chapter 6.7 that DEA strain response to voltage induced creep experiment can be divided into two. The first one is the strain response to applied creep load and the second one is the strain response to applied voltage. In wing demonstrative 3D model, there is no possibility to measure the creep loading force. On the other hand, the load on DEA is not constant as previous experiments demonstrated. Due to rotational motion of the wing, the applied loading varies. On the other hand, there is only one displacement sensor located to measure the rotational movement of the wing. Thus, using the kinematic analysis of the structure is the only method to estimate the straining (stretching) of the DEA. In Chapter 6.7, it is shown that, the applied voltage effect on DEA can be estimated correctly whatever creep load is applied. It means that the uncertain or varying creep loading of DEA on the wing structure do not affect the applied voltage response. Using the kinematic equations and the solely voltage response functions, the actual and mathematically estimated straining of DEA shall be coincident. 1 kV and 2 kV step voltage inputs are applied to the DEA on wing structure which are given in Figure 7-28 and Figure 7-29 where black lines indicate the DEA actual strain response according to kinematic analysis and the red lines indicate the estimated voltage strain response. As can be seen from Figure 7-29, the error between the actual and estimated strain increases at high applied voltages.

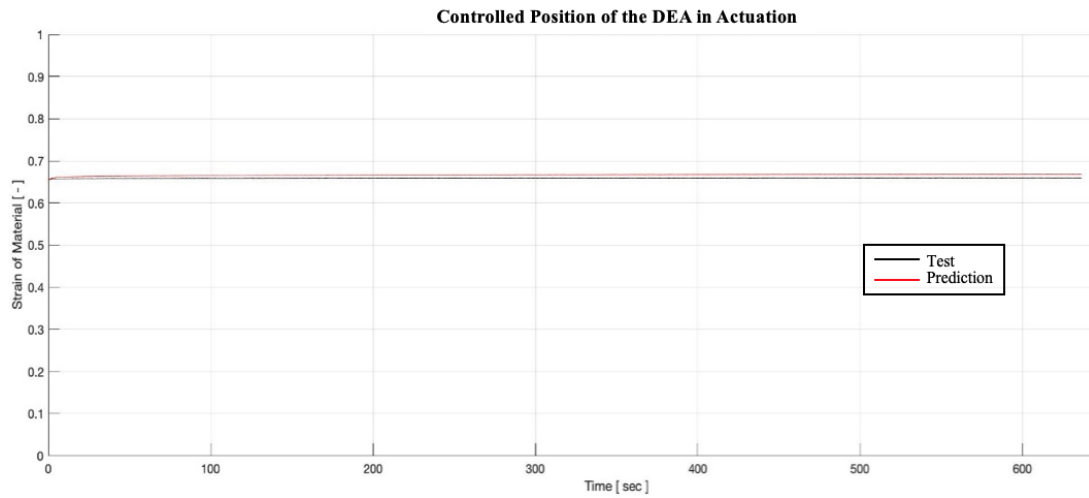


Figure 7-28 The response of DEA to 1 kV applied step voltage

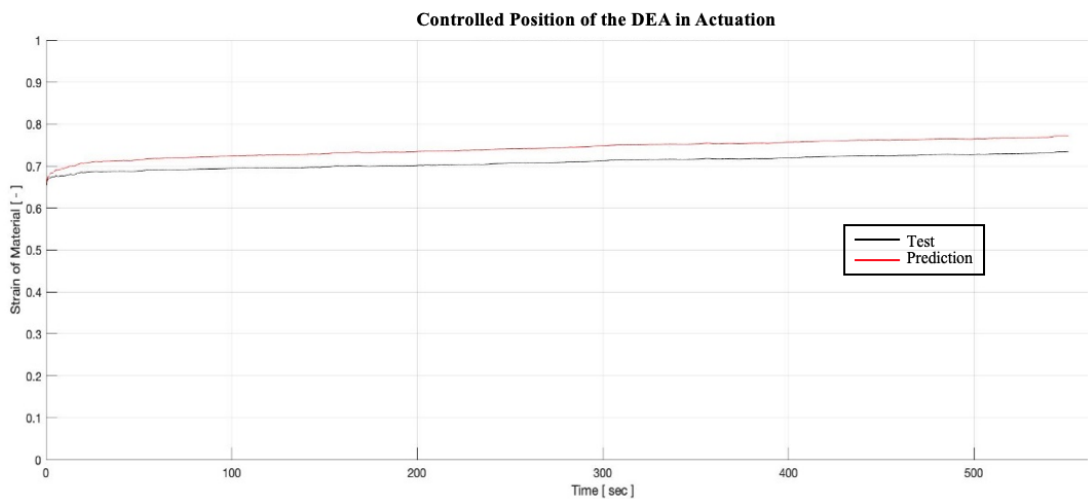


Figure 7-29 The response of DEA to 2 kV applied step voltage

When the DEA is installed on the wing structure, due to installation and geometric constraints, DEA stretches itself resulting in trailing edge to be positioned at 35 degrees upwards which can be illustrated as given in Figure 7-22 setting the  $\theta = 35$  degrees. Note that the  $\theta = 0$  degree position corresponds to the trailing edge's lower surface horizontally aligned. Starting from  $\theta = 32.5$  degree, a series of tests are

performed where the trailing edge mechanism so the corresponding DEA is let to rest for two minute and then step voltage is applied starting from 0 with 500 V increments up to 2500 V for two more minutes. At the end, the applied voltage is removed and the trailing edge is returned to its stabilized position. Note that, the residual angular positions are due to moment balance and friction. No more than 2500 V is applied to DEA due to safety concerns and not to damage the DEA. The angular position result of trailing edge to applied step voltages are given in Figure 7-30. As seen, trailing edge responded to 0.5 and 1.0 kV DEA step activations very limited while the maximum angular displacement is observed at 2.5 kV. Minor deviations are observed at the response plots due to instantaneous laser sensor reading errors.

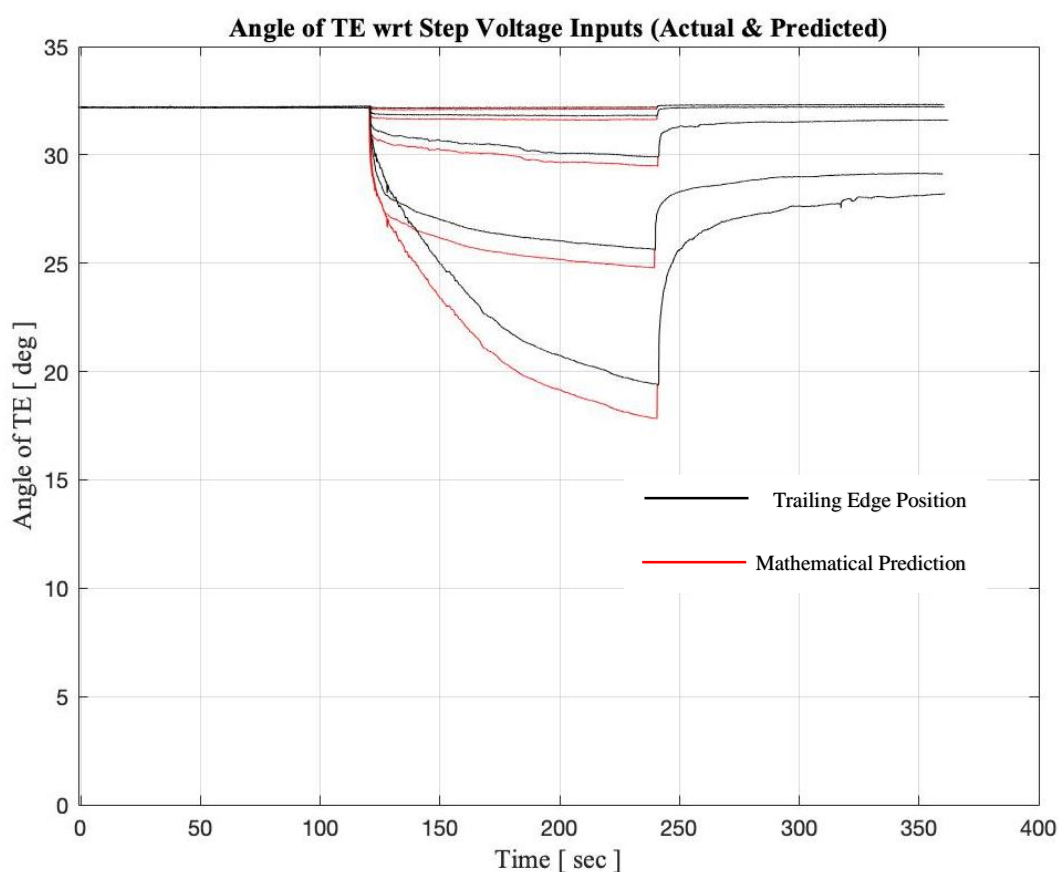


Figure 7-30 The angular response of TE to applied step voltages

In Figure 7-30, maximum angular position prediction error is 2 degree at most with applied 2.5 kV step input. This error shall be increased with larger applied voltages and voltage application duration. But note that the error presented is with the mathematical formulation obtained in Chapter 6.7. A more robust parameter estimation can be performed directly using the response values of DEA as installed on trailing edge. But re-estimation of parameters is not performed in this study to emphasize the unique performance of the material characterization and modeling method. Meanwhile, two minutes of response observation time is sufficient in order to understand the motion characteristics. The predicted and actual motion both performs similar. On the other hand, reader should note that, only the response of DEA to applied voltage is analyzed in this study.

Using the results illustrated in Figure 7-30, a simple angular position and applied voltage relationship can be constructed as given in Table 7-2.

Table 7-2 Angular displacement and applied voltage relationship

Applied Voltage [kV]	Actual Angular Change [deg]	Estimated Angular Change [deg]
0	0°	0°
0.5	0.1°	0.2°
1.0	0.4°	0.6°
1.5	2.3°	2.7°
2.0	6.5°	7.4°
2.5	12.8°	14.4°

The straining of the DEA is expressed with the appropriate Prony series functions which are previously evaluated in Chapter 6.7. In these functions, strain is the calculated variable where the applied voltage value with the time induced Prony series is the input. It means that, it is easy to estimate the straining using formula input parameters; on the other hand, estimation is very cumbersome if it is required to change the voltage as a calculated variable with the applied strain (angular position) is the input. Using the in Table 7-2, it is easy to define a relation between the angular

effect of the applied voltage using an exponential function where both with Prony series can be used in modeling purposes. The two term exponential function fit is applied using Matlab Curve fit tool box and the resulting equation is given below

$$\theta(V) = ae^{bx} + ce^{dx} \quad (7.7-4)$$

Where,  $a = 1.405$ ,  $b = 0.04605$ ,  $c = -1.362$  and  $d = -3.187$  within a %95 confidence bound. The result of the fit is illustrated in Figure 7-31.

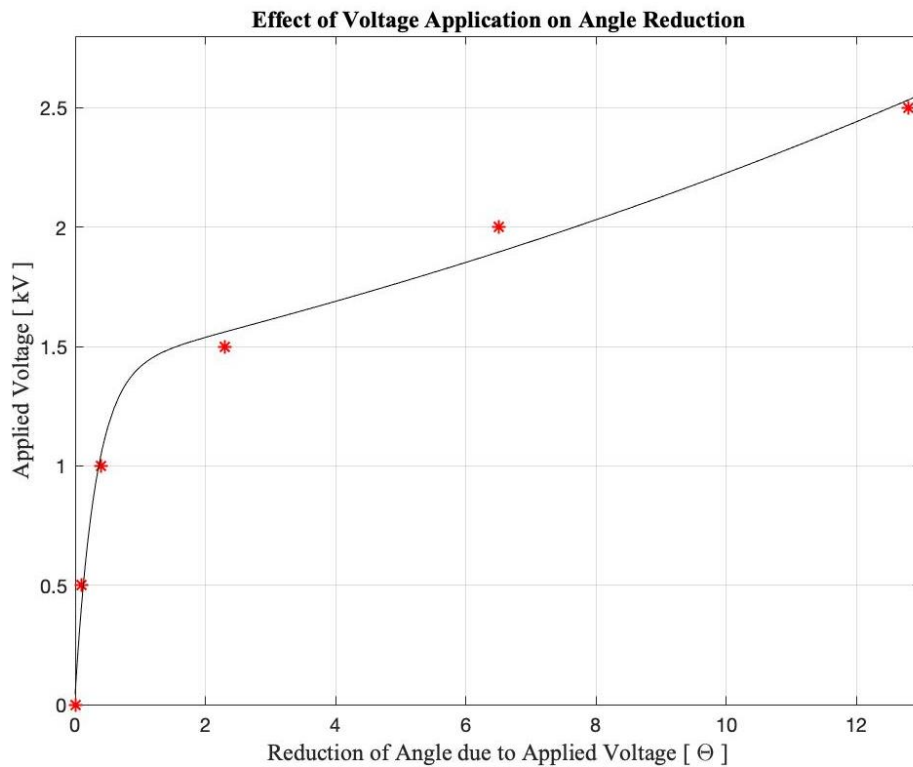


Figure 7-31 The angular reduction of TE with applied step voltage inputs

The equation formulated in eqn. (7.7-4) is used to position the trailing edge to the desired position. The plot provided in Figure 7-31 shows the effect of applied voltage on angle change. All angle reductions are started from  $\theta = 32.5$  degree and the final

difference angle value is considered at the end of two minutes simulation. It is straight forward to say that keeping the step input value for a much longer time would result higher angle differences. The difference between the input reference and the observed trailing edge angle suits to mathematical model which means that it is possible to design the curve given in Figure 7-31 according to specific needs for wider application regime.

Finally, a control demonstration is presented to camber trailing edge using the procedure outline above. The logic of proportional controller is established. At a given current angle of trailing edge, if a target camber angle is provided, the controller inputs the required amount of voltage based on the equation given in eqn. (7.7-4) using the calculated error angle (reference angle – target angle) computed in Matlab. A proportional constant of 3 is used in all demonstrations due that as the error value gets smaller the controller provides less amount of voltage to DEA. It is noticed that if a unity proportional constant is used it takes so long achieve target. Below given Figure 7-32 to Figure 7-34 presents the results of the simulations for target 25, 16 and 2 degrees.

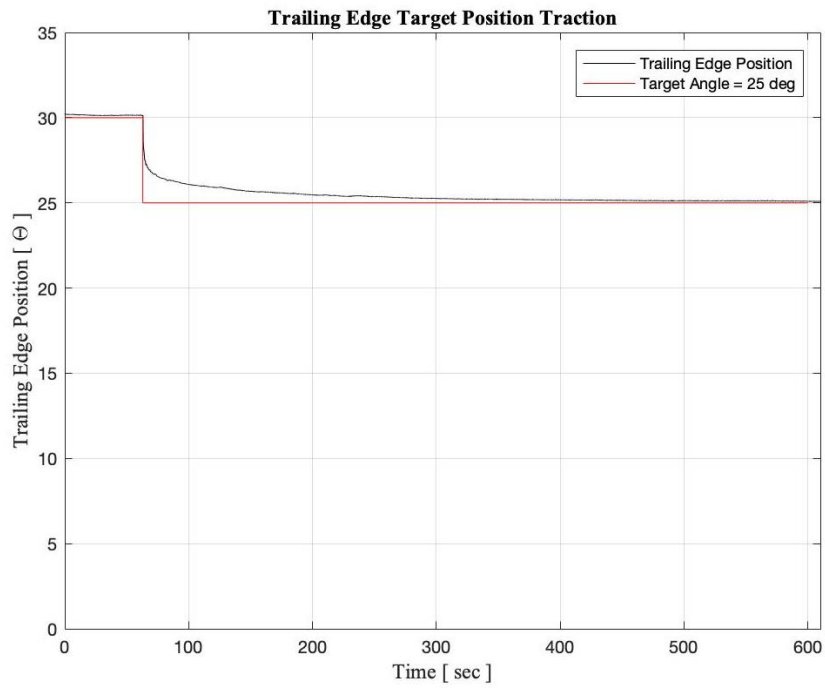


Figure 7-32 Target applied 25-degree camber position

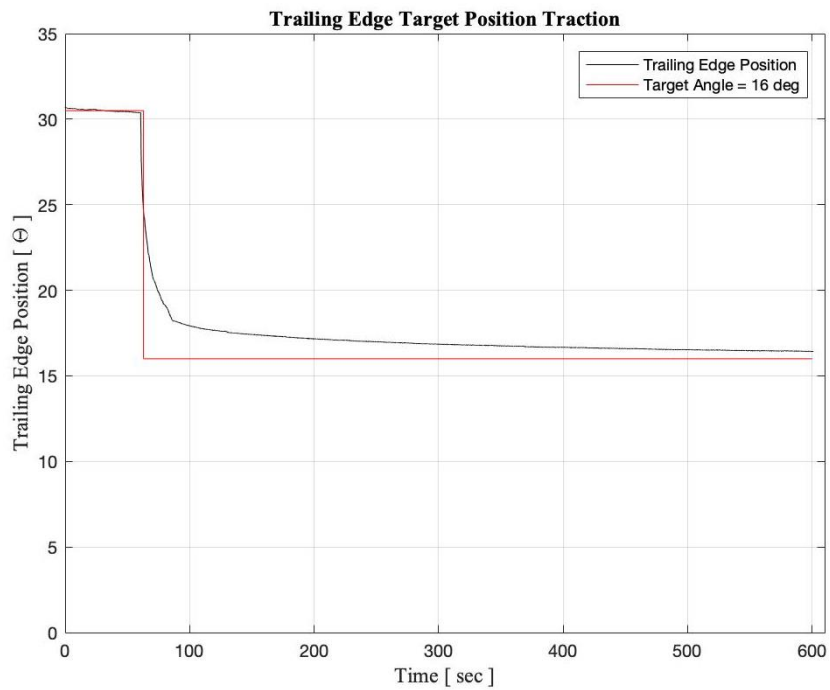


Figure 7-33 Target applied 16-degree camber position

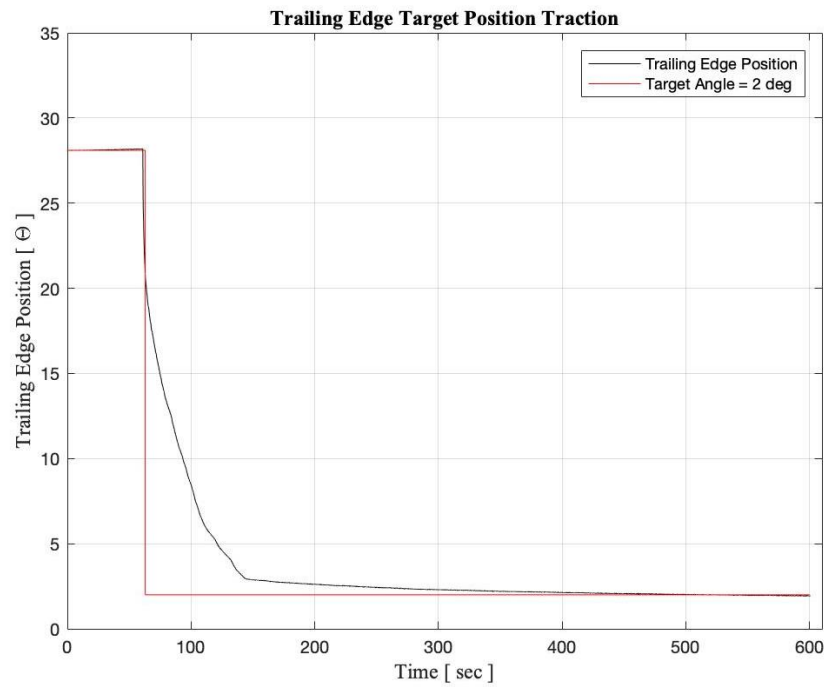


Figure 7-34 Target applied 2-degree camber position

Due to the application of voltage to DEA, trailing edge responds to target angular positions well. On the other hand, the response speed can be adjusted by the keeping the proportional constant high. The applied voltage is tuned by the controller according to the error calculation. The maximum allowed voltage is set to 2.5 kV. Thus, the response speed of DEA highly influenced. In fact, the manufactured DEA can sustain up to 4 kV, but such high voltages are not applied due to safety considerations. The applied voltage levels by the controller for the 2 degree camber position which is given in Figure 7-34 can be viewed in Figure 7-35. The controller applied the maximum 2.5 kV to DEA for 100 seconds and then decreased the voltage according to the calculated error.

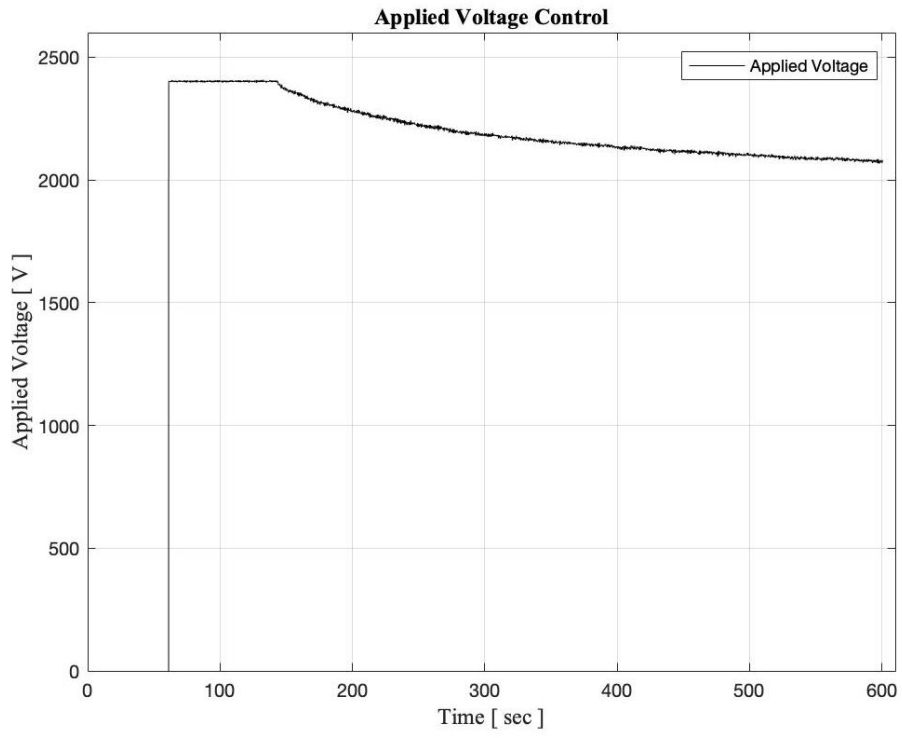


Figure 7-35 Applied voltage levels for target 2 degree camber position

## CHAPTER 8

### CONCLUSION

#### 8.1. Concluding Remarks

In this study, dielectric elastomer materials to be used in actuators as alternatives to conventional actuators and their potential is evaluated on the basis of a representative selection. The commercially available 3M's VHB 4905 and 4910 tape materials are selected in this research. It is observed that the performance characteristics of VHB 4905 and VHB 4910 are similar. However, VHB 4905 material is not a good choice when it comes to manufacturing; The sticky nature of the material combined with super thin structure proved to be hazardous. Thus, VHB 4905 is only used in material characterization phase.

The first step in the study was the material characterization. Mechanical behavior of the material was evaluated via uniaxial tensile tests, quad lap shear tests and volumetric compression tests. The quad lap shear tests and volumetric compression tests were used to calculate the shear and bulk modulus of the material to validate the incompressibility of the material. Uniaxial test results agreed well with the results from the strain energy function equations. The uniaxial tension tests were continued up to break levels that were not used in the later stages, but provided very meaningful information to understand material behavior. All the tests were performed at the predefined testing speeds. The strain energy function coefficients were obtained from parameter optimizations using these test results which might vary if alternative test speed were used. Since the final actuation demonstration was designed to actuate linearly, only uniaxial tests results were used to optimize the parameters; thus, no multi test optimization was required.

The second group of characterization tests were the creep and relaxation tests. These tests were good enough to represent the mechanical behavior of the material qualitatively, but the repetition of these tests with variable test speeds is strongly recommended.

In the second characterization stage, the dielectric elastomer actuator was used. DEA was manufactured for this purpose. As the actuation of the DEA was designed to operate linearly, VHB 4910 material was selected for ease of DEA production. Single and double layered DEAs were manufactured. For the demonstration of the concepts a model of a trailing edge of a 3D model wing like structure where the rotation of the trailing edge will be fulfilled via a linear actuating DEA was selected. The actuation with a single layer DEA was only considered in the model, but two layered DEA manufacturing and testing was also applied for a capability demonstration. The two layered DEA manufacturing is much more difficult with respect to single layer DEA, and the difficulty comes from the processing of the two single layers separately and combining them together.

Electromechanical tests involved four test groups. First group included the relaxation tests where the DEA was stretched to a predefined position and the internal stress drop was measured. The second group covered the blocking force experiments where the force drop on DEA with voltage application was measured. The third group of experiments were related to the creep tests, in which the DEA was loaded with a constant force and the resulting displacement was measured. The fourth and the final group included the voltage induced creep tests where the effect of voltage on creep response was monitored. It was shown that the stiffness of the DEA was higher than the base material itself.

Three strain energy functions are used throughout the study. These were Yeoh, Mooney-Rivlin and the Ogden models. These models are well known hyperelastic models that are capable to model the material while it is highly stretched. Ogden model has shown better performance for the region of applicability in both mechanical and

DMA tests. It is shown that the hyperelastic strain energy function coefficients can be estimated using relaxation and creep results. But, unfortunately these modes are not fast enough to react to the DEA motion when real time monitoring and control are considered. As a result, a more generic way of modeling, using creep/relaxation response functions, is chosen. The models are reformulated according to the applied end forces and combined creep compliances that can be used to model the DEAs using just the applied creep force and voltage value. The creep modeling of these models are among the major contributions of this study. It is shown that the mathematical models and test results are inline and the use of hyperelastic strain energy functions for real time applications is not necessary.

All the mathematical models are used in a 3D model wing structure. NACA 6520 profile is selected and used as an airfoil geometry. Electromechanical test setups and physical manufacturing of the wing structure are completed and the manufactured single layer DEA is used to activate the trailing edge.

It is shown that it is possible to camber a trailing edge using a linear single layer DEA. The angle position of the trailing edge can be adjustable and controllable. The aim of this study is to model and demonstrate the application of DEA to an aerial structure. It is shown in basic terms that the control of DEA on such a system is feasible. This study is the first concept investigation that concerns the use of the DEAs in a demonstrative wing concept.

## **8.2. Future Research Concerns**

Working with artificial muscle actuators is an exciting new research area. Especially the material parameters of the available and future dielectric elastomers require more investigations. A summary of the problems encountered in the study as well as the future research concerns revealed in various stages are given in the following.

Even though a significant number of publications are available in the literature, the material characterization phase is performed with a minimum number of experiments. For example, tests at different speeds rather than at a single test speed must be performed to clarify the effect of test speed on material behavior and material modeling. Also, a full analysis of the nonlinearity which is a serious concern in the variation of hyperelastic coefficients of the material is needed. For the quad lap shear test, the elastomer material is commonly tested in cured condition, but it is highly recommended to repeat the test without curing the material. It is observed in the study that the cured material results in a stiff compound which would be more meaningful if the material response is compared with the cured uniaxial and volumetric compression is used.

In this study, only the constant step voltages are applied on DEA while the DEA was continuously under constant creep loading. The researcher may try to apply constant voltages on DEA where there is no creep load i.e. applying voltage while material is as rest. On the other hand, even if the DEA is creep stressed, the high voltage can be applied at different time intervals. In this study, the voltage is applied after material is crept for a certain amount of time. This time duration was selected to be 600 seconds in electromechanical tests. Researchers can decrease or increase this time and shall record the result variations. Meanwhile, the type of voltage signal is an important concern which has not yet been exhaustively studied. The researcher may apply sinus, saw tooth, ramp or any other signal types to the DEA.

The production of DEA involves many aspects requiring further studies. The single layer DEA production is always straight forward. But when it comes to manufacturing more than one layer a speedy and reliable methodology is needed. 3D printing of the carbon black layer can be a solution which is a new era in literature. On the other hand, the geometry of the carbon black should be considered. Different geometries of carbon black would expected to have different electrical bonding which may results in different DEA actuator capabilities even in single layer. Thus, the electrical conductivity shall be a research area. In this study, only carbon black dust particles

and carbon grease are tried. It is observed that there are local aggregations occur on DEA if carbon grease is used. Moreover, the use of carbon grease is much more practical. It is suggested that the researchers investigate other electrode material options and the ways to avoid aggregations.

The frequency response of DE is investigated in literature but the frequency response analysis as a DEA is very limited. The frequency response can be studied for different actuator geometries with different applied carbon black electrode types. The frequency response should not be only considered as the response to applied voltage but it should also be considered as the frequency response of the applied creep and relaxation function parameters.

Pre-stretch is a major concern and a life-saving concept in DEAs. In this study, many pre-stretch levels are tried and it is observed that higher the pre-stretch superior the response of DEA to applied stimulus. In literature, it is shown that the pre-stretch and mathematical modeling can be combined, but the effect of pre-stretch on actuation performance does not appear. Especially for linear DEAs, the effect of width and length directional pre-stretches should be better understood.

The mathematical modeling of DE materials has been performed for a long time in literature. But these models are mainly limited to extraction of parameters from relaxation tests. There is almost no literature on modeling creep behavior using strain energy functions. So, creep models would be a good starting point for modeling purposes.

The failure modes of DEAs are shown and the observed ones during this study are presented. The effect of failure modes should be a hot topic for a researcher. The amount of stress decrease, fatigue and damage tolerance, life time of material and the boundary condition effect including the use and temperature conditions should be well outlined.

It is assumed that the DEA in action has a rectangular planar carbon coated area which means that there is no stress concentration exists through width direction. On the other

hand, this is just an assumption. The carbon coated area is not rectangular shaped thus the thickness variation along the DEA surface is not constant. The thinner region of DEA is its center.

Different and/or new DEA actuation models can be tried. In this study, only linear actuation is investigated but actuator based on contraction, rolled or bent actuators still are an alternative to the linear actuator.

The voltage source used in this study is massive which restricts out of laboratory applications. However, there are new alternative DC to DC voltage converters reported in literature. It is expected that development of miniaturized voltage sources will contribute significantly to a wider range of applications for the DEA.

## REFERENCES

- [1] T. Scheve, “How many muscles do we have?,” 2019. [Online]. Available: <https://science.howstuffworks.com/life/inside-the-mind/emotions/muscles>. [Accessed: 08-Mar-2019].
- [2] L. J. Romasanta, M. A. Lopez-Manchado, and R. Verdejo, “Increasing the performance of dielectric elastomer actuators: A review from the materials perspective,” *Prog. Polym. Sci.*, vol. 51, pp. 188–211, 2015.
- [3] W. C. Wang, “Electroactive polymers,” 2008. [Online]. Available: <http://depts.washington.edu/mictech/optics/sensors/week7.pdf>. [Accessed: 08-Mar-2018].
- [4] P. Ariano *et al.*, “Polymeric materials as artificial muscles: an overview.,” *J. Appl. Biomater. Funct. Mater.*, vol. 13, no. 1, pp. 1–9, 2015.
- [5] P. Brochu and Q. Pei, “Advances in dielectric elastomers for actuators and artificial muscles,” *Macromol. Rapid Commun.*, vol. 31, no. 1, pp. 10–36, 2010.
- [6] F. Zhu, C. Zhang, J. Qian, and W. Chen, “Mechanics of dielectric elastomers : materials , structures , and devices,” *Appl. Phys. Eng.*, vol. 17, no. 1, pp. 1–21, 2016.
- [7] Y. Bar-Cohen, “Electroactive Polymers as Artificial Muscles - Reality and Challenges,” in *Handbook on Biomimetics*, 2001, pp. 1–13.
- [8] K. Yuse, D. Guyomar, M. Kanda, L. Seveyrat, and B. Guiffard, “Development of large-strain and low-powered electro-active polymers (EAPs) using conductive fillers,” *Sensors Actuators A Phys.*, vol. 165, no. 2, pp. 147–154, 2011.
- [9] P. Hakansson, “Finite Element Modelling of A Rubber Block Exposed to Shock Loading,” M.Sc. Thesis, Lund University, Sweden, 2000.
- [10] MSC, “Nonlinear Finite Element Analysis of Elastomers,” 2014.
- [11] K. Çalışkan, E. I. Konukseven, and Y. S. Ünlüsoy, “Product-oriented material testing and FEA for hyperelastic suspension jounce bumper design,” *Int. J. Des. Eng.*, vol. 3, no. 4, pp. 374–391, 2010.
- [12] F. Carpi *et al.*, “Standards for dielectric elastomer transducers,” *Smart Mater. Struct.*, vol. 24, no. 10, p. 25, 2015.
- [13] M. Landgraf, U. Zorell, T. Wetzel, S. Reitelshöfer, I. S. Yoo, and J. Franke, “Dielectric elastomer actuators as self-sensing devices: a new method of superimposing actuating and sensing signals,” in *Electroactive Polymer Actuators and Devices (EAPAD)*, 2015, vol. 9430, no. 0, p. 943014.
- [14] Y. Bar-Cohen, “Artificial Muscles using Electroactive Polymers (EAP):

Capabilities, Challenges and Potential,” 2002.

- [15] K. J. Kim, X. Tan, H. R. Choi, and D. Pugal, *Biomimetic Robotic Artificial Muscles*. Singapore: World Scientific Publishing Co. Pte. Ltd., 2013.
- [16] Q. Pei, R. Pelrine, and R. D. Kornbluh, “Electroactive Polymers,” 2004. [Online]. Available: [http://en.wikipedia.org/wiki/Electroactive\\_polymers](http://en.wikipedia.org/wiki/Electroactive_polymers). [Accessed: 18-May-2015].
- [17] G. Errico, V. Fava, F. Resta, and F. Ripamonti, “Use of spring-roll EAP actuator applied as end-effector of a hyper-redundant robot,” *Act. Passiv. Smart Struct. Integr. Syst.*, vol. 9431, p. 94312V, 2015.
- [18] W. Kaal and S. Herold, “Electroactive polymer actuators in dynamic applications,” *IEEE/ASME Trans. Mechatronics*, vol. 16, no. 1, pp. 24–32, 2011.
- [19] Y. Bar-Cohen, “Low Mass Muscle Actuators (LoMMAs).” p. 18, 1997.
- [20] P. Thummala, L. Huang, Z. Zhang, and M. A. E. Andersen, “Analysis of Dielectric Electro Active Polymer actuator and its high voltage driving circuits,” in *2012 IEEE International Power Modulator and High Voltage Conference (IPMHVC)*, 2012, vol. 2, no. 2, pp. 458–461.
- [21] P. Lotz, M. Matysek, and H. F. Schlaak, “Fabrication and application of miniaturized dielectric elastomer stack actuators,” *IEEE/ASME Trans. Mechatronics*, vol. 16, no. 1, pp. 58–66, 2011.
- [22] S. H. Akbari, S. Rosset, and H. R. Shea, “More than 10-fold increase in the actuation strain of silicone dielectric elastomer actuators by applying prestrain,” in *Electroactive Polymer Actuators and Devices (EAPAD)*, 2013, vol. 8687, p. 86871P.
- [23] K. Kadooka, M. Taya, K. Naito, and M. Saito, “Modeling of a corrugated dielectric elastomer actuator for artificial muscle applications,” in *Electroactive Polymer Actuators and Devices (EAPAD)*, 2015, vol. 9430, p. 943020.
- [24] M. Fontana, “New mechanisms and concepts for exploiting electroactive Polymers for Wave Energy Conversion,” 2015. [Online]. Available: [http://www.wavec.org/content/files/01\\_Marco\\_Fontana\\_Scuola\\_SantAnna.pdf](http://www.wavec.org/content/files/01_Marco_Fontana_Scuola_SantAnna.pdf). [Accessed: 05-Mar-2017].
- [25] S. J. A. Koh *et al.*, “Mechanisms of large actuation strain in dielectric elastomers,” *J. Polym. Sci. Part B Polym. Phys.*, vol. 49, no. 7, pp. 504–515, 2011.
- [26] M. Potter, K. Gouder, and J. F. Morrison, “A numerical model for electro-active polymer actuators with experimental validation,” *Sensors Actuators, A Phys.*, vol. 170, no. 1–2, pp. 121–130, 2011.

- [27] R. Sarban, R. W. Jones, B. R. Mace, and E. Rustighi, "A tubular dielectric elastomer actuator: Fabrication, characterization and active vibration isolation," *Mech. Syst. Signal Process.*, vol. 25, no. 8, pp. 2879–2891, 2011.
- [28] G. Kofod, "Dielectric Elastomer Actuators," Ph.D. Thesis, The Technical University of Denmark, Denmark, 2001.
- [29] S. Lee, K. J. Kim, and I.-S. Park, "Modeling and experiment of a muscle-like linear actuator using an ionic polymer–metal composite and its actuation characteristics," *Smart Mater. Struct.*, vol. 16, no. 3, pp. 583–588, 2007.
- [30] V. K. Nguyen, J. W. Lee, and Y. Yoo, "Characteristics and performance of ionic polymer-metal composite actuators based on Nafion/layered silicate and Nafion/silica nanocomposites," *Sensors Actuators, B Chem.*, vol. 123, no. 1, pp. 183–190, 2007.
- [31] M. C. Akbay, "Performance of Compliant Electrodes in Electro Active Polymer (EAP) Actuators," M.Sc. Thesis, North Carolina State University, U.S., 2004.
- [32] "Intelligent Polymer Research Institute." [Online]. Available: <http://ipri.uow.edu.au/index.html>. [Accessed: 25-Dec-2015].
- [33] G. Alici and N. N. Huynh, "Performance quantification of conducting polymer actuators for real applications: A microgripping system," *IEEE/ASME Trans. Mechatronics*, vol. 12, no. 1, pp. 73–84, 2007.
- [34] G. Alici, G. Spinks, J. D. Madden, Y. Wu, and G. Wallace, "An Investigation into Behaviour of Electroactive Polymers as Mechanical sensors," *IEEE/ASME Int. Conf. Adv. Intell. Mechatronics*, pp. 1–6, 2007.
- [35] A. Punning, M. Kruusmaa, and A. Aabloo, "A self-sensing ion conducting polymer metal composite (IPMC) actuator," *Sensors and Actuators*, vol. 136, no. 2, pp. 656–664, 2007.
- [36] F. Branz, A. Antonello, A. Carron, R. Carli, and A. Francesconi, "Kinematics and control of redundant robotic arm based on dielectric elastomer actuators," in *Electroactive Polymer Actuators and Devices (EAPAD)*, 2015, vol. 9430, pp. 1–13.
- [37] J. Shintake, S. Rosset, B. E. Schubert, D. Floreano, and R. S. Herbert, "A Foldable Antagonistic Actuator," *IEEE/ASME Trans. Mechatronics*, vol. 20, no. 5, pp. 1997–2008, 2015.
- [38] G. Buchberger, J. Schoeftner, S. Bauer, B. Jakoby, and W. Hilber, "A comparison of the electromechanical characteristics of dielectric elastomer minimum energy structures (DEMES) and planar dielectric elastomer actuators (p-DEAs)," in *Electroactive Polymer Actuators and Devices (EAPAD)*, 2013, vol. 8687, p. 86871G.

- [39] R. Pelrine *et al.*, “Dielectric elastomer artificial muscle actuators: toward biomimetic motion,” in *Electroactive Polymer Actuators and Devices (EAPAD)*, 2002, vol. 4695, no. 3, pp. 126–137.
- [40] S. J. A. Koh, C. Keplinger, T. Li, S. Bauer, and Z. Suo, “Dielectric Elastomer Generators: How Much Energy Can Be Converted?,” *IEEE/ASME Trans. Mechatronics*, vol. 16, no. 1, pp. 33–41, 2011.
- [41] N. H. Chuc *et al.*, “Fabrication and Control of Rectilinear Artificial Muscle Actuator,” *IEEE/ASME Trans. Mechatronics*, vol. 16, no. 1, pp. 167–176, 2011.
- [42] T. A. Gisby, B. M. O’Brien, S. Q. Xie, E. P. Calius, and I. A. Anderson, “Closed loop control of dielectric elastomer actuators,” in *Electroactive Polymer Actuators and Devices (EAPAD)*, 2011, vol. 7976, 7976, pp. 1–9.
- [43] 3M, “3M™ Technical Data VHB™ Tape - Specialty Tapes,” 2016.
- [44] J. Biggs *et al.*, “Electroactive polymers: Developments of and perspectives for dielectric elastomers,” *Angew. Chemie - Int. Ed.*, vol. 52, no. 36, pp. 9409–9421, 2013.
- [45] M. Wissler, “Modeling Dielectric Elastomer Actuators,” Ph.D. Thesis, Swiss Federal Institute of Technology, Switzerland, 2007.
- [46] G. Yang, G. Yao, W. Ren, G. Akhras, J. P. Szabo, and B. K. Mukherjee, “The strain response of silicone dielectric elastomer actuators,” in *Electroactive Polymer Actuators and Devices (EAPAD)*, 2005, vol. 5759, pp. 134–143.
- [47] J. W. Fox and N. C. Goulbourne, “On the dynamic electromechanical loading of dielectric elastomer membranes,” *J. Mech. Phys. Solids*, vol. 56, no. 8, pp. 2669–2686, 2008.
- [48] K. Jung, K. J. Kim, and H. R. Choi, “A self-sensing dielectric elastomer actuator,” *Sensors Actuators A Phys.*, vol. 143, no. 2, pp. 343–351, 2008.
- [49] W. Jung and Y. Toi, “Computational Modeling of Electromechanical Behaviors of Dielectric Elastomer Actuators,” in *Proceedings of the International MultiConference of Engineers and Computer Scientists*, 2010, vol. 0958.
- [50] M. Wissler and E. Mazza, “Electromechanical coupling in dielectric elastomer actuators,” *Sensors and Actuators*, vol. 138, no. 2, pp. 384–393, 2007.
- [51] F. Carpi and D. De Rossi, “Theoretical Description and Fabrication of a New Dielectric Elastomer Actuator Showing Linear Contractions,” in *International Conference on New Actuators*, 2004, pp. 344–347.
- [52] F. Carpi, P. Chiarelli, A. Mazzoldi, and D. De Rossi, “Electromechanical characterisation of dielectric elastomer planar actuators: comparative evaluation of different electrode materials and different counterloads,” *Sensors and Actuators*, vol. 107, no. 1, pp. 85–95, 2003.

- [53] H. R. Choi *et al.*, “Soft actuator for robotic applications based on dielectric elastomer: quasi-static analysis,” in *Proceedings 2002 IEEE International Conference on Robotics and Automation (Cat. No.02CH37292)*, 2002, vol. 3, no. May, pp. 2–7.
- [54] N. C. Goulbourne, E. M. Mockensturm, and M. I. Frecker, “Electro-elastomers: Large deformation analysis of silicone membranes,” *Int. J. Solids Struct.*, vol. 44, no. 9, pp. 2609–2626, 2007.
- [55] J. W. Fox and N. C. Goulbourne, “Electric field-induced surface transformations and experimental dynamic characteristics of dielectric elastomer membranes,” *J. Mech. Phys. Solids*, vol. 57, no. 8, pp. 1417–1435, 2009.
- [56] F. Carpi and D. De Rossi, “Dielectric elastomer cylindrical actuators: Electromechanical modelling and experimental evaluation,” *Mater. Sci. Eng. C*, vol. 24, pp. 555–562, 2004.
- [57] Akzonobel, “Ketjenblack EC-300J,” 2011.
- [58] AkzoNobel, “Ketjenblack EC-600JD,” no. November, pp. 1–2, 2011.
- [59] G. Kofod, P. Sommer-Larsen, R. D. Kornbluh, and R. Pelrine, “Actuation Response of Polyacrylate Dielectric Elastomers,” *J. Intell. Mater. Syst. Struct.*, vol. 14, no. 12, pp. 787–793, 2003.
- [60] J. S. Plante and S. Dubowsky, “Large-scale failure modes of dielectric elastomer actuators,” *Int. J. Solids Struct.*, vol. 43, no. 25–26, pp. 7727–7751, 2006.
- [61] J. S. Plante and S. Dubowsky, “On the performance mechanisms of Dielectric Elastomer Actuators,” *Sensors and Actuators*, vol. 137, no. 1, pp. 96–109, 2007.
- [62] G. Kofod and P. Sommer-Larsen, “Silicone dielectric elastomer actuators: Finite-elasticity model of actuation,” *Sensors Actuators, A Phys.*, vol. 122, no. 2, pp. 273–283, 2005.
- [63] C. Federico, M. Antonio, S. Giorgio, and R. Danilo De, “Helical dielectric elastomer actuators,” *Smart Mater. Struct.*, vol. 14, no. 6, p. 1210, 2005.
- [64] M. Wissler and E. Mazza, “Mechanical behavior of an acrylic elastomer used in dielectric elastomer actuators,” *Sensors and Actuators*, vol. 134, no. 2, pp. 494–504, 2007.
- [65] V. Kanyanta and A. Ivankovic, “Mechanical characterisation of polyurethane elastomer for biomedical applications,” *J. Mech. Behav. Biomed. Mater.*, vol. 3, no. 1, pp. 51–62, 2010.
- [66] O. D. Okay, “Validation of Structural Analysis Model of a Layered Structure

- With Elastomeric Components,” M.Sc. Thesis, Middle East Technical University, Turkey, 2010.
- [67] P. Sommer-Larsen, G. Kofod, S. Mh, M. Benslimane, and P. Gravesen, “Performance of dielectric elastomer actuators and materials,” in *Electroactive Polymer Actuators and Devices (EAPAD)*, 2002, vol. 4695, no. 1, pp. 158–166.
- [68] H. R. Choi *et al.*, “Biomimetic soft actuator: Design, modeling, control, and applications,” *IEEE/ASME Trans. Mechatronics*, vol. 10, no. 5, pp. 581–593, 2005.
- [69] L. Liu, H. Chen, J. Sheng, and J. Zhang, “Experimental study on the dynamic response of in-plane deformation of dielectric elastomer under alternating electric load,” *Smart Mater. Struct.*, vol. 23, p. 12, 2014.
- [70] G. Yang, W. Ren, B. K. Mukherjee, J. Leidner, and J. P. Szabo, “Performance of Multi-Layer Electroactive Polymer Actuators Used for Active Vibration Control,” in *CanSmart International Workshop on Smart Structures and Materials*, 2004.
- [71] F. Carpi and E. Smela, *Biomedical Applications of Electroactive Polymer Actuators*, First Edit. West Sussex, United Kingdom: John Wiley & Sons Ltd., 2009.
- [72] G. Yang, W. Ren, G. Akhras, and B. K. Mukherjee, “Transverse strain of silicone dielectric elastomer actuators,” *J. Adv. Sci.*, vol. 18, pp. 166–169, 2006.
- [73] Z. Suo, “Theory of dielectric elastomers,” *Acta Mech. Solida Sin.*, vol. 23, no. 6, pp. 549–578, 2010.
- [74] M. Moscardo, X. Zhao, Z. Suo, and Y. Lapusta, “On designing dielectric elastomer actuators,” *J. Appl. Phys.*, vol. 104, no. 9, p. 093503, 2008.
- [75] M. Hossain, D. K. Vu, and P. Steinmann, “Experimental study and numerical modelling of VHB 4910 polymer,” *Comput. Mater. Sci.*, vol. 59, pp. 65–74, 2012.
- [76] G. A. Holzapfel, *Nonlinear Solid Mechanics A Continuum Approach for Engineering*. New York, USA: John Wiley & Sons Ltd., 2000.
- [77] K. . Y. Volokh, “Mechanics of Soft Materials,” in *MEchanics of Soft Materials*, Israel Institute of Technology, 2010, pp. 1–84.
- [78] G. Berselli, R. Vertechy, M. Pellicciari, and G. Vassura, “Hyperelastic Modeling of Rubber-Like Photopolymers for Additive Manufacturing Processes,” *Rapid Prototyp. Technol. - Princ. Funct. Requir.*, pp. 135–152, 2011.
- [79] B. McGinty, “Continuum Mechanics.” [Online]. Available: <http://www.continuummechanics.org/mooneyrivlin.html>. [Accessed: 27-May-

- 2017].
- [80] L. Crocker and B. Duncan, “Measurement Methods for Obtaining Volumetric Coefficients for Hyperelastic Modelling of Flexible Adhesives,” Teddington, Middlesex, UK, 2001.
- [81] B. Duncan and L. Crocker, “Characterisation of Flexible Adhesives for Design,” Teddington, Middlesex, UK, 2001.
- [82] K. Miller, “Some Things About Elastomers,” *MSC Elastomers Seminar*, 2012. [Online]. Available: <http://www.axelproducts.com/downloads/MSCElastomerSeminarApril2012.pdf>. [Accessed: 06-Mar-2017].
- [83] R. Abeyaratne, “Continuum Mechanics, Volume II of Lecture Notes on The Mechanics of Elastic Solids,” 2012. [Online]. Available: [http://web.mit.edu/abeyaratne/lecture notes.html](http://web.mit.edu/abeyaratne/lecture%20notes.html). [Accessed: 17-Apr-2017].
- [84] A. Ali, M. Hosseini, and B. B. Sahari, “A Review of Constitutive Models for Rubber-Like Materials,” *Am. J. Eng. Appl. Sci.*, vol. 3, no. 1, pp. 232–239, 2010.
- [85] O. H. Yeoh, “Characterization of Elastic Properties of Carbon-Black-Filled Rubber Vulcanizates,” in *Rubber Division, American Chemical Society*, 1990, vol. 63, no. 5, pp. 792–805.
- [86] M. A. Hassan, M. Hamdi, and A. Noma, “The Nonlinear Elastic and Viscoelastic Passive Properties of Left Ventricular Papillary Muscle of a Guinea Pig Heart,” *J. Mech. Behav. Biomed. Mater.*, vol. 5, no. 1, pp. 99–109, 2012.
- [87] J. S. Plante, “Dielectric Elastomer Actuators for Binary Robotics and Mechatronics,” Ph.D. Thesis, Massachusetts Institute of Technology, U. S., 2006.
- [88] J. W. Fox, “Electromechanical characterization of the static and dynamic response of dielectric elastomer membranes,” M.Sc. Thesis, Virginia Polytechnic Institute and State University, U. S., 2007.
- [89] M. Rackl, “Curve Fitting for Ogden , Yeoh and Polynomial Models.” p. 18, 2015.
- [90] U. of Minnesota, “Long term performance of polymers,” *Univ. Minnesota*, pp. 1–11, 2001.
- [91] MSC, “Nonlinear Finite Element Analysis of Elastomers,” *MSC. Software Corporation*, 2000. [Online]. Available: <http://www.axelproducts.com/downloads/MARCFEAELASTOMERS2000.pdf>. [Accessed: 23-Apr-2017].

- [92] J. S. Bergström, *Mechanics of Solid Polymers*. Elsevier, 2015.
- [93] G. C. Papanicolaou and S. P. Zaoutsos, “Viscoelastic constitutive modeling of creep and stress relaxation in polymers and polymer matrix composites,” in *Creep and Fatigue in Polymer Matrix Composites*, Woodhead Publishing Limited, 2010, pp. 3–47.
- [94] P. J. G. Schreurs, “Computational Material Models, Lecture Notes - Course 4K620,” Eindhoven, 2014.
- [95] T. Chen, “Determining a Prony Series for a Viscoelastic Material Series for a From Time Varying Strain Data,” Hampton, Virginia, U. S., 2000.
- [96] H. Danielsson and P. Björnsson, “Strength and Creep Analysis of Glued Rubber Foil Timber Joints,” M.Sc. Thesis, Lund University, Sweden, 2005.
- [97] J. S. Bergström, “Calculation of Prony Series Parameters From Dynamic Frequency Data,” 2005.
- [98] Simulia, “Abaqus 6.14 Analysis User’s Guide.” [Online]. Available: <http://abaqus.software.polimi.it/v6.14/books/usb/default.htm>. [Accessed: 08-Jun-2017].
- [99] V. L. Tagarielli, R. Hildick-Smith, and J. E. Huber, “Electro-mechanical properties and electrostriction response of a rubbery polymer for EAP applications,” *Int. J. Solids Struct.*, vol. 49, no. 23–24, pp. 3409–3415, 2012.
- [100] D. Roylance, “Engineering Viscoelasticity,” in *Material Science*, 2001, pp. 1–37.
- [101] K. Miller, “Testing and Analysis,” *Testing and Analysis*, 2004. [Online]. Available: <http://www.axelproducts.com/downloads/TestingForHyperelastic.pdf>. [Accessed: 08-Jun-2017].
- [102] MSC, *Experimental Elastomer Analysis*. 2010.
- [103] D. D. Bortoli, E. Wrubleski, and R. J. Marczak, “Hyperfit – Curve Fitting Software For Incompressible Hyperelastic Material Models,” in *21st Brazilian Congress of Mechanical Engineering*, 2011.
- [104] B. Rashid, M. Destrade, and M. D. Gilchrist, “Mechanical characterization of brain tissue in tension at dynamic strain rates,” *J. Mech. Behav. Biomed. Mater.*, vol. 28, pp. 1–31, 2012.
- [105] M. Destrade, J. G. Murphy, and G. Saccomandi, “Simple shear is not so simple,” *Int. J. Non. Linear. Mech.*, vol. 47, pp. 210–214, 2012.
- [106] B. Rashid, M. Destrade, and M. D. Gilchrist, “Hyperelastic and Viscoelastic Properties of Brain Tissue in Tension,” *Proc. ASME 2012 Int. Mech. Eng.*

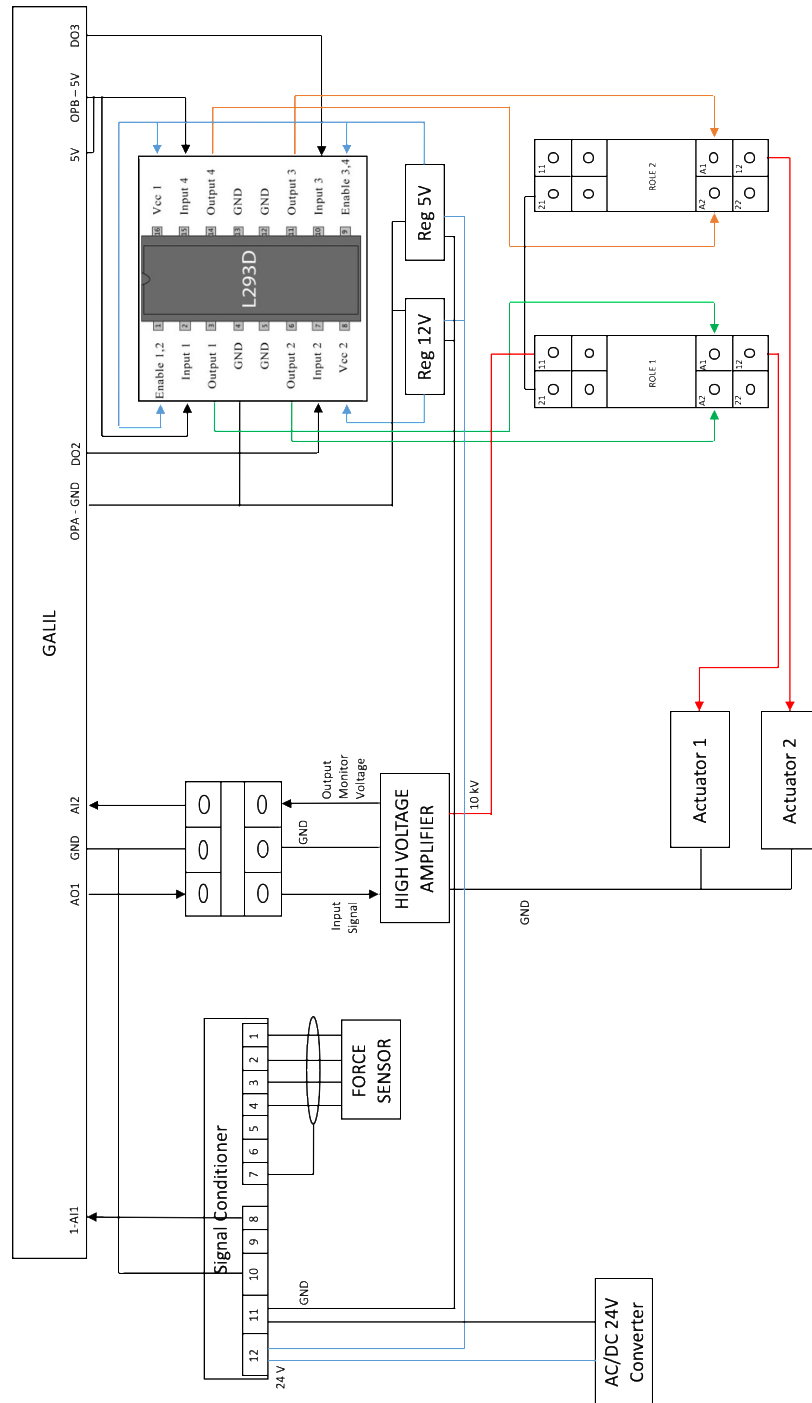
*Congr. Expo.*, p. 921, 2012.

- [107] M. Hamid and R. Ghoreishy, “Determination of the parameters of the Prony series in hyper-viscoelastic material models using the finite element method,” *J. Mater. Des.*, vol. 35, pp. 791–797, 2012.



# APPENDICES

## A. WIRING DIAGRAM



## B. GALIL CODE

```
'POWER-UP SUBROUTINE
#AUTO
'SUBROUTINE MAIN run at startup
#MAIN
'Set default Kp, Ki and Kd
d_Kp=13;d_Ki=0.1;d_Kd=20
Kp_d_Kp;Ki_d_Ki;Kd_d_Kd
'Set current position as 0
DPA=0
'Set default position error [micrometer]
d_er=5
ERd_er
'Disable the off on error function
OE0
'Set analog input configurations to +-10 Volt
'Analog Input 1: Force sensor
AQ1,2
'Analog Input 2: Applied voltage
AQ2,2
'Set motor type as servo motor
MT1
'Set default spd, acc & dec values
d_spd=500000;d_acc=1000000;d_dec=1000000
'Set encoder type as normal quadrature
'Each pulse is 1 micrometer
CE0
'Set limit switches as active low
CN-1
'Set default volt2newton conversion coefficient
v2n_d=-10.265
'Logical variable to check if force sensor will be read
'Force => readF=1, Ext. Dist => readF=0
readF=1
'Logical variable to check if voltage or current will be read
'Volt => readV=1, Current => readV=0
readV=1
'Initialize necessary variable to avoid errors
L0=0;'initial length of sample in mm
lambda=1;'default stretch ratio
vApp=0;'defaul applied voltage
```

```

fOfs=0;'default force reading offset value in [N]
spd_R=500000;'default spd for relaxation
acc_R=999424;'default acc for relaxation
dec_R=999424;'default dec for relaxation
home=0; 'checks if table is homed
lambda=1; 'stretch ration
reading=0; 'checks if reading should start
F_0=0;'offset value for force readings
delta_t=-10;'default waiting duration between each sensor measurement [msec]
dt_Start=-10;'default period for taking sensor measurements in the beginning of
'Relaxation test [msec]
dt_Test=-10;'default period for taking sensor measurements during relaxation
'[msec]
tDur=1000;'default duration of the test in [msec]
'DEFAULT VARIABLES FOR CREEP TEST
fOfs=0;'default force reading offset value in [N]
spd_C=5000;'default spd for creep
acc_C=9216;'default acc for creep
dec_C=9216;'default dec for creep
fTol_C=0.01;'default force tolerance value in [N]
deltaT_C=-100;'default period of measurements for creep [microSec]
cTest=0;'logical variable to check if creep test is in progress
tSteady=3600000;'default waiting time before starting to apply voltage
T=-60000;'default period of voltage application cycle
spd_end=500;'default ending speed
acc_end=1024;'default ending acceleration
dec_end=1024;'default ending deceleration
fLength=0;'final position of the cart at the end of test
vApp=0;'default applied voltage value
WT1000
MG"DEVICE OPENED"
EN
'-----'
'Table homing subroutine
#HOME
'Start the motor
SHA
'Wait 500 milliseconds
WT500
'Set current position as 0
DPA=0
'Start jogging to the left with 5000 cnts/sec
'Each count/pulse is 1 micrometer
JG-5000

```

```

'Define target as finding home index
FIA
'Start motion
BGA
'After finding home, inform user & define new 0
AMA;MG"AXIS HOMED";WT500;DPA=0
'Turn off the motor and set home variable to 1
WT500;MO;home=1
EN
'-----'
'Creep test subroutine
#CREEP
MG"Length of sample=",L0
MG"Target force=",fTar
MG"CREEP TEST STARTED"
'Set output voltage to 0V to be on the safe side
AO2,0
'Set spd, acc and dec values
SPA=spd_C;ACA=acc_C;DCA=dec_C
'Set current position as 0
DPA=0
'Start the motor
SHA
'Start with finding out force reading offset
JS#FORCE0
'Set force tolerance value
fTol=fTol_C
'Set delta_t for test readings
delta_t=deltaT_C
'Set logical variable reading to 1 to indicate sensor reading in progress
reading=1
stopRead=0
cTest=1
'Start taking sensor measurements
XQ#READFPV,1
'Start force control
XQ#FCONT,2
'Continue controlling the force for tSteady msec with 0V applied voltage
WTtSteady
'Start applying voltage to the sample
JS#VPWM
'After completing voltage application stop force control
cTest=0
'Set fLength as final length of the material

```

```

fPose=L0-fLength
fPose=fPose*1000
WT500
PAfPose
'Re-set spd, acc and dec values for closing
SPA=spd_end;ACA=acc_end;DCA=dec_end
BGA
AMA
stopRead=1
#wCreep
WT10
JP#wCreep,(reading<>0)
ST
MO
MG"CREEP TEST COMPLETED"
EN
'-----'
#VPWM
MG"VOLTAGE IS BEING APPLIED"
#prdLoop
'Set duty time Td
Td=T*duty
'initialize test number with current duty cycle
tCount=1
AT0
#dtyLoop
'Apply vApp to the sample
AO2,vApp
ATTd
AO2,0
ATT,0
tCount=tCount+1
JP#dtyLoop,(tCount<=testNum)
'After completing testNum many tests with current dutyCycle increase duty
duty=duty+dutyInc
JP#prdLoop,(duty<=dutyMax)
MG"VOLTAGE APPLICATION COMPLETED"
EN
'-----'
'Subroutine to control force reading equal to target value
#FCONT
'Period of force reading and control sequence
fTime=-50
AT0

```

```

#fLoop
'Take force measurement and convert to N
fRead=@AN[1]*v2n-fOfs
'Calculate difference btwn. reading and target force values
fDiff=fRead-fTar
'Calculate absolute value of the force difference
afDiff=@ABS[fDiff]
'Check if the force difference is higher than the tolerance value
IF(afDiff>fTol)
'set the realtive distance to be traveled to eliminate force difference
relDist=fDiff*1000
PRrelDist
BGA
AMA
ENDIF
ATfTime,0
JP#fLoop,(cTest=1)
MG"FORCE CONTROL STOPPED"
EN
'-----'
'Subroutine to find the offset value for force readings
#FORCE0
'Check if force or ext. dist. sensor will be read
IF(readF=0)
'Set v2n to unity
v2n=1
'Set measurement offset to 0
fOfs=0
ELSE
'Set v2n to default sensor coefficient
v2n=v2n_d
'Find out force reading offset
'Initialize force reading and force ofset value storing variable
fOfs=0
'Time between each measurements
t_inc=-5;index=0
AT0
#lpF0
'Read the force value and convert it to newton
f_read=@AN[1]*v2n
'Update fOfs with the new value
fOfs=fOfs+f_read
'increase the index number by 1
index=index+1

```

```

'wait for t_inc milliseconds
ATt_inc,0
'Keep collecting data till 3000 measurements are taken
JP#lpF0,(index<3000)
'Calculate the force reading offset after collecting 3000 measurements
fOfs=fOfs/3000
'Inform the user that ofset in the force reading is found
MG"FORCE READING OFFSET DETERMINED"
ENDIF
EN
'-----'
'Force, position and voltage reading subroutine
#READFPV
'Deallocate all the arrays, if there is any
DA*[0]
'Create pose,AI1,AI2 arrays
'pose for lathe's position
'AI1 for force or ext. dist. sensor measurements
'AI2 for volt or current measurements
DMpose[1000],AI1[1000],AI2[1000]
'Set INDEX of reading to 0
INDEX=0
MGTIME
MGdelta_t
AT0
#lpRead
'Calculate the position relative to the starting point
pose[INDEX]=L0-(TPA/1000)
'Take sensor measurement on analog input 1
'If force is read, then convert it to newton
AI1[INDEX]=@AN[1]*v2n-fOfs
'Take sensor measurement on analog input 2
'Read the applied voltage/current to the sample
AI2[INDEX]=@AN[2]
INDEX=INDEX+1
'wait for delta_t milliseconds
ATdelta_t,0
'Keep looping till the whole array is filled
JP#lpRead,((INDEX<1000)&(reading=1))
MG"POSE ARRAY";QUpose[,,,1]
MG"AI1 ARRAY";QUAI1[,,,1]
MG"AI2 ARRAY";QUAI2[,,,1]
IF(stopRead<>1)
INDEX=0

```

```

MGTIME
MGdelta_t
AT0
JP#lpRead
ENDIF
reading=0
'MG"SENSOR READING STOPPED"
EN
'-----'
'Relaxation subroutine
#RELAX
'Display to user initial length,lambda and vApp
MG"L=",L0
MG"lambda=",lambda
MG"RELAXATION TEST STARTED"
'Set output voltage to 0V to be on the safe side
AO2,0
'Calculate sensor reading offset
JS#FORCE0
'Set current position as 0
DPA=0
'Set spd, acc and dec values
SPA=spd_R;ACA=acc_R;DCA=dec_R
'set period for taking measurements in the beginning of relaxation test
dt_Rs=dt_Start
'set period for taking measurements during relaxation test
dt_Rt=dt_Test
'Run relaxation test start procedure
JS#RELAX_S
'Set logical variable reading to 1 to indicate sensor reading in progress
reading=1
stopRead=0
delta_t=dt_Rt
XQ#READFPV,1
'Wait for tDur msec. and keep collecting relaxation test data
WTtDur
'Set fLength as final length of the material
fPose=L0-fLength
fPose=fPose*1000
PAfPose
'Re-set spd, acc and dec values for closing
SPA=spd_end;ACA=acc_end;DCA=dec_end
BGA
AMA

```

```

stopRead=1
#wRelax
WT10
JP#wRelax,(reading<>0)
ST
MO
MG"RELAXATION TEST COMPLETED"
EN
'-----'
'Starting subroutine of relaxation test
#RELAX_S
MG"RELAXATION PROCEDURE IN PROGRESS"
'Compute the elongation of sample in mm
deltaX=L0*(1-lambda)
'Compute target position xTar in um
xTar=deltaX*1000
'Set reading variable to 1 to start reading procedure
reading=1
stopRead=0
'Turn on the motor
SHA
'Set delta_t to dt_Start
delta_t=dt_Rs
'Start reading p, f & v in background parallel to control actions
XQ#READFPV,1
WT500
'Set target position and start moving
PAxTar;BGA
'After reaching target position check for error in pos. till reading ends
AMA
'Set stop reading logical variable to 1 after reaching target position
stopRead=1
#lpPose
x_dif=xTar-_TPA
'If position error is higher than tolerance values, then adjust position
IF(@ABS[x_dif]>_ERA)
PRx_dif;BGA
AMA
ENDIF
'Keep looping till the reading procedure ends
JP#lpPose,(reading=1)
EN
'-----'
'Distance sensor measurement routine

```

```
#DIST
AT0
'Take distance and voltage measurements and send to computer with time
'@AN[1] for distance and @AN[2] for voltage reading
t=TIME
d=@AN[1]
v=@AN[2]
IF@OUT[2]
v=v*(-1)
ENDIF
MGt,d,v
'wait for delta_t milliseconds
ATdelta_t,0
'Go back to DIST and keep reading sensors till program stopped
JP#DIST
EN
```

## CURRICULUM VITAE

### PERSONAL INFORMATION

Surname, Name : Çamlıca, Fahri Buğra  
Nationality : Turkish (TC)  
Date and Place of Birth : 31 January 1978, Ankara  
Phone : -  
E-mail : bugracamlica@gmail.com

### EDUCATION

Degree	Institution	Year of Graduation
MS	METU, Mechanical Engineering	2004
BS	DEU, Mechanical Engineering	2000
High School	Antalya Lisesi, Antalya	1996

### WORK EXPERIENCE

Year	Place	Enrollment
2008-Present	Turkish Aerospace	Structural Analysis Engineer
2001-2008	Başkent Üniversitesi	Lecturer

### FOREIGN LANGUAGES

English

### PUBLICATIONS

1. Çamlıca, F. B., Erden A., “Uçan Robotlar”, Bilim ve Teknik, Robotik-1, sf.16-17, 2003
2. Çamlıca, F.B., Erden A., “Flying Robot Technologies”, Industry & Automation Magazine, 2001
3. Genç, Y.K., Çamlıca, F.B., “Mechanical Component Selection Optimization”, Industrial Engineering Congress, Adana, Turkey, 2004
4. Ozkok O, Pakdil F., Camlica F.B., Bektaş T., Kara I., “A Pathway for process Improvement Activities in a Production Environment: A Case Study in a Rework Department”, BMP Conference, France, 2005

5. amlıca F.B., Ünlüsoy S., “Dielectric Material Characterization and Modeling for Use in Aerial Structures”, VII. Polymer Science & Technology Congress with International Participation, Eskisehir, 2018

## **HOBBIES**

Computer Technologies, Farming, Arts & Crafts, Cooking